

# Nanoscale Modelling of Point and Extended Defects in mc-Si Solar Cell



Oras A Al-Ani

Newcastle University

Newcastle upon Tyne, UK.

A thesis submitted for the degree of

*Doctor of Philosophy*

June 2018

# Dedication

*Every challenging work needs effort as well as the guidance of elders,  
especially those who are very close to our heart.*

*My humble efforts I dedicate to:*

*my parents **Mr Ahmed Al-Ani and Mrs Aida Abdul-Lateef**, whose  
affection, encouragement and prayers day and night have enabled me to  
achieve such success and honour. Thanks for your great support and  
continuous care.*

*my beloved husband **Laith** for his patience over my PhD study, and my sweet  
and loving kids **Melak and Mustafa**, and my sisters and brother.*

*Also, I would like to dedicate my thanks to my supervisors, especially  
**Dr Jonathan Goss**. I am really proud to be one of his PhD students.*

## Acknowledgements

After the end of my four-year journey for my PhD study, I must begin my acknowledgements by thanking the almighty Allah for giving me the strength and courage to be what I am now.

First and foremost I wish to thank my first supervisor, Dr Jonathan Goss, for his inspiring guidance and constructive criticism which have paved the way during my study. I am sincerely grateful to him for being supportive and helpful ever since I began working on my project. Also, I would also like to show my greatest appreciation to my second supervisor, Prof Patrick Briddon, for his lectures, motivation and development of AIMPRO. Really, it has been a great pleasure to work with them, and I am very proud to be one of their PhD students.

I would like to acknowledge the financial, academic and technical support of the Higher Committee of Education Development in Iraq, particularly in the award of a fully-sponsored scholarship that provided the necessary financial support for this research. I would like to show my deepest appreciation to the Ministry of Higher Education in Iraq and the College of Electrical and Electronic Engineering Techniques for providing me with study leave to gain the degree of PhD from Newcastle University. I also thank the School of Engineering for their assistance and support since my first day in the school.

I express my warm thanks to Dr Ahmed Sabaawi for his endless support, and also to my fellow graduate students from the School of Engineering (Dr Mead and Dr Raid) for sharing their scientific skills and experiences, as well as other colleagues in the ETM group who provided me with a great academic and social atmosphere which motivated me to do my best.

Last but not least, my heartfelt appreciation goes to my parents, sisters and brother, as well as to my husband and my kids for their personal support and great patience at all times.

# Abstract

Multi-crystalline silicon (mc-Si) based photovoltaic cells are generally accepted to be cost-effective for large scale production techniques. However, it contains a relatively high concentration of point and extended defects (EDs), both of which act as recombination centres limiting the cell efficiency. EDs such as dislocations, stacking faults, grain boundaries (GBs) and voids interact with mobile point defects, such as iron which is a common contaminant in some grades of silicon. Fe is a problem since interstitial iron ( $\text{Fe}_i$ ) diffuses rapidly, is electrically active, and is a non-radiative recombination centre.

Different processing techniques are used to getter Fe to improve solar cell efficiency; internal gettering by EDs is one possibility. Fe-Si interactions are complex and not fully understood, particularly when they are associated with EDs; there is relatively little atomistic-level data for the mechanism of the segregation of iron and its complexes at EDs, partly because modelling of the EDs is challenging in terms of the system size, and partly because GB structure is a matter of debate.

In this work, density functional theory was used to investigate Fe behaviour in bulk Si and at EDs. Trends in the energetics, magnetic, geometric, electronic and electrical properties of substitutional, Fe–vacancy, interstitial and interstitial-pair structures have been studied. Of particular note, the formation of  $\text{Fe}_i$ -pairs in bulk Si is energetically favourable, with the equilibrium spin states being sensitive to the Fe inter-nuclear separation. Overall, the third-neighbour pair structure in an antiferromagnetic form is the most stable, bound relative to two isolated  $\text{Fe}_i$  by 0.2 to 0.6 eV, depending upon charge state and inter-nuclear distances. Furthermore, the migration barrier for  $\text{Fe}_i$ -pairs is lower than that of individual interstitials, suggesting pairs may be key contributors to Fe diffusion and precipitation. Fe-defects are also modelled in intrinsic stacking faults,  $\Sigma 3$ -(110),  $\Sigma 5$ -(001) twist GBs and voids, and it is concluded that all forms of EDs represent binding sites for  $\text{Fe}_i$ .

Although  $\text{Fe}_i$  binds relatively weakly at fully bonded GBs, it is strongly

trapped by vacancies at the GB, for example and, perhaps more critically, by Fe already trapped there: the binding energy of a  $\text{Fe}_i$ -vacancy pair at a  $\Sigma 5$ -(001) twist GBs is 1.6 eV, and the binding of a second  $\text{Fe}_i$  atom to the GB is found to be greater than the first (also by around 1.6 eV). The results showed that the most stable site for iron lies just outside the modelled void (bound by 2 eV), which may explain the experimental observations that only a single layer of iron forms at voids.

Finally, quantum-chemical simulations were combined with TCAD device modelling to examine the properties of the EDs before and after segregating iron impurities, in an attempt to balance the interoperation of the advantageous and disadvantageous properties of these defects and impurities on the performance of Si solar cells. The results show that reasonable efficiency gains were obtained and the overall efficiency of the cell is improved by segregating iron from the grains to the GBs.

# Contents

Nomenclature	xx
<b>1 Introduction</b>	<b>1</b>
1.1 Background	1
1.2 Fundamentals of Solar Cell	4
1.3 Loss Mechanisms in Solar Cell	6
1.3.1 Optical losses	6
1.3.2 Recombination losses	7
1.3.3 Ohmic loss	10
1.4 Type of PV Cell Material	11
1.4.1 Thin film materials	12
1.4.2 Gallium Arsenide	13
1.4.3 Single-crystal silicon wafers	13
1.4.4 Multicrystalline silicon wafer	14
1.5 Development of High Efficiency c-Si Solar Cells	17
1.6 Defects and Impurities Associated with The Processing of mc-Si Ingots	20
1.6.1 Fundamentals of extended defects	22
1.6.2 Stacking faults, grain boundaries and voids	23
1.6.3 Iron-extended defect interaction	24
1.7 Thesis Outline	25
1.7.1 Part I - Theory and Method	25
1.7.1.1 Chapter 2 - <i>Ab Initio</i> Background and AIMPRO Package	25
1.7.1.2 Chapter 3 - Modelling of Derived Properties	25

1.7.1.3	Chapter 4 - Device Simulation Background and the Synopsys TCAD Package . . . . .	26
1.7.2	Part II - Application . . . . .	26
1.7.2.1	Chapter 5 - Iron Contamination in Pure Si . . . . .	26
1.7.2.2	Chapter 6 - Interstitial Fe-pairs in Bulk Silicon . . . . .	27
1.7.2.3	Chapter 7 - Analysis of Iron Segregation at Stacking Faults in mc-Si . . . . .	27
1.7.2.4	Chapter 8 - Analysis of Iron Segregation at Twist Grain Boundaries in mc-Si . . . . .	27
1.7.2.5	Chapter 9 - Voids in Silicon as a Sink for Interstitial Iron .	28
1.7.2.6	Chapter 10 - Extended Defects Engineering with Iron Contamination for Improved mc-Si Solar Cells . . . . .	28
1.7.3	Part III - Conclusions and Future Work . . . . .	28
<b>I</b>	<b>Theory and Method</b>	<b>29</b>
<b>2</b>	<b><i>Ab Initio</i> Background and the AIMPRO Package</b>	<b>30</b>
2.1	Introduction . . . . .	30
2.2	Many-Body Problem . . . . .	32
2.3	Born-Oppenheimer Approximation . . . . .	34
2.4	Solving the Many-body Wave Function Problem . . . . .	35
2.4.1	Hartree-Fock Approximation . . . . .	35
2.4.2	Density Functional Theory (Electron Density Approach) . . . . .	36
2.4.2.1	Kohn-Sham Equations . . . . .	37
2.5	Exchange-Correlation Functional . . . . .	37
2.6	The AIMPRO Software Package . . . . .	38
2.7	Material Modelling Supercells . . . . .	39
2.8	Basis Set Functions . . . . .	40
2.9	Brillouin Zone Sampling . . . . .	44
2.10	Self-Consistency Cycle . . . . .	46
2.11	Pseudopotential Approximation . . . . .	47
2.12	Chapter Summary . . . . .	48

---

<b>3</b>	<b>Modelling of Derived Properties</b>	<b>49</b>
3.1	Introduction . . . . .	49
3.2	Structure Optimisation . . . . .	49
3.3	Electronic Structure . . . . .	50
3.4	Electrical Levels . . . . .	51
3.4.1	Formation energy method . . . . .	53
3.5	Binding Energies . . . . .	55
3.6	Diffusion Barrier . . . . .	56
3.6.1	Minimum energy path and saddle point . . . . .	56
3.6.2	Nudged elastic band calculations . . . . .	56
3.7	Optical Absorption . . . . .	58
3.8	Dielectric Function . . . . .	60
3.9	Electron Energy Loss Spectrum . . . . .	61
3.10	Chapter Summary . . . . .	63
<b>4</b>	<b>Device Simulation Background and The Synopsys TCAD Package</b>	<b>64</b>
4.1	Introduction . . . . .	64
4.2	Synopsys Sentaurus TCAD . . . . .	64
4.3	Poisson Equation . . . . .	65
4.4	Carrier Transport . . . . .	67
4.5	TCAD Numerical Models . . . . .	69
4.5.1	Transfer matrix method . . . . .	69
4.5.2	Finite element method . . . . .	70
4.6	Modelling of Iron in Silicon . . . . .	71
4.6.1	Iron diffusion model . . . . .	71
4.6.2	Iron trap model . . . . .	72
4.7	Traps As Doping . . . . .	74
4.8	Chapter Summary . . . . .	74
<b>II</b>	<b>Applications</b>	<b>75</b>
<b>5</b>	<b>Iron Contamination in Pure Si</b>	<b>76</b>
5.1	Introduction . . . . .	77
5.1.1	Interstitial iron . . . . .	77

5.1.2	Iron-vacancy pair . . . . .	79
5.1.3	Substitutional iron . . . . .	80
5.2	Computational Method . . . . .	81
5.3	Results and Discussion . . . . .	83
5.3.1	Modelling $Fe_i$ in crystalline Si . . . . .	83
5.3.1.1	Geometrical structure . . . . .	83
5.3.1.2	Role of spin and charge states . . . . .	84
5.3.1.3	Band structure and electrical level . . . . .	85
5.3.1.4	Optical properties . . . . .	86
5.3.1.5	Diffusion of $Fe_i$ . . . . .	86
5.3.2	$Fe_iV$ pair . . . . .	88
5.3.3	$Fe_s$ in pure Si . . . . .	89
5.4	Summary . . . . .	92
<b>6</b>	<b>Interstitial Fe-pairs in Bulk Silicon</b>	<b>93</b>
6.1	Introduction . . . . .	93
6.2	Computational Method . . . . .	95
6.3	Results and Discussion . . . . .	96
6.3.1	Modelling of interstitial-iron pairs . . . . .	96
6.3.1.1	$Fe_i-Fe_i$ at nearest neighbour (1NN) . . . . .	97
6.3.1.2	$Fe_i-Fe_i$ at second neighbour (2NN) . . . . .	99
6.3.1.3	$Fe_i-Fe_i$ at third neighbour (3NN) . . . . .	101
6.3.1.4	More distance pairs . . . . .	103
6.3.2	Bond-Strain deviation . . . . .	104
6.3.3	Binding energy . . . . .	105
6.3.4	Iron pair migration pathways . . . . .	106
6.3.4.1	Single hop for $Fe_i$ at 3NN . . . . .	106
6.3.4.2	Pair hop for $Fe_i$ at 3NN . . . . .	108
6.3.4.3	Hopping $Fe_i$ pair as a unit . . . . .	110
6.4	Summary . . . . .	113
<b>7</b>	<b>Analysis of Iron Segregation at Stacking Faults in mc-Si</b>	<b>114</b>
7.1	Introduction . . . . .	114
7.2	Computational Method . . . . .	115

---

7.3	Results and Discussion . . . . .	117
7.3.1	Undecorated intrinsic stacking faults . . . . .	117
7.3.1.1	Modelling ISF . . . . .	117
7.3.1.2	Electronic and electrical properties . . . . .	118
7.3.2	Fe-ISF complexes . . . . .	118
7.3.2.1	Role of spin and charge states . . . . .	119
7.3.2.2	Electronic and electrical properties . . . . .	120
7.3.2.3	Optical properties . . . . .	123
7.3.2.4	Binding energy . . . . .	123
7.3.2.5	Bond-strain calculations . . . . .	125
7.3.3	Iron-vacancy pairing and substitutional iron at ISF . . . . .	126
7.3.4	Iron pairs at ISFs . . . . .	129
7.4	Summary . . . . .	130
<b>8</b>	<b>Analysis of Iron Segregation at Twist Grain Boundaries in mc-Si</b>	<b>131</b>
8.1	Introduction . . . . .	131
8.2	Computational Method . . . . .	134
8.3	Results and Discussion . . . . .	135
8.3.1	Undecorated twist grain boundaries . . . . .	135
8.3.2	Fe <sub>i</sub> -GBs complexes . . . . .	137
8.3.2.1	Role of spin and charge states . . . . .	137
8.3.2.2	Electronic and electrical properties . . . . .	138
8.3.2.3	Optical properties . . . . .	141
8.3.2.4	Binding energy . . . . .	141
8.3.2.5	Bond-strain calculations . . . . .	143
8.3.3	Fe–twist GBs complexes . . . . .	144
8.3.3.1	Iron-vacancy pairing and substitutional iron . . . . .	144
8.3.3.2	Iron pairs . . . . .	146
8.4	Summary . . . . .	147
<b>9</b>	<b>Voides in Silicon as a Sink for Interstitial Iron</b>	<b>149</b>
9.1	Introduction . . . . .	149
9.1.1	Void formation . . . . .	150
9.1.2	Role of voids in Si . . . . .	151

9.2	Computational Method . . . . .	152
9.3	Results and Discussions . . . . .	153
9.3.1	Undecorated voids . . . . .	153
9.3.2	Interactions of Fe with a model void . . . . .	154
9.3.2.1	Geometrical structure . . . . .	154
9.3.2.2	Electronic properties . . . . .	155
9.3.2.3	Binding energy and bond-strain . . . . .	157
9.3.2.4	Coordination of Fe at the internal surface . . . . .	158
9.3.2.5	Optical properties . . . . .	160
9.4	Summary . . . . .	161
<b>10</b>	<b>Engineering of Extended Defects with Iron Contamination for Improved mc-Si Solar Cells</b>	<b>163</b>
10.1	Introduction . . . . .	164
10.2	Methodology . . . . .	165
10.2.1	Atomic simulations . . . . .	165
10.2.2	Device simulations . . . . .	166
10.2.3	Photovoltaic device modelling . . . . .	166
10.2.4	Grain specification . . . . .	166
10.2.5	Meshing distribution . . . . .	167
10.2.6	Incident light . . . . .	168
10.2.7	Fe-contamination in PV . . . . .	169
10.3	Results and Discussion . . . . .	170
10.3.1	Extended defects . . . . .	170
10.3.2	Fe <sub>i</sub> in pure silicon . . . . .	173
10.3.3	Fe–extended-defect complexes . . . . .	176
10.4	Summary . . . . .	179
<b>III</b>	<b>Conclusions</b>	<b>180</b>
<b>11</b>	<b>Summary, Conclusions and Future Work</b>	<b>181</b>
11.1	Summary and Conclusion . . . . .	181
11.1.1	Atomic level . . . . .	182
11.1.2	Device level . . . . .	187

11.2 Future Work . . . . .	188
<b>References</b>	<b>189</b>
<b>References</b>	<b>211</b>

# List of Figures

1.1	The future sources of electricity (2013–2030).	2
1.2	Total market share in 2014 for different solar cell technologies, and the cost distribution of the PV module.	4
1.3	Auger recombination mechanism.	8
1.4	The SHR recombination mechanism.	9
1.5	Major types of photovoltaic cell materials.	11
1.6	Crystalline structure of single crystalline silicon	14
1.7	Schematics showing single crystal growth techniques including Czochralski growth and FZ growth.	15
1.8	Grain boundary configurations.	15
1.9	Crystallisation process: a) the Bridgman method, b) the heat-exchange method and c) block-casting technology to solidify a mc-Si block.	16
1.10	The highest power conversion efficiency for mono- and multi-crystalline Si cells and modules.	18
1.11	Schematic views of (left) Al-BSF and (right) PERL solar cells.	18
1.12	Projection of market share of of different Si solar cell design.	19
1.13	A schematic of current flow in a solar cell.	19
1.14	Projections for the predicated power of a fixed module size (60 cells with dimensions of 156 mm×156 mm).	20
1.15	Block diagram of the main classification of defects in silicon.	21
2.1	Plot showing convergence in the total energy of interstitial iron in bulk silicon as a function of the plane wave energy cut-off.	41

2.2	(a) Calculated lattice constant and bulk modulus of pure Si. (b) Computed time and band gap using different basis sets for a primitive silicon cell. Labels indicate the exponent and number of functions. . . . .	43
2.3	Relative energies ( $\Delta E$ ) that associated with the spin and charge states of $Fe_i$ in Si. . . . .	44
2.4	Effect of Brillouin zone sampling on the modelling accuracy of pure Si for different cell sizes. . . . .	45
2.5	Difference energies ( $\Delta E$ ) that associated with the Brillouin zone sampling as a function of spin and charge states of $Fe_i$ in 64 Si atoms. . . . .	46
2.6	The schematic flowchart of the self-consistent algorithm for density functional-based calculations. . . . .	47
3.1	Silicon band structure calculated by DFT-LDA. The structure is plotted along high-symmetry branches for primitive structure (2-atom). . . . .	52
3.2	Plot showing deep and shallow levels of material. . . . .	53
3.3	Schematic diagram showing the formation energy $E^f(q)$ for three charge states ( $q = 0, +1$ and $-1$ ) of a structure as a linear function of the electron chemical potential ( $\mu_e$ ). . . . .	55
3.4	Schematic diagram showing the steps in performing NEB calculations. . . .	57
3.5	Schematic illustration of tow possible mechanisms to transfer electrons from the valence band to the conductive band. . . . .	59
5.1	Conventional unit cell of crystalline silicon with iron (red atom) located at a tetrahedral interstitial site. . . . .	78
5.2	The $Fe_iV$ pair (left) has $Fe_i$ trapped outside V on a trigonal axis. The tetrahedral $Fe_s$ (right) is at a location in an almost unrelaxed substitutional position. . . . .	79
5.3	Conventional unit cell of crystalline silicon at the tetrahedral substitutional site. . . . .	80
5.4	Flowchart showing the methodology used to determine the bond-strain deviation caused by presenting iron atoms with respect to bond-strain before decoration. . . . .	82
5.5	Modelled interstitial iron at a) tetrahedral interstitial site of Si lattice; b)at H-site of Si lattice. . . . .	84

---

5.6	Electronic band structures of $\text{Fe}_i$ in neutral state ( $S = 1$ ) modelled in 216 Si-atom at (a) T-site; (b) at H-site, plotted along high-symmetry branches in the first BZ. . . . .	86
5.7	Computed real ( $n$ ) and imaginary ( $k$ ) parts of the refractive index, showing the impact of interstitial Fe ( $S = 1$ ) on the complex refractive index of the Si supercell. . . . .	87
5.8	Migration path of single iron along a trigonal axis starting near T-site, over the hexagonal site to the T-site. . . . .	88
5.9	Electronic band structures of $\text{Fe}_i\text{V}$ pair in neutral state ( $S=0$ ) modelled in 216 Si-atom. . . . .	90
5.10	Fraction of the Si supercell, showing the bond lengths and angles for neighbours of substitutional iron in Si. . . . .	90
5.11	Electronic band structures of $\text{Fe}_s$ in neutral state in 216 Si atoms, plotted along high-symmetry branches in the first BZ. . . . .	91
5.12	Formation energy $E^f(q)$ for three charge states of $\text{Fe}_s$ as function of electron chemical potential ( $\mu_e$ ). . . . .	91
5.13	Computed real ( $n$ ) and imaginary ( $k$ ) parts of the refractive index for pure silicon compared with that containing either $\text{Fe}_i$ and $\text{Fe}_s$ . . . . .	92
6.1	Schematics showing: a) prototypical interstitial sites (1NN–6NN) for the second interstitial iron with respect to the first one at T-site; b) another view of the nearest-neighbour separating the two sites of the interstitial iron with displacement vector in unit ( $a_0/4$ ) along with table 6.1. . . . .	96
6.2	Illustrations of iron pair defects at distances $n\text{NN}$ in Si, $n = 1-3$ : (a) a section of pure silicon; with (b) the first; (c) second; and (d) third nearest neighbours. . . . .	97
6.3	Binding energy of neutral interstitial iron pair with the spin-average compared to the two interstitial $\text{Fe}_i$ as a function of inter-nuclear separation, including first, second and third nearest neighbours with different cell size. . . . .	98
6.4	Plot showing: (a) the formation $E^f(q)$ energy for three charge states of Fe pair at 1NN in 216 Si atoms as a function of electron chemical potential ( $\mu_e$ ); (b) electronic band structures of $\text{Fe}_i$ pair in neutral state (AFM, $S=0$ ) for 1NN structure. . . . .	100

6.5	Plots showing: (a) the formation $E^f(q)$ energy for different charge states of the Fe pair at 2NN in 216 Si atoms as a function of electron chemical potential ( $\mu_e$ ); (b) electronic band structures of the $\text{Fe}_i$ pair in neutral state (FM, S=2) for 2NN structure. . . . .	101
6.6	Plot showing: (a) the formation $E^f(q)$ energy for three charge states of the Fe pair at 3NN in 216 Si atoms as a function of electron chemical potential ( $\mu_e$ ); (b) electronic band structures of $\text{Fe}_i$ pair in neutral state (AFM, S=0) for 3NN structure. . . . .	102
6.7	Evaluated root mean square bond lengths of Fe-pair, showing the amount of shift Si-Si and Fe-Si bonds than the bond lengths in pure and $\text{Fe}_i$ structures.	104
6.8	Binding energy of iron pairs at the first, second and third nearest neighbour sites as a function of site and charge state. . . . .	106
6.9	Binding energy of iron pairs at 4NN, 5NN and 6NN nearest neighbour sites as a function of site and charge state. . . . .	107
6.10	Minimum energy paths for AFM iron pairs along a triangular axis starting from the third (3NN) to: a) 2NN; (b) 4NN; and (c) 6NN. . . . .	108
6.11	Minimum energy paths for anti-ferromagnetic iron pair and ferromagnetic iron pair along a triangular axis. . . . .	109
6.12	Minimum energy paths for anti-ferromagnetic iron pair (blue solid) and ferromagnetic iron pair (dashed red) along a triangular axis starting near a T-site, over the hexagonal site to the second and first T sites. . . . .	110
6.13	Initial, saddle-point, and final configurations for diffusing $\text{Fe}_i$ atom: (a) 1NN→2NN; and (b) 2NN→3NN. . . . .	111
6.14	Initial, saddle-point, and final configurations for diffusing $\text{Fe}_i$ atom: (a) 3NN→2NN; and (b) 2NN→5NN. . . . .	112
7.1	Projection of the stacking faults in Si. . . . .	116
7.2	Projection of optimised structures of the ISF. Labels a e indicate the non-equivalent interstitial sites investigated. . . . .	118
7.3	Electronic band structures of purely ISF. . . . .	119
7.4	Relative energies for different spin configurations in neutral ( $q = 0$ ), positive ( $q = +$ ) and negative ( $q = -$ ) charge states examined for the sites in the ISF. . . . .	120

7.5	Electronic band structures corresponding to the most stable neutral state of Fe at site a and b of ISF structure ( $S = 1$ ). . . . .	121
7.6	Diagram showing the ionisation energy in (eV) as a function of Fe-site in the ISF of figure 7.2. . . . .	122
7.7	Schematic diagram showing the formation energy for $Fe_i$ in: (a) the equilibrium site of ISF (site a and b); (b) site c, and (c) site d, which represent a bulk-like site. . . . .	122
7.8	Calculated optical absorption coefficient versus wavelength for intrinsic stacking fault and ideal Si together with the AM1.5 solar power spectrum. . . . .	123
7.9	Computed real ( $n$ ) and imaginary ( $k$ ) parts of the refractive index showing: (a and b) the impact of ISF on pure Si, (c and d) the effect of Fe decorated ISF as compared with interstitial iron in bulk Si, and (e and f) the comparison between Fe-decorated ISF and Fe-free ISF regarding the refractive index. . . . .	124
7.10	Binding energy of iron to the ISF as a function of site (figure 7.2) and charge state. In each case, the energies of the lowest energy spin configurations are used. . . . .	124
7.11	Schematics of equilibrium structures showing the differences in bond lengths and angles of iron in the bulk Si (a) compared with the higher coordination of Fe at the gettering site of the ISF (b). . . . .	126
7.12	Electronic band structures corresponding to the most stable Fe-site at ISF structure in neutral spin polarise ( $S = 0$ ). . . . .	127
7.13	Schematics of equilibrium structures showing the differences in bond lengths and angles of $Fe_i$ -V in the bulk Si (left) compared with the higher coordination of $Fe_i$ -V at the ISF (right). . . . .	128
8.1	Schematic illustration for (a) tilt and (b) twist GB. . . . .	132
8.2	Optimised structures of (a)-(b) $\Sigma 5$ -(001) and (c) $\Sigma 3$ -(110) twist GBs. . . . .	136
8.3	Electronic band structures of undecorated (a) $\Sigma 5$ -(001) and (b) $\Sigma 3$ -(110) twist GBs in 480 and 384 Si atoms respectively. . . . .	137
8.4	Relative energies for different spin configurations in neutral ( $q = 0$ ) and positive charge states examined for the sites in the $\Sigma 5$ -(001) twist GBs. . . . .	139

8.5	Relative energies for different spin configurations in neutral ( $q = 0$ ) and positive ( $q = +$ ) charge states examined for the sites in the $\Sigma 3$ -(110) twist GBs. . . . .	139
8.6	Electronic band structures of Fe at the more stable site (a' and e'') of (a) $\Sigma 5$ (480 Si-atom) and (b) $\Sigma 3$ (384 Si-atom) twist GBs in neutral charge state ( $S = 0$ and $S = 1$ respectively). . . . .	140
8.7	Plot of formation energy as function of electron chemical potential for Fe in the equilibrium sites of (a) $\Sigma 5$ -(001) (a') and (b) $\Sigma 3$ -(110) (e'') structures. . . . .	141
8.8	Calculated optical absorption coefficient versus wavelength for extended defects and ideal Si together with the AM1.5 solar power spectrum. . . . .	142
8.9	Computed real ( $n$ ) and imaginary ( $k$ ) parts of the refractive index for different structures as a function of wavelength showing the impact of ED and Fe contamination. . . . .	142
8.10	Binding energies (eV) of iron to the (top) $\Sigma 5$ -(001) and (bottom) $\Sigma 3$ -(110) twist grain-boundaries as a function of site and charge state. . . . .	143
8.11	Schematic diagram showing the high coordination of iron at the ground state site of (b) $\Sigma 5$ -(001) and (c) $\Sigma 3$ -(110) twist GBs. (a) shows the calculated geometry of $Fe_i$ in the bulk Si. . . . .	144
9.1	Calculated optical absorption coefficient versus wavelength for void and ideal silicon together with the AM1.5 solar power spectrum for comparison. . . . .	154
9.2	Computed real and imaginary parts of the refractive index for undecorated void showing its impact on bulk Si. . . . .	155
9.3	Kohn-Sham band structures in the vicinity of the band-gap for a) clean voids (651 Si atoms); b) for the most stable neutral state ( $S = 0$ ) of Fe site at distance $d_{(o,v)}=7.49\text{\AA}$ from the void centre of void structure. . . . .	156
9.4	Binding energy (eV) of iron to the void as a function of distance from the void centre (circles), and rms strain in the Fe-neighbouring Si-Si bonds as described in the text (squares). . . . .	157
9.5	Schematics of equilibrium structures showing differences in bond lengths and angles of iron in the bulk Si (left) compared with the higher coordination of Fe at the gettering site of the void after relaxation (right). . . . .	159

9.6	Calculated optical absorption coefficient versus wavelength for undoped and Fe-doped voids together with the AM1.5g solar power spectrum for comparison. . . . .	160
9.7	Computed real and imaginary parts of the refractive index for Fe-doped voids showing the impact of Fe contamination. . . . .	161
10.1	Projection of optimised structures of the ISF (left) and $\Sigma$ 5GB (right). Shaded area highlight the interface region. . . . .	166
10.2	Part of solar cell structure generated by Sentaurus Structure Editor . . . .	168
10.3	Impact of the horizontal line spacing of the grid on the solar cell efficiency at different iron concentrations. . . . .	168
10.4	Schematic illustration of donor levels produced due to iron impurities for the case of the GB structure. . . . .	169
10.5	Calculated optical absorption coefficient versus wavelength for extended defects and ideal Si together with the AM1.5 solar power spectrum for comparison. . . . .	171
10.6	Computed real ( $n$ ) and imaginary ( $k$ ) parts of the refractive index for different structures, showing the impact of ED and Fe contamination. . . .	171
10.7	$J$ - $V$ characteristics of a silicon solar cell in comparison to simulations involving silicon containing ISF and $\Sigma$ 5GB defects. . . . .	172
10.8	Variation of carrier densities under illumination as a function of Fe concentration. . . . .	173
10.9	Current density (left) and open circuit voltage (right) versus impurity concentration for Fe in pure Si. . . . .	174
10.10	Conversion efficiency versus impurity concentration for Fe in pure Si. . . .	174
10.11	$J$ - $V$ characteristics for the model solar-cell constituted from pure silicon and three different Fe-doping concentrations. . . . .	175
10.12	$J$ - $V$ characteristics for solar-cells containing both ISFs and $Fe_i$ . . . . .	177
10.13	$J$ - $V$ characteristics for solar-cells containing both $\Sigma$ 5GB and $Fe_i$ . . . . .	177
10.14	Parasitic series resistance in a solar cell circuit. . . . .	178
10.15	Effect of energy gap of silicon on the $J$ - $V$ characteristics with the presence of ISF. . . . .	178
10.16	Effect of energy gap of silicon on the $J$ - $V$ characteristics with the presence of GB. . . . .	179

# List of Tables

5.1	Evaluation of root mean square bond-strain changes of $\text{Fe}_i$ from values for crystalline pure Si as function of number of Si atoms in the supercell. . . .	84
5.2	Difference in energies ( $\Delta E$ ) in eV associated with $\text{Fe}_i$ structure as a function of number of Si atoms in supercell ( $n_{\text{sc}}$ ) and spin. . . . .	85
5.3	Calculated activation energy of interstitial iron compared with collected experimental and theoretical data. . . . .	88
6.1	List of ideal sites of pairs of $\text{Fe}_i$ defects in order of increasing inter-site distance. . . . .	96
6.2	Energy differences ( $\Delta E$ ) in eV associated with the three $\text{Fe}_i\text{-Fe}_i$ structures as a function of cell size and spin. . . . .	103
6.3	Energy differences ( $\Delta E$ ) in eV associated with the fourth-sixth $\text{Fe}_i\text{-Fe}_i$ structures as a function of cell size and spin. . . . .	103
6.4	Si-Si and Si-Fe bond changes due to the formation of interstitial iron pairs at the first, second and third neighbours in bulk Si as a function of cell size. The reference used to calculate the rms strain is Si-Si in bulk Si. . . .	105
6.5	Si-Si and Si-Fe bond deviations due to the formation of interstitial iron pairs at the first, second and third neighbours in bulk Si as a function of cell size. The reference used to calculate the rms strain is single interstitial iron. . . . .	105
6.6	Si-Si and Si-Fe bond deviations due to the formation of interstitial iron pairs at the first, second and third neighbours in bulk Si as a function of cell size. The reference used to calculate the rms strain is $\beta\text{-FeSi}_2$ . . . . .	105
6.7	Possible migration pathways for $\text{Fe}_i$ pair. $E^a$ is the activation energy in eV, calculated for both AFM and FM spin configurations. . . . .	109

7.1	Si–Si and Si–Fe bond-strain due to segregation of the diffusing iron at the sites provided by ISF. . . . .	125
7.2	Spin energy differences ( $\Delta E$ ) in eV associated with the different structures.	130
8.1	Si–Si and Si–Fe bond-strain variation due to segregation of the diffusing iron at the sites provided by $\Sigma 5$ -(001) twist GBs. . . . .	145
8.2	Enthalpy of chemical reaction ( $\Delta H$ ) and the energy differences ( $\Delta E$ ) in eV associated with the different structures. . . . .	147
9.1	Distances from the void centre with respect to the whole void structure. . .	159
10.1	Summary of solar-cell electrical parameters and efficiency with and without the EDs. . . . .	172
10.2	Impact of electron cross-section ( $\sigma_n$ ) of interstitial iron on device performance.	176
10.3	Summary of solar-cell electrical parameters and efficiency for Fe-containing the systems under AM1.5 illumination. . . . .	176

# List of Publications

## Journal papers

1. **Oras A. Al-Ani**, J. P. Goss, Ahmed M.A. Sabaawi, N. E. B. Cowern, P. R. Briddon and M J Rayson, "Multiscale modeling of extended defects with iron contamination in improved mc-Si solar cells", Submitted to the IEEE Journal of Photovoltaics (under review), 2018.
2. **O. A. Al-Ani**, J. Goss, P. Briddon, M. Rayson, and N. Cowern, "Interstitial Fe-pairs in silicon", J. Cryst. Growth, vol. 468, pp. 54–56, 2017.
3. **O. A. Al-Ani**, J. P. Goss, M. Al-Hadidi, P. R. Briddon, N. E. B. Cowern, and M. J. Rayson, "Impact of grain boundary structures on trapping iron", J. Cryst. Growth, vol. 468, pp. 448–451, 2017.
4. **O. A. Al-Ani**, J. P. Goss, M. Al-Hadidi, P. R. Briddon, N. E. B. Cowern, and M. J. Rayson, "Voids in silicon as a sink for interstitial iron: a density functional study", J.Cryst. Growth, vol. 468, pp. 101–103, 2017.
5. Meaad Al-Hadidi, J.P. Goss, **Oras A. Al-Ani**, P.R. Briddon, M.J. Rayson, "Density functional calculations of carbon substituting for Zr in barium zirconate", J.Cryst. Growth, vol.468, pp.728–731, 2017.
6. **O. A. Al-Ani**, J. P. Goss, N. E. B. Cowern, P. R. Briddon, M. Al-Hadidi, R. Al-Hamadany, and M. J. Rayson, "A density functional study of iron segregation at ISFs and  $\Sigma 5$ -(001) GBs in mc-Si", Solid State Phenomena, vol. 242, pp. 224–229, 2016.

- 
7. **O. A. Al-Ani**, A. M. Sabaawi, J. P. Goss, N. E. B. Cowern, P. R. Briddon, R., and M. J. Rayson, "Investigation into efficiency-limiting defects in mc-Si solar cells", *Solid State Phenomena*, vol. 242, pp. 96–101, 2016.

## Conference papers

1. **Oras A. Al-Ani**, J. P. Goss, N. E. B. Cowern and P. R. Briddon," Impact of grain boundary structures on trapping iron", The 18th International Conference on Crystal Growth and Epitaxy (ICCGE-18), Japan, 2016.
2. **Oras A. Al-Ani**, J. P. Goss, N. E. B. Cowern and P. R. Briddon," Interstitial Fe-pairs in silicon", The 18th International Conference on Crystal Growth and Epitaxy (ICCGE-18), Japan, 2016.
3. **Oras A. Al-Ani**, J. P. Goss, N. E. B. Cowern and P. R. Briddon,"Multiscale investigation of electronic structures and optical properties induced by mc-Si defects on solar cell performance", The 18th International Conference on Crystal Growth and Epitaxy (ICCGE-18), Japan, 2016.
4. **Oras A. Al-Ani**, J. P. Goss, M Al-Hadidi. R. Briddon and N. E. B. Cowern, "Void growth in silicon as sink for interstitial iron: First principle study", The 18th International Conference on Crystal Growth and Epitaxy (ICCGE-18), Japan, 2016.
5. Meaad Al-Hadidi, J.P. Goss, **Oras A. Al-Ani**, P.R. Briddon, M.J. Rayson, "Density functional calculations of carbon substituting for Zr in barium zirconate", The 18th International Conference on Crystal Growth and Epitaxy (ICCGE-18), Japan, 2016.
6. **O. A. Al-Ani**, J. P. Goss, N. E. B. Cowern, P. R. Briddon, M. Al-Hadidi, R. Al-Hamadany, and M. J. Rayson, "A density functional study of iron segregation at ISFs and  $\Sigma 5$ -(001) GBs in mc-Si", *Gettering and Defect Engineering in Semiconductor Technology 2015 (GADEST2015)*, Germany, 2015.
7. **O. A. Al-Ani**, A. M. Sabaawi, J. P. Goss, N. E. B. Cowern, P. R. Briddon, R., and M. J. Rayson, "Investigation into efficiency-limiting defects in mc-Si solar cells", *Gettering and Defect Engineering in Semiconductor Technology 2015 (GADEST2015)*, Germany, 2015.

8. **Oras A. Al-Ani**, Ahmed M.A. Sabaawi, J. P. Goss, N. E. B. Cowern, P. R. Briddon and M J Rayson "Multi-scale Modelling of Multicrystalline Silicon Solar Cell Devices", first HCED conference, London, UK, 2015.
9. Ahmed M.A. Sabaawi and **Oras A. Al-Ani**, "Heavily-Doped Semiconductor Infrared Antennas for Solar Energy Harvesting", Loughborough Antennas and Propagation Conference (LAPC), UK, 2015.

## Presentation

1. Poster Presentation title: "A Density Functional Study of interstitial iron at voids in mc-Si", a meeting of High-Performance-Computing applied to materials (N8 PHC network event), York, UK, 2018.
2. Poster Presentation title: "A Density Functional Study of interstitial iron and its pair-segregation at extended defects in mc-Si", a meeting of High-Performance-Computing applied to materials (N8 PHC network event), York, UK, 2017.
3. Poster Presentation title: "Theory of interstitial iron and its pair-formation in silicon", a meeting of High-Performance-Computing applied to materials (N8 PHC network event), York, UK, 2016.
4. Oral presentation title: "Extended defects engineering with iron contamination for improved Si solar cells", Annual Research Conference (ARC2016), Newcastle University, UK, 2016.
5. Oral Presentation title: "First Principle Investigations of Iron in Planar Defects in mc-Si", Annual Research Conference (ARC2015), Newcastle University, UK, 2015.
6. Oral Presentation title: "Atomistic Modelling of Segregation of Iron at Twist Grain Boundary", a meeting of High-Performance-Computing applied to materials (N8 PHC network event), York, UK, 2015.
7. Poster Presentation title: Oras A. Al-Ani, J. P. Goss and N. E. B. Cowern "A preliminary Literature Review Impurities and Defects in Photovoltaic Si solar cell", Annual Research Conference (ARC2014), Newcastle University, UK, 2014.

# Introduction

“We need to invest dramatically in green energy, making solar panels so cheap that everybody wants them. Nobody wanted to buy a computer in 1950, but once they got cheap, everyone bought them.”

Bjorn Lomborg

## 1.1 Background

Global demand for clean energy is growing rapidly and is predicted to increase over the coming decades due to population growth and the improved living standards that accompany economic development [1]. Fundamentally, primary energy resources can be classified into depleting or renewable [1]. Depleting resources, such as fossil and nuclear fuels, account for up to 78% of total energy usage. Fossil fuels such as oil, coal, and natural gas meet the majority of energy demand. However, deriving energy from fossil fuels causes greenhouse gases like carbon dioxide and nitrogen oxide to be released into the Earth’s atmosphere, which are believed to be significant contributory factors in climate change [2, 3]. Furthermore, fossil fuels, especially oil, are depleting at a rapid pace. In contrast, renewable energy is generated from natural sources such as the sun, wind, water, tides, and geothermal heat. Renewable energy sources are becoming essential for power generation as alternatives to fossil fuels as they have minimum impact on the environment. Renewable sources already contribute around 22% of global energy supply [4]. Among different renewable energy sources, only solar energy has the capacity to fill the demand gap and in particular energy supply from the sun is essentially free, unlimited, and not localised to any part of the world. Based on statistical studies [5, 6], it is reported that

the use of less than 0.02% of solar resources would be sufficient to entirely replace fossil fuels and nuclear power as an energy source. Consequently, solar cells can solve energy and environmental problems simultaneously.

Figure 1.1 shows a projection of the global demand for energy over the 20 years, where it is predicted [7] that renewable energy sources will account the biggest projection of energy used in electricity generation. It is also expected that solar energy will supply up

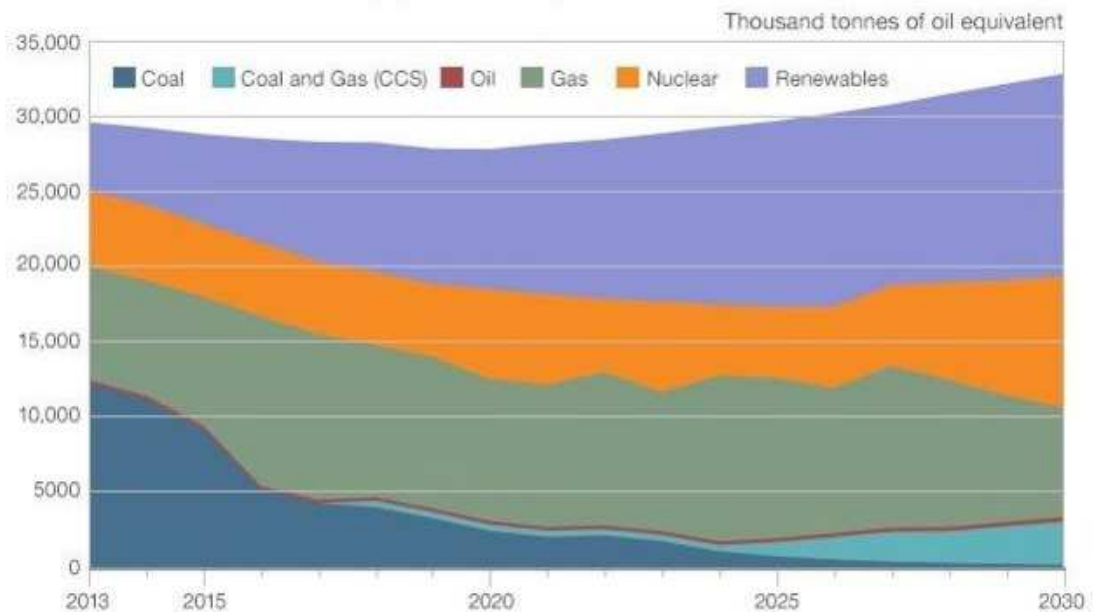


Figure 1.1: The future sources of electricity (2013–2030). Source: Department of Energy and Climate Change in the UK [7].

to 30% of the world's energy demand by 2050. Based on a projection of substantial growth in energy production predicted by 2060 [8], it is thought that the global use of fossil fuel will decline to 2000 levels and over two-thirds of energy will come from non-fossil fuel sources. Growing demand for renewable energy is the main reason behind the dramatic developments in solar cells with different features that has been witnessed in recent years. For example, during the period 2004 to 2009, grid-connected photovoltaic (PV) capacity increased at an annual average rate of 60%, causing it to be the world's fastest-growing energy technology [3]. The impacts of the size and structure of solar cells, as well as the type of material used on solar cell efficiency are outlined in a previous study [9]. Moreover, improvements in fabrication techniques for low cost, high efficiency wafer-based crystalline solar cells has encouraged industry to investigate the best materials which can satisfy these requirements. Silicon as a raw material in the wafer manufacturing process is commonly used for microelectronic devices and solar cells. Based on recent data (2016),

it has been reported [10] that Si-wafer based PV technology accounts for about 94% of total production, and the share of multi-crystalline technology is now about 70% of total production. The market share of all thin film technologies accounted for around 6% of the total annual production. The general properties of Si and these wafers are explained later in section 1.4.

Fundamentally, two types of wafer-based c-Si are used in the solar cell industry: monocrystalline silicon (mono c-Si) and multicrystalline silicon (mc-Si), where cells with mono c-Si have higher conversion efficiency and higher wafer cost than mc-Si cells. More details of materials can be found in section 1.4.

The properties of PV Si wafers and solar cells, however, can be affected by many factors, including the distribution and interaction of intrinsic point defects, extrinsic impurities, structural defects, residual stresses induced by processing and surface conditions [11]. The fundamentals of the common defects and impurities associated with the processing of crystalline Si ingots are described in detail in section 1.6.

Figure 1.2 (left) gives an overview of commercially available PV technologies with their respective market shares. It is clear that wafer-based c-Si (with two types) is the dominant technology [12], representing in 2014 about 92% of the total as compared with thin-film solar cells which are commercially used in several technologies, including CIGS, CdTe and amorphous thin film Si. Thin-film technology has always been cheaper but less efficient than conventional c-Si technology. Recent study (in 2017) [13] presented record lab cell efficiency levels of 26.7% and 21.9% for mono c-Si and mc-Si wafer-based technology, respectively. Furthermore, the highest lab efficiency in thin film technology has been recorded [13] as 21.7% and 21.0% for CIGS and CdTe solar cells, respectively. Furthermore, high concentration multi-junction solar cells can achieve an efficiency of 46.0% in the laboratory, and have reached 38.9% using concentrators. It can be concluded that c-Si is expected to be one of the most appropriate technologies for massive scale-up due to the abundance of the raw material together with the high efficiency and longevity of Si modules [11].

The right-hand image in figure 1.2 shows the proportion of the production price of wafers using non-metallised silicon substrate that account for the major cost fraction in producing multicrystalline solar cell panels [14]. There is an option to reduce the cost by reducing the silicon content, by moving toward thinner wafers. However, thickness reductions lead to a high breakage risk of Si solar cells with metallised Si substrate. However, for c-Si cells to satisfy future energy needs, there is still a significant requirement

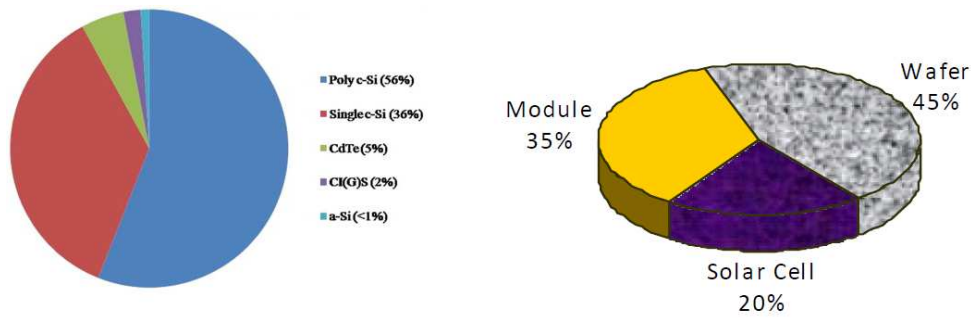


Figure 1.2: Total market share in 2014 for different solar cell technologies (left). Images taken from [12]. The right-hand image shows the cost distribution of the PV module, where wafer production represents around 45% of the total module price [15].

for reductions in system costs and improvements in manufacturing to increase throughput and production yield. It is expected [16] that PV technology will continue to compete with other energy sources in terms of electricity generation capacity and investment costs by reducing production costs via lower materials consumption and/or by enhancing energy conversion efficiency in terms of the ratio of cost to performance.

This study attempts to contribute to the research effort investigating material which can satisfy the needs for cost reduction and reasonable conversion efficiency. The mc-Si based solar cell (section 1.4.4) is generally accepted to currently satisfy the requirements for cost-effective large-scale production techniques of PV material compared with single c-Si, and thus sufficiently high solar cell efficiency [17–19] could be gained in spite of the impurities and defects mostly induced by processing and surface conditions.

The focus of this study concerns the most common point and extended defects present in these materials and their effects on Si solar cell performance, focusing on iron–EDs interaction.

## 1.2 Fundamentals of Solar Cell

PV solar cells are semiconductor devices constructed to convert sunlight directly into electricity using a p-n junction, which is the basic component of most common electrical devices. The physical process in which a PV cell can achieve this conversion is called the photovoltaic effect, in which a voltage across the junction is generated from the absorption of photons. Basically, a simple cell consists of p-type (positive, as it contains an excess of holes) and n-type (negative, as it contains an excess of electrons) semiconductor materials in close contact. Fundamentally, the p-n junction is created by doping a semiconductor

material, and p- and n-doped semiconductors ("e.g." boron- and phosphorous-doped silicon, respectively) are relatively conductive. In contrast, the junction between them is a non-conductor (also called the space charge region), which occurs due to the exchange of carriers (electrons and holes). The diffusion of the electrons and holes into the other type of material eliminates each other's charge. In the p-n junction, an equilibrium condition is reached in which a voltage difference (also called the "built-in electric field") is formed across the junction. Near the p-n interface, electrons and holes tend to diffuse into the p-type (leaving positive charge holes) and n-type regions (leaving fixed negative charge electrons) respectively. Since the regions close to the p-n interfaces lose their neutrality and become charged, the space charge region is formed.

Current generation in solar cells (i.e. light-generated current) occurs due to two processes: absorption and collection. In the absorption process, the incident photons create an electron-hole pair given that the incident photon energy is greater than that of the band gap. The electrons generated in p-type material and holes in the n-type material are minority carriers and are meta-stable, and hence will recombine after a length of time called the minority carrier lifetime. The recombination process will cause a loss of the light-generated pair and no power will be generated.

The p-n junction plays an important role here in separating the generated electrons and holes by the existing electric field on both sides of the junction. When the light-generated minority carriers (i.e. electrons in the p-type side and holes in the n-type side) reach the interface region, they will be swept across the junction due to the existing electric field and will be majority carriers. If both the emitter and base of the solar cell are connected through a load, the electrons will move to the n-type side and will exit the solar cell as light-generated current, which flows through the external circuit.

Several factors can affect the output power density and efficiency of a solar cell. These include material quality, light intensity, and environmental conditions such as temperature and humidity. More details of the loss mechanism in solar cells are described in section 1.3.

Regarding solar cell design, two different types of PV systems are available: flat plate and concentrators. In the flat plate system, the PV modules have been built on a rigid and flat surface to capture solar rays, whereas sunlight can be concentrated on the PV cells using concentrator systems in which lenses are used for this purpose to increase the PV cell power output. Although flat plate systems are typically less complicated than concentrators, concentration systems need more sophisticated and expensive tracking systems.

In terms of PV material, there are a wide range of solar cell configurations that have been explored [20,21] and presented in section 1.4.

### 1.3 Loss Mechanisms in Solar Cell

Fundamental limitations on efficiency have been discussed in many studies, and generally loss mechanisms in solar cells have been classified into optical and electrical losses. Optical losses involve reflection, shadowing and unabsorbed radiation. Electrical losses are mainly classified into ohmic loss, related to the solar cell and contact materials and recombination losses that occur in the emitter, base and space charge regions of the solar cell structure.

#### 1.3.1 Optical losses

In order to maximise the current which can be extracted from the contact of a solar cell, and thus to gain high conversion efficiency, a high rate of generation of electron-hole pairs is required. However, the presence of electrical contact in the p- and n-type regions of the solar cell cause a contact grid on the side exposed to sunlight, and this situation has been avoided in the back contact cell. As the metal contacts are opaque-shading losses can result which can reduce the solar cell efficiency by several percent, and are independent of the light's wavelength. In the back contact cell, a typical thickness is  $120\ \mu\text{m}$ , which entails a loss of potential current equal to the gain obtained by removing the front metal contacts of about  $0.8\ \text{mA}/\text{cm}^2$ . Furthermore, the quality of the antireflection coating contributes a small gain. However, avoidable losses from free carrier absorption and insignificant light trapping are very small, leading to the conclusion that a current density of more than  $43\ \text{mA}/\text{cm}^2$  can be achieved in practice with current technology using an optimised back contact solar cell or a bifacially contacted cell [22].

A texturing technique for the solar cell surface is used to change the reflection of incident light at a tilted plane towards the solar cell, thus increasing the probability of incoming photons entering the cell. A covering of dielectric layers is also used to reduce reflection losses. On the other hand, the absorbed light in the bulk depends on the wavelength. The indirect bandgap of Si means the absorption probability of low energy (long wavelength) photons (where  $\lambda \geq 1\ \mu\text{m}$ ) is weak [23]. In contrast, with photons of short wavelengths within several tenths of micrometres, several internal reflections are needed before being absorbed. Light which is not absorbed by the bulk can be lost

through the bulk at the rear, or the front after internal reflection is used [23].

### 1.3.2 Recombination losses

As this project is interested in the effect of impurities and extended defects in the mc-Si solar cell, it is important to consider some details of the recombination processes that always occur near the upper surface, in the depletion region or on the lower surface of the cell. As mentioned before in section 1.1, absorbing photons of sufficient energy creates electron-hole pairs which are exposed to various recombination mechanisms. Generally, carrier generation and recombination are processes by which mobile charge carriers are created and eliminated, where a recombination process occurs when an electron falls from the  $E_c$  into the valence band ( $E_v$ ) of a semiconductor, with the energy of recombination emerging as a photon of light. In contrast, the generation of an electron-hole pair can occur when a valence electron gives an energy ( $\geq$  the energy gap) which is transferred to the conduction band ( $E_c$ ).

Generally, there are three types of recombination: the Auger (occurs in the bulk [24]), radiative (occurs in the direct band gap, such as in solar cell-based GaAs) and Shockley-Read-Hall (SHR) [25, 26] recombination (occurs in the case of the existence of defects, where an extra energy level in the forbidden region is unintentionally or deliberately introduced through defects in the crystal lattice).

Radiative recombination represents the inverse of the optical absorption process and is less important in Si than other types, as Si has energy and momentum conservation needs the additional participation of phonons. Radiative recombination is negligible and cannot be affected by the design and processing of the solar cell if the concentration of doping is around  $10^{16} \text{ cm}^{-3}$  [27]. In this recombination type, an electron from the  $E_c$  directly combines with a hole in the  $E_v$  and releases a photon. The emitted photon has an energy similar to the band gap and is thus only weakly absorbed in which it can exit the piece of semiconductor.

Auger recombination (Figure 1.3) can occur when an electron and a hole recombine together without emitting heat or photons but where the excess energy of the electron in the  $E_c$  is given to a third electron in the  $E_c$ , and then the third electron relaxes back to its original energy by emitting phonons. This type of recombination is very important in cases of heavy doping or high level injection of high carrier concentrations under concentrated sunlight.

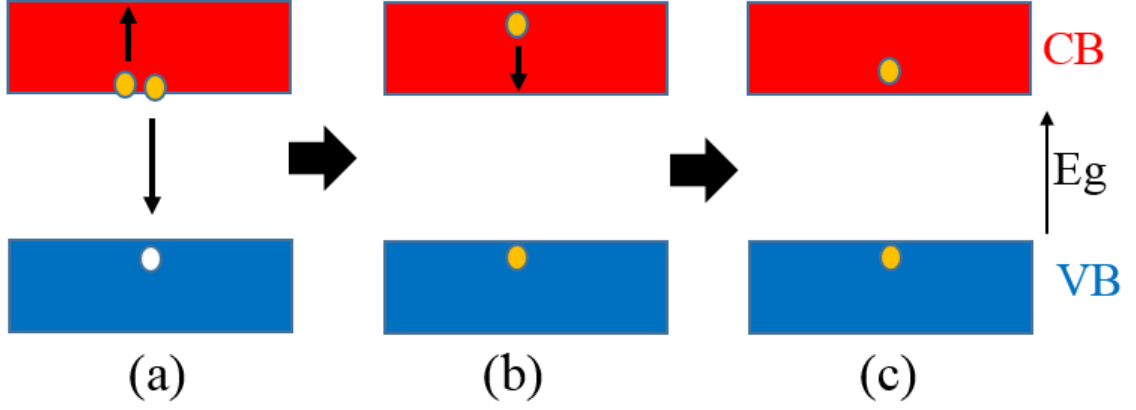


Figure 1.3: Auger recombination mechanism: (a)  $e/h$  recombination with releasing energy to second pushing it high into the  $E_c$ ; (b) the electron gradually gives off its energy thermally; and (c) relaxes back to the band edge.

The characteristic lifetime ( $\tau_{\text{Auger}}$ ) associated with this type of recombination, which is defined as the average time which a carrier spends in an excited state after  $e/h$  generation and before they recombine, is inversely proportional to the square of carrier concentration. In the case of low level injection,  $\tau_{\text{Auger}}$  has the following expression:

$$\tau_{\text{Auger}} = \Delta n / R \quad (1.1)$$

where  $\Delta n$  is the excess minority carrier concentration and  $R$  is the recombination rate [28, 29], which is the sum of the individual recombination processes.

Based on equation 1.1, lower doping yields higher limits of Auger recombination. Hence, the minority carrier lifetime can be affected by the design of the diffusion emitter and the doping of the base material [27].

In general, the presence of impurities and defects in semiconductors can introduce energy levels within the forbidden gap of these materials. These levels create a two-step recombination process. First, electrons relax from the  $E_c$  to the defect state, and then the electron and hole recombine in the  $E_v$ . Figure 1.4 shows the case of an electron (or hole) that is trapped by this level. It is worth mentioning that the movement of a carrier into the defect level relies on the distance of the introduced energy level from either band edge. If this level is close to either band edge, recombination is less likely as the electron will probably be re-emitted to the  $E_c$  edge rather than recombining with a hole that transfers into the same energy state from the  $E_v$ . Therefore, defect levels close to the mid-gap represent an active region for recombination. The mechanism of this type of recombination is called Shockley-Read-Hall (SHR) recombination [25].

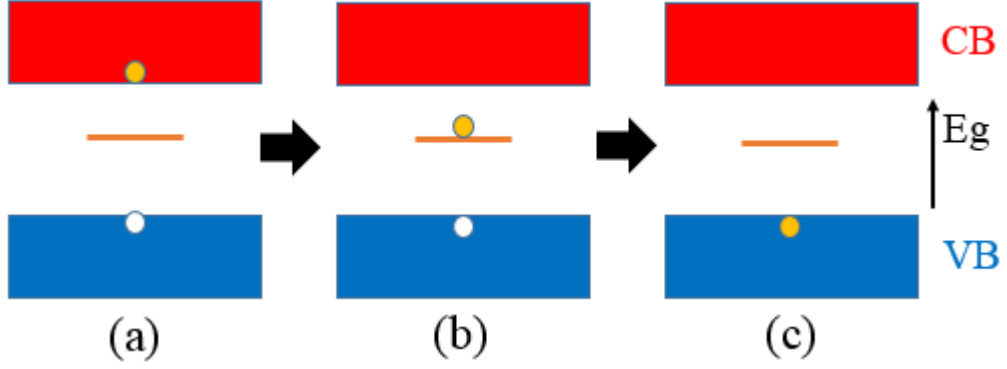


Figure 1.4: The SHR recombination mechanism: (a) via extra energy level; (b) movement of an electron to an extra level in the forbidden gap with the releasing of energy as a photon or multiple photos; (c) a further photon or photons released due to e/h recombination.

This section gives a mathematical description of the SHR recombination process which is used in device simulation in chapter 10 to model carrier exchange between the  $E_c$  and the  $E_v$ . The SRH recombination rate,  $R^{SHR}$ , through a deep single defect level in the gap is given in equation 1.2, which is implemented in the Sentaurus Device in chapter 10:

$$R^{SHR} = \frac{np - n_i^2}{\tau_{p0}(n + n_1) + \tau_{n0}(p + p_1)} \quad (1.2)$$

Here  $n$  and  $p$  are equilibrium electron and hole densities, and  $\tau_{p0}$  and  $\tau_{n0}$  are the fundamental electron and hole lifetimes respectively which are associated with the thermal velocity of charge carriers ( $v_{th} \approx 10^7$  cm/s). The density of recombination defects ( $N_t$ ) and the capture cross-sections,  $\sigma_n$  and  $\sigma_p$ , for the specific defects are given by:

$$\tau_{p0} \equiv \frac{1}{\sigma_p v_{th} N_t} \quad (1.3)$$

$$\tau_{n0} \equiv \frac{1}{\sigma_n v_{th} N_t} \quad (1.4)$$

The auxiliary parameters  $n_1$  and  $p_1$  are statistical factors, which for simplicity take trap-level energy into consideration and are defined as:

$$p_1 = N_V / \exp\left(\frac{E_V - E_d}{KT}\right) \quad (1.5)$$

$$n_1 = N_C / \exp\left(\frac{E_d - E_C}{KT}\right) \quad (1.6)$$

Here,  $N_{C,V}$  are the effective densities of states at the  $E_c$  edges, and  $E_V$ ,  $E_C$ , and  $E_d$  are the energy levels for the  $E_v$ ,  $E_c$ , and the defect bands, respectively.  $KT$  is the product of

the Boltzmann constant,  $k$ , and the temperature,  $T$ .

For the equilibrium electron and hole concentrations,  $n_0$  and  $p_0$ , respectively, the SHR recombination lifetime ( $\tau_{\text{SHR}}$ ) can be expressed as a function of the injection level, the doping density, and the defect parameters. These defect parameters include the concentration of traps, traps energy levels, and trap capture cross-sections.  $\tau_{\text{SHR}}$  has the following formula:

$$\tau_{\text{SHR}} = \frac{\tau_{n0}(p + p_1 + \Delta n) + \tau_{p0}(n + n_1 + \Delta p)}{n_0 + p_0 + \Delta n} \quad (1.7)$$

Here,  $\Delta n$  and  $\Delta p$  are the excess carrier densities taken to be equal in the absence of trapping [30].

As mentioned before, for deep levels when energy levels are near to the middle of the gap, the recombination centres are considered to be more detrimental than those of shallow levels close the band edges. In order to reduce recombination following the SHR process, various techniques can be used to avoid impurities by gettering or the passivation of defect levels [27].

### 1.3.3 Ohmic loss

Part of the carriers generated will be recombined, as explained previously. The rest of the generated carriers will need to be extracted at the contacts. However, there is a level of power dissipation associated with the extraction process due to non-zero contact resistance that produces ohmic losses. In order to reduce the ohmic losses, wider contact lines are needed. However, increasing the contact area might increase the recombination rate and also the shadowing. It is desirable to make the series resistance of the emitter as low as possible in order to enable a smooth current flow. To this end, a highly doped emitter is required, but it is expected that higher Auger (section 1.3.2) and surface recombination will result [27]. There are two possible ways to minimise the series resistance, by either increasing the base doping, which in turn decreases the minority lifetime (i.e. Auger recombination), or by employing a thinner substrate which decreases the probability of absorption. A reasonable compromise between the aforementioned techniques is to find the optimum design parameters of the solar cell structure.

A large series resistance significantly reduces the fill factor and might reduce the short-circuit current if it is too high. In this work, the impact of iron impurity on series resistance, and hence solar cell performance, is investigated and reported in chapter 10.

## 1.4 Type of PV Cell Material

Solar cells are typically named based on the semiconducting material they are made of, and the ability of these materials to absorb sunlight that reaches the Earth's surface depends on certain characteristics. Solar cells can be designed as single-junction, where only one single layer of light-absorbing material is used, or as multi-junction designs with multiple physical configurations in order to take advantage of various absorption and charge separation mechanisms.

As mentioned in section 1.1 and presented in figure 1.5, solar cells can be grouped into three generations of cells. First generation cells are conventional or traditional wafer-based cells made from c-Si. The commercially predominant PV technology uses polysilicon and mono c-Si. Second generation cells are thin film solar cells, including amorphous silicon, CdTe and CIS cells [31]. They are commercially significant in utility-scale PV power stations, building-integrated PVs or in small stand-alone power system. Third generation

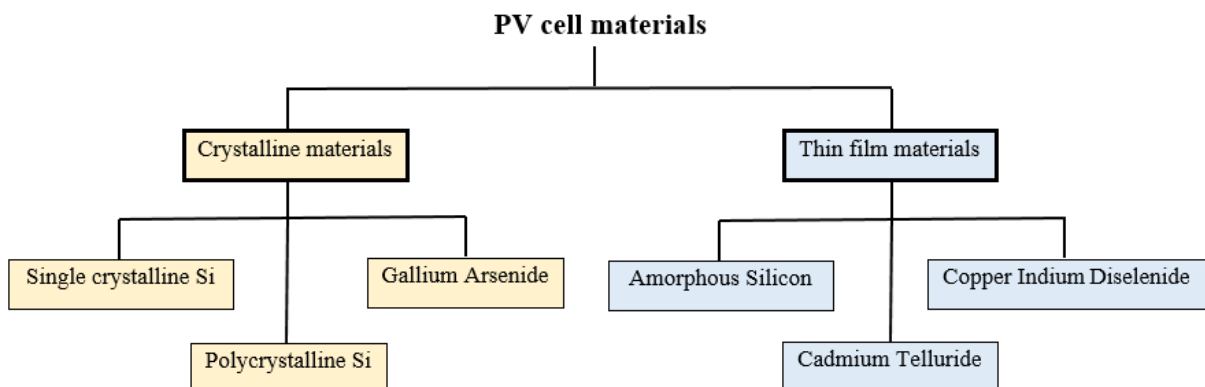


Figure 1.5: Major types of photovoltaic cell materials.

cells include a number of thin-film technologies, described as emerging PVs, most of them which have not yet been commercially applied and are still in the research or development phases.

Many material systems have been considered for solar cell fabrication, including combinations of semiconductors, metals, oxides, electrolyte solutions, organic molecules and polymers, but the vast majority of all commercial solar cells are made from silicon.

Si is cheap and extremely abundant representing about 26% of the earth's crust [32], which has led it to dominate solar cell technology. In addition, c-Si PV modules have proved to exhibit stable operation in the long term outdoors (>20 years) [33]. Si has a negative temperature coefficient of resistance, where the number of free charge carriers

increases with temperature. The physical properties of Si can be summarised as it being an element within group IV having an indirect band gap (1.12 eV at 300 K). In the periodic table, atoms from groups III and V like boron and phosphorus act as dopants in Si, where phosphorus and boron atoms have an extra electron and excess hole and are therefore called a donor and acceptor respectively. The electrical conductivity of Si is affected by increasing this doping, where doping concentrations usually range from  $10^{15}$  to  $10^{16}$   $\text{cm}^{-3}$  (i.e. with a resistivity in the range of 0.01–0.1  $\Omega$  m) [34]. The following sections describe the dominant models of PV cells on the market, including the c-Si cell and thin film Si cell design [35].

### 1.4.1 Thin film materials

In a thin-film PV cell, a thin semiconductor layer of PV materials is deposited on a low-cost supporting layer like glass, metal or plastic foil. Thin-film materials have higher light absorptivity than crystalline materials, where the deposited layer is extremely thin (from a few micrometres to even less than a micrometre) as compared with a single thin amorphous cell (0.3 micrometres), for example.

In general, thinner layers of material yield significant cost savings. In addition, the deposition techniques in which PV materials are sprayed directly onto glass or metal substrate are cheaper, and the manufacturing process is faster, using up less energy and mass production is made easier than with the ingot-growth approach of c-Si. Thin film PV cells, however, suffer from low cell conversion efficiency due to their non-single crystal structure, which in turn requires larger array areas and increasing area-related costs such as mountings.

The most common materials that are used for thin film PV modules are amorphous silicon (a-Si), cadmium telluride (CdTe) and copper indium diselenide (CuInSe<sub>2</sub>, or CIS). a-Si has high light absorptivity, which is about 40 times higher than that of single c-Si. Hence, only a thin layer of a-Si is sufficient in making PV cells, at around 1 micrometre thick as compared to 200 or more micrometres thick for c-Si cells [36].

CdTe has a conversion efficiency for a commercial module of about 7%. However, one of the major drawbacks of using CdTe for PV cells is the instability of cell and module performance. Additionally, Cd is a toxic substance even in the small amounts used in CdTe modules, and thus extra precautions have to be taken into account in the manufacturing process. CIS is able to deliver such high energy conversion efficiency without suffering

from outdoor degradation, and thus thin film PV cells have been demonstrated to be a viable and competitive selection for the solar power industry in the future. Additionally, it has been found to be one of the most light-absorbent semiconductors at a thickness of 0.5 micrometres it can absorb 90% of the solar spectrum [36].

### 1.4.2 Gallium Arsenide

Gallium Arsenide (GaAs) is another semiconductor material used in the PV cell industry. GaAs has a crystal structure similar to that of Si. However, the difference between these materials is the number of layers that are needed to absorb the same amount of sunlight. GaAs needs only a layer of few micrometers thick, whereas c-Si needs a wafer of around 200 to 300 micrometres thick. Additionally, GaAs has a much higher energy conversion efficiency than c-Si by about 25–30%. Since GaAs has high resistance to heat, it is an ideal selection for concentrator systems where cell temperatures are high. In space applications, GaAs is popular where strong resistance to radiation damage and high cell efficiency are needed. However, the biggest disadvantage of GaAs-based PV cells is the high cost of the single-crystal substrate that GaAs is grown on, and thus it is most often used in concentrator systems where only a small area of GaAs cells is required.

### 1.4.3 Single-crystal silicon wafers

Typically, single c-Si solar cells outperform mc-Si wafers; however, they are more expensive. Geometrically, the c-Si cell has a diamond-ordered crystal structure. Although it exhibits predictable and uniform behaviour, it is also the most expensive type of Si due to the complicated manufacturing processes required. In the single c-Si, the regular arrangement of Si atoms produces a well-defined band structure. Each Si atom has four electrons in its outer shell, and pairs of electrons from neighbouring atoms are shared, so that each Si atom shares four bonds with the neighbouring atoms, as shown in figure 1.6 [37]. Fundamentally, c-Si is grown as a large cylindrical ingot forming circular or semi-square solar cells. Consequently, a number of cells can be more efficiently packed into a rectangular module. The growth of a single crystal can be achieved in two ways: FZ (float-zoning) and CZ (Czochralski growth). In the case of the CZ method (Figure 1.7-left) [38], a crucible is used to melt electronic grade polycrystalline c-Si. The attachment of a small Si seed crystal to the end of a spinning rod forms a contact with the surface of the molten Si, and then a crystal of Si is slowly pulled from the melt in a carefully controlled manner in order to

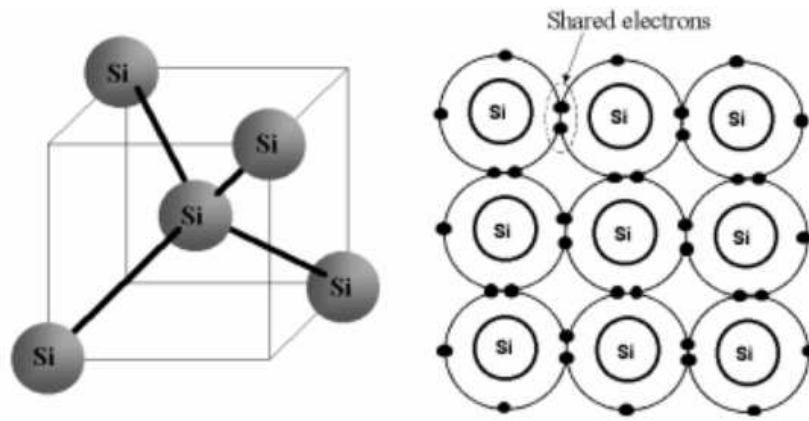


Figure 1.6: Crystalline structure of single crystalline silicon. .

maintain the diameter of the ingot and a stable growth front, and also to prevent spurious nucleation that would result in polycrystallinity. The reaction between the melt Si and many materials is extended. For example, using a silica a reaction can occur with Si, and evaporates easily from the melt. CZ-grown crystals, nevertheless, contain interstitial oxygen atoms with concentrations of  $10^{17}$ – $10^{18}$  atoms/cm<sup>3</sup> [39]. Another possible crystal growth technique is the FZ technique (see figure 1.7-right). In this technique, highly purification process are done for a solid rod. However, poly c-Si is melted by induction heating and a single crystal is pulled from this molten zone. Since there is no need to use a crucible, this material is of exceptional purity and more costly than CZ material. Although CZ material has high oxygen impurities which are unavoidable due to the effect of the quartz crucible [40], the main technological drawback of the FZ method is the need for a uniform, crack-free cylindrical feed rod. Currently, the FZ Si method is employed for premium high-efficiency cell applications. In contrast, for higher-volume, lower-cost applications, CZ Si is utilised.

#### 1.4.4 Multicrystalline silicon wafer

In general, mc-Si solar wafers have a significant cost advantage compared to mono c-Si wafers (described in section 1.4.3) due to more cost-effective crystallisation methods [11]. The directional solidification process of molten Si is used to produce mc-Si, starting at certain nucleation points from small crystallites expanding in the growth direction. Based on the crystallisation technology employed, crystallites of different size are produced with various compositions and distributions of contamination in the wafers. Fundamentally, the mc-Si wafer consists of single crystalline grains with different crystallographic orientations separated by grain boundaries (GBs), as shown in figure 10.16. These boundaries

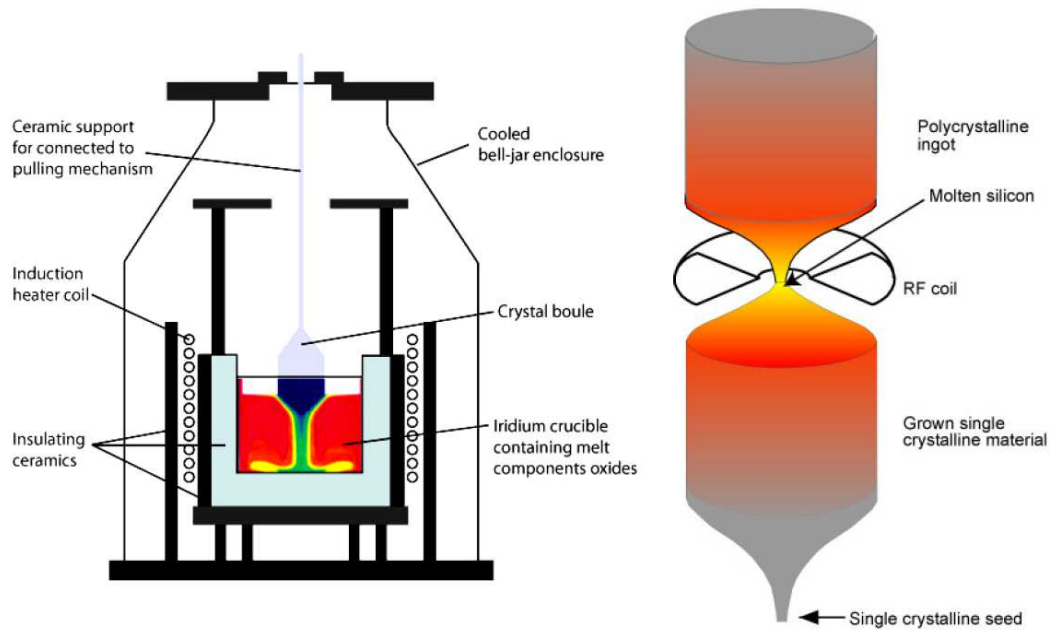


Figure 1.7: Schematics showing single crystal growth techniques including Czochralski growth (left) and FZ growth (right) [38].

can introduce defect energy levels into the band gap, producing highly localized regions of carrier recombination, and thus reducing the overall minority carrier lifetime of the material. Consequently, GBs in the material can affect solar cell performance. For example, the presence of GBs blocks the flow of carriers, providing shunting paths for current flow across the p-n junction [41]. Recombination losses at GBs can be significantly avoided

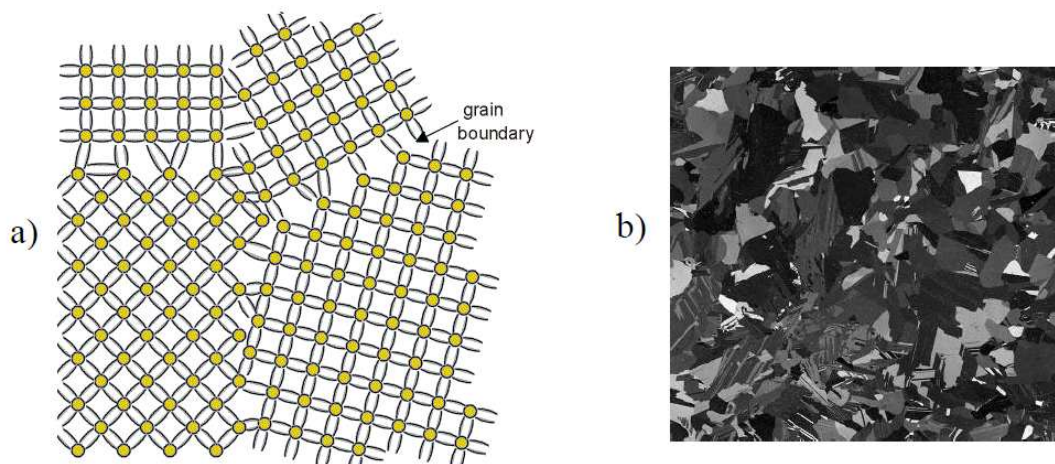


Figure 1.8: Grain boundary configurations: two crystal grains are separated by a boundary where the bonds are strained (a) amended from [42]; b) a  $10 \times 10 \text{ cm}^2$  multicrystalline wafer, where the wafer has been etched, so that grains of different orientation show up as light and dark. Source: [37].

by controlling grain sizes to the order of at least a few millimetres. Using this technique, single grains can extend from the front to the back of the cell, causing a reduction in resistance against carrier flow while reducing the GB length per unit of cell. These effects

allow multicrystalline material to be widely used in solar cell production. However, the use of mc-Si is potentially limited by rather high concentrations of point and extended defects (EDs) originating from the module growth environment and wafer processing under non-clean-room conditions. More details about the common point defects and EDs commonly present in mc-Si are given in section 1.6.

During the past 20 years, several techniques have been developed for the ingot-based crystallization process, but these techniques have the same processing basics, including ingot casting and sizing and wafer slicing. Directional solidification is the basis of the predominant techniques.

Firstly, Si is melted and poured into a square crucible, and kept in the liquid state in a high purity silicon-nitride coated quartz crucible. Then, a directional solidification process is applied by slowly lowering the crucible from the heated casting frame. This method is called the Bridgman method, as shown in figure 1.9 (a): Alternatively, heat is extracted from the bottom of the crucible in a technique called the heat-exchange method, as shown in figure 1.9 (b). The upper zone of the crucible is maintained at a temperature above the melting point of Si. Then, the solidification front moves from the bottom towards the top. The challenges in the development of the crystallisation process include the maintenance

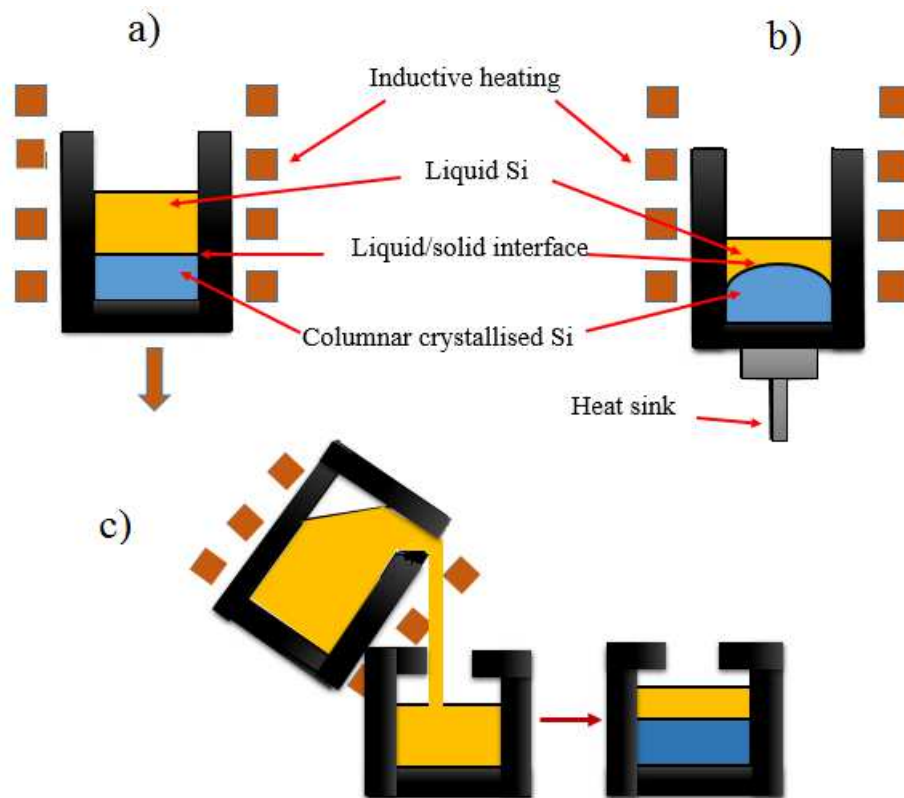


Figure 1.9: Crystallisation process: a) the Bridgman method, b) the heat-exchange method and c) block-casting technology to solidify a mc-Si block.

of a planar solidification front and controlling the velocity of crystallisation, as well as the avoidance of the formation of extensive dislocations in the crystal [11].

Polycrystalline Si has a higher contaminant content due to the direct contact with the crucible, which is the main reason for its reduced carrier lifetime and efficiency as compared with mono c-Si. After Si-ingot processing, all the regions of the mc-Si ingot formed, including the top, bottom and side, are cut away (contouring). Then, the ingot is divided into multiple blocks based on the desired cross-section; for example, a size of  $125 \times 125$  mm or  $200 \times 200$  mm. After that, the mc-Si bricks are wire-sawn into a number of mc-Si wafers with a certain thickness, such as  $200 \mu\text{m}$  [11].

## 1.5 Development of High Efficiency c-Si Solar Cells

A high-performance Si solar cell should have excellent optics including excellent light trapping, low reflection and low parasitic absorption from free carriers and metal contacts. It should also have low levels of avoidable recombination, including at the surface and in the junction, in the bulk, and around the cell perimeter. There should also be low ohmic losses. To achieve these attributes, several promising PV technologies have been investigated over the years [22, 43], in particular by research groups and companies interested in the c-Si field, and the capabilities developed are then incorporated into the manufacture of c-Si materials, cells and modules.

Figure 1.10 shows the current world-record efficiency for modules and cells. Generally, the term module is interchangeable with panel, reflecting the products sold by photovoltaic manufactures, whereas the term cell refers to the constituent building block of a module. From the figure, it is noticed that the highest efficiencies for devices with mono-crystalline Si are 25.6% in 2016 (and 26.6% in 2017) for cells and 23.8% for modules. The difference noticed between module and cell efficiency in this figure shows that individual cells are typically more efficient than modules (at least for now). The presence of areas that cannot produce power, which is called dead space, such as in the module frame and spaces between cells, is one of the main reasons why modules are less efficient than individual cells. Also efficiency is due to electrical losses occurring along connections linking individual cells. It is expected that further innovations with these panels can increase efficiency. Based on a recent study [44], some key developments are used to predict typical panel efficiency in 10 years time. During the transition period of the standard cell architecture towards higher efficiency models, different cell and contact structures are being developed, and the

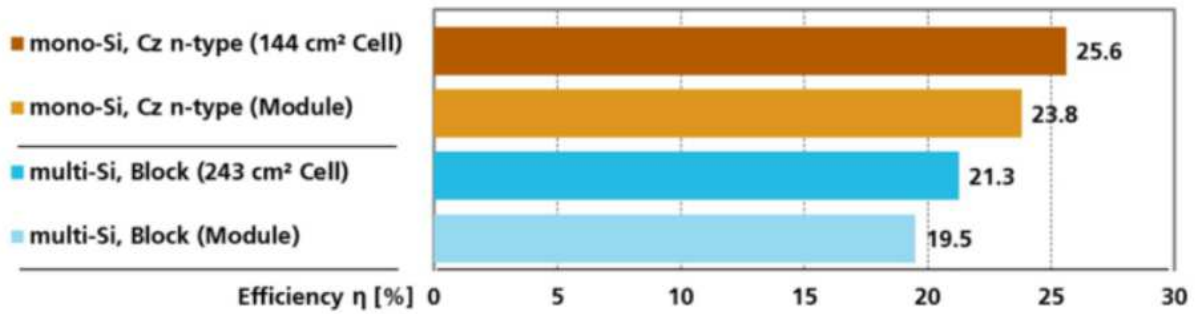


Figure 1.10: The record power conversion efficiency for mono- and multi-crystalline Si cells and modules. Source: [44].

following are major trends that are likely to drive up efficiency in commercial modules.

- Aluminium back surface field (Al-BSF) designs account for 80% of the Si cells manufactured. However, this proportion is expected to decline in the next few years. This design is shown schematically in figure 1.11 (left).
- The passivated emitter and rear cell (PERC) is more sophisticated design which is more efficient than the Al-BSF, and is predicted to become dominant. The presence of a non-continuous dielectric (insulating) layer at the back side of the cell improves the reflection at the (Al) electrode. The inclusion of this layer contributes to reflecting back more light towards the cell, increasing the opportunity to absorb the light again, and also to reduce electrical losses at the back (Al) side. Figure 1.11 (right) shows a passivated emitter, rear locally-doped (PERL) cell which is a member of the PERC family, but with higher efficiency (25%).

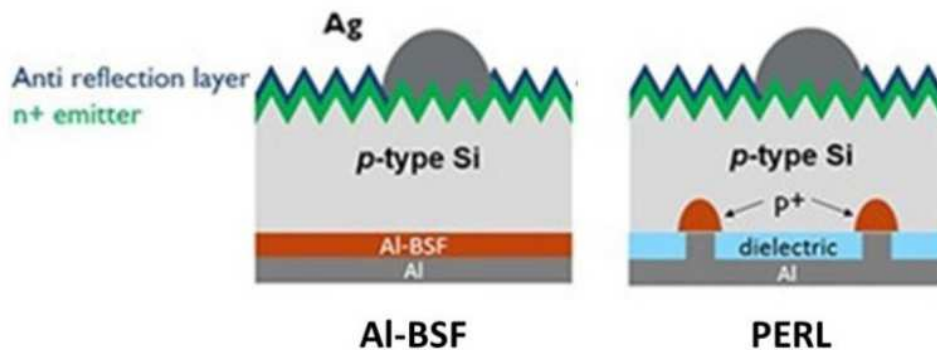


Figure 1.11: Schematic views of (a) Al-BSF and (b) PERL solar cells. Source: [44].

Figure 1.12 [44] presents data obtained in 2017 of the market share of different present solar cell models, including Al-BSF, PERC, PERL, Si-heterojunction, integrated back-contact, and Si-based tandem cells.

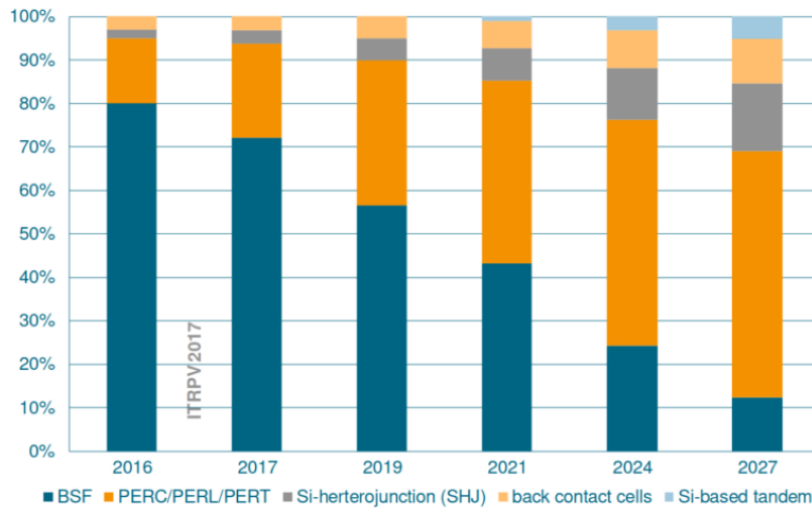


Figure 1.12: Projection of market share of of different Si solar cell design. Source: [45].

Regarding the method used to extract the current from the c-Si wafer to the external solar cell circuit, improvements in cell contact for some structures are presented below:

- Since current is transported axially in the wafer between the top and bottom sides and then laterally along the contacts, a conducting grid (lying at the top contact) assists lateral current flow. The grid consists of fingers and busbars as shown in figure 1.13, where the width of a finger is tens of micrometres; and that for busbars is in the order of millimetres. Usually, there are hundreds of fingers and 3–4 busbars.

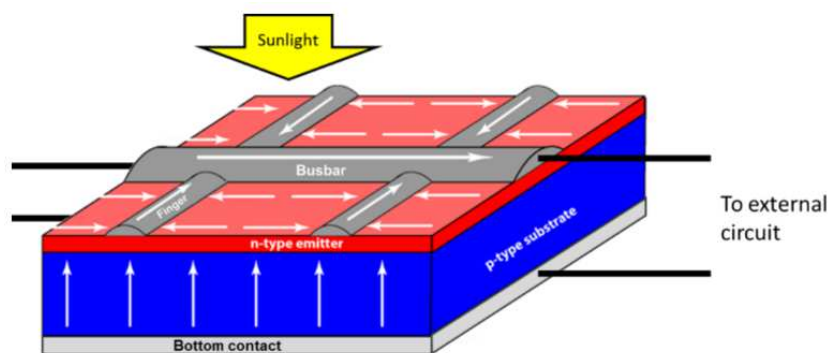


Figure 1.13: A schematic of current flow in a solar cell, where current is collected along the fingers (white arrows) and then fed into the busbars. Image taken from [44].

Figure 1.14 shows a recent industry study (2016) for the predicted power of a fixed module constructed from 60 cells with dimensions of 156 mm × 156 mm. The expected

## 1.6 Defects and Impurities Associated with The Processing of mc-Si Ingots

efficiencies are approximately 20% and 26% for low- and high-end technologies (such as p-type multi-crystalline Al-BSF and n-type monocrystalline IBC), up from around 17% and 21% today respectively. Consequently, it is expected that an average premium module will be able to convert more than a quarter of all incident light into electricity in 2027, which represents a very significant increase (by approximately 20%, relative) compared to today's products.

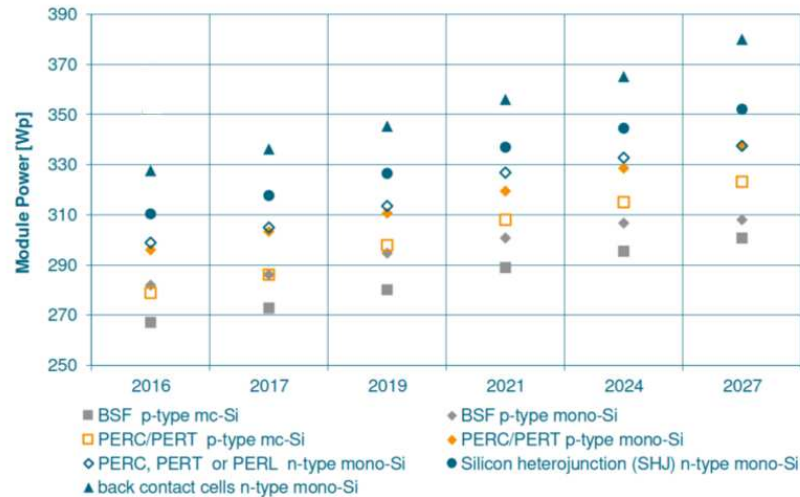


Figure 1.14: Projections for the predicated power of a fixed module size (60 cells with dimensions of 156 mm×156 mm). Source: [45].

## 1.6 Defects and Impurities Associated with The Processing of mc-Si Ingots

All deviations from unexcited, perfect, infinite crystal structures represent defects which may occur due to accidents of growth and processing. The purpose of this part of the thesis is to understand the formation processes of the most common point and extended defects that are usually present in mc-Si solar cells. The main classification of defects in silicon is shown in figure 1.15, where the classification depends on defect dimensions, including point defects (zero dimensions) and extended defects (in one, two and three dimensions) [46]. Point defects are occupied isolated sites in the crystal structure such as a solute or impurity atom that alter the crystal form at a single point. One-dimensional defects, also called dislocations, represent lines along the crystal pattern which is broken. Surface defects (2D) include those on the external surface and the GBs along which distinct crystallites are joined together. Lastly, 3D defects change the crystal pattern

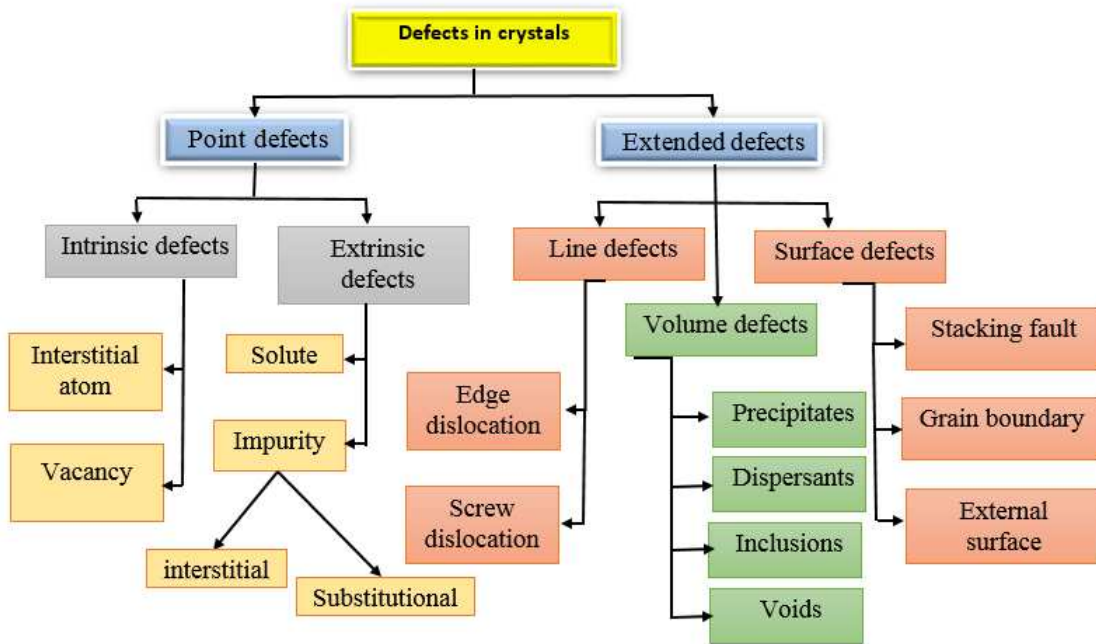


Figure 1.15: Block diagram of the main classification of defects in silicon.

over a finite volume and include voids and precipitates, for example [47].

Intrinsic defects are formed when an atom is missing from a site that used to be filled in the crystal, creating a vacancy, or when an atom occupies an interstitial site to form an interstitial. In most crystalline solids, interstitial defects are small (as in the diamond structure) and have an unfavourable bonding configuration, and interstitial atoms are high-energy defects that are relatively uncommon but can aggregate. In contrast, vacancies are present in significant concentrations in all crystalline materials. The most obvious impact is to control atom migration on the crystal lattice via solid state diffusion. For the easier motion of an atom from one crystal lattice site to another, the target site must be vacant.

Extrinsic point defects, which represent foreign atoms, are classified according to the method of doping into solutes if they are intentionally added to the material and types of impurities if they are unintentionally added to the material. The foreign atom may occupy lattice sites (substitutional solutes, or impurities), or it may fill an interstitial site as an interstitial solute. The sites are relatively depend on the atom's size. For example, hydrogen, carbon and nitrogen are small atoms and are often found in interstitial sites, whereas larger atoms are usually substitutional. Extrinsic defects are used to control electrical properties, and in structural metals and alloys extrinsic defects are added to increase mechanical strength and, consequently, they affect almost all of the engineering specifications of semiconducting crystals. Since the silicon bonds are saturated, Si has

very low conductivity in its pure state, so that pure silicon can only conduct electricity when electrons are excited into high energy electron states. Therefore, point defects are intentionally added to semiconductors to control the type and concentration of charge carriers in order to create exchange between valence electrons and holes in the bonding pattern. For example, when boron is added to the Si lattice, a valence electron is missing from the immediate neighbourhood of the boron atom, producing a hole in the bonding pattern. Electrons can then move between the bonds by exchanging with the hole. The energy required to separate the hole from the boron ion core is relatively small as compared with that required to excite an electron from a Si-Si bond into a high-energy state. At room-temperature, the conductivity of Si is significantly increased when a small amount of boron is added. Electron-deficient solutes like boron that cause holes in the Si configuration of bonding electrons are called acceptors.

Similarly, conductivity increases when a solute with extra electrons is added to a semiconductor with saturated bonds. For example, if phosphorus is added to Si, the 5 valence electrons of P are sufficient to fill the local covalent bonds with one electron left over which can only change into an excited state. It requires a relatively small energy increment to free this electron from the P core, in which case it can transport current by moving through the lattice. As a result, the electronic conductivity of Si rises significantly if a small amount of P is added. Electron-excess solutes such as P in Si are called donors [47].

It is important to mention here that these defects are deliberately added to materials to form p- and n-type conductivity in integrated circuits. These types of defects are essential for many optoelectronic devices like solar cells.

### 1.6.1 Fundamentals of extended defects

Any permanent deviations from the correct placement of atoms in real crystals represent EDs, as mentioned in section 1.6. They are usefully grouped according to the number of dimensions in which they are extended, into those of greater than atomic size, into lines, surface and volume defects. The theory behind these EDs is described in detail in the following section, whereas the analysis of results obtained in investigating them is presented in Chapters 7–9. They include the intrinsic stacking fault (ISF) $\langle 111 \rangle$  and  $\Sigma 5$  (001) GB as examples of a low-strain stacking error, and much more bond-length and bond-angle strain, respectively, as well as voids. The interaction of these EDs with mobile

point defects such as iron which represent a more deleterious types of contamination in Si, is also analysed. Although the distribution and density of EDs and point defects vary from one mc-Si sample to another, depending on their conditions of preparation (such as rapid growth), both of these defect types are understood to act as recombination centres, limiting the operational efficiency of mc-Si solar cells [48]. Furthermore, EDs themselves are major defects affecting the stability, mechanical behaviour and transport properties of materials [49], and thus the performance of solar energy application devices [50].

The interaction of point defects with EDs in semiconductors in general and Si in particular has been the subject of close interest over the last decade [51]. In particular, impurities have been observed to segregate at EDs. This influence, called gettering, shows how EDs may play an important role in controlling the detrimental impact of contamination in the active region of semiconducting devices such as solar cells.

One of the main reasons behind changes in process conditions is the segregation of impurities that may be present due to the high solubility of most materials in the liquid Si phase [52]. An advantage to this is the cleaning of Si via the segregation of impurities at the top of the block. In contrast, the drawback of this segregation is the change in oxygen, carbon and doping concentrations in the wafers, depending on the wafer position in the block. Extra contamination from the crucible further results in different wafer characteristics in the bottom and side areas of the wafer in close contact with the crucible walls. Together these phenomena produce location-dependent behaviour in the Si wafers, yielding a broadening of the solar cell efficiency distribution represented by change in a short circuit current of 5–10% depending on the position of the wafer in a block.

At the same time, EDs may themselves be detrimental to the performance of such devices. Hence, understanding the properties of EDs and their interactions with point defects is crucial to developing better semiconducting devices.

Different dimensions of EDs in mc-Si are studied in this work including intrinsic stacking faults, grain boundaries and voids.

### **1.6.2 Stacking faults, grain boundaries and voids**

Since Si does not grow as a perfect crystal under normal growth conditions, stacking faults and GBs are often present. A stacking fault is a local region of the irregular stacking of crystal planes related to the presence of partial dislocations that cause reductions in the elastic strain energy of the crystal. Detailed analyses of intrinsic stacking faults are

concluded in chapter 7. A GB is a region separating two grains (crystals) of the same phase.

### 1.6.3 Iron-extended defect interaction

Iron is a common and unavoidable contaminant in the semiconductor industry and PV silicon [53, 54]. It has been widely investigated and the effects of Fe in mc-Si solar cells have been recently reviewed [55]. Generally, it is agreed that Fe is especially problematic because it introduces deep levels in the band gap, reducing the minority carrier lifetime, and it diffuses very rapidly. Even in the slowly cooled directional solidification growth technique, Fe is supersaturated in the form of highly detrimental interstitial point defect form [54] residing at the tetrahedral interstitial site in the positively charged form ( $\text{Fe}_i^+$ ) in p-type Si or the neutral form ( $\text{Fe}_i^0$ ) in intrinsic and n-type Si [56]. In addition, its detrimental effects in mc-Si solar cells have also been reviewed [55]. Interstitial iron ( $\text{Fe}_i$ ) is understood to be an active recombination centre, lowering device efficiency even at less than 1 ppb [57]. Furthermore, recombination, mobility reduction and minority carrier lifetime effects are directly associated with both impurities and structural imperfections in the crystal structure, hence degrading solar cell performance [57, 58]. The properties of Fe and its complexes in bulk Si have been previously investigated both experimentally and theoretically [59–64]. According to previous studies [55, 65, 66], different technical methods have been used to getter  $\text{Fe}_i$  such as nanoprecipitation [67], structural damage [68], electrically charged regions [69] or phosphorus in-diffusion [70]. Among these, structural/extended damage which causes an irregular disordered sequence of atoms has received more extensive attention than other techniques [71, 72].

In this work, however, internal gettering by EDs, including stacking faults, GBs and voids is one possibility. In particular, there is evidence that these EDs interact with mobile point defects, such as iron, which in turn is a common contaminant in some grades of silicon. However, there is relatively little understanding of the mechanism of the segregation of iron at EDs at an atomistic level, possibly because the modelling of EDs is itself challenging in terms of the system size required, and the detailed structure of GBs in mc-Si remains a matter of some debate. A better understanding of the characteristics of iron related defects and their reactions and formation as well as their transformation will contribute to efforts to improve solar cell fabrication and efficiency.

The main aim of this thesis is to explain the interaction between  $\text{Fe}_i$  atoms and EDs

including intrinsic stacking faults,  $\Sigma 5$ -(001) and  $\Sigma 3$ -(001) twist GBs and voids. The relevant analyses are presented in chapters 5–9. In this work, density functional theory, as implemented in AIMPRO, has been employed, with systems modelled using periodic boundary conditions and large supercells. The fundamental rationale of this computational method is presented in chapters 2 and 3. Then, the data obtained from DFT simulations have been employed in the TCAD Sentaurus tool to model Si solar cells using the transfer matrix method, and the results are analysed in chapter 10.

## 1.7 Thesis Outline

This thesis is divided into three parts. The first part introduces the theoretical background of this study. The second part covered the considered applications. Finally, conclusions along with suggestions for future work are presented in the third part of this study. Furthermore, each part is subdivided into chapters and a summary of the content of each is introduced below, along with representative references.

### 1.7.1 Part I - Theory and Method

#### 1.7.1.1 Chapter 2 - *Ab Initio* Background and AIMPRO Package

This chapter presents a brief overview of the computational method used for atomic level analysis presented by the AIMPRO code, which stands for the Ab Initio Modelling PROGRAM. This code is used to determine the structure of an assembly of atoms by solving the Schrödinger equation for both the ions and electrons. Simplification of the many-body problem given by the Born-Oppenheimer approximation is assumed by most techniques outlined here. The common theoretical approaches, and the general parameters of computer code applied in the research are described, focusing on density functional theory which represents the best tool for large-scale calculations. Using this method, the total energy of a system can be described as a function of electronic density only. Furthermore, the chapter highlights the sources of error that affect the stability of solutions and accuracy of calculations.

#### 1.7.1.2 Chapter 3 - Modelling of Derived Properties

In this chapter, definitions and explanations of various physical quantities are outlined, which correspond to the computational methods adopted in the application chapters of

this thesis. Moreover, preliminary results are recorded in the relevant sections of this chapter to show the convergence of the computational approach adopted. This includes, for example, calculations of binding energy, migration energies, electronic structures, electrical levels and optical absorption.

### **1.7.1.3 Chapter 4 - Device Simulation Background and the Synopsys TCAD Package**

As an attempt to investigate the effects resulting from impurity-defect interactions on the performance of Si photovoltaic devices, the data obtained at the quantum-mechanical level provide the basis for device-level simulation using the technology computer-aided design (TCAD) Sentaurus. Synopsys TCAD [73] is a package of simulation software used to simulate electrical properties of devices such as solar cells. This chapter provides general information of about the use of TCAD to model, simulate and design silicon solar cell devices. By understanding the fundamentals of this code, one can optimise a device for particular applications and gain deep insights into the physical phenomena that dominate the features of devices. In this way, the semiconductor technology can progress in a timely and cost-effective manner whilst bridging the gap between manufacturing and electronic design automation.

## **1.7.2 Part II - Application**

The chapters within this part of the thesis provide in depth details of the results obtained in this study. The majority of chapters 5–9 present the analysis of the behaviour of Fe in bulk Si and at EDs using density functional theory. Trends in the energetics, and magnetic, geometric, electronic and substitutional electrical properties, Fe-vacancies and interstitial and interstitial-pair structures have been studied in these chapters. In contrast, the analysis of iron-EDs complexes in silicon solar cells using TCAD device modelling is presented in chapter 10.

### **1.7.2.1 Chapter 5 - Iron Contamination in Pure Si**

Theoretical investigations into deep-level  $Fe_i$  in bulk silicon and when facing a vacancy to become a substitutional impurity are the scope of this chapter. Calculations of the spin energies, electrical levels and migration barrier of  $Fe_i$  in pure silicon have been performed, and compared with values in the literature, confirming the deleterious effects of iron in

---

silicon by investigating the electronic levels introduced in the Si band gap, which are the main reason for the reduction the minority carrier lifetime and thus have significant impacts on solar cell efficiency. Furthermore, the relatively high diffusivity of Fe throughout the silicon lattice is also confirmed. Trends in the magnetic, electrical and optical properties of  $\text{Fe}_i$  have been also investigated in this chapter.

### 1.7.2.2 Chapter 6 - Interstitial Fe-pairs in Bulk Silicon

The results of first-principle calculations of iron pair formation with respect to individual iron atoms are given in this chapter. Of particular note is that the formation of  $\text{Fe}_i$  pairs in bulk Si is energetically favourable, with the equilibrium spin states being sensitive to the inter-nuclear separation of Fe. The magnetic order predicted for pairs as a function of inter-nuclear distance is also studied. Furthermore, the migration barrier for  $\text{Fe}_i$ -pairs has been found to be lower than that of individual interstitials, suggesting that pairs may be a key contributor to Fe diffusion and precipitation. Consequently, in this chapter, it is predicted that the role  $\text{Fe}_i$  pair play in diffusion, iron-precipitation and segregation to, for example, EDs, is likely to be of significance.

### 1.7.2.3 Chapter 7 - Analysis of Iron Segregation at Stacking Faults in mc-Si

This chapter introduce the fundamentals of intrinsic stacking faults and reviews studies that support the hypothesis behind the gettering of iron by intrinsic stacking faults. Prior to the calculation of this gettering, the structural, electronic, electrical and optical properties of intrinsic stacking faults themselves have been validated as an example with very low-strain, comparable to the  $\Sigma 3$ -(111) GB. The results for segregation and other investigations of  $\text{Fe}_i$  and its pairs at intrinsic stacking faults have been compared with other forms of planar defects, as shown in the next chapter.

### 1.7.2.4 Chapter 8 - Analysis of Iron Segregation at Twist Grain Boundaries in mc-Si

In an attempt to develop a fundamental understanding of the mechanism for iron-GB interaction, the analysis of Fe gettering by  $\Sigma 5$ -(001) and  $\Sigma 3$ -(110) twist GBs is the main focus of this chapter. In particular, there is some evidence of the gettering of Fe at GBs being a viable route to the reduction of the deleterious effects of Fe in mc-Si solar cells. The modification of the spin energies and electrical and optical properties of iron

decorated GBs are also presented in this chapter. Additionally, the novel aspect of this chapter concerns the binding that is greatly increased by  $\text{Fe}_i$  being trapped at vacancies at the GB, or perhaps more critically by Fe already trapped there. The latter result indicates that the precipitation of Fe at GBs is strongly energetically favourable, even in the absence of direct chemical bonding afforded by the substitution of Si by iron.

### **1.7.2.5 Chapter 9 - Voids in Silicon as a Sink for Interstitial Iron**

The focus of this chapter is the gettering of Fe by voids as an example of 3D EDs. The theoretical background of different void-related entities and their formation, structure, growth and evolution in silicon are introduced. By investigating Fe decorated and undecorated voids with different spin and charge states, it is surprisingly found that the most stable sites lie just outside the void, which may explain the experimental observation that only a single layer of iron forms at voids.

### **1.7.2.6 Chapter 10 - Extended Defects Engineering with Iron Contamination for Improved mc-Si Solar Cells**

The bond-strain may beneficially alter the band-gap and absorption coefficient, and these play a role in the segregation of deleterious mobile impurities such as iron. In this chapter, the results of first-principle quantum-chemical simulations are combined with TCAD device modelling to examine the advantageous and disadvantageous effects of these EDs on the performance of solar cells in the presence of Fe. Perhaps, the most valuable outcome of this chapter is the conclusion that the segregation of diffusing iron at these EDs is likely to have a positive impact on device characteristics.

## **1.7.3 Part III - Conclusions and Future Work**

Finally, the results presented in this thesis as well as suggestions for relevant future work are summarised in this chapter.

# Part I

## Theory and Method

# *Ab Initio* Background and the AIMPRO Package

“As far as the laws of mathematics refer to reality, they are not certain; and as far as they are certain, they do not refer to reality.”

Albert Einstein

This chapter describe the computational method used at the atomic level to investigate material properties. The first section (section 2.1) provides a general introduction to the theory behind the AIMPRO code used to determine the structure of an assembly of atoms by solving the Schrödinger equation for both ions and electrons, starting by simplifying the many-body problem given by the Born-Oppenheimer approximation that is employed in most of the techniques described here. Following this, the common theoretical used approaches and general parameters of computer code applied in this research are described, highlighting the sources of error that may affect the stability of solutions and accuracy of calculations. All these concepts are described in detail in the following section.

## 2.1 Introduction

Irrespective of the theoretical methods and approximations utilised by those in the academic community to study the properties of materials, understanding some of the fundamental concepts of solid state physics, including the quantum-mechanical behaviour of a given system with its interacting elections can be employed to predict, analyse and interpret experimental results. In general, according to the general laws of nature, the

properties of a material are dependent on its structure and composition. Atomic structure of a solid material can be fundamentally described as a collection of atoms, and each atom consists of a nucleus of positive charge, surrounded by a number of neutralising electrons. Electrons that occupy the filled inner shells of the atoms are called core electrons, which screen the nuclear charges from the valence electrons. Material's characteristics depends on the electrostatic interactions occurring between valence electrons and nuclei, as well as interactions arising from the quantum-mechanical characteristics of the electron. In this chapter, the fundamentals of the many-body problem is presented in section 2.2 , with reference to the approximations that have been achieved to tackle this problem. The first approximation that can be considered is when the outer shells' electrons only participate in physical processes in the solid form, while the electrons in the inner shells do not take part in the process. The second approximation, is a result of Born and Oppenheimer (section 2.3), which allows the decoupling of electronic and nuclear motion. For context, number of methods adopted to solve the corresponding Kohn-Sham equations have been outlined in section 2.4.2.1, which are required to select the electrons that are involved in the calculations. Moreover, the fundamentals of density functional theory are also described in this chapter (see section 2.4.2), highlighting local density and generalised gradient approximations for exchange-correlation energy (section 2.5). The main goal of this chapter, however, is to set out the approximations and techniques employed in AIMPRO (section 2.6), which is a self-consistent density functional code applied to atomic structures real space. AIMPRO can be used to calculate and estimate a number of experimental observables such as electronic transition energies, localised vibrational modes, migration barriers and binding energies. With this computing program, wavefunctions are expanded on a Gaussian basis (section 2.8), and electron-ion interaction is modelled via norm-conserving pseudopotentials. The later method has been successfully applied to eliminate the effect of core electrons in practical applications, where these electrons have been replaced by an effective potential acting on valence electrons, as outlined in section 2.11. Finally, the steps required to perform calculations which achieved the required accuracy are included in choosing the basis set, for example, used to describe the wave functions of the electrons. Details of all these concepts are given in the following sections.

## 2.2 Many-Body Problem

Wavefunctions in quantum mechanics have been utilised to provide an accurate theoretical description of the quantum state of any given system. Here, the ultimate objective of the quantum *Ab Initio* method is to find a solution for the quantum mechanical wave equation known as the Schrödinger equation. The solution of the many-body Schrödinger equation for a specific configuration involves the mass ( $m$ ), relative coordinate ( $r$ ) and interaction potential ( $V$ ) between the particle and the interaction centre given by:

$$-\frac{\hbar^2}{2m} \nabla^2 \Psi + V\Psi = E\Psi \quad (2.1)$$

where  $\hbar$  is the reduced Planck's constant. By solving this equation, a clear description of a system's behaviour, from atoms and molecules to more complex solid systems can be achieved.

The problem posed is to find the solution for a many-body system by solving the eigenvalue problem with using quantum mechanics. This is reflected in calculations of the most realistic electronic structure, including interacting particles, where it is difficult to perform these calculations precisely even using the most powerful super-computers. Additionally, it is not possible to solve the Schrödinger equation exactly for a structure of an assembly of atoms containing both ions and electrons. Consequently, approximations have been used as shown in the following sections. The stationary state of a quantum-mechanical system is described by the non-relativistic time-dependent Schrödinger equation, which generally has the formula:

$$\hat{H}\Psi(r) = E\Psi(r) \quad (2.2)$$

where  $\hat{H}$  is the many-body Hamiltonian operator, in which both the kinetic and potential energies of the nuclei and electrons are described.  $E$  is the total energy of the system, and  $\Psi$  is the many-body wave function, which generally is a function of the electron spin, co-ordinates and nuclear positions:

$$\Psi = \Psi(r_1, r_2, \dots; R_1, R_2, \dots) \quad (2.3)$$

where  $(r_1, r_2, \dots, r_N)$  are the electrons' coordinates and  $(R_1, R_2, \dots, R_M)$  are the coordinates of the nuclei of masses  $(M_1, M_2, \dots, M_M)$ . The electronic Hamiltonian formula can

be expressed as:

$$\hat{H} = \hat{T}_e + \hat{T}_N + \hat{V}_{N-e} + \hat{V}_{e-e} + \hat{V}_{N-N} \quad (2.4)$$

where  $\hat{T}_e$ ,  $\hat{T}_N$  refer to the kinetic energy of electrons and nuclei respectively.  $\hat{V}_{e-e}$ ,  $\hat{V}_{N-N}$  are the repulsive Coulomb potentials of electron-electron and nuclear-nuclear interactions respectively, and  $\hat{V}_{e-N}$  is the attractive Coulomb potential of electron-nuclear interaction. Then, the Hamiltonian operator in the Schrödinger equation for a set of electrons in a field due to atomic number  $Z_A$  at sites  $R_A$  can be written as:

$$\begin{aligned} H = & -\sum_{i=1}^N \frac{\hbar^2}{2m_e} \nabla_i^2 - \sum_{A=1}^M \frac{\hbar^2}{2M_A} \nabla_A^2 - \sum_{i=1}^N \sum_{A=1}^M \frac{Z_A e^2}{4\pi\epsilon_0 r_{iA}} \\ & + \sum_{i=1}^N \sum_{j>i}^N \frac{e^2}{4\pi\epsilon_0 r_{ij}} + \sum_{A=1}^M \sum_{B>A}^M \frac{Z_A Z_B e^2}{4\pi\epsilon_0 R_{AB}}, \end{aligned} \quad (2.5)$$

where

$$r_{ij} = |r_i - r_j|, r_{iA} = |r_i - R_A|, R_{AB} = |R_A - R_B|. \quad (2.6)$$

The atomic units,  $e$ ,  $\hbar$ ,  $m_e$  and  $4\pi\epsilon_0$  are assumed to be equal to one. Then, 1 a.u. of energy is equivalent to 27.212 eV, and 1 a.u. of length is equivalent to a Bohr radius (0.529Å). Hence, the Hamiltonian of a system consisting of electrons and nuclei can be given in atomic units as:

$$\hat{H} = \overbrace{\sum_{i=1}^N \frac{1}{2} \nabla_i^2}^{\text{term 1}} - \underbrace{\sum_{A=1}^M \frac{1}{2M_A} \nabla_A^2}_{\text{term 2}} - \overbrace{\sum_{i=1}^N \sum_{A=1}^M \frac{Z_A}{r_{iA}}}_{\text{term 3}} + \underbrace{\sum_{i=1}^N \sum_{j>i}^N \frac{1}{r_{ij}}}_{\text{term 4}} + \overbrace{\sum_{A=1}^M \sum_{B>A}^M \frac{Z_A Z_B}{R_{AB}}}_{\text{term 5}} \quad (2.7)$$

The first and second terms represent the kinetic energies of the electrons and nuclei respectively. The third term refers to the Coulombic attraction between the  $i^{\text{th}}$  electrons and the  $A^{\text{th}}$  nucleus, and the fourth represents the Coulombic repulsion between the  $i^{\text{th}}$  and  $j^{\text{th}}$  electrons. The last term includes the nuclear Coulombic repulsion between the  $A^{\text{th}}$  and  $B^{\text{th}}$  nucleus. Practical methods used to solve this equation need, firstly, to decouple the motion of electrons and ions, and then one can calculate the effective potential felt by each electron that results from the other electrons and ions. Subsequently, the forces on the ions can be calculated, and thus, the ion coordinates can be optimised with respect to the total energy. Consequently, the equilibrium geometry is derived.

Indeed, finding a direct numerical solution for the Hamiltonian expression seems rather complicated, and, consequently, solving the Schrödinger equation directly for this Hamil-

tonian is difficult even on the largest and highest speed computer available. This is due to the motions of electrons and nuclei which are coupled. Therefore, a set of approximations can be used to simplify the numerical complexity, taking into account the large discrepancy in magnitude between the masses of nuclei and electrons. Furthermore, by returning to the first step, one needs to separate the electron and ion components of the many-body wavefunctions, and this is achieved under the adiabatic or Born-Oppenheimer approximation that was formulated in 1925 by Born and Oppenheimer [74].

## 2.3 Born-Oppenheimer Approximation

Due to the reality behind the large mass of the ions compared to that of an electron, where the mass of a proton or a neutron is about 1836 times larger than the electron mass, the motion of the ions simply modulates the electronic wavefunction. This leads to a Hamiltonian for the electrons in a field generated by static nuclei. In the Born-Oppenheimer approximation [74], it is assumed that the nuclei are stationary objects while the electrons are moving in a field of fixed nuclei.

Therefore, according to this approximation, the term of kinetic energy of the nuclei ( $T_N$ ) can be removed from the Hamiltonian equation (Eq. 2.4) and the repulsive nuclear-nuclear term ( $V_{N-N}$ ) can be considered as a constant. Consequently the total wavefunction can be decoupled into electronic and nuclear wavefunctions:

$$\Psi_{\text{total}} = \Psi_{\text{electronic}} \Psi_{\text{nuclear}} \quad (2.8)$$

or, in a more explicit formula:

$$\Psi_{\text{total}}(r, R) = \psi_{r,R}(r) \phi(R) \quad (2.9)$$

where  $\phi(R)$  is an amplitude dependent on the positions of the ions. The electronic wavefunction  $\psi_R(r)$  depends upon the position of the nuclei, where  $\psi_{\text{electronic}}$  explicitly depends on the electronic coordinates  $r$  and parametrically upon the nuclear positions  $R$ . Then, the electronic Hamiltonian ( $\hat{H}_{\text{electronic}}$ ) for a system with fixed atomic positions takes the form:

$$\hat{H}_{\text{electronic}} = \sum_{i=1}^N \frac{1}{2} \nabla_i^2 - \sum_{i=1}^N \sum_{A=1}^M \frac{Z_A}{r_{iA}} - \sum_{i=1}^N \sum_{j>i}^N \frac{1}{r_{ij}} \quad (2.10)$$

this is equal to:

$$\hat{T}_e + \hat{V}_{N-e} + \hat{V}_{e-e} \tag{2.11}$$

Equation 2.10 allows the electron problem to be solved separately, with a considerable reduction in the calculation time.

## 2.4 Solving the Many-body Wave Function Problem

As mentioned above, the behaviour of the motion of electrons in solids can be described by applying the theory of quantum mechanics. Calculations based on this theory are implemented by either popular methods, such as Hartree-Fock (the wave function approach) or density functional theory (DFT) (see section 2.4.2). The calculations involve additional details for characterising the electronic and atomic structures of the nano-scale system. Exchange and correlation (section 2.5) are two quantum-mechanical concepts utilised to describe electron-electron interactions. The correlation interaction means that the electrostatic field obtained by moving an electron will influence the positions of other electrons. This effect is completely missing in Hartree-Fock theory. The exchange interaction, which is a purely quantum-mechanical energy term, reflects the anti-symmetry of a Fermi-Dirac wave function with respect to the exchange of two equivalent particles for the case of electrons.

### 2.4.1 Hartree-Fock Approximation

Based on the Pauli exchange principle, and because electrons are indistinguishable Fermions, the electronic wave functions should be anti-symmetric with respect to a change in any two electron coordinates. According to the many-electron wave-function description, this can be enforced by forming one Slater determinant of single-electron wave functions. This represents the Hartree-Fock (HF) approximation, which is defined by the expression:

$$\Psi(r_1, \dots, r_n) = (n!)^{-1/2} \begin{vmatrix} \Psi_1(r_1) & \Psi_1(r_2) & \dots & \Psi_1(r_n) \\ \Psi_2(r_1) & \Psi_2(r_2) & \dots & \Psi_2(r_n) \\ \cdot & \cdot & \cdot & \cdot \\ \cdot & \cdot & \cdot & \cdot \\ \Psi_n(r_1) & \Psi_n(r_2) & \dots & \Psi_n(r_n) \end{vmatrix} \tag{2.12}$$

By utilising the frame of the Slater determinant, and to achieve the interchange of two electrons, the wave function is multiplied by  $-1$ , while a null wave function can result from the presence of two electrons with the same coordinates. Although the HF method gives a reasonable representation of atoms and many molecules, HF equations have the computational disadvantage that each electron moves in a different potential (dependent orbital). In addition, exchange in the HF approach is treated exactly, but correlation effects caused by the specific Coulomb interaction between the electrons are omitted by definition. Thus, the neglect of correlation effects between the electrons probably leads to significantly overestimated band-gaps, as well as incorrect ground state results. Moreover, first-principle HF methods are computationally demanding, particularly for solid-state problems.

### 2.4.2 Density Functional Theory (Electron Density Approach)

In order to perform first principle calculations for large atomic systems, the electron density approach has been applied very successfully over the past decade, initially by Walter Kohn in 1998. He received the Nobel Prize in chemistry for well-establishing a framework to measure the electronic properties of solids based on density functional theory (DFT) [75].

The principal feature of this approach is that the many-body problem is solved directly for the charge density  $n(r)$ , which only depends on position, instead of the many-electron wavefunctions as in HF theory (section 2.4.1).

In general, the major challenge of any many-body theory is the reduction of the major parameters required to describe the system. DFT is an extremely successful quantum mechanical modelling method used in physics and chemistry to understand the electronic interaction of a many-body system in the ground state, and such an approach can be utilised to describe the ground state characteristics of atoms, molecules and solids [76], as well as to examine effectively the properties of surfaces and interfaces in a material. This approach is simple in that the basic variable of the system depends on only three variables, which are the spatial coordinates  $x$ ,  $y$  and  $z$ , rather than the  $3n$  variables in the problem above. The exact form of the functional is not known but the related conditions which satisfy DFT have been formulated.

### 2.4.2.1 Kohn-Sham Equations

From a practical point of view, it is necessary to formulate DFT in such a way that it could be applied for computational applications. The total energy functional of a system can be written as:

$$E[n] = T[n] + V_{\text{external}}[n] + V_{e-e}[n] \quad (2.13)$$

Here,  $V_{\text{external}}$  is an external potential that acts on the system, which has the form:

$$V_{\text{external}}[n] = \int V_{\text{external}} \cdot n(r) dr \quad (2.14)$$

In addition,  $V_{e-e}[n]$  represent the electron-electron interaction, while  $T[n]$  is the kinetic energy functional. Both of these forms resolved for systems of interacting electrons were solved in 1963 using the Kohn and Sham (KS) approach [77]. The main idea behind the KS approach is to replace the original interacting electrons of the system with a density  $n(r)$  by electrons of a non-interacting system which has the same density. The KS equations should be solved iteratively until reaching self-consistency, where iteration cycles are required due to the interdependence between orbitals and potential, as discussed in section 2.10 below.

In this study, the Kohn-Sham eigen-functions of the valance electrons are expanded using atom centred Gaussian functions [78], consisting of independent sets of  $s$ -,  $p$ - and  $d$ -type Cartesian Gaussian functions with 4 and 6 different widths for the Si and Fe, respectively, corresponding to 28 and 60 independent functions per atom.

## 2.5 Exchange-Correlation Functional

In order to produce the correct ground state energy and charge density, the electron density of a homogeneous electron gas is the basis for most approximations. Several approximations of  $E_{\text{xc}}[n]$  have been proposed to describe the exchange-correlation. One of the simplest approximations is the local density approximation (LDA) [79]. Here the idea is that, for a system with a given electron density  $n(r)$ , the exact  $E_{\text{xc}}[n]$  density at each point in space will be replaced by the  $E_{\text{xc}}[n]$  density of a homogeneous electron gas of the same electron density; in other words  $n(r) = n_0$ . This treats the inhomogeneous electron as locally uniform. This approximation applies to a spin zero system, and the

exchange-correlation is approximated by:

$$E_{xc}[n] = \int n(r)\varepsilon_{xc}(n)dr \quad (2.15)$$

Here  $\varepsilon_{xc}(n)$  is the exchange-correlation density for the homogeneous electron gas of a system  $n(r)$ . Although the DFT method in LDA is very successful for a large variety of problems, giving reasonable descriptions of non homogeneous systems, the description of many interesting systems requires improvements, especially for surfaces. Many ground state characteristics including, lattice constants and bulk moduli, are successfully performed using LDA and can be compared to experimental values [80]. This approximation can be extended by including not only the magnitude of the charge density at a specific point, but also its gradient, producing an alternative method to LDA called generalised gradient approximation (GGA).

Mathematically, GGA involves a first order expansion of  $E_{xc}[n]$  in density that includes terms in  $\nabla n$ , and thus carries additional computational cost.

The gradient of the exchange-correlation energy density  $\varepsilon_{xc}(n, |\nabla(n)|)$  at each point in the system that is taken into account such that the functional,  $E_{xc}[n]$ , is expressed as:

$$E_{xc}[n] = \int n(r)\varepsilon_{xc}(n, \nabla n)dr \quad (2.16)$$

Both LDA and GGA generally result in underestimation of the bandgap. For example, the values of calculated bandgap for bulk silicon are about 0.5 and 0.7 eV using LDA and GGA, respectively, whereas the experimental value is 1.17 eV. In general, LDA is more appropriate for the large scale modelling of solids, while GGA is suitable for accurate studies of molecules. More details in section 2.8.

## 2.6 The AIMPRO Software Package

In order to analyse observations recorded during experimental work, or to plan future experiments in a rational way, theoretical study (modelling) methods are used to improve or systematically design multi-scale materials. From this point, calculations are performed using DFT as implemented in the code known as AIMPRO [81–85]. In quantum mechanics, the term *Ab Initio* means that, for a simulation of a material, it is sufficient to know its constituent atoms but the rest is governed by quantum mechanics. AIMPRO is a

quantum mechanical code used to simulate, and thus to determine, the specific properties of various types of materials such as semiconductors, metals and insulators. Within this code, it is possible to determine the relevant physical quantities that correspond directly or indirectly to experimental results for a system under study. By knowing the properties of the system, it is possible to choose appropriate fundamental approximations in the quantum mechanical calculations computed within DFT. The majority of the results in this thesis (chapter 5–chapter 9) are performed using the DFT framework, where the essential quantity for any system under investigation is the electron charge density, with Cartesian Gaussian orbitals chosen as the basis to describe the wave function. There, LDA is used to model exchange-correlation energy, and thus total energies and acting forces for an atomic structure can be obtained. Moreover, the non-conserving pseudopotential of Harwigsen, Geoedecker and Hutter (section 2.11) by which the core electrons are eliminated, as described in the following sections of this chapter.

## 2.7 Material Modelling Supercells

Defects are created in crystals when the periodic structure is altered by displacing, removing, adding or substituting one or more atoms. This perturbs the structure, and thus modifies the properties of the system. For example it may display the ability to trap and/or release electrons into states which are very localized, and also the density of the material can be altered by the presence of defects, specially if any structural relaxation takes place. Since defects can affect atomic and device properties, it is important to understand the mechanisms relating to defects, and the changes in properties in crystals is a considerable challenge. Computational models are useful tools for atomistic modelling; for example, the calculation of electronic structures can help in evaluating the energies implicated in the formation, relaxation and migration of defects [86].

Defect modelling in crystals needs specific calculations related to cost and atomic size. Two common computational models have been adopted to study the properties of a defect in bulk material, or at its surface. The first model includes a small number of atoms or molecules, termed a cluster, where at its boundary are dangling bonds that are chemically terminated by hydrogen, as an example, to remove the surface states. Alternatively, in the supercell approach a unit cell is defined which is repeated throughout space in an appropriate lattice using the periodic boundary conditions. This method has been used to study the properties of materials that contain impurities or vacancies, as well as those

that contain structural defects such as stacking faults and grain boundaries.

However, when defects or impurities have been introduced into the unit cell these are arranged periodically, which means that they are repeated throughout the three dimensions. Therefore, one should consider the avoidance of defect-defect interaction by using large supercells in order to deal with the problems of defect concentration and periodic potential that generally have an effect upon the properties of materials.

Various structures of decorated and undecorated bulk silicon are investigated in this study using the DFT framework. For example, iron as an interstitial and substitutional element has been introduced to silicon lattice with vectors ( $[n00]a_0$ ,  $[0n0]a_0$  and  $[00n]a_0$ ), where  $n=2,3$  and  $4$  respectively, yielding an Fe-doped Si structure in cell sizes of 64, 216 and 512 respectively. Analysis of Fe in bulk Si is presented in chapters 5 and 6. In contrast, the contraction of some extended defects such as ISF is performed with lattice vectors ( $3[110]a_0/2$  and  $3[101]a_0/2$ ), making the investigation of Fe in 198 or 352 Si-atom quite easy to study without defect-defect interaction (see chapter 7). Another example for different structures that have been included in this work is Fe decorated  $\Sigma$  5-(001) twist GBs with lattice vector  $[001]$  and  $[110]$  and a cell size of 480 Si atoms (see chapter 8).

## 2.8 Basis Set Functions

A basis set can be described as a mathematical tool used to simplify a complicated mathematical function in terms of a sum of suitable simpler functions to facilitate computation. In terms of quantum-mechanical functions, basis sets are common in the representation of electron states and charge densities. Generally, two common types of basis sets used in DFT software package to represent charge density and KS orbitals include plane wave basis [87] and Cartesian Gaussian functions. By using plane-wave expansion, the parameters do not need to change by more than the maximum value of the reciprocal lattice vector  $|G|$ , enabling transparency.

Furthermore, the cut-off energy ( $E_{\text{cut-off}}$ ) provided by plane waves can be used in the calculations including the plane waves with  $\frac{G^2}{2} < E_{\text{cut-off}}$ .

The values of  $E_{\text{cut-off}}$  should be large enough to cover the number of plane waves, and thus to achieve quantitative convergence in the calculations of electron charge density. To explain this further, figure 2.1 illustrates the cut-off energy as a function of total energy for a relaxed structure of interstitial iron in bulk silicon, where the total energy of the structure has been converged at  $E_{\text{cut-off}}$  equal to 150 Hartree. This value represents the

default value and is used for all of the calculations in this thesis.

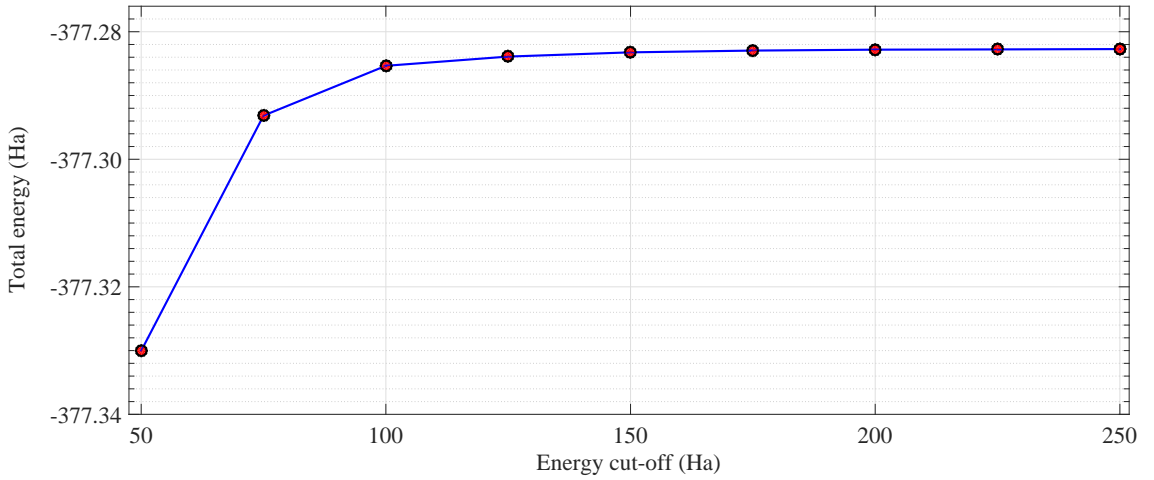


Figure 2.1: Plot showing convergence in the total energy of interstitial iron in bulk silicon as a function of the plane wave energy cut-off. These values have been achieved using one interstitial iron atom in 64-atoms of silicon.

In AIMPRO, the Cartesian Gaussian orbital set is employed to expand the KS function, as it is more localised and rapidly decays from the centre of the atomic site, and also because these functions have analytical integrals. The Gaussian basis function ( $\phi_i$ ) in the following form is localised at the coordinates of atom ( $R_i$ ):

$$\phi_i(r - R_i) = \alpha_i(x - R_{ix})^{n_1}(y - R_{iy})^{n_2}(z - R_{iz})^{n_3} \exp(-\alpha_i(r - R_i)^2) \quad (2.17)$$

Here,  $\alpha_i$  is a constant for each function,  $n_i$  ( $\geq 0$ ) are integers, which are chosen based upon the kinds of atomic orbitals being described. Consequently, in the case of  $\sum_i n_i = 0$ , the orbital has spherical symmetry ( $s$ -type orbital).

It is recommended [78] that there is a compromise to be made between accuracy and computational cost in selecting the best basis set which can cover the needs for orbitals and to converge energy difference in pure and doped systems. Various basis sets that are provided by the AIMPRO package have been examined in this study to simulate the silicon lattice, as shown in figure 2.2(a), where the numbers of labelled basis sets indicate the exponent and number of functions for each. For example, the labelled basis function “*ddpp*” consists of 4 letters, meaning four different exponents. The first (smallest) has  $s/p/d$  and gives 10 functions, and similarly for the next letters  $s/p/d$  that give 10 functions. The last two (largest exponents) have  $s/p$  (4 each). Consequently, this basis set consists of 28 functions per atom. More  $d$ -functions, such as in basis set with 40 functions per atom (known in AIMPRO terminology as “*dddd*”) can be important if high states in the

$E_c$  are needed, and this is crucial for elements like iron. In another example, 13-functions per atom (in AIMPRO known as “*C44G\**”) gives computation  $(28/13)^3$  times faster than “*ddpp*”. For diamond, as an example, this is generally good, but for silicon the  $E_c$  does not converge with this basis set.

Calculated elastic properties including lattice constants ( $a_0$ ) and bulk modulus ( $b_0$ ), energy gap and times taken corresponding to some of the common basis sets are illustrated in figure 2.2(a). It is clear that “*ddpp*” and “*C44G\**”, with 28 and 18 functions per atom respectively, have almost similar values in  $a_0$  and  $b_0$ . These two bases are able to describe the pure Si bands clearly with high accuracy as compared with the other basis set in figure 2.2(a), but “*ddpp*” is faster than “*C44G\**” with the same calculated bandgap value (see figure 2.2(b)).

Consequently, “*ddpp*” is found to be sufficient for Si species regarding accuracy and time, and thus it is used for all DFT calculation with LDA approximation for Si species. However, in the calculations that need a *3d*-orbital, such as with Fe, different basis sets have been examined, which have an effect on *d* level contribution. Using one or two iron atoms in this study has no effect on accuracy because the basis mathematically depends on the eigenvalue, which takes long time to solve. Therefore, because Fe has *3d*-orbitals with high localisation, a heavier basis (“*dddddd*”) is used in Fe-doped Si systems. Furthermore, the use of a diversity of basis sets examined along with their functions used for pure silicon has been supported by comparison related to the use of LDA and GGA approximations. For example, using LDA approximation, the calculated equilibrium lattice parameter and bulk modulus for two Si atoms with the basis set “*ddpp*” give  $5.39\text{\AA}$  and 95.6 GPa respectively, as shown in figure 2.2(a), compared with another LDA study [88] that gave  $5.40\text{\AA}$  and 96.5 GPa, respectively. In contrast, these values have been obtained as  $5.49\text{\AA}$  and 84.7 GPa compared with another theoretical study using GGA [88] that gave  $5.47\text{\AA}$  and 88.8 GPa respectively. However, the experimental values are  $5.43\text{\AA}$  and 97.9 GPa for  $a_0$  and  $b_0$  respectively [89–93]. The energy gap has also been calculated in this study, giving 0.52 and 1.20 eV using LDA and GGA respectively, compared with theoretical values (0.51 and 0.50 eV using LDA and GGA respectively [94] and [95]) and experimental data (1.17 eV). Although the LDA is an attractive and effective method to calculate exchange correlation energy and to give acceptable structural parameters, the level of disagreement between the theoretical and experimental values of the elastic parameters is around 0.5 %.

In contrast, there is a serious underestimation of the energy of excited states, lead-

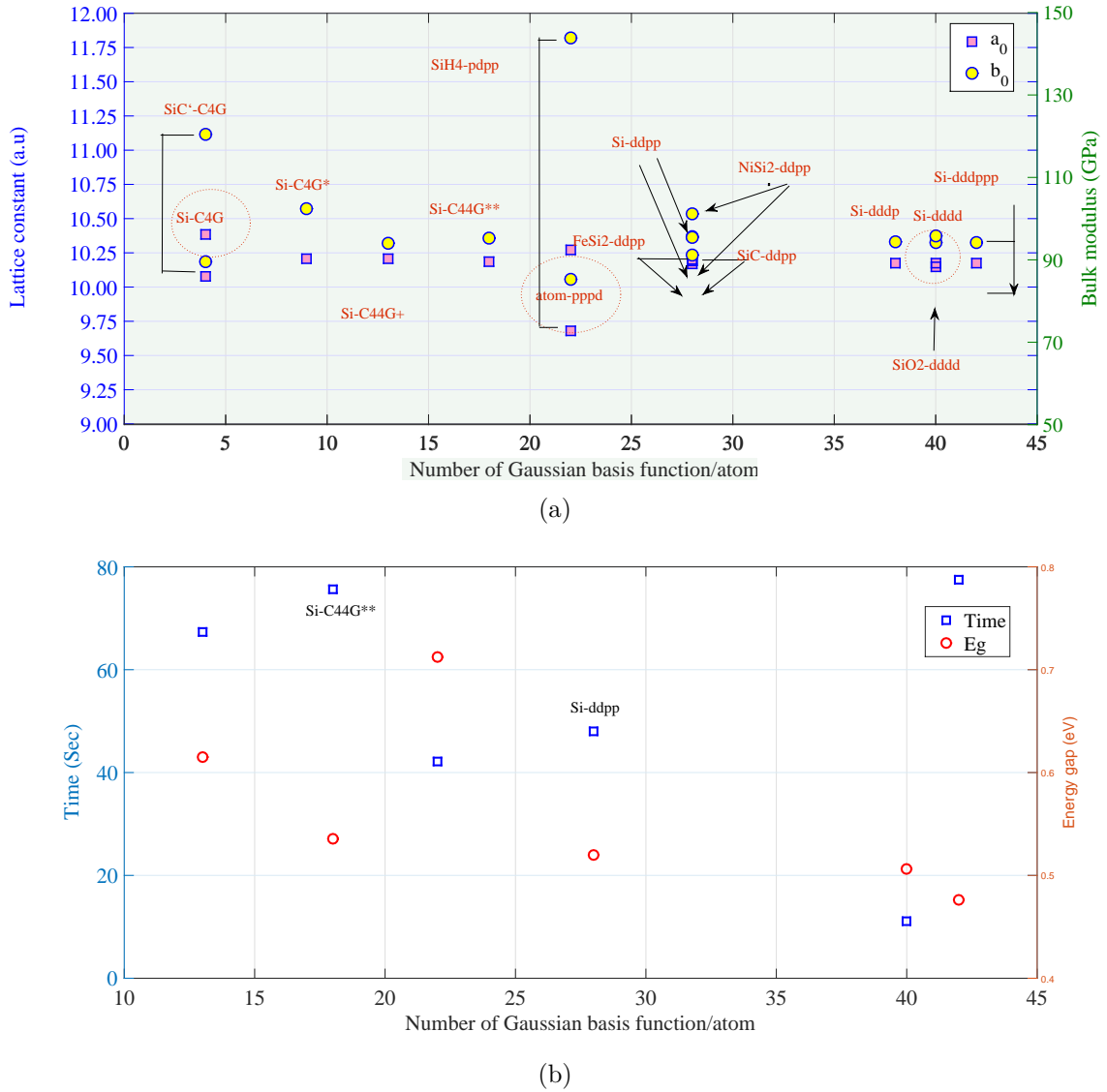


Figure 2.2: (a) Calculated lattice constant and bulk modulus of pure Si. (b) Computed time and band gap using different basis sets for a primitive silicon cell. Labels indicate the exponent and number of functions.

ing to an obvious underestimation of the band gap by around 50 %, which reflects the well-documented problem arising from the underpinning methodology. Underestimations of the calculated band gap by LDA are in accordance with reports in the literature. Furthermore, this problem also involves defects, where energy levels may be introduced into the gap. However, using LDA, accurate properties for occupied bands can be obtained without knowledge of the band gap.

In this study, the basis set has been selected in which the best minimum energy of the iron in bulk Si system is given. Several test calculations have been performed to choose the most promising basis set for  $Fe_i$  and  $Fe_s$  in Si, as shown in figure 2.3 in which detailed analyses of  $Fe_i$  atom in different spin states were treated using different Gaussian basis

are presented. The results in this work are converged with respect to basis. The basis set, “atom-ddddd” has been chosen for Fe which consists of 60 functions per atom. The six letters indicate the use of six different exponents, where each letter ( $d$ ) represents exponents of  $s$ ,  $p$  and  $d$  functions (10 functions) up to and including the orbital angular momentum  $l = 2$ . The first exponent is the smallest and the final one is the largest. Adding more  $d$ -functions can be important if high states in the conduction band are needed, such as in EELS calculations. Therefore, this basis is found to be good enough for the property that needed in this work regarding convergence of energy differences in spite of the time taken per iteration is high as compare with other basis sets.

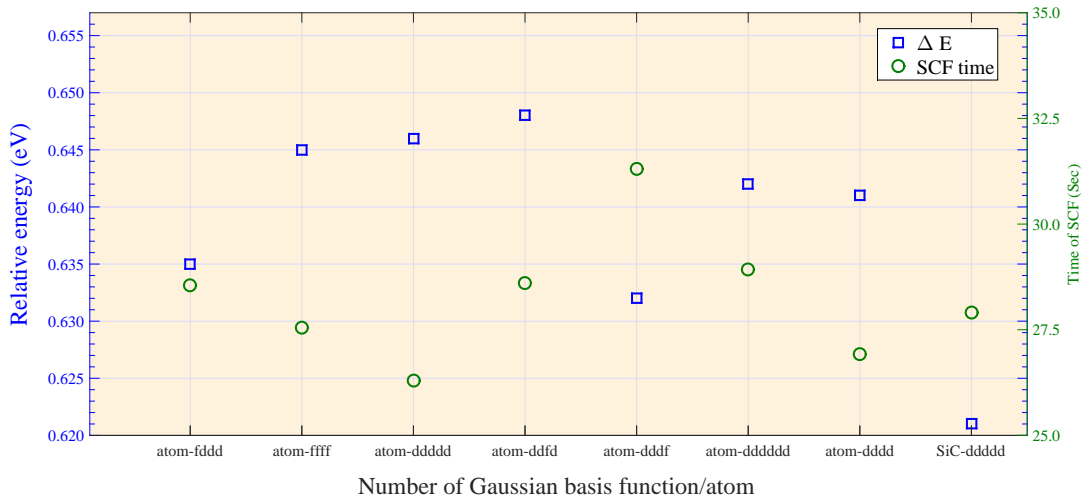


Figure 2.3: Relative energies ( $\Delta E$ ) that associated with the spin and charge states of  $Fe_i$  in primitive Si atoms. These values indicate of how much each of the other  $Fe_i$  structures with other spin states are higher than the ground state structure ( $S = 1$ ) in neutral case. Labels indicate the exponent and number of functions.

## 2.9 Brillouin Zone Sampling

To calculate the physical properties of a supercell system, including total energy, charge density and density of states, integration over the Brillouin zone (BZ) is required. In the DFT frame, AIMPRO uses a Monkhorst-Pack (MP) sampling mesh [96–98], with a special  $k$ -point sampling grid. In this study, MP sampling schemes are used to integrate the band structure [96], and the notation  $MP_n$  for an  $n \times n \times n$  grid has been adopted. Matrix elements of the Hamiltonian are determined using a plane wave expansion of the density and Kohn-Sham potential [82] with a cutoff of 150 Ha, that shown in figure 2.1, in which the cut-off energy of relaxed structure for interstitial iron in the bulk silicon is shown as a function of total energy. According to the MP scheme,  $k$ -points can be defined

by three integers  $I, J, K$  that define a grid in a reciprocal space:

$$\vec{k}(i, j, k) = \frac{2i - I - 1}{2I} \vec{a}_1 + \frac{2j - J - 1}{2J} \vec{a}_2 + \frac{2k - K - 1}{2K} \vec{a}_3 \quad (2.18)$$

where:

$$\begin{aligned} i &= 1, 2, 3, \dots, I \\ j &= 1, 2, 3, \dots, J \\ k &= 1, 2, 3, \dots, K \end{aligned} \quad (2.19)$$

Here,  $\vec{a}_1, \vec{a}_2$  and  $\vec{a}_3$  are the unit vectors of reciprocal space,  $I, J$  and  $K \geq 1$ . However, for a uniform sampling grid,  $I = J = K$ , which can be represented by  $MP-I^3$ . In contrast, for a non-uniform sampling grid such as structures that contain ISFs for example, the MP is selected to be  $4 \times 4 \times 2$ . Figure 2.4 shows the  $k$ -point sampling of  $1 \times 1 \times 1, 2 \times 2 \times 2$  and  $3 \times 3 \times 3$  that have been performed for pure silicon, modelled in a simple cubic cell with a side length of  $2a_0, 3a_0$  and  $4a_0$  containing 64, 216 and 512-Si atom supercells respectively.

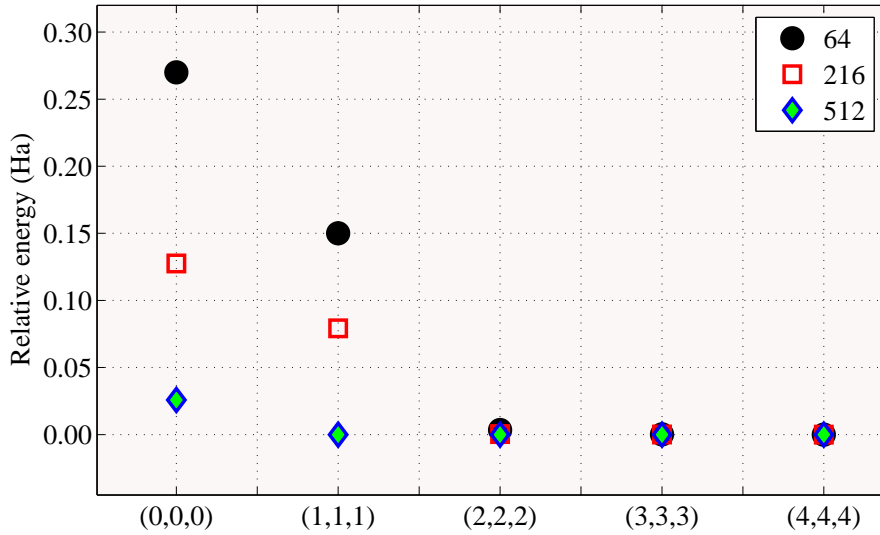


Figure 2.4: Effect of Brillouin zone sampling on the modelling accuracy of pure Si for different cell sizes. The relative energies have been calculated with respect to MP-  $4 \times 4 \times 4$  as a reference energy for each cell size.

From this figure, the sampling densities for the structure contain 216-Si atom (as an example) converging with about  $1.25979 \mu\text{eV}$  per atom. This value is negligible, and therefore the MP sampling of  $2 \times 2 \times 2$  has been used for subsequent calculations in this work. Furthermore, the convergence of larger cell size with less sampling is clear in this

figure.

In these calculations, structures are optimised via a conjugate gradients algorithm, with convergence requiring forces less than  $10^{-3}$  atomic units, and the final structural optimisation step is less than  $10^{-5}$  Ha.

By varying the cell-size, it is possible to evaluate the convergence of the iron in Si properties, and in particular the energies, while allowing direct comparison with literature values.

Figure 2.5 shows the relative energies related to the BZ sampling as a function of spin and charge states of  $Fe_i$  in bulk Si. From this figure, the convergence in energy difference is clear between MP2 and MP3 for all spin and charge states of  $Fe_i$  structures.

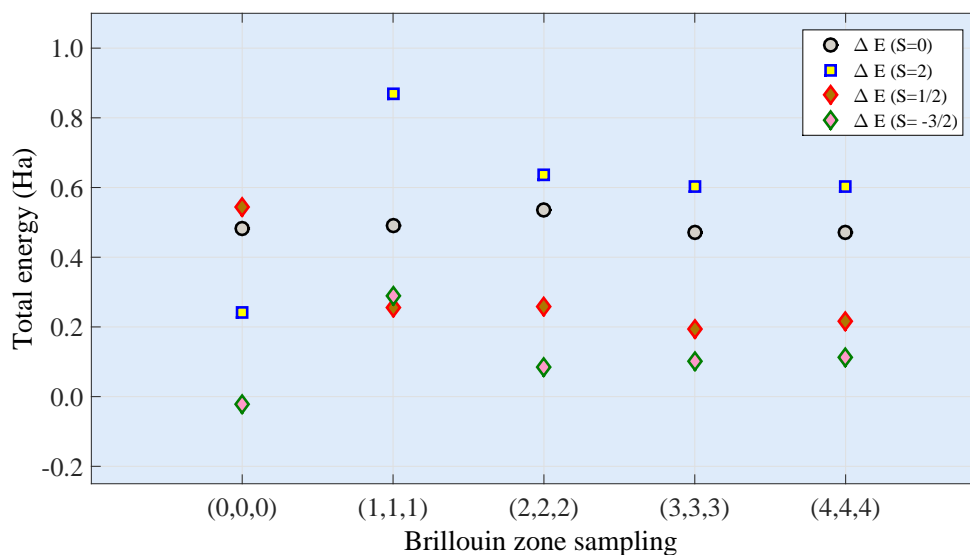


Figure 2.5: Difference energies ( $\Delta E$ ) that associated with the Brillouin zone sampling as a function of spin and charge states of  $Fe_i$  in 64 Si atoms. These values indicate of how much each of the the other  $Fe_i$  structures with other spin states are higher than the reference with  $S = 1$  system,  $S = \frac{3}{2}$  and  $S = \frac{1}{2}$  for neutral, single positive and negative charge state, respectively.

## 2.10 Self-Consistency Cycle

The self consistency cycle (S-C) is an iterative procedure used to solve K-S equations (section 2.4.2) accurately by determining the effective potential. In this process, charge is redistributed around the system until the minimum total energy is achieved. Consequently, an accurate simulation of charge distribution in a real system can be obtained.

Basically, the charge density  $n(r)$  is guessed by taking the density of neutral atoms or the output of a previously optimised structure to generate a potential, which is generated

from the initial charge density used to solve the KS equations. As a result, a new output charge density,  $n(r)$ , is obtained.

Figure 2.6 shows the computational steps of the density functional S-C loop, which attempt to ensure that the value of  $n(r)$  obtained from the KS potential is the same as the input charge density  $n_0^{IN}(r)$  used to generate it within a certain numerical tolerance (difference in energy between input and output charge density). The obvious strategy is to start with an  $n_0^{IN}(r)$ . This is generally taken from a superposition of neutral atomic species for the same system, and is used to solve the KS equations (2.13). Then the output density  $n_0^{OUT}(r)$  is formed from the KS states.

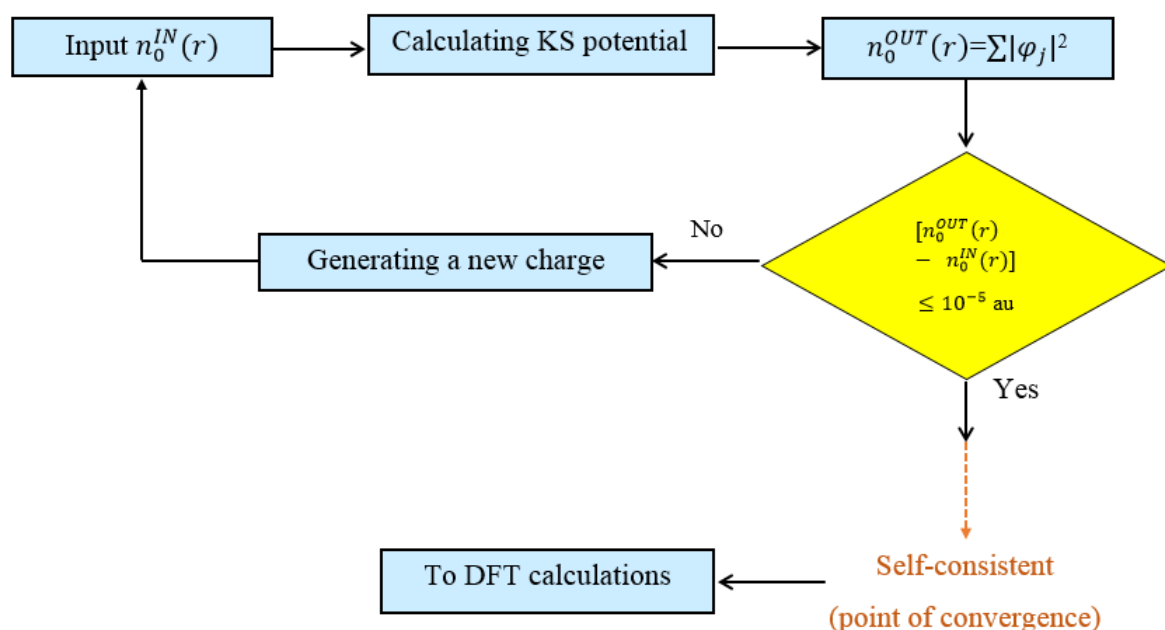


Figure 2.6: The schematic flowchart of the self-consistent algorithm for density functional-based calculations.

Generally, the charge density converges very rapidly, and when the difference in the input and output Hartree energies is less than  $10^{-5}$  au, the self-consistency of charge density is considered to have reached the point of convergence.

## 2.11 Pseudopotential Approximation

In solid state systems, the chemical reactions of an atom are generally controlled by its valence electrons without any significant participation of the core electrons, since the latter are highly localised in the nucleus. However, the calculation of the effect of the motion of a large number of core electrons of an atom and its nucleus is computationally

demanding, and it is also a challenge to achieve results with good accuracy. This is due to the prohibitive requirements of providing a large number of basis functions to represent all electronic states, given the highly localised core states in the vicinity of the nucleus, and in order to maintain orthogonality with the core electrons, the valence states should oscillate rapidly. Large amounts of kinetic energy for the valence electrons in the core region can result from this rapid oscillation, which may almost cancel out the large potential energy due to strong Coulombic potential. The core electrons are much more strongly bound than the valence electrons.

Therefore, the effect of core electrons is eliminated in computational physics by utilising a rather simple but highly effective Coulombic potential, termed the pseudopotential, that is felt by valence electrons. Among many choices of pseudopotentials that are available in the AIMPRO package, the HGH (Hartwigsen, Goedecker and Hutter) [99] pseudopotential approximation has been used for all DFT calculations in this thesis, as this is the standard AIMPRO choice.

In this study, atoms are modelled using norm-conserving separable pseudopotentials, with  $3d^64s^2$  and  $3s^23p^2$  valence sets for Fe and Si, respectively.

## 2.12 Chapter Summary

In this chapter, a relatively detailed description of the rationale for the computational methods used in AIMPRO has been introduced, explaining all relevant theoretical principles behind this code, such as the many-body problem of the Schrödinger equation and the approximations that have been employed to simplify the complexity of this equation. Comparison of results calculated using LDA and GGA with different Gaussian basis functions has been presented for the interstitial iron in bulk silicon. Moreover, the facilities are described that can be provided by using DFT as a more standard theory to model atomic systems by adopting the electron density to find the minimum energy structure, even with relatively large structures. More details related to modelling of physical quantities using this code are presented in the next chapter.

# Modelling of Derived Properties

“An expert is someone who knows some of the worst mistakes that can be made in his subject and how to avoid them.”

Werner Heisenberg

## 3.1 Introduction

A wide range of experimental techniques are employed to observe the properties of materials. Some of these properties can be studied directly, or indirectly by using modelling approaches such as DFT, which has become a solution for the complex problems that face experimental investigations. This study attempts to combine and correlate data from experimental methods to model the most common impurities and extended defects present in mc-Si, and a brief explanation of the relevant experimental quantities related to this research is presented in this chapter. This includes binding energy (section 3.5), migration energy (section 3.6), electronic structures (section 3.3), electrical levels (section 3.4) and the optical absorption (section 3.7). For this purpose, the modelling of derived properties and other relevant aspects are described in detail in the following sections.

## 3.2 Structure Optimisation

After achieving a self-consistent charge density (section 2.10), the corresponding total energy and potential energy can be determined. Then, analytical calculations of the forces acting on each atom ( $f$ ) are achieved to optimise the structure. The process by which atoms are moved to minimise energy, and thus to find the equilibrium structure

is called structural optimisation or relaxation. The force of any atom in the system is analytically calculated using the following expression:

$$f_{l\alpha} = -\partial E / \partial R_{l\alpha}. \quad (3.1)$$

Here,  $R_{l\alpha}$  is the position of the atom, and  $f_{l\alpha}$  is the  $\alpha$  components ( $x$ ,  $y$  and  $z$ ) of the force on it [85]. This may also be evaluated by calculating  $\Delta E_{l\alpha}$  for a displacement  $\Delta R_{l\alpha}$ . Once the forces of an atomic configuration have been obtained, the conjugate gradient method [100, 101] is adopted to minimise the energy by displacing the atoms in a specific direction so that the energy is minimised. However, there is no guarantee that the minima determined will be the global rather than a local minimum, depending on the starting structure. Therefore, to address this uncertainty, several tests must be performed in AIMPRO using different initial configurations to determine the accurate structure which corresponds to the global energy minimum. Among these is the pattern when the minimum energy is viewed as the best estimate of the ground state structure. For example, the global energy minimum of a model of interstitial iron in silicon can be found at the tetrahedral (T-site) of the Si lattice, where the amount of energy required to move the iron toward a hexagonal (H)-site transition state is about 0.8 eV, where the H-site is metastable, with the transition state lying slightly away from the D3d symmetry H-site structure. Detailed analyses of the migration of Fe in Si can be found in chapter 5 and chapter 6.

Since the energy difference between the sequence iterations is below  $10^{-5}$  atomic units, the structure is considered to be optimised.

During the optimisation process, the restrictions on the atoms that are allowed to move, and the point group symmetry which the structure must be transformed into have a considerable effect on the speed of running of the program. This means that the structure can be considered as optimised structure. The symmetry operation is still the same along the optimisation steps.

### 3.3 Electronic Structure

The electronic band structures of solid materials are representations of the allowed electronic energy levels, and thus, can be used to describe their electrical properties. In a crystalline material, a band structure is a diagram plotting various key electron energy

levels (Fermi level and nearby energy band edges) as a function of the wave vector of an electron. The Fermi level (chemical potential for electrons) is generally referred to the zero energy of the valence band top. By using a band structure diagram, many material properties can quickly be revealed such as the type of material (metallic, semi-metallic, semiconductor or insulating), band gap type (direct or indirect), as well as the magnitude of the energy gap. Moreover, the carrier mobility throughout those bands can be calculated from their curvature. In particular, the performance of most devices depends on the mobility of the charge carriers. Fundamentally, the energy bands of a material include the valence band ( $E_V$ ) that contains electrons, and the conduction bands ( $E_C$ ) or empty bands, as well as the band gaps or forbidden bands between the  $E_V$  and  $E_C$ . For example, the band structure for pure silicon is shown in figure 3.1 along high-symmetry directions in the Brillouin-zone (section 2.9), where the  $E_C$  minimum (red lines) and the  $E_V$  maximum (blue lines) are not vertically aligned, reflecting the indirect band gap of Si, in good agreement with another DFT calculation [94].

As mentioned before in chapter 2 (section 2.8), calculations of band gap performed by DFT-LDA reflect an underestimation of the Si energy gap by around 50 %, which reflect the well-documented problem arising from the underpinning methodology. However, using LDA, accurate values of other properties for occupied bands can be obtained without knowledge of the band gaps. To explain this, an example was considered in section 2.8.

The movement of electrons from the  $E_V$  to the  $E_C$  after gaining energy, producing two mobile carriers, is described by carrier generation processes. In contrast, recombination describes processes by which the  $E_C$  electron loses energy and re-occupies the energy state of a hole in the  $E_V$ . These processes are balanced when a material is formed at thermal equilibrium conditions, where the net charge carrier density remains constant. These two processes have been described in detail in chapter 1.

## 3.4 Electrical Levels

For any defect in the crystal, the electrical level is represented by the electron chemical potential, when the relevant charged states have the same energy [102]. The formation energy method explained in section 3.4.1 can be used to find these levels by finding the formation energies ( $E^f$ ) of neutral and charged defects. The presence of defect-related states in the bandgap of the host material, which arise from the defects breaking the symmetry of the perfect crystal, can be both advantageous and disadvantageous for device

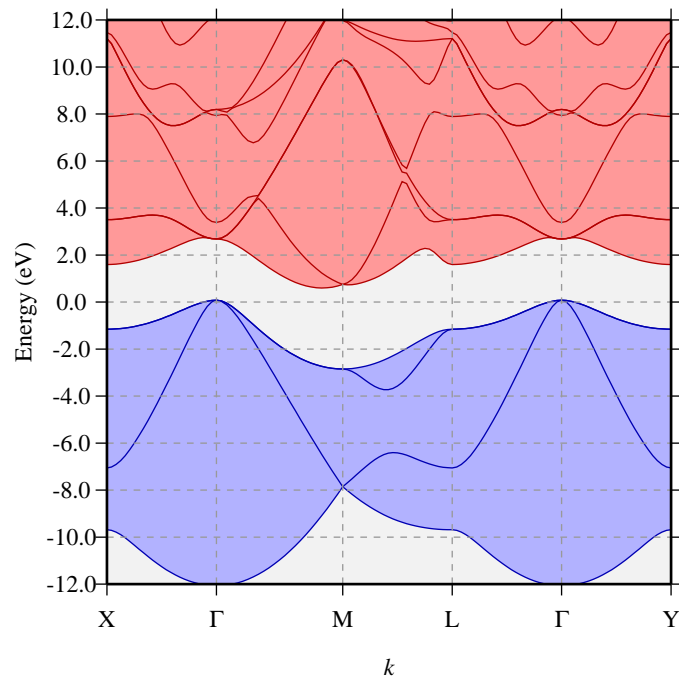


Figure 3.1: Silicon band structure calculated by DFT-LDA. The structure is plotted along high-symmetry branches for primitive structure (2-atom). Labelling on the  $x$ -axis follows the conventions for special points at the zone-boundary for simple cubic Brillouin-zone (section 2.9). Occupied ( $E_V$ ) illustrated in a solid blue line, while empty bands ( $E_C$ ) are shown as red lines. The band gap of approximately 0.5 eV can be determined through the difference in energy ( $y$ -axis). The  $E_V$  maximum and  $E_C$  minimum are not vertically aligned; the band gap is indirect. The zero on the energy scale is defined to be the highest occupied state.

performance due to their influence on the electrical properties of a crystalline material. In particular, conductivity at a certain temperature corresponds to the free-carrier concentration, and thus depends on the donor level (occupied states located close to the  $E_C$ ) or acceptor level (empty states located close to the  $E_V$ ) depth of the dominant dopant. Furthermore, because carrier traps deep in the bandgap are detrimental to conductivity due to their impact in reducing free-carrier concentration where the resulting charged defects are scattering centres, that in turn reduces carrier mobility. It is rather interesting that the importance of the characterising electrical properties of defects has driven a huge effort to develop reliable computational approaches that may both explain experimental observations and facilitate the prediction of dopants with desired characteristics.

Defect energy levels can fail to predict correctly the symmetry-breaking distortions around defects investigated in experiments. Theoretical modelling has had an effective

impact in semiconductor physics. Hence, in this work and by using DFT calculations, the electrical levels of a contaminant corresponding to a thermodynamic property of the system can be calculated as functions of the electron chemical potential ( $\mu_e$ ). In this method, a quantitative investigation of the positions of these levels allows then to be recognised as donor or acceptor levels, as shown in figure 3.2 with different possible cases of  $\mu_e$ .

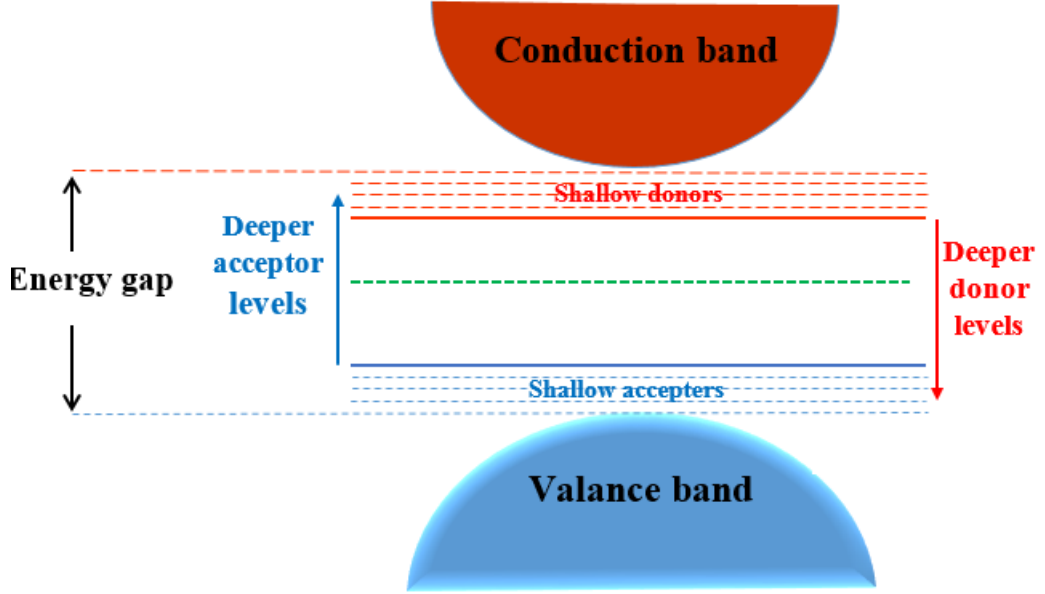


Figure 3.2: Plot showing deep and shallow levels of material. Blues and red shaded curves refer to the valence and conduction bands, respectively. Blue lines reflect the acceptor level, red lines represent donor level, and both are separated by energy gap.

The formation energy approach (section 3.4.1) proposes a comparison of the formation energies of two individual systems having different charge states as shown below.

### 3.4.1 Formation energy method

The formation energy is the energy difference between the configuration of the particles and the sum of their free energies within reference states. According to a previous study [103], the charge-state- $(q)$  dependent, zero-temperature formation energy of a system of atoms and electrons ( $X$ ) can be expressed as:

$$E^{f(X,q)} = E^{\text{total}(X,q)} - \left( \sum_i n_i \mu_i \right) + q (E_v(X, q) + \mu_e) + \xi(X, q) \quad (3.2)$$

Here,  $E^{\text{total}}(X, q)$  is that of the lowest-energy configuration of  $X$ , which consist of  $n_i$  of type  $i$  in a charge state  $(q)$ .  $\mu_e$  is the electron chemical potential,  $\mu_i$  is the atomic

chemical potential, and  $E_v(X, q)$  represents the energy of the valence band maximum ( $E_v$ ), often chosen to be the zero of the  $E^F$ . The term  $q\mu_e$  can be described as  $q(E_v + E^F)$  and this term can often be cancelled in cases of neutral charge state,  $q=0$ . The last term of equation 3.2,  $\xi(X, q)$ , is a term introduced by the computational framework as a correction to compensate for artefacts of boundary conditions, including the Madelung energy term for the charge centres where the Madelung term scales as  $q^2$  and therefore grows rapidly with  $q$ . Hence, the Madelung term can be derived in the form:

$$\xi(X, q) = \frac{\alpha_M q^2}{L\epsilon} \quad (3.3)$$

where  $\alpha_M$  is the Madelung constant of the super-lattice,  $L$  is the lattice parameter ( $L = \sqrt[3]{V}$  and  $V$  is the supercell volume), and  $\epsilon$  is the static dielectric constant (section 3.8) of the host material (i.e. the permittivity of Si) [104].

Equation 3.2 represents the defect formation energy as a linear function of electron chemical potential, and it can be applied to estimate the electrical levels of  $X$ , and to examine the stability of the defect in different cell sizes and for all possible charge states of the system.

Figure 3.3 illustrates schematically the formation energy that is plotted as a function of the electron chemical potential, which can be used to estimate the electrical energy levels of the defect.

The labels in figure 3.3 include the details of the charge states of the defects in terms of whether ( $E^F$ ) is above (left of the label) or below (right of the label) the transition energy. The slash between them refers to the change in the charge of the defects. For example, the notation (0/+) indicates that the defect will be stable in a neutral charge state when  $\mu_e$  is above a critical values, while the charge state becomes more stable for value of  $\mu_e$  smaller than the critical value. The chemical potential at which the defect has the same formation energy in each charge state is the ionization energy. Based on figure 3.2, the donor level (0/+) is the value of chemical potential of an electron, for which the neutral and positive charge states have the same formation energy, as shown in:

$$\mu_e(0/+) \text{ when } E^f(X, 0) = E^f(X, +) \quad (3.4)$$

In contrast, the acceptor level (-/0) is the chemical potential of an electron for which the

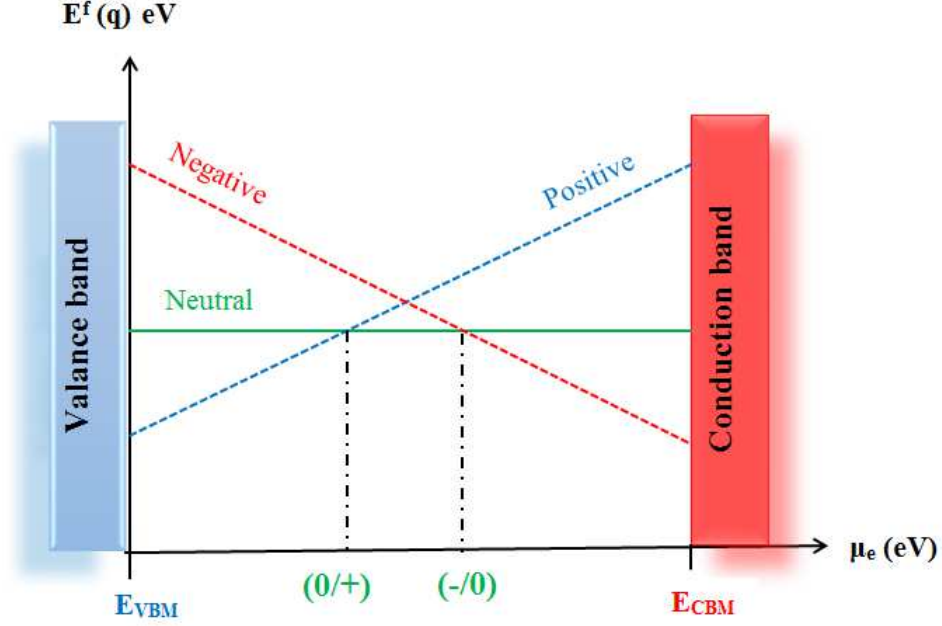


Figure 3.3: Schematic diagram showing the formation energy  $E^f(q)$  for three charge states ( $q = 0, +1$  and  $-1$ ) of a structure as a linear function of the electron chemical potential ( $\mu_e$ ). The bulk valence bands ( $E_V$ ) are represented by the shaded blue region, while the shaded red region represent the conduction band ( $E_C$ ).

formation energies of negative and neutral charge states are the same (see equation 3.5).

$$\mu_e(-/0) \text{ when } E^f(X, -) = E^f(X, 0) \quad (3.5)$$

## 3.5 Binding Energies

Defects can be formed in individual form or as complexes, and the energy released when one defect complex is formed is called the binding energy  $E^b$ . It is an important quantity in assessing the thermodynamic of complex defects, providing valuable information concerning whether or not two defects are likely to be constituted as complex defects. In addition, is used to predict the energy required for surmounting the forces needed to hold two defects together. For example, the value of  $E^b$  of two defects  $X, Y$  with respect to its individual component defects  $X$  and  $Y$  can be determined from their formation energies as:

$$E^b(X, Y) = (E^f(X) + E^f(Y)) - E^f(X, Y) \quad (3.6)$$

Here,  $E^f(X)$  and  $E^f(Y)$  are the formation energies of systems  $X$  and  $Y$  in their isolated forms.  $E^f(X, Y)$  is the formation energy after the two defects are bonded. If the result of equation 3.6 is positive, which means that the individual parts have higher

potential energy than the complex, the defect is bound rather than dissociate. It is worth mentioning that the temperature affects  $E^b$ , where, with increasing temperature, additional terms should be added to the total energy of the system which are created by different types of entropy, including configuration, electronic and spin entropies [105]. In this work, a wide range of values of  $E^b$  have been calculated to examine the binding relationship between interstitial iron and extended defects-based mc-Si.

## 3.6 Diffusion Barrier

The movement of atoms in a solid in general, and the migration of impurities and defects through a lattice in particular, have attracted enormous attention since they are critical physical phenomena in studies of material properties and their applications in device manufacturing. For example, in the crystalline Si solar cell fabrication process, the migration of impurities and defects from electrically inactive to active regions in bulk Si has a critical impact on cell performance. Therefore, and prior to describing the method used to investigate the mechanism of the diffusion of atoms, it is important to understand the energetics of the diffusion path of atoms through a lattice.

### 3.6.1 Minimum energy path and saddle point

The minimum energy path (MEP) is the lowest energy path for the rearrangement of a group of atoms from one stable configuration to another. Along the MEP, the structure with the highest energy is called the transition structure or saddle point (SP) structure, where the SP, which is the maximum potential energy along the MEP, represents a barrier to migration between two minima. This barrier represents the activation energy.

### 3.6.2 Nudged elastic band calculations

Various methods have been proposed to find reaction paths. One efficient and reliable scheme, which is the method used in this work, is the climbing nudged elastic band (NEB) [106, 107], where the SP structure is revealed by finding the MEP between two end-points.

The schematic flowchart in figure 3.4 highlights the procedures used for performing NEB calculations, starting by obtaining the structures, such as A and B and the activation energy barrier for each ( $E^a$  and  $E^b$ ) of the two end-points between which transition

occurs. In one case, if the diffusion rates in the both forward and backward reactions are equivalent, the diffusion process is considered to be symmetrical. In another case, when

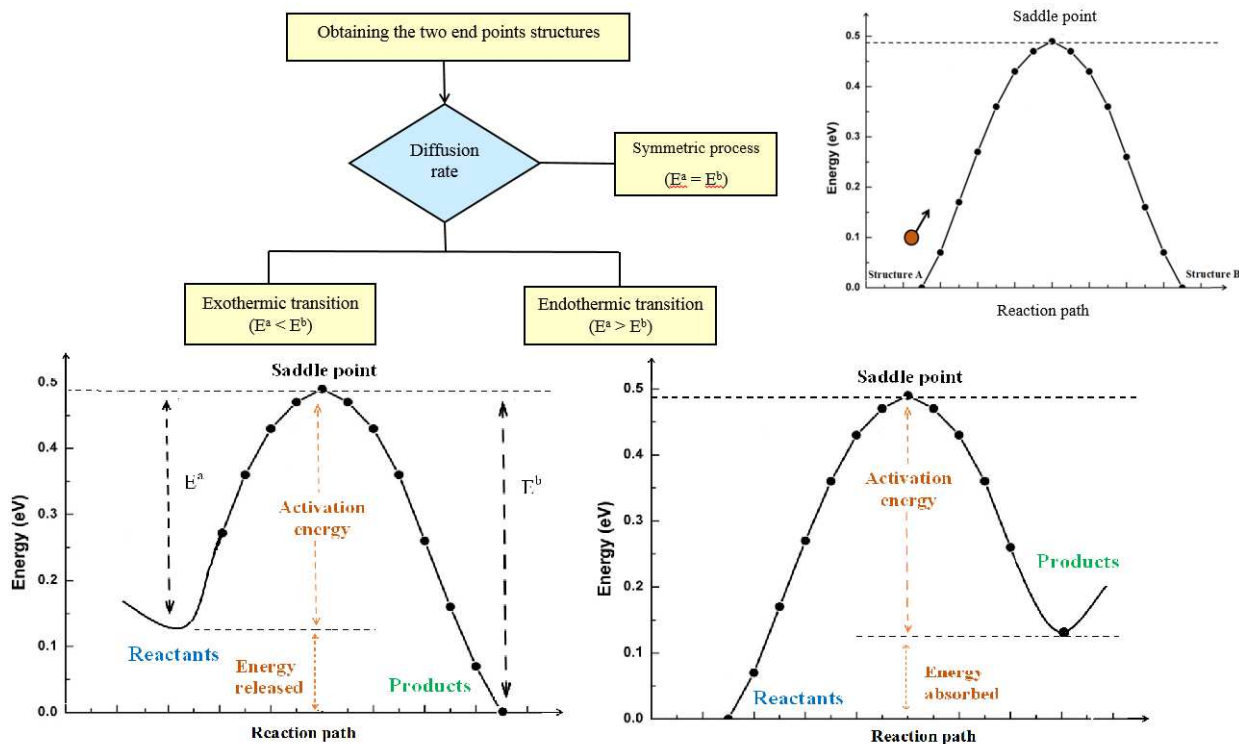


Figure 3.4: Schematic diagram showing the steps in performing NEB calculations. The locations of saddle points are shown, as well as the forward (left) and backward (right) activation energies  $E^a$  and  $E^b$  for initial and final states respectively.

thermal excitation is applied to the atom at initial state (A), overcoming the activation energy barrier ( $E^a$ ) to reach the final state (B) yields forward transition. In this type of reaction, the energy of the initial structure,  $E^a$ , is lower than that of the final structure  $E^b$ . This can lead to rapid symmetrical reactions in the direction from the higher energy structure to the lower energy one.

In contrast, the reverse or backward transition can occur when an atom resides at state B and moves to state A with a reverse activation energy barrier ( $E^b$ ), where  $E^b < E^a$ . However, this type of reaction is not favoured as compared with the forward one, and the difference between them is the energy difference between states A and B. Both reaction types are also illustrated in figure 3.4.

By providing an initial guess of the diffusion path, obtained by linearly interpolating between these two end-point structures, these two end-point structures are considered as inputs in starting the diffusion barrier calculations. Consequently, a number of intermediate structures can be formed where more intermediate points on the path are required to reflect more complicated reactions. The optimisation of these intermediate structures in a con-

strained sense is required to find the minimum energy in the directions perpendicular to the MEP, with equivalent spacing between neighbouring structures. In order to achieve this, forces along the diffusion direction are replaced by elastic forces. Iteration to complete this process is continued until a path with the MEP is obtained, in which the forces perpendicular to the reaction direction are quite small (about  $10^{-3}$  au). In this work, all data related to NEB calculations are implemented in a way that allows the climbing process (increasing energy) for the structure to occur. This implementation is accompanied with increased energy and minimised force in the direction of the reaction. A single negative eigenvalue of the dynamical matrix for this structure can be obtained from the first derivative of this force with respect to displacement, where this eigenvalue represents the imaginary frequency corresponding to displacement along the reaction co-ordinate. As a result, a first order SP can be obtained. Then, after achieving the MEP, one can calculate the energy barrier as a difference energy between the lowest energy structure and the maximum energy along the path, represented by one of the end structure points and that of the SP structure respectively.

It is worth mentioning that, in this work, the number of intermediate structures has been routinely changed to ensure that the full diffusion path has been captured in the simulation. Additionally, the effect on barrier height is considered, with convergence in the calculation by about an order of 10 meV or better.

Typically, seven intermediate structures are chosen to represent the simple reactions that fully resolve the barrier, as obtained by investigating selected reactions with more than 30-intermediates.

In contrast, to provide one or more additional minima between the end-point structures (intermediate or meta-stable structures), a series of reaction steps is required to cover the data obtained from NEB. In particular, in some special cases when some symmetry in the SP structure is found, a relaxation of one of the end-points should be prevented in order to possess this symmetry operation and thus to avoid a defect reflection that may occur at one end-point to another.

## 3.7 Optical Absorption

Deep levels are also non-radiative recombination centres affecting optical properties. Optical absorption measures the amount of light absorbed by a material as a function of wavelength. According to the absorption spectrum of a material, its characteristics can

be identified, and concentrations of defects in the material can be estimated; in particular, when defects have a well-known absorption level that may change the absorption spectrum of the host material. The measurements of absorption spectra considered when a beam of electromagnetic radiation consisting of photons passes through a material, and then the photons may interact with atoms in this material in various possible ways. In one case, when a material absorbs an incident photon, the excitation of electrons so that they jump from a ground state to an excited state can occur. In intrinsic semiconductors, this process can occur if the energy of the photon ( $E_{ph}$ ) is greater than the semiconductor bandgap. This process is represented in figure 3.5 (a), where in this case an electron is excited by promotion from the valence band to the conduction band, leaving a hole. However, in the case of an extrinsic semiconductor in which defects introduce states in the bandgap, an optical transition can happen for energies lower than the  $E_g$ , as shown in figure 3.5 (b).

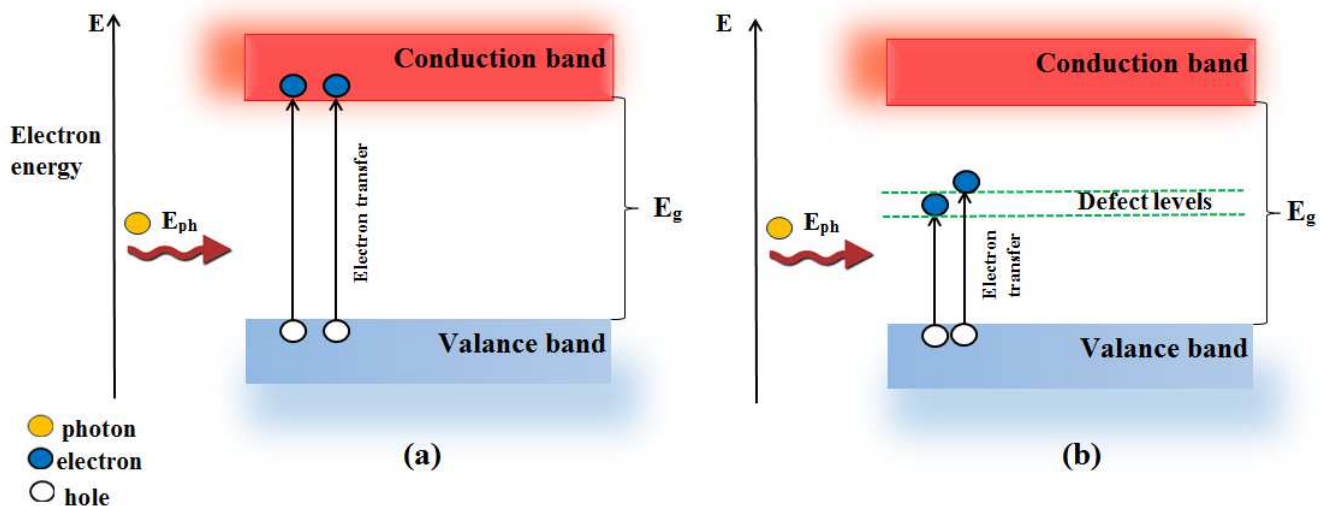


Figure 3.5: Schematic illustration of two possible mechanisms to transfer electrons from the valence band to the conduction band: (a) process of promoting an electron from the valence band to the conduction band when an incident photon has energy ( $E_{ph}$ ) higher than the bandgap energy ( $E_g$ ); (b) excited electrons move to defect-related levels within the bandgap of the material with a lower excitation energy

Alternatively, when the photon absorbed by the lattice creates one or more phonons (a unit of vibrational energy that arises from oscillating atoms within a lattice structure), the intensity of the electromagnetic beam can be written as [108]:

$$I = (h\nu)N \tag{3.7}$$

Here,  $N$  is the photon flux, which is reduced when passing through a material that has a thickness  $dx$ , and the number of transmitted photons is  $N - dN$ , so that the absorbed photons can be related to both the material's thickness and incident flux as:

$$dN = -\alpha N dx \quad (3.8)$$

where  $\alpha$  is the absorption coefficient, which represent a proportional unique constant for each material which depends on its density. Integrating equation 3.8 for the total thickness of the material  $x$  yields the solution:

$$N = N_0 e^{-\alpha x} \quad (3.9)$$

where  $N_0$  is the incident flux and  $N$  is the transmitted flux. The intensity of incident light is reduced when it travels within a material. Absorption increases by increasing the thickness of material  $x$  and the absorption coefficient  $\alpha$ , where the latter is dependent on frequency (the incident photon energy), and thus can allow the absorption spectrum to be measured. In solids, the observation of optical processes such as absorption and transmission are observed and can be quantified by a number of parameters. These parameters can be described in terms of the properties of solids at the microscopic and macroscopic levels.

## 3.8 Dielectric Function

A dielectric material is a substrate that is a relatively poor conductor of electricity, but an efficient supporter of an electrostatic field. Recently, these materials have been found attractive for use in different applications. For example, to improve the performance of some electronic devices in terms of power consumption, speed, and size, a high dielectric constant is required. Light spectroscopy has been developed as the most important tool for collecting data in dielectric function calculations, as shown in section 3.9.

The complex dielectric function of a material reflects its response to an applied electromagnetic field, describing the electrical and optical properties of the material represented by polarisability and absorption respectively.

In IR, visible and UV spectral regions of the spectrum of radiation, the wave vector of the radiation is tiny (about zero) compared with the shortest reciprocal lattice. Thus,

the dielectric function can be given at a zero wave vector as:

$$\epsilon(\omega) = \epsilon'(\omega) + i\epsilon''(\omega) \quad (3.10)$$

where  $\epsilon'$  and  $\epsilon''$  are the real and imaginary parts of dielectric function respectively, and  $\epsilon'$  is used to calculate the degree to which the material polarises in response to an applied field. In contrast,  $\epsilon''$  controls the relative phase of this response with respect to the applied field. Both real and imaginary parts of the dielectric function are valuable parameters to calculate due to their effect on each other in a bidirectional mathematical relationship called Kramers-Kronig relations, which are often used to calculate the real part from the imaginary part (or vice versa) for response functions in physical systems.

Of particular interest are the impurities and defects that may be present in materials, such as interstitial impurities, stacking faults and grain boundaries. These defects represent the main source of large accumulations of charge in the bulk of dielectric materials. Finally, polarisability is caused by random or layered homogeneities in the dielectric material.

One of the limitations which causes variations between theoretical calculations and experimental measurements is the difficulty of measuring the static dielectric constant in the low frequency (about 1 Hz) range as a result of the real value of the dielectric constant that excludes interfacial polarisation.

## 3.9 Electron Energy Loss Spectrum

In order to analyse materials, especially at the nano-scale, the electron energy loss spectrum (EELS) is generated to visualise structural and chemical information pertaining to a solid, with special resolution down to the atomic level in favourable cases. EELS is a method in which a narrow beam of electrons (having kinetic energy) interacts with a material, yielding energy loss as electronic band transitions, scattering and phonon interactions, where the intensities of these energy losses can be calculated. The characteristics of the sample is the key to specifying the low-loss end of the energy spectrum related to inter- and intra-electronic band transitions (the bandstructure). This is the idea behind the fundamental of low loss, which represents the magnitude of energy involved in promoting electrons to move between states, including valence electrons rather than the more closely bound core electrons. The calculation of the dielectric function can be achieved by

taking into account the number of bands involved, the number of  $k$ -points used, and the magnitude of any broadening. The EELS spectrum can be generated by AIMPRO, involving fundamental treatments [109] in which the rates of energy and momentum loss are proportional to the magnitude of the inverse longitudinal dielectric constant that can be determined by the KS equations (2.13). Depending on the random phase approximation, the energy loss function has the form:

$$\epsilon(q, \omega) = 1 + \left(\frac{e^2}{\epsilon_0 \Omega}\right) \sum_k \frac{1}{E_{k+q,c} - E_{k,v} - \hbar\omega} |(r)_{k\nu, k+qc}|^2 \quad (3.11)$$

Here,  $\Omega$  is the crystal volume,  $E_{k,c}$  is the  $E_C$  energy,  $E_{k,v}$  is the  $E_V$  energy.  $(r)_{k\nu, k+qc}$  is the matrix element of the position operator as a function of an occupied valence and empty conduction levels  $k$ ,  $\nu$  and  $k + q$ ,  $c$  respectively.

This calculation is very difficult to describe experimentally due to the inverse proportion of its energy loss to the dielectric constant (section 3.8), where the relationship depends on a constant, and thus depends very weakly on energy. The scalar expression of equation 3.11 represents the transverse optical dielectric constant.

The absorption coefficient can be determined from the complex dielectric function by calculating the complex part of the refractive index, and the optical absorption coefficient ( $\alpha$ ) is written as:

$$\alpha = 2\omega \cdot \text{Im}\left(\frac{\sqrt{\epsilon}}{c}\right) \quad (3.12)$$

First, the imaginary part of  $\epsilon$  ( $\epsilon''(q, \omega)$ ) is calculated. Then, the real part of  $\epsilon$  ( $\epsilon'(q, \omega)$ ) can be found by using the Kramers-Kronig relation between the real and imaginary part of the dielectric function. By this method, the imaginary part can be calculated from the real part of a complex form provided it is an analytic function of  $\omega$  and vanishes as  $|\omega|$  tends to infinity:

$$\epsilon'(q, \omega) = 1 + \frac{2P}{\pi} \int \frac{\omega' \epsilon''(q, \omega')}{\omega'^2 - \omega^2} d\omega' \quad (3.13)$$

Here,  $P$  is the Cauchy principle value, which is basically the value of the real finite integrals of the function ( $f$ ) form:

$$\int_a^b f(x) dx, \quad (3.14)$$

where  $x$  is real [110].

The energy and momentum loss of electrons can be simulated for different energy levels, since the dielectric constant can be determined from the matrix elements of the

KS wavefunctions.

However, there are many reasons for the  $\epsilon$  form to be not totally accurate for a real system [109]. These include its generation through perturbation theory, neglecting plasmon, exciton and local field effects which could alter the dielectric constant. Therefore, spectra will differ from experimental values for this reason, and as well as this there are some shortcomings of DFT that resulted from the KS equations (2.13) as mentioned earlier in section 3.3. A range of various smearings or “broadenings” is considered by the AIMPRO code, where the user may choose the most meaningful and easily interpreted spectrum. The oscillations of data become more and more erratic at higher energies (about 40 eV) leaving the low loss regime where loss based solely on dielectric function (section 3.8) breaks down [111].

## 3.10 Chapter Summary

In summary, the modelling of derived properties calculated in AIMPRO based on the DFT and supercell method enable quantitative estimates to be made of band structure and formation, binding and migration energies, as well as electrical levels and absorption coefficients. This opens up the possibility for multiscale simulations of the role that defects play in semiconductor devices.

To bridge the gap between atomic- and device-scale simulations by employing the results obtained from DFT simulation into TCAD device modelling, the following chapter attempts to present the fundamental of the Synopsys TCAD package and its relative equations and models.

# Device Simulation Background and The Synopsys TCAD Package

“Your test equipment is lying to you and it is your job to figure out how.”

Charles Rush

## 4.1 Introduction

Impurities and defects affect the physical properties of mc-Si, and are thus relevant to its use as a photovoltaic material. In order to investigate the effects resulting from impurity-defect interactions on the performance of Si PV devices, the data obtained from the quantum-mechanical level provides the basis for device-level simulation using the technology computer-aided design (TCAD) Sentaurus software. In this chapter, the fundamentals of TCAD and its related modelling and simulation are introduced in section 4.2. Solving the Poisson equation (section 4.3) which is at the core of commonly used TCAD and is also explained in this chapter. A description of the mechanism for adding iron to the Si substrate is described in section 4.6.1, including the utilisation of the trap model (see section 4.6.2), and its effect on the electrical and optical characteristics of Si and thus on solar cell efficiency is discussed.

## 4.2 Synopsys Sentaurus TCAD

Problem solving at the atomic scale has become an essential part of both fundamental science and modern device development. Together with the desire and ability to control

materials at the level of atoms, there is a need to model, simulate and design advanced devices using TCAD [112]. Synopsys TCAD is a commercial package of simulation software that can be used for process simulation and device modelling in microelectronics [73], and increasingly for research into the design of solar cells. This can be achieved by solving the Poisson equation, which is essential to photovoltaics [113] as mentioned in section 4.3.

Consequently, results obtained from TCAD can give very useful information, such as the open circuit-voltage and short-circuit current, and from these the fill factor and efficiency of the device. These include also all additional layers such as the buffer, back and front contact [114]. Moreover, using this tool, device engineers can optimise a device for a particular application and gain a deeper insight into the physical phenomena that affect the device's features, and thus semiconductor technology can be developed in a timely and cost-effective manner whilst bridging the gap between manufacturing and electronic design automation.

Furthermore, the simulation mesh behind TCAD tools can be automatically adapted during the simulation of the process steps for annealing and implantation, yielding accurate results related to dopant profiles.

The main areas of modelling and simulation using TCAD include process and device simulations [115]. In a process simulation, the essential semiconductor fabrication steps such as ion implantation and diffusion which are utilised to fabricate a device can be characterised. Also, an accurate model of the geometrical shape and doping profile distribution of the device can be obtained. In device simulation, the information taken from the process simulation is utilised to understand how the devices operate by simulating electrical, optical and thermal features and the other physical properties of the semiconductor device.

## 4.3 Poisson Equation

Solving the Poisson equation is at the core of commonly used TCAD software employed for process simulation and device modelling in microelectronics, and also increasingly used in research into and the design of solar cells [113].

The Poisson equation relates the charge distribution  $n(x)$  in the device to the electrostatic potential  $\phi(x)$ . It can be written as:

$$\frac{d^2\phi}{dx^2} = \frac{n(x)}{\epsilon} \quad (4.1)$$

where  $\epsilon$  is the dielectric constant.

In general, the total charge in the device (equation 4.2) results from ionized donor and acceptor impurities with the concentration profiles  $N_A$  and  $N_D$  and the charges  $q_A$  and  $q_D$ , and also from free charge carriers:

$$n(x) = q_A N_A(x) + q_D N_D(x) + n + p \quad (4.2)$$

The concentrations of electrons and holes ( $n$  and  $p$  respectively) are related to the Fermi energy according to the following expressions:

$$n = N_C \exp\left(\frac{E_C - E_F}{K_B T}\right) \quad (4.3)$$

and:

$$p = N_V \exp\left(\frac{E_F - E_V}{K_B T}\right) \quad (4.4)$$

Here,  $N_C$  and  $N_V$  are the effective densities of states, and  $E_C$ , and  $E_V$  are the band edge energies at the conduction and valence band edges, respectively.

By combining these equations, the relationship between the Fermi energy, the band edges and the electrostatic potential can be obtained as written in equation 4.5. This equation can be solved for any given level of impurity concentration. For example, in the current pattern, the dopants each have one fixed charge state,  $q_A$  and  $q_B$ , and  $n_i$  is the intrinsic carrier density.

$$\frac{d^2 \phi}{dx^2} = \frac{1}{\epsilon} \left[ q_A N_A(x) + q_D N_D(x) + n_i \exp\left(-\frac{\phi}{K_B T}\right) - n_i \exp\left(-\frac{\phi}{K_B T}\right) \right] \quad (4.5)$$

It is worth mentioning that there is no conceptual problem in writing the Poisson equation for any number of dopants and with charge states depending on the  $E_F$ .

Solving equation 4.5 yields useful information, such as the electric field, charge distribution, and potential distribution [114].

Away from thermal equilibrium, the concentrations  $n$  and  $p$  are not directly related to a single value of  $E_F$ . There is one quasi-Fermi level each,  $E_{F_n}$  and  $E_{F_p}$ , for electrons and holes respectively, where both simply replace the equilibrium  $E_F$  in the above concentration expressions:

$$n = N_C \exp\left(\frac{E_C - E_{F_n}}{K_B T}\right) \quad (4.6)$$

and:

$$p = N_V \exp\left(\frac{E_{F_p} - E_V}{K_B T}\right) \quad (4.7)$$

It is important to understand that the concentrations of electrons as well as holes can become large under illumination, when many electron-hole pairs are generated [114].

## 4.4 Carrier Transport

Carriers move freely throughout the semiconductor lattice in random directions and will continue in those directions until they collide with another atom. The carrier moves for a distance called the scattering length before colliding with a lattice atom. The two basic transport mechanisms are drift and diffusion. Drift is the movement of carriers due to an external electric field, whereas diffusion is the movement of carriers due to the density gradient. The continuity form of carrier transport can generally be written as:

$$\nabla \cdot \vec{J}_n = qR_{\text{net},n} + q\frac{\partial n}{\partial t}, \quad (4.8)$$

$$-\nabla \cdot \vec{J}_p = qR_{\text{net},p} + q\frac{\partial p}{\partial t}, \quad (4.9)$$

where  $R_{\text{net},n}$  and  $R_{\text{net},p}$  are the electron and hole net recombination rate respectively,  $\vec{J}_n$  is the electron current density,  $\vec{J}_p$  is the hole current density and  $n$  and  $p$  are the electron and hole densities respectively.

Several transport models are implemented in TCAD Sentaurus, which differ in the method used to compute the current density. The selection of a suitable transport model depends mainly on the device under investigation and the accuracy of modelling. The drift-diffusion model is the default carrier transport model in TCAD Sentaurus. For this drift-diffusion model, which is adopted in this thesis, the simplified current densities for electrons and holes are given by:

$$\vec{J}_n = -nq\mu_n \nabla \Phi_n, \quad (4.10)$$

$$\vec{J}_p = -nq\mu_p \nabla \Phi_p, \quad (4.11)$$

where  $\Phi_n$  and  $\Phi_p$  are the electron and hole quasi-Fermi potentials respectively. The

current density  $J$  of a  $pn$  junction solar cell can be expressed by [116]:

$$J = -J_{ph} + J_0 \left[ \exp\left(\frac{qV}{k_B T}\right) - 1 \right], \quad (4.12)$$

where  $J_0$  is the  $pn$  junction saturation current density and  $J_{ph}$  is the photon-generated current density, which is defined as

$$J_{ph} = qG(L_n + L_p), \quad (4.13)$$

where  $G$  is the generation rate and  $L$  is the diffusion length.

The dark characteristics of the solar cell are similar to a  $pn$  diode J-V curve, while the presence of light  $J_{ph}$  will shift the curve. From the J-V characteristics formula, the open-circuit voltage  $V_{oc}$  can be calculated by setting  $J = 0$  as follows:

$$J = \left[ J_0 \left[ \exp\left(\frac{qV_{oc}}{k_B T}\right) - 1 \right] - J_{ph} \right] = 0, \quad (4.14)$$

where this leads to:

$$V_{oc} \cong \frac{k_B T}{q} \ln \left[ \frac{J_{ph}}{J_0} \right]. \quad (4.15)$$

In contrast, the short-circuit current density  $J_{sc}$  is calculated by setting the voltage across the junction to zero as follows:

$$J_{sc} = \left\{ -J_{ph} + J_0 \left[ \exp\left(\frac{qV}{k_B T}\right) - 1 \right] \right\}_{V=0}, \quad (4.16)$$

which leads to  $J_{sc} = J_{ph}$ . The fill factor  $FF$ , which is a measure of curve squareness, is given by:

$$FF = \frac{J_{mp} V_{mp}}{J_{sc} V_{oc}}, \quad (4.17)$$

where  $J_{mp}$  and  $V_{mp}$  are the current density and voltage at the maximum power point respectively.

By calculating the fill factor, the solar cell efficiency can be directly defined as:

$$\eta = \frac{J_{sc} V_{oc} FF}{P_{in}}, \quad (4.18)$$

where  $P_{in}$  is the incident power on the cell's surface, which is set to 100 mW/cm<sup>2</sup> in this work.

## 4.5 TCAD Numerical Models

For photovoltaic simulations, the modelling of light propagation through different media and also the scattering from interfaces is a crucial step. Many approaches are available to cover the light propagation pattern, each with a trade-off between computational load and accuracy. Since photovoltaic technologies tend towards thin films and nanoscale structures, methods such as Raytracing, which provide solutions depending on only geometric optics, cannot provide accurate results when wavelengths are comparable to the feature size [117].

For numerical simulation tools, the physical and optical models can be adjusted to the specific demands of solar cells [117]. In this study, optical simulations have been performed by using the transfer matrix method (TMM) [118].

### 4.5.1 Transfer matrix method

Sentaurus has a built-in TMM solver which has been adopted to model light propagation by plane waves through layered media [115] within 1D spatial domains, with the assumption that the devices contain stacks of parallel layers with planar interfaces, where each layer are considered to be homogeneous, isotropic and optically linear. Furthermore, the amplitudes of forward and backward running waves in each layer are obtained in each layer by means of transfer matrices. These matrices are functions of the complex wave impedances that depend on the complex index of refraction and the complex counterpart of the angle of refraction. Moreover, the method using the transfer matrix is suitable for the simulation of thin multi-layer anti-reflection coating layers, which reduce the amount of reflected light at the front interface. In addition to that, it is reported [119] that TMM can compute the polarization-dependent optical intensity and rate of optical generation inside the solar cell. Furthermore, TMM is used to compute the polarization-dependent reflectance and transmittance of solar cells using the properties of incident light, including wavelength, polarization, and intensity and the properties of the semiconductor layer including its complex refractive index and quantum yield. In addition, the optical generation rate in solar cells under illumination in the AM1.5G solar spectrum is obtained using TMM [120]. A summation process over all of the wavelengths of the AM1.5G solar spectrum is used to calculate the optical generation rate. The wavelength-dependent complex refractive index is used. Calculations of the photo-generated current density and short circuit current density are achieved as a function of wavelength. The equations related to

these parameters are shown in section 4.4 (4.13).

### 4.5.2 Finite element method

TCAD Sentaurus employs the finite element method (FEM) to solve various physical problems such as electrostatic potential carrier concentration (Poisson and continuity equations) and carrier transport (drift-diffusion). These problems are generally formulated in terms of partial differential equations (PDEs) with specific boundary conditions. The number and type of equations vary from one problem to another due to the diversity of the physical phenomena occurring during the system processes [121]. FEM was originally developed for structural analysis. However, in the late 1960s, this method was widely adopted to solve electromagnetic problems. FEM is one of the most efficient and powerful numerical methods in solving problems of irregular and complex geometries in non-homogeneous material. FEM generates a set of non-linear equations that can be solved utilising the Newton-Raphson algorithm. The finite element solution of any physical problem involves the following basic steps [122]:

- Discretising the solution domain into a finite number of non-overlapping subdivisions or elements
- Deriving the governing equations and forming the element matrix
- Assembling all element matrices into one system matrix
- Solving the system matrix obtained.

After defining the device geometry and material and setting the doping profiles and contact, the discretising or meshing process is defined for the subsequent FEM simulation process. The FEM simulator implemented in TCAD tools uses an automatic meshing tool in Sentaurus Structure Editor (SSE). The meshed structure can be visualised in the SVisual tool and the system matrix is solved in the Sentaurus Device tool where the solver is defined. Sentaurus Device has no graphical interface platform, but is rather based on instructions introduced in command files that define the physics models (for mobility, recombination, etc.) and the type of analysis (i.e. coupled, transient, quasistationary, etc.). During the discretisation process, several cell shapes might be employed, where it is unnecessary to mesh the structure with identical cells throughout the entire structure. The cell shape could be triangular, rectangular or quadrilateral, or a combination of all

these types taking into consideration the position of the element such as edges between metal and dielectric. Meshing is considered to be a key difference between the analytical solutions and numerical analysis, where arbitrary shapes with material non-homogeneity can be analysed and the governing equation is solved at every single element individually.

After meshing the device structure, a system of linear equations will be generated in matrix form with  $N \times N$  size, where  $N$  is the number of unknown coefficients. The accuracy of the solution depends primarily on the number of elements (mesh size), where the finer the meshing, the better the accuracy achieved. However, fine meshing consumes long simulation time and requires more computational resources.

## 4.6 Modelling of Iron in Silicon

As mentioned in chapter 1, the performance of commercial silicon solar cells is strongly controlled by the defects and impurities that may be present at high concentrations in the substrates of the photovoltaic Si [123]. Iron impurities have been modelled as traps and dopants as well as in the donor level as described in the following subsections.

### 4.6.1 Iron diffusion model

A customised diffusion model of iron in silicon is written in Alagator scripting language and implemented in Sentaurus Process models for the 1D, 2D and 3D process simulators for developing and optimising silicon process technologies. Alagator can be widely used to specify partial differential equations and the boundary conditions for use with diffusion simulations in the TCAD tool Sentaurus Process [115], to solve diffusion equations related to dopants, defects and impurities.

The general diffusion problem of iron can be described as reported elsewhere [124]:

$$\frac{\partial C_{Fe}}{\partial t} = \nabla D_{Fe} \nabla C_{Fe} - 2k_1(C_{Fe}^2 - k_2 C_{Fe-clus.}) \quad (4.19)$$

$$\frac{\partial C_{Fecl}}{\partial t} = k_1(C_{Fe}^2 - k_2 C_{Fe-clus.}) \quad (4.20)$$

where  $C_{Fe}$  is the concentration of the species Fe,  $C_{Fe-clus.}$  is the concentration of trapped clusters of two Fe's,  $k_1 = 4\pi \times 2.7 \times 10^{-8} D_{Fe}$  is the forward reaction rate of diffusion Fe,  $k_2 = 5 \times 10^{22} \times \exp\left(-3eV/KT\right)$  is the binding coefficient of Fe clusters, and  $D_{Fe}$  is the

Fe diffusivity, which is given by:

$$D_{Fe} = 1.3 \times 10^{-3} \times \exp\left(-E^a/KT\right), E^a = 0.68 \text{ eV} \quad (4.21)$$

In general, for the procedure of the solution of Fe diffusion in Si can be outlined in the following steps:

- Step1: define the parameters such as precipitate volume and initial radius, diffusivity, and solubility, as  $Sol. \times \exp\left(-2.94\text{eV}/KT\right)$ , where the combination of entropy and enthalpy result 2.94 eV. The variable  $Sol.$  has been varied in the Sentauros Process from  $1.8 \times 10^{22}$  to  $1.8 \times 10^{28}$  in order to control the Fe concentration inside the solar cell substrate.
- Step2: set up the grid and substrate initial structure as well as the boundary conditions.
- Step3: define the diffusion equation using call-back procedures. This will enable TCAD to implement the diffusion of several different species with different parameters using the same equation. In this step, the diffusion time and temperature will also be specified.
- Step4: store the spatial distribution of Fe in silicon substrate in a specific file to be recalled in the following Sentauros Device Editor.
- Step5: create geometry file if necessary to monitor and display the distribution of Fe atoms inside the silicon substrate at different depths.

In the iron diffusion process, the horizontal line spacing of the grid has been varied to study the impact of the grid on the device efficiency at different iron concentrations. More details of this are described in chapter 10 (Figures 10.2 and 10.3), which show the horizontal line spacing of the grid through the Fe diffusion process in the Si substrate, and their impact on the efficiency of the solar cell at different iron concentrations.

### 4.6.2 Iron trap model

Traps are important physical quantities in device physics, as they have a drastic impact on the electrical performance of a device by acting in a way similar to doping, in addition to their contribution to supplying free carriers, enhancing recombination and increasing

leakage. Furthermore, after charging, they can contribute to an overall charge in the right-hand side of the Poisson equation (equation 4.1), and thus have a significant influence on the device's electrical properties. One of the trap objects that is available in Santaurus Device is rechargeable traps that are energetically distributed inside a semiconductor material bandgap. Generally, this trap object is available in two different forms, acceptor (e-neutral) and donor (h-neutral) traps, where both are uncharged when they are unoccupied, but become negatively and positively charged, when capturing an electron and a hole respectively. For both trap forms, electron-hole recombination through such a trap is allowed. Another available trap object, which is not used in this work, is a trap with a fixed charge which is fully occupied by either electrons or holes, so that its charge stays unchanged throughout the simulation and does not depend on electrical bias conditions.

Santaurus Device can provide more parameters than just the form of the distribution of the trap energy inside a material bandgap, such as level, uniform, exponential, Gaussian, or table. In this work, the trap density of the state is specified as a single-energy trap level.

The trap cross-section represents the key parameter used to define the charge-distribution trapping dynamics and the rate of carrier recombination through a trap. The time required for a single trapping (de-trapping event), which is called the trap time constant ( $\tau_{trap}$ ), has the following estimation:

$$\tau_{trap} = \frac{1}{N_t \cdot v_{th} \cdot \sigma} \quad (4.22)$$

Here,  $N_t$  is the concentration of the trap level,  $v_{th}$  is the thermal velocity, and  $\sigma$  is the trap cross-section. In this thesis, the trap distribution, capture cross-section and energy level for Fe-contamination are described in terms of a spatially-dependent SRH recombination process, with a capture cross-section of  $1.3 \times 10^{-14} \text{cm}^2$  [125]. This also include the intrinsic electron density and band-gap narrowing.

In the case of a transient simulation, the carrier trap capture and emission are specified by a detailed balance equation under the steady-state assumption. By assuming that electron and hole trap cross-sections are equal, and degeneration factors are unity, The net carrier recombination through a single trap level has been presented in equation 1.2, which represents a form of the well-known SRH approximation.

---

## 4.7 Traps As Doping

Charge traps act as scattering centres (i.e. as doping). Therefore, their impact on carrier kinetics is significant when using a doping-dependence carrier mobility.

Sentaurus Device utilises a modular approach to describe the carrier mobilities for electrons and holes. In doped semiconductors, carriers can be scattered by charged (impurity) ions, which results in the degradation of carrier mobility. Sentaurus Device supports several built-in models, while, in most cases, only one doping-dependent mobility model should be specified. In this way, double counting mobility effects can be avoided. In contrast, Sentaurus Device allows more than one model to be used in a simulation. In this work, all calculations related to device simulation used the Masetti model [126].

## 4.8 Chapter Summary

The fundamental models and parameters that contribute to the process and device simulation of the electrical and other characteristics of the Si solar cell have been introduced in this chapter. For example, diffusion and trap models for iron in Si solar cell. The understanding of these models and parameters can contribute to the design of a process schedule in which the deleterious effects of defects and impurities present in the substrate can be engineered. In addition, this can help semiconductor technology to develop in a timely and cost-effective manner, whilst bridging the gap between manufacturing and electronic design automation.

In an attempt to examine the effects resulting from impurity-defect interactions on photovoltaic devices, the data obtained at the quantum-mechanical level will provide the basis for device-level simulation using TCAD, with the results presented in chapter 10.

# Part II

## Applications

## Iron Contamination in Pure Si

“One never notices what has been done; one can only see what remains to be done.”

Marie Curie (1867 - 1934)

The foundations of the relevant DFT code used in this thesis have been described in chapters 2 and 3. In this chapter, applications of this theory are presented with the aim to study the structural, optical and electrical properties of iron contamination in silicon. Iron in general, and as interstitial (section 5.1.1) in particular, is arguably the most important detrimental impurity in lower-grade silicon, and it is a problem in photovoltaic devices as it is understood to be an active recombination centre lowering device efficiency [53,54,57,71].

Theoretical investigations into the behaviour of iron as interstitial and substitutional in bulk silicon are the subject of this chapter. The chapter is organised as follows. As an introduction (section 5.1.1), a brief review of the theory of iron formation in Si is provided. Then, the computational method used for this specific study is outlined in section 5.2. The results of first principle calculations of interstitial iron and in some cases substitutional iron and vacancies, in bulk Si are given in section 5.3, along with comparisons made with experiments and previous theory. A summary is then presented in section 5.4. In contrast, a comparison of individual iron with iron pairs in bulk Si is the main subject of the next chapter. Finally, the analysis of individual iron in bulk Si has been published in some sections of other publications [127,128], while a comparison of interstitial iron and its pair-formation in bulk Si has also been published elsewhere [129].

## 5.1 Introduction

As mentioned before in chapter 1, multicrystalline silicon (mc-Si) offers a cost-effective option for Si solar cells compared with single crystalline Si [17–19], although mc-Si generally contains higher concentrations of efficiency-reducing defects. Transition metal (TM) impurities in general, and iron in particular, are common impurities [53,130] incorporated during growth and processing [131]. These defects readily diffuse, and their high diffusivity leads to the distribution of deleterious effects throughout a solar cell, limiting its operational efficiency [48]. Iron as the most common and unavoidable TM contaminant in Si [53,54,57,71] has been widely investigated, and the effects of Fe in mc-Si solar cells have been reviewed [48,55]. Generally, it is agreed that Fe in Si is especially problematic because it introduces deep levels in the band gap, reducing the minority carrier lifetime, and also because it diffuses very rapidly. Generally, interstitial diffusion occurs when an interstitial atom moves from its position to another interstitial site that is empty [132]. Furthermore, Fe exhibits uncontrolled behaviour after any heat treatment of Si.

Numerous Fe-related complexes have been experimentally detected using electron paramagnetic resonance (EPR) [133], electron nuclear double resonance (ENDOR) [134] and Mössbauer studies [135,136], as well as other experimental methods.

Iron exists in silicon in two forms, as interstitial (section 5.1.1) and as substitutional (section 5.1.3), as shown in the following sections. Also Fe can interact and form complexes with other defects, as described in chapters 6–8.

### 5.1.1 Interstitial iron

An interstitial impurity is an atom which occupies a true off-lattice site between the lattice atoms. EPR, ENDOR and Mössbauer studies have found that  $\text{Fe}_i$  resides at the unperturbed tetrahedral interstitial (T-site) in the Si crystal [137,138], as shown in figure 5.1 [139]. Even in the slowly cooled directional solidification growth technique, iron is supersaturated in the form of highly detrimental interstitial point defects [54]. Ludwig and Woodbury [61,138], proposed a model for the electronic structure of 3d TM, including Fe contaminations in silicon.

Their model depends on the local crystal field, in which the breaking of degeneracies of electron orbital states is described. In the model, it is supposed that the silicon host shifts the degeneracy of the 3d orbitals of an iron atom into the  $e$  (doublet state) and  $t_2$  (triplet state) in the neutral case of iron ( $\text{Fe}_i^0$ ) in silicon.

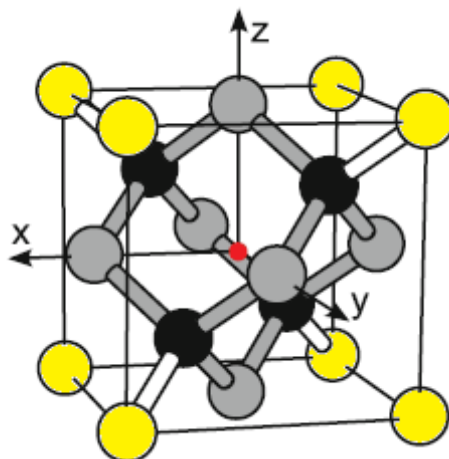


Figure 5.1: Conventional unit cell of crystalline silicon with iron (red atom) located at a tetrahedral interstitial site. Black atoms represent the Si first neighbour, while the gray ones are the second Si neighbours. Image taken from [139].

Based on previous research [56,62], it is predicted that  $\text{Fe}_i^0$  and  $\text{Fe}_i^+$  have an electronic structure with occupancy  $t_2^6.e^2$  and  $t_2^5.e^2$  that correspond to triplet and quartet spin states ( $S = 1$  and  $S = 3/2$ , respectively).

Iron is known to migrate as a neutral atom and as a positively charged ion at high temperature and near to room temperature respectively [132].

Based on EPR and ENDOR studies [134,140], the diffusion barrier of  $\text{Fe}_i$  is obtained by a strong interaction of Fe valence electrons with up to a hundred surrounding Si atoms. Experimental results [141,142] reveal a slight difference in the barrier of the diffusion of the neutral and positive charge states. By using NEB calculations, described in chapter 3 (Sec 3.6.2), the migration barrier of moving iron from T-site to the next T-equilibrium site through a hexagonal interstitial site (H-site) is investigated in section 5.3.1.5, with good agreement with other studies [141] and the results listed in table 5.3.

Experimental observations and theoretical calculations indicate that  $\text{Fe}_i$  introduces a donor level above the valence band top of Si, which is confirmed in this chapter (section 5.3). The effect of donor level-energy on Si solar cell performance is examined at device level in chapter 10.

Consequently, it is worth studying the physical trends of  $\text{Fe}_i$  in Si in this chapter, as iron is understood to be an active recombination centre lowering device efficiency even at less than 1 ppb [57], and also because its interactions with other impurities such as vacancies (Sec 5.1.2) and structural imperfections in the crystal structure all may degrade solar cell performance [57,58]. The Fe-structural defect complexes were studied in chapters 7–10.

### 5.1.2 Iron-vacancy pair

When  $\text{Fe}_i$  encounters a neutral vacancy ( $\text{V}^0$ ), an iron-vacancy ( $\text{Fe}_i\text{V}$ ) pair forms. This pair has been observed via channeling experiments [143]. Figure 5.2 shows the formation of the  $\text{Fe}_i\text{V}$  pair by trapping  $\text{Fe}_i$  outside  $\text{V}$  on a trigonal axis, then forming a substitutional iron ( $\text{Fe}_s$ ). The change in the barrier that interstitial iron must overcome to hop from the

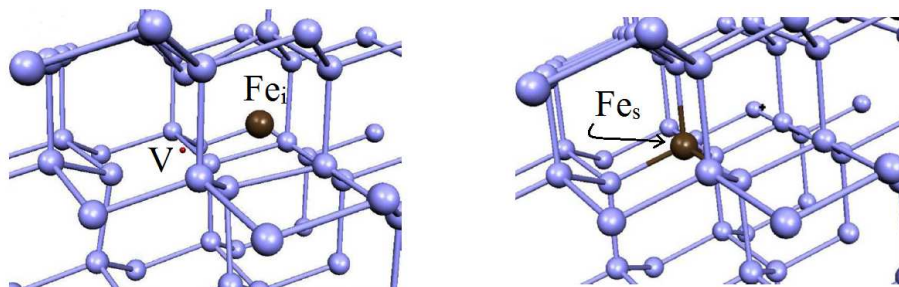


Figure 5.2: The  $\text{Fe}_i\text{V}$  pair (left) has  $\text{Fe}_i$  trapped outside  $\text{V}$  on a trigonal axis. The tetrahedral  $\text{Fe}_s$  (right) is at a location in an almost unrelaxed substitutional position. Images taken from [144].

$\text{Fe}_i\text{V}$  pair configuration to the substitutional location have been found, with respect to the amount of lattice relaxation allowed, the spin, and charge state [144], to be 0.45–0.75 eV, where the barrier height is consistent with the thermal stability of the NL19 EPR centre at 160 °C [137].

The configuration of  $\text{Fe}_i\text{V}$  has been deduced from the channeling pattern [145], and was observed by EPR and photo EPR in  $e^-$ -irradiated silicon following 400 °C anneals. Based on calculations [146], it is reported that  $\text{Fe}_i\text{V}$  has a hole trap at  $E_V+0.51$  eV and survives 500 °C anneals, associating with the NL19 EPR centre [137] even through its thermal stability appears to be higher.

$\text{Fe}_i\text{V}$  in silicon has also been investigated theoretically [147], where a trigonal  $\text{Fe}_i\text{V}$  forms with  $\text{Fe}_i$  off the T-site by 0.3–0.5 Å, depending on the charge and spin state, toward  $\text{V}$  along the trigonal axis. An overlapping is noted also between an electron in a valence orbital and other electrons in the system, where electron spin can easily flip to the ground state configuration [144]. In contrast, a nuclear spin (i.e. a localized spin) remains very stable unless in the presence of a magnetic field. It has been calculated [147] that the energy difference between  $\text{Fe}_i$  at T-site far away from  $\text{V}$  and at the T-site adjacent to  $\text{V}$  is about 1.7 and 1.5 eV for neutral (spin=0) and positive (spin=3/2) charge states respectively.

The binding energies of neutral and positive charge states for an  $\text{Fe}_i\text{V}$  pair with  $S = 1$  and  $S = 1/2$  respectively have been calculated [144] relative to individual  $\text{Fe}_i$  with  $S = 1$

and  $S = 3/2$  for the neutral and positive charge state respectively. The lowest spin state energies of this  $\text{Fe}_i\text{V}$  pair were 0.21 and 0.15 eV respectively, creating a donor level located in the Si gap at  $E_v+0.20$  eV [147]. The results of modelling  $\text{Fe}_i\text{V}$  in Si are presented in section 5.3.2.

### 5.1.3 Substitutional iron

As shown in the previous section, the  $\text{Fe}_i\text{V}$  pair can form substitutional iron, where the structure is viewed as one Si atom being replaced by a Fe atom as depicted in figure 5.3 [139]. To achieve this position,  $\text{Fe}_i\text{V}$  must still overcome a barrier, the lower value of which has been found [147] to be 0.5 eV, which is obtained from the relaxation of the crystal as interstitial to become substitutional, with an additional gain in energy of the order of 1 eV (depending on the charge state).

The fitting of  $\beta$ -channeling patterns [145] has suggested that  $\text{Fe}_i$  becomes  $\text{Fe}_s$  after high-temperature (above 800 °C) anneals. The properties of  $\text{Fe}_s$  have been investigated by Mössbauer spectroscopy [148, 149], and inferred from channeling experiments [150] as well as theoretical studies [143, 151].

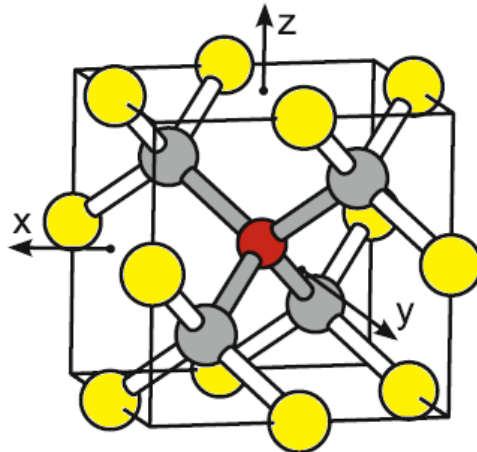


Figure 5.3: Conventional unit cell of crystalline silicon at the tetrahedral substitutional site, which is represented by the red atom at the centre. Gray colours reflect the first neighbouring silicon atoms and bonds.

Green's function method [151] predicted that  $\text{Fe}_s$  has no levels in the Si gap, which means that the  $e$  and  $t_2$  states were expected to be located below  $E_V$  and above  $E_C$  respectively. In contrast, a theoretical study using DFT calculations indicates that the  $t_2$  state lies within the gap, with a shallow state in the upper half of the gap at  $E_c-0.41$  eV or at  $E_c-0.29$  eV (depending on the appropriate calculations, such as basis functions and pseudopotential types).

In section 5.3.3, the ground state of  $\text{Fe}_s$  is examined in good agreement with Green's function calculations reported elsewhere [150, 151]. Another study has indicated that  $\text{Fe}_s$  is electrically inactive and has zero spin as its electrons are involved in covalent interactions with four silicon neighbours; that is, the  $3d$  shell of Fe is only partially filled by six electrons. Therefore, it is still invisible to EPR or ENDOR [56]. Green's function expectations indicate that  $\text{Fe}_s$  has a deep acceptor level at  $E_c - 0.29$  eV, and also a negative charge state is predicted for  $\text{Fe}_s$  ( $S = 1/2$ ) in an n-type material lower than  $S = 3/2$  by about 0.51 eV.

It is generally agreed that the diffusion rate of the atom in the interstitial configuration significantly exceeds that of the atom in the substitutional configuration. Therefore, to answer the relevant questions proposed by theoretical and experimental research regarding the behaviour of  $\text{Fe}_i$  and  $\text{Fe}_s$  in Si, further studies are carried out in section 5.3.3.

## 5.2 Computational Method

As mentioned in chapters 2 and 3, first-principles density-functional theory, as implemented in AIMPRO [81], has been used to investigate iron-doped Si. Atoms are modelled using norm-conserving separable pseudopotentials (section 2.11). The Kohn-Sham eigenfunctions of the valence electrons are expanded using atom-centred Gaussian functions, and more detail is given in section 2.4.2.1 To selecting the basis set that gives the best minimum energy of the iron in the bulk Si system, several test calculations were performed to choose the most promising basis set for  $\text{Fe}_i$  and  $\text{Fe}_s$  in Si, as shown in figure 2.3 which presents the results of detailed analyses of  $\text{Fe}_i$  atoms in different spin states conducted using different Gaussian basis sets. More details are given in section 2.8. MP sampling schemes are used to integrate the band structure [96], as described previously in section 2.9.

Bulk silicon is modelled using primitive, 216- and 512-atom, simple cubic cells with lattice vectors being  $[n00]a$ ,  $[0n0]a$  and  $[00n]a$ , where  $a$  is the lattice constant, and  $n$  is 3 and 4 for the 216 and 512 atom cells, respectively.

As shown previously in figure 2.5, the relative energies that are related to the BZ sampling are a function of spin and charge states of  $\text{Fe}_i$  in bulk Si, indicating the convergence in energy difference between MP2 and MP3 for all spin and charge states of  $\text{Fe}_i$  structures. The optical properties of pure Si and Si doped by  $\text{Fe}_i$  and  $\text{Fe}_s$  are determined through the real and imaginary parts of the dielectric function and by representing photo-absorption

properties. [152, 153]. The minimum energy path for diffusion processes is obtained using climbing nudged elastic bands [106, 107], as described in section 3.6.2. The binding energy ( $E^b$ ) for the stable  $\text{Fe}_i\text{V}$  structure is calculated using equation 5.1, where a negative value represents a bound pair:

$$E^b = E^f(\text{Fe}_i) + E^f(\text{V}) - E^f(\text{Fe}_i\text{V}) \quad (5.1)$$

The bond-strains for  $\text{Fe}_i$  have been calculated based on the flowchart shown in figure 5.4. For these calculations, the equilibrium atomic coordination of optimised iron silicide ( $\beta\text{-FeSi}_2$ ), as well as the original values of the ideal Si structures, are used to study the impact of the  $\text{Fe}_i$  contamination of Si atoms.

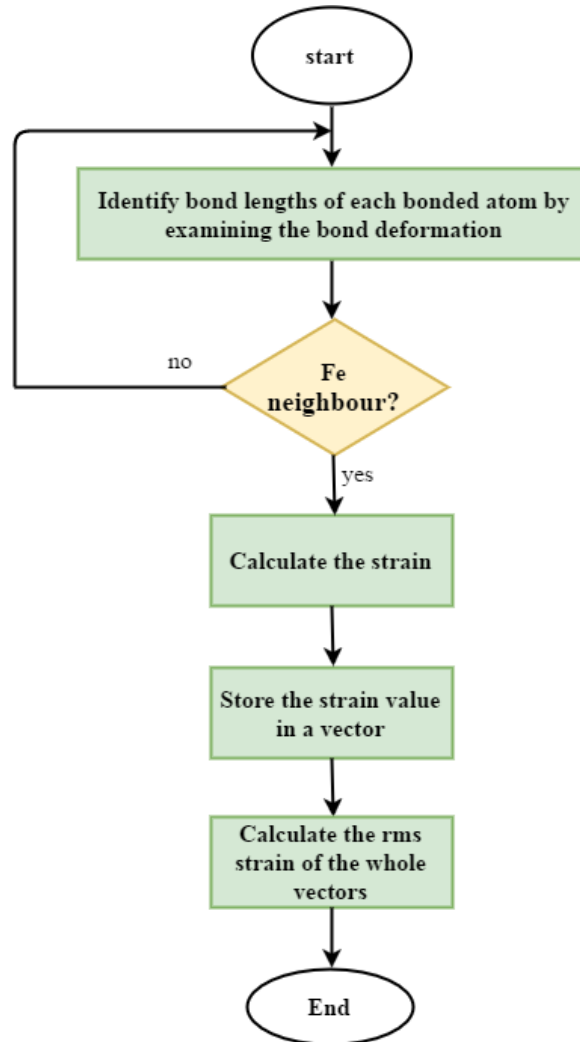


Figure 5.4: Flowchart showing the methodology used to determine the bond-strain deviation caused by presenting iron atoms with respect to bond-strain before decoration.

## 5.3 Results and Discussion

### 5.3.1 Modelling $\text{Fe}_i$ in crystalline Si

#### 5.3.1.1 Geometrical structure

The results of DFT in this work provide valuable information about the occupancy of iron on interstitial Si lattice sites, where different sites in constructed and unconstructed structures have been examined. It is confirmed that  $\text{Fe}_i$  resides at the tetrahedral (T) interstitial site, which is in agreement with experimental results and previous calculations [147,154]. For accurate geometrical calculations, the modelling of  $\text{Fe}_i$  in a crystalline silicon environment needs to consider whether or not the outer periodicity of the supercell is adequate in terms of size. In particular, spurious effects can take place in the form of defect-image coupling through elastic and Coulomb interactions. Quantitative and qualitative investigations of the cell size and structure host shape have been demonstrated in this work for most calculations of the derived properties and the same results of the ground states are obtained for both shapes. Therefore, accurate calculations achieved for bulk Si supercells containing 216-atoms were used to study the derived properties of  $\text{Fe}_i$  and its complexes in bulk Si. To demonstrate this effect, the occupation of  $\text{Fe}_i$  in different sites of the simple-cubic unit-cells and at hexagonal host Si structure have firstly been demonstrated.

In cubic Si host structures,  $\text{Fe}_i$  that resides at the T-site (Figure 5.5-a) with high symmetry ( $T_d$ ) has lower energy than in the hexagonal (H)-site (Figure 5.5-b) with lower symmetry ( $D_{3d}$ ) by 0.76 eV. Calculations of the Si–Si bond length deviation in each of these sites have been examined with respect to pure and  $\beta\text{-FeSi}_2$ . The changes in Fe–Si bond lengths before and after relaxation are  $0.041\text{\AA}$  and  $0.065\text{\AA}$  when Fe resides at the T-Site and H-site respectively.

Table 5.1 lists the Si–Si and Si–Fe strains which can be caused by adding iron as compared with Si–Si in pure Si and  $\beta\text{-FeSi}_2$ . Calculations show that the presence of  $\text{Fe}_i$  leads to increasing the Si–Si bond length by around 0.2% as compared with the bonds in pure Si, whereas the difference in bond length when compared with  $\beta\text{-FeSi}_2$  is 7% for Si–Si and about 2% for Fe–Si. These findings can be employed to indicate if the system exhibits interstitial or precipitate performance by comparing the Si–Si and Fe–Si bond lengths in table 5.1 with their counterparts which result after iron-segregation and precipitation at extended defects.

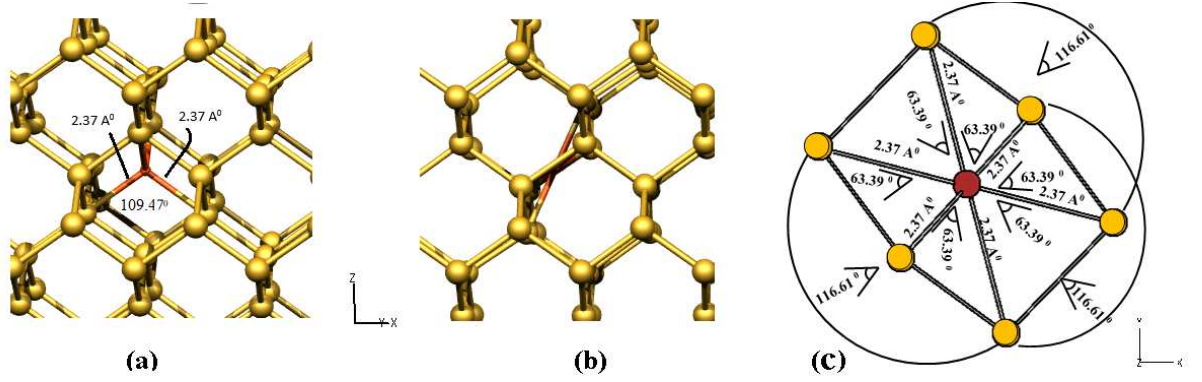


Figure 5.5: Modelled interstitial iron at a) tetrahedral interstitial site of Si lattice, with cubic structure,  $T_d$  isogonal point group, numerical symmetry operation: 24. b) at H-site of Si lattice, with cubic structure, isogonal point group ( $D_{3d}$ , symmetry operation is 12); c) another view of  $Fe_i$  location at H-site showing the Fe-Si bond lengths and angles.

Table 5.1: Evaluation of root mean square bond-strain changes in atomic unit from values for crystalline pure Si as function of number of Si atoms in the supercell ( $n_{sc}$ ). Strain 1 has been calculated with respect to Si-Si in pure Si, which is Si-Si=4.41 au. Strain 2 for Si-Si and Si-Fe have been determined using those bond lengths in  $\beta$ - $FeSi_2$ , which are Si-Si=4.76 au and Fe-Si=4.39 au.

$n_{sc}$	Bond	rms bond length	rms strain 1 (%)	rms strain 2 (%)
2	Si-Si	4.42	0.48	7.21
	Fe-Si	4.49	1.76	2.30
3	Si-Si	4.42	0.48	7.19
	Fe-Si	4.49	1.81	2.35
4	Si-Si	4.42	0.49	7.20
	Fe-Si	4.47	1.56	2.04

### 5.3.1.2 Role of spin and charge states

In order to study the magnetic behaviour of interstitial iron in bulk Si, different structures have been investigated with different spin and charge states. Table 5.2 shows that, for all the cell size structures for  $Fe_i^0$ , the ground state is a spin triplet, with the singlet and quintet energies determined to be 0.5 and 0.6 eV (higher) respectively, which is in good agreement with previous calculations [56]. Similarly, for  $Fe_i^+$ , the calculated energy difference between the doublet and quartet states at 0.2 eV agrees with values in the literature [155]. The stability of these structures ( $S = 1$  and  $S = 3/2$ ) for neutral and positive forms respectively of interstitial iron have also been observed experimentally also using paramagnetic resonance [133].

Table 5.2: Difference in energies ( $\Delta E$ ) in eV associated with  $\text{Fe}_i$  structure as a function of number of Si atoms in supercell ( $n_{\text{sc}}$ ) and spin. These values indicate how much each of the other spin states are higher than the reference  $\text{Fe}_i$  model with  $S = 1$  and  $S = \frac{3}{2}$  for neutral and single positive charge states respectively.

$n_{\text{sc}}$	$\text{Fe}_i^0$		$\text{Fe}_i^+$	
	$\Delta E(S = 0)$	$\Delta E(S = 2)$	$\Delta E(S = 1/2)$	$\Delta E(S = 5/2)$
2	0.47	0.60	0.19	0.10
3	0.53	0.59	0.15	0.10
4	0.53	0.59	0.18	0.10

### 5.3.1.3 Band structure and electrical level

Electronic band structures of neutral Fe at the T- and H-sites are shown in figure 5.6. It is found that states occupied near the valance band top indicate that  $\text{Fe}_i$  creates a state in the gap which may act as a recombination centre, since it traps either free carriers or excitons (electron-hole pairs that are formed when light interacts with certain materials). The departure of  $\text{Fe}_i$  from one tetrahedral site to the next necessarily involves passing through the hexagonal configuration or vice versa, as shown later in section 5.3.1.5. Fe at the H-site shifts the Fe-state to the upper half of the Si bandgap. This can be considered to be the established model for the electronic structure of  $\text{Fe}_i$  in bulk Si, where the coupling between the iron with a 4s orbital and the Si leads to a shift in the 4s orbital to a higher energy level, and the 4s electron is transferred to the lower energy Fe 3d orbital. It is predicted that  $t_2$  and  $e$ -levels are present in the Si bandgap ( $t_2$  below the  $e$ -state) [61,138]. The formation energy of  $\text{Fe}_i$  in Si as a function of the chemical potential of species is calculated as in Eq. 3.2.

It is found that the absolute value of neutral  $\text{Fe}_i$  ( $S = 1$ ) with respect to pure Si and Fe metal is 0.8 eV in the 64-atom and 1.3 eV in a 512-atom supercell. As these values of this interaction are positive and extremely small (as compare with the case of individual parts), so this reaction can be formed easily according to the standard enthalpy of formation.

Furthermore, the formation energy of the defect (section 3.4.1) used to estimate the donor and acceptor levels is calculated and is in good agreement with other studies [156, 157], considering that  $\text{Fe}_i$  has a donor level represented as the intersection of neutral and positive charge states. The position obtained for the donor state is  $E_V+0.12$  in a 64-Si atom and  $E_V+0.15$  eV in a 512-Si atom supercell respectively. It is found also that there is no acceptor level.

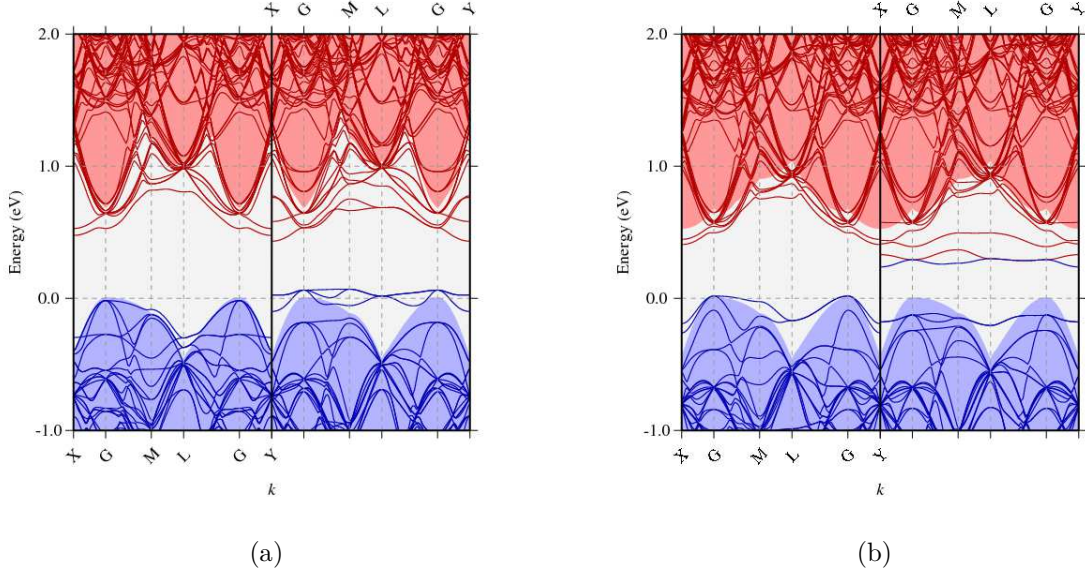


Figure 5.6: Electronic band structures of  $\text{Fe}_i$  in neutral state ( $S = 1$ ) modelled in 216 Si-atom at (a) T-site; (b) at H-site, plotted along high-symmetry branches in the first BZ. Occupied and unoccupied states are depicted as solid blue and red lines respectively. The left and right panels show the spin up and down spectra, respectively. The underlying shaded regions show the electronic band structure for the corresponding bulk Si supercell (216 atoms). The energy scale for each system is defined such that the valence band maxima are at zero.

#### 5.3.1.4 Optical properties

To study the optical effect of  $\text{Fe}_i$  in Si, the complex refractive index of neutral state ( $S = 1$ ) is plotted in figure 5.7, comparing the real ( $n$ ) and imaginary ( $k$ ) parts of bulk Si as a function of wavelength. The plot indicates the similarity of the real and imaginary parts of interstitial iron with the complex refractive index of bulk silicon. However, iron as an impurity with high concentration is predicted [158] to have a significant impact on the refractive index of bulk silicon.

#### 5.3.1.5 Diffusion of $\text{Fe}_i$

The experimental observation [137] shows that  $\text{Fe}_i$  has a high diffusivity in pure Si, with theory suggesting that the diffusion pathway is a hop between neighbouring tetrahedral interstitial sites via the hexagonal (H)-site transition state [159], and confirming the convergence of the diffusion energy in the 216 atom cell. Models of  $\text{Fe}_i$  at the T-site (symmetry  $T_d$ ) and H-site (symmetry  $D_{3d}$ ) of the Si lattice are shown in figure 5.5.

Figure 5.8 shows the migration path of  $\text{Fe}_i$  from one T-site to another through the Si lattice. The process of this diffusion has been described previously in section 3.6.2.

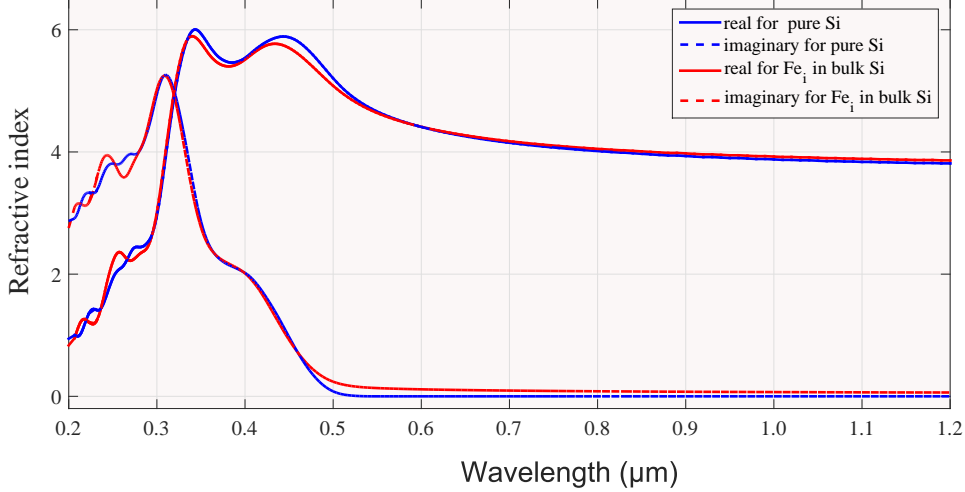


Figure 5.7: Computed real ( $n$ ) and imaginary ( $k$ ) parts of the refractive index, showing the impact of interstitial Fe ( $S = 1$ ) on the complex refractive index of the Si supercell.

The saddle point structure defines the higher migration barrier, whereas an intermediate metastable structure defines the second structure where the transported atom or ion sits halfway along the trajectory connecting the two ends of the migration path.

The calculations of the minimum energy of the saddle point are used to determine the energy barrier. This can be achieved by subtracting the energy of the initial (or end in this case) structure from that of the saddle point structure.

In this work, the activation energies have been calculated for both the 216 and 512 atom bulk cells as 0.80 and 0.74 eV for  $\text{Fe}_i^0$  and  $\text{Fe}_i^+$  respectively (Figure 5.8), which compare favourably with values in the literature [155]. As can be seen from the energy profile in figure 5.8, the H-site is metastable, with the transition state lying slightly away from the  $D_{3d}$  symmetry H-site structure.

The effects of the charge state of iron on the diffusion path has been studied previously. It is concluded [160] that the diffusion path is independent of the charge state of all the  $3d$  elements. However, in this study, change in activation energy between the neutral and positively charged iron states of interstitial iron in bulk Si is found, as shown in figure 5.8. Hence one may conclude that positive ions migrate faster than neutral atoms, which means that ions have higher flexibility than electrons to diffuse toward the H-site.

In addition, it is assumed that one will obtain a smaller difference in elastic strains when  $\text{Fe}_i$  at each site is neutral than that corresponding to positively charged iron at a T-site and  $\text{Fe}_0$  at an H-site. In order to explain the effect of temperature on the diffusion path, an experimental study [160] has examined the effect of low temperature

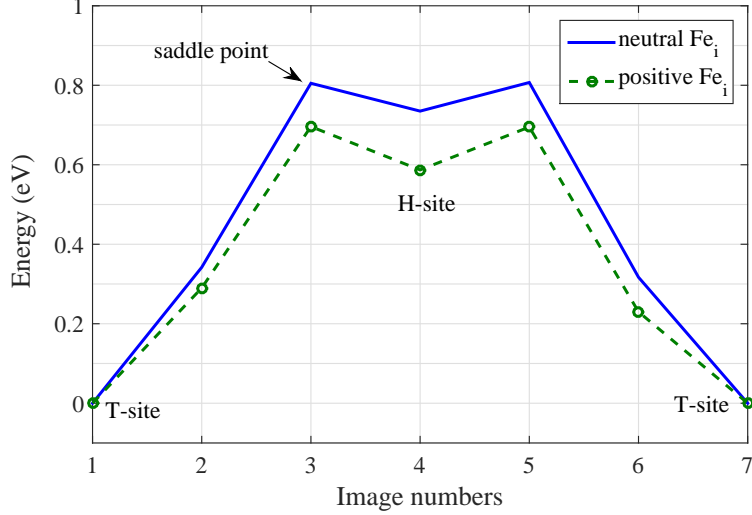


Figure 5.8: Migration path of single iron along a trigonal axis starting near a T site, over the hexagonal site to the T-site. The circles show the images used in the NEB calculations.

Table 5.3: Calculated activation energy of interstitial iron compared with collected experimental [71, 155, 161] and theoretical data [162].

Charge States	Present work (eV)	Other studies (eV)				
		LDA	PBE*	RevPBE**	RPBE	Experiment
neutral $\text{Fe}_i$ ( $S = 1$ )	0.80	0.88	0.85	0.83	0.86	0.84
positive $\text{Fe}_i$ ( $S = 3/2$ )	0.74	0.82	0.71	0.74	0.69	0.69

\*PBE:Perdew-Burke-Ernzerhof [163], \*\*revPBE [164] and RPBE [165].

on both  $\text{Fe}_i^0$  and  $\text{Fe}_i^+$  achieved on the same samples having the same thermal condition, doping level, concentration of iron and the same density of precipitation sites. In that study [160], it was found that the value of migration enthalpy of  $\text{Fe}_i^0$  is smaller than that of  $\text{Fe}_i^+$  and the corresponding diffusivities vary by more than an order of magnitude. It was thus concluded that Fe diffusivity does depend on its charge state, contrary to theoretical and other experimental predictions. In contrast, in this work, theoretical and experimental data of activation energies obtained using different techniques have been collected and listed in table 5.3 and compared with results obtained from this work using NEB calculations. It is found that the value of activation energy of neutral iron is higher by a small amount than that of positively charged  $\text{Fe}_i$ .

### 5.3.2 $\text{Fe}_i\text{V}$ pair

$\text{Fe}_i$  is a recombination centre in p-type silicon that can be annealed out at a temperature of  $175^\circ\text{C}$  and captured by a pre-existing vacancy to form an  $\text{Fe}_i\text{V}$  pair, which is also a recombination centre in p-Si, and it is desirable to deactivate this defect. Therefore, the behaviour of this pair is studied in this section in terms of geometry and electronic

structure.

In a supercell containing 216 Si atoms,  $\text{Fe}_i$  and a monovacancy were allowed to relax with the  $C_{3v}$  point group symmetry operation. Figure 5.2 (left) shows the nearest neighbour of the  $\text{Fe}_i\text{V}$  pair that is formed from the trapping of  $\text{Fe}_i$  by V on a trigonal axis. The tetrahedral  $\text{Fe}_s$  is at an almost unstrained substitutional site [144].

The results show that stable spin state of the neutral  $\text{Fe}_i\text{V}$  pair is  $S = 0$  lower in energy than the triplet and quintet by 0.24 and 0.65 eV respectively. For negative states,  $S = 3/2$  higher in energy than  $S = 1/2$  by 0.42 eV. This can describe the overlapping of an electron in the valence orbital in the  $\text{Fe}_i\text{V}$  pair system with other system electrons, where its spin easily flips to the ground state configuration. Calculations show that the spin 1 and 2 states of an individual vacancy were 0.18 and 0.82 eV higher than the  $S = 0$  state respectively. The spin 3/2 state of positive and negative states for an individual vacancy were 0.48 and 0.29 eV above the spin 1/2 state. This spin modification of the pair compared to the individual interstitial iron and vacancy is due to geometric changes and also due to increasing state splitting after adding the monovacancy, where charges can be transferred between states. Figure 5.9 shows the electronic structure of this pair, showing the mid-gap state in the gap, where overlaps between V and  $\text{Fe}_i$  to form the pair can cause modifications in the state as compared with them as individuals.

The binding energy of  $\text{Fe}_i\text{V}$  relative to isolated triplet  $\text{Fe}_i$  plus an isolated vacancy is 2 eV, which is the energy that is released upon the creation of a bound state.

### 5.3.3 $\text{Fe}_s$ in pure Si

Different bulk Si supercells containing  $\text{Fe}_s$  have been optimised to achieve accurate calculations to study the behaviour of iron as substitutional in bulk Si (Figure 5.10). The results show that  $\text{Fe}_s$  in Si is stable at the ideal substitutional site with  $T_d$ -symmetry.

Detailed analyses in this work have found that, in the neutral charge state, the spin state of  $\text{Fe}_s$  is 0, where  $S = 1$  is higher in energy by 0.33 eV which is in good agreement with predictions from the Green's functions [63,151] and molecular-dynamic simulations [144]. For the negative charge state, the doublet spin ( $S = 1/2$ ) is lower than the quartet state by few electron volts. The stability of the low spin of  $\text{Fe}_s$  is in agreement with theoretical predictions regarding the neutral state with singlet spin in p-type Si and negative spin half in n-type Si [144]. Since the stabilised spin of  $\text{Fe}_s$  is  $S = 0$ , it is invisible to EPR in its ground state. Furthermore, this relatively low value (about zero) of the spin reflects

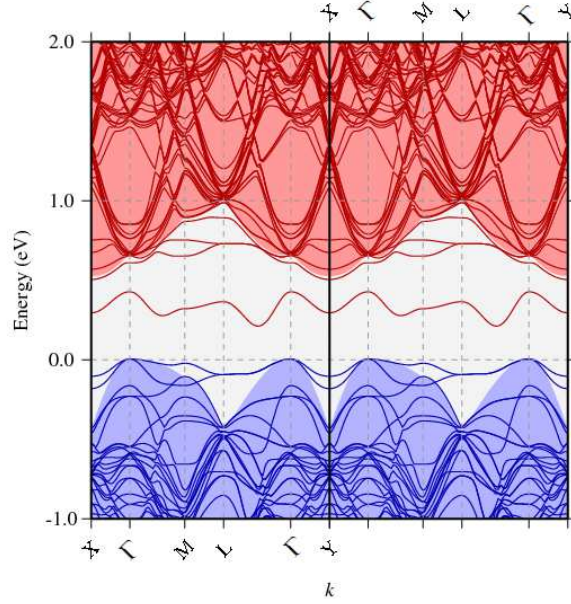


Figure 5.9: Electronic band structures of  $\text{Fe}_i\text{V}$  pair in neutral state modelled in 216 Si-atom. Occupied and unoccupied states are depicted as solid blue and red lines respectively. The underlying shaded regions show the electronic band structure for the corresponding bulk Si supercell. The energy scale for each system is defined such that the valence band maxima are at zero.

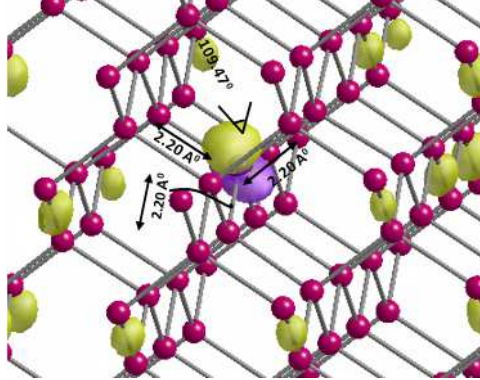


Figure 5.10: Fraction of the Si supercell, showing the bond lengths and angles for neighbours of substitutional iron in Si.

the fact that the  $d$ -orbital of iron hybridizes with the neighbours of the neutral vacancy, yielding electron pairing in covalent bonds. The energy difference between  $\text{Fe}_s$  ( $S = 0$ ) and  $\text{Fe}_i\text{V}$  ( $S = 0$ ) is about 1 eV (with  $\text{Fe}_s$  lower than  $\text{Fe}_i\text{V}$ ). Consequently, and as mentioned above (section 5.3.2), the binding energy of  $\text{Fe}_i\text{V}$  relative to isolated  $\text{Fe}_i$  plus an isolated vacancy is 2 eV and to form  $\text{Fe}_s$  is 3 eV. The electronic band structures of  $\text{Fe}_s$  are shown in figure 5.11, where no donor level is associated with it, and there is a shallow state near the conductive band edge, leading to the conclusion that  $\text{Fe}_s$  has no mid band gap state. This is also supported by the electrical levels shown in figure 5.12. The complex refractive index of the  $\text{Fe}_i$  and  $\text{Fe}_s$  are plotted in figure 5.13, comparing the real and imaginary

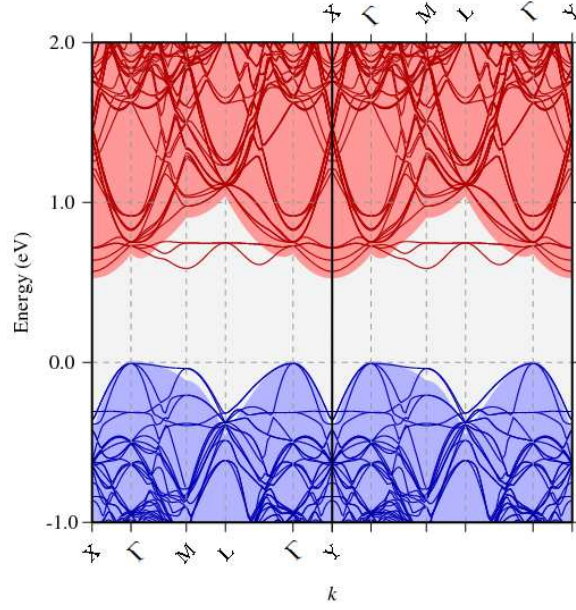


Figure 5.11: Electronic band structures of  $\text{Fe}_s$  in neutral state in 216 Si atoms, plotted along high-symmetry branches in the first BZ. Lines, shading and scales are as defined in figure 5.6(a)

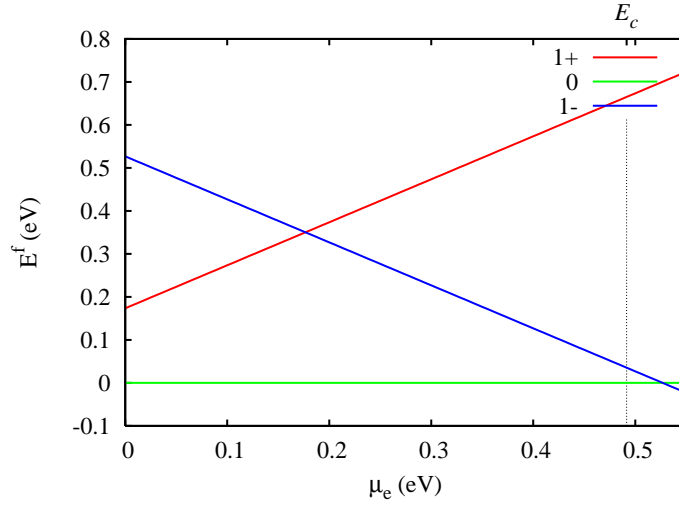


Figure 5.12: Formation energy  $E^f(q)$  for three charge states of  $\text{Fe}_s$  as function of electron chemical potential ( $\mu_e$ ).  $E^f$  is defined as zero for the neutral charge state. The sign of the slope indicating the sign of the charge state. The donor level is the value of  $\mu_e$  above which the neutral system (0 charge state) is preferred over the + charge state

parts with bulk Si as a function of wavelength. The figure shows the deviation from bulk behaviour, reflecting the similarity of the complex refractive index of Fe and that of the real and imaginary parts of bulk Si. However, increasing impurity concentration in general disturbs the internal electric field and thereby modifies the absorption properties of the crystal. Therefore, iron as an impurity with high concentration is predicted to have a significant impact on the refractive index of bulk Si [158], due to its impact on SRH

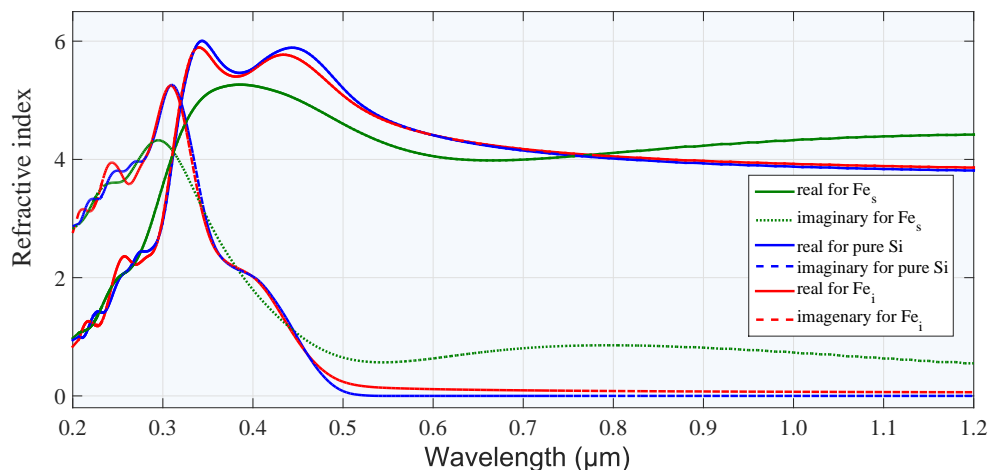


Figure 5.13: Computed real ( $n$ ) and imaginary ( $k$ ) parts of the refractive index for pure silicon compared with that containing either  $\text{Fe}_i$  and  $\text{Fe}_s$ .

recombination, and thus this can affect device efficiency.

## 5.4 Summary

In conclusion, the calculations suggest stable structures for  $\text{Fe}_i$  ( $S = 1$ ),  $\text{Fe}_i\text{V}$  ( $S = 0$ ) and  $\text{Fe}_s$  ( $S = 0$ ) in bulk Si, creating energy states in the Si bandgap.

The migration barrier for  $\text{Fe}_i$  to diffuse from T-site to another T-site in the Si lattice is less than 1 eV for both neutral and positively charged iron states. The energy cost to form  $\text{Fe}_s$  in Si from the interaction of  $\text{Fe}_i$  and a monovacancy is 1 eV, yielding binding energies of  $\text{Fe}_i\text{V}$  and  $\text{Fe}_s$  relative to isolated  $\text{Fe}_i$  plus an isolated vacancy of 2 and 3 eV respectively, which is in good agreement with theoretical values and EPR observations. From the latter, it was proposed that the interstitial position is favoured over the substitutional one for iron-group TM elements in Si. Therefore, this study focuses deeply on  $\text{Fe}_i$  in Si rather than  $\text{Fe}_s$  in most calculations. The next chapter investigates interstitial iron as a pair in Si.

# Interstitial Fe-pairs in Bulk Silicon

“The best preparation for good work tomorrow is to do good work today.”

Elbert Hubbard

Iron is a common deleterious transition metal contaminant in multicrystalline silicon solar cell material. Although most attention to date has focused upon mobile interstitial Fe, it is shown in this chapter that the formation of pairs is energetically favourable. Of particular note is the magnetic order predicted for pairs as a function of inter-nuclear distance. Also, the third-neighbour pair is the most favourable form but is predicted to exist in antiferromagnetic form, bound relative to isolated interstitials by 0.3 eV. It will also be shown that the pair has a lower migration energy relative to individual interstitial Fe, suggesting that Fe diffusion and gettering at extended defects may proceed via a more complex route than previously suggested. The details of the approach to Fe-pairs adopted in AIMPRO are discussed in this chapter, where the layout is organised as follows. Firstly, section 6.1 covers the background theory of iron pair-related centres. Then, the computational method used for this specific study is outlined in section 6.2. The results of first-principle calculations of iron pair-formation with respect to individual iron as a reference are given in section 6.3. Section 6.4 then summarises the main conclusions of the formation of interstitial iron pairs in bulk Si which is exothermic. Note that the analysis of interstitial iron and its pair-formation in bulk Si has been published elsewhere [129].

## 6.1 Introduction

As mentioned in chapters 1 and 5, iron is a common and unavoidable contaminant in Si [53,54]. It introduces deep levels in the band gap, reducing the minority carrier lifetime

and, because it diffuses very rapidly and acts as a recombination centre, it thus lowers device efficiency even at concentrations of  $<1$  ppb [57].

Currently it is understood that a significant fraction of Fe impurities do not precipitate during growth, but rather form a supersaturation in the highly mobile interstitial point-defect form,  $\text{Fe}_i$  [54], residing at the tetrahedral interstitial site where it behaves as a deep donor [166]. When positively charged ( $\text{Fe}_i^+$ ) it has an effective spin of  $S = 3/2$ , although it is expected to be neutral ( $\text{Fe}_i^0$ ) in intrinsic and n-type Si, with an effective spin of  $S = 1$  [56]. It is worth noting that the distributed interstitial form occurs even in the slowly cooled directional solidification growth technique [54]. The basic behaviour of individual  $\text{Fe}_i$  in bulk Si has been reviewed in the previous chapter (section 5.3), while the behaviour of interstitial iron as pairs in Si is the focus of this chapter.

EPR [137] suggests the formation of small iron-clusters in electron-irradiated iron-doped samples, possibly in complexes of iron with vacancies,  $V$ . Some EPR centres are thought [137, 154] to contain two iron atoms, such as in  $\text{Fe}_i\text{-Fe}_i$ ,  $\text{Fe}_i\text{-Fe}_iV$  and  $\text{Fe}_i\text{-Fe}_iV_2$ . Of particular interest is the proposal that the monoclinic-I NL24 EPR centre consists of two  $\text{Fe}_i$  separated by an Si-Si bond [154]. This complex can also be observed in quenched non-irradiated samples [137], indicating that the complex does not contain irradiation-induced components. Extracting specific parameters, such as effective-spin, zero-field splitting and hyperfine tensors, has proved problematic [154], but NL24 is probably  $S = 5/2$ , and positively charged. It disappears after storage at room temperature for 12 hours, or after annealing at  $75^\circ\text{C}$  for 1 hour [154], indicating that there is a binding of iron-pairs, assuming that the assignment is correct, but it is unclear whether they dissociate or migrate to a sink as a unit.

Previous atomistic simulations [147] of interstitial-iron pairs approximately at nearest-neighbour T-sites separated by  $2.47 \text{ \AA}$  have suggested that the neutral charge state is not bound. The reaction, however, between  $\text{Fe}_i^+$  and  $\text{Fe}_i^0$  was found to form a pair, bound by  $0.34 \text{ eV}$ . However, it is unclear the extent to which alternative  $\text{Fe}_i\text{-Fe}_i$  structures were analysed, and in particular there is no indication regarding the properties of the structure proposed for NL24.

Data in this chapter presented that the formation of  $\text{Fe}_i\text{-Fe}_i$  pairs in bulk Si driven by magnetic interactions are strongly dependent upon inter-nuclear distances.

Since a movement of an interstitial impurity, in general, involves a considerable distortion of the host lattice, in particular when the interstitial atom is smaller than the atoms on the normal lattice positions, the probabilities of iron diffusion are included in

this chapter also. It is shown in section 6.3.4 that the migration energy ( $E^m$ ) of  $\text{Fe}_i\text{-Fe}_i$  is significantly lower than that of  $\text{Fe}_i$ , so that the aggregation of mobile  $\text{Fe}_i$  centres into pairs will lead to the more rapid transport of Fe within silicon, which may also relate to the experimentally observed activation energy [167].

## 6.2 Computational Method

In the present work, the same computational approach has been used as in chapter 5 and described in chapters 2 and 3.

As mentioned in chapter 5, the charge density for spin-averaged ( $S = 0$ ) calculations is initialized by a superposition of spinless atomic charge densities. Spin-polarized anti-ferromagnetically coupled pairs of otherwise identical atoms are initialized with equal magnitude and opposite sign of spin-densities so that the integral of the spin-density over the system is zero. It is found that, for  $\text{Fe}_i$  centres in Si, the self-consistent charge density obtained requires careful consideration of the spin-density initialisation. By varying the cell size, the convergence of iron-pair properties has been evaluated, and in particular the energies, while allowing direct comparison with values in the literature. Generally, 216-atom, simple-cubic supercells of side length  $3a_0$  are used to ensure that the iron pair atoms are closer to one another than in any of the periodic images. However, the calculations of 512-atom are also included in this work so as to present accurate results. The formation energy,  $E^f(X, q)$ , of a defect with respect to the atomic and electron chemical potentials is obtained using equation 3.2.

The minimum energy path for diffusion processes is obtained using climbing nudged elastic bands [106, 107] as described in section 3.6.2, where nine images have been used. The barrier is optimised so that the image-forces are less than 0.01 atomic units and the saddle-point energy changes by less than 1 meV. The binding energy ( $E^b$ ) for a defect pair is  $2E^f(\text{single}) - E^f(\text{pair})$ , so that a negative value represents a bound pair.

The bond-strain calculations of Fe-pair in different neighbouring sites have been determined based on the flowchart shown in chapter 5 (Figure 5.4). For these calculations, the equilibrium atomic coordination of optimised single  $\text{Fe}_i$  in bulk and iron silicide ( $\beta\text{-FeSi}_2$ ), as well as the original values of the ideal Si structures, are used to study the impact of the presence of Fe-pair contamination on the neighbours.

## 6.3 Results and Discussion

### 6.3.1 Modelling of interstitial-iron pairs

The agreement with values in the literature regarding individual  $\text{Fe}_i$  (section 5.3) provides the basis for using this approach to determine the properties of interstitial iron pairs.

Pairs of  $\text{Fe}_i$  centres may be categorized either by the number of “[111] $a_0/4$ ” steps, or by the straight-line distance between the two T-sites prior to any optimization (Table 6.1), and supported by illustrating the possible neighbouring interstitial sites for the first Fe at the T-site in the Si lattice (Figure 6.1).

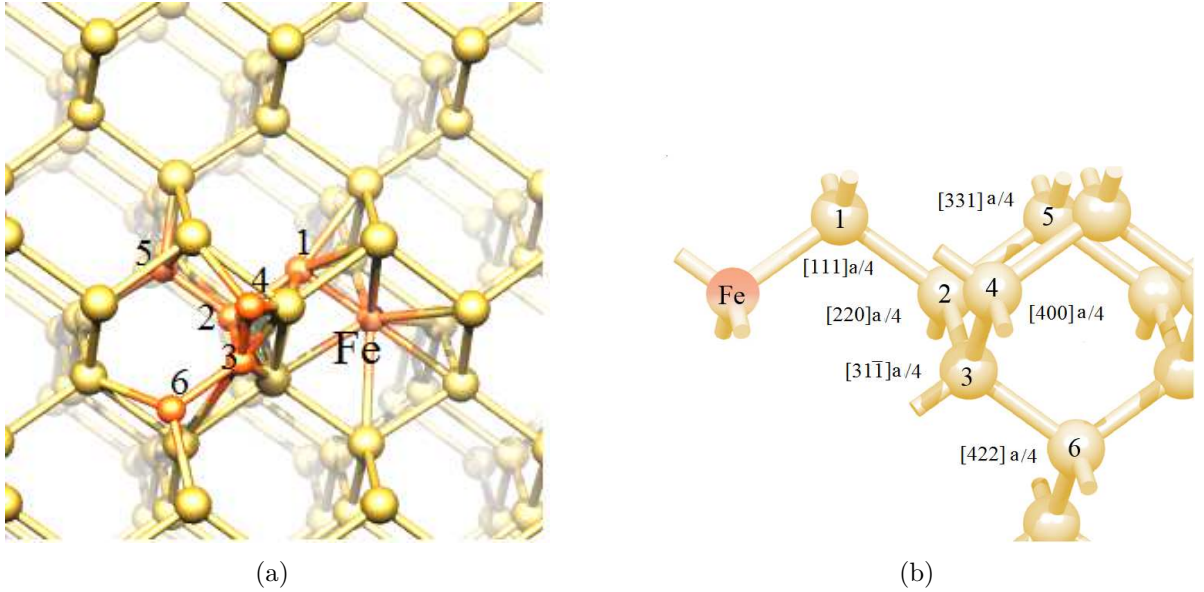


Figure 6.1: Schematics showing: a) prototypical interstitial sites (1NN–6NN) for the second interstitial iron with respect to the first one at T-site; b) another view of the nearest-neighbour separating the two sites of the interstitial iron with displacement vector in unit ( $a_0/4$ ) along with table 6.1.

Table 6.1: List of ideal sites of pairs of  $\text{Fe}_i$  defects in order of increasing inter-site distance. In each case  $\vec{d}$  indicates the displacement vector between one Fe site and the second, in units of  $a_0/4$ .  $n$  is the number of nearest-neighbour T–T steps separating the two sites.

nNN	$\vec{d}$	$ \vec{d} $	$n$	Symmetry
1NN	[111]	$\sqrt{3} \sim 1.732$	1	$D_{3d}$ (Trigonal)
2NN	[220]	$2\sqrt{2} \sim 2.828$	2	$C_{2v}$ (Orthorhombic)
3NN	[311]	$\sqrt{11} \sim 3.317$	3	$C_{2h}$ (Monoclinic)
4NN	[400]	4	4	$D_{2d}$ (Tetragonal)
5NN	[331]	$\sqrt{19} \sim 4.359$	3	$C_{2h}$ (Monoclinic)
6NN	[422]	$2\sqrt{6} \sim 4.899$	4	$C_1$ (Triclinic)

It is important to keep in mind the nature of the isolated interstitial, especially in respect to the electronic-spin states that the defect adopts in different charges. When

bringing two  $\text{Fe}_i$ -centres together, there are two limiting likely possibilities. Firstly, the electronic states associated with the  $3d$  components of the Fe-atoms might remain relatively unperturbed, so that in the pairs the effective spin is made up from the sum of the spins of the two components. Then, for example, in the neutral charge state where  $\text{Fe}_i$  adopts a spin state of  $S = \pm 1$ , the pair is expected to have a ground state spin of  $S = 0$  in an anti-ferromagnetic case, or  $S = 2$  in a ferromagnetic combination. The other possibility is that the two  $\text{Fe}_i$  centres interact strongly in terms of the orbitals, so that the gap states are made up from combinations of the  $3d$ -orbitals on the two sites and the effective spin of the pair is the result of the nature of these combinations. Either way, what happens in practice is expected to be a function of inter-nuclear separation.

For  $\text{Fe}_i$ - $\text{Fe}_i$ , the properties have been examined as a function of the distance between initial T-sites at which the Fe atoms are located. Relative to one T-site, the first six non-equivalent T-sites at increasing distances lie at  $[111]a_0/4$ ,  $[110]a_0/2$ ,  $[3\bar{1}\bar{1}]a_0/4$ ,  $[100]a_0$ ,  $[331]a_0/4$ , and  $[4\bar{2}\bar{2}]a_0/4$ , where  $a$  is the host lattice constant. The notation  $n\text{NN}$  is adopted for the  $n^{\text{th}}$  most distant pair.

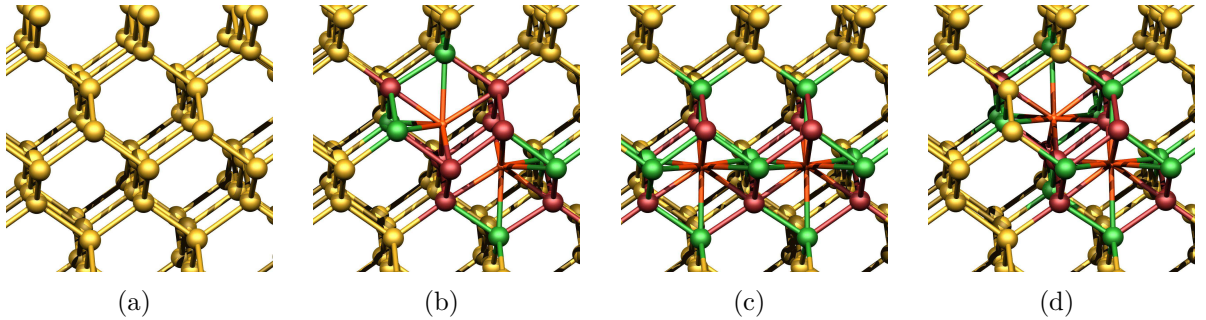


Figure 6.2: Illustrations of iron pair defects at distances  $n\text{NN}$  in Si,  $n = 1-3$ : (a) a section of pure silicon; with (b) the first; (c) second; and (d) third nearest neighbours. Yellow and orange spheres represent Si and Fe, respectively. The horizontal and vertical axes are  $[110]$  and  $[001]$ , respectively, with the slightly tilted view chosen to aid clarity. Si sites in the first two co-ordination shells of each Fe atom are highlighted, with green sites being the six sites along octahedral directions, and red sites those along tetrahedral directions.

### 6.3.1.1 $\text{Fe}_i$ - $\text{Fe}_i$ at nearest neighbour (1NN)

It is instructive to begin with  $\text{Fe}_i$ - $\text{Fe}_i$  at 1NN (Figure 6.2(b)), since this is the form for which detailed quantum-chemical results have been reported [147]. The previously published data suggested that there is no pair formation when the two iron pairs involved have the same charge state, while the reaction between the neutral ( $S = 1$ ) and positive charge state ( $S = 3/2$ ) lead to the formation of a pair with  $S = 5/2$  with the energy

obtained 0.34 eV. This spin state ( $S = 5/2$ ) for the positively charged pair is stable and lower than  $S = 1/2$  and  $S = 3/2$  by 0.42 and 0.73 eV respectively. In the +1 charge state, the inter-Fe distance was reported to be 2.47 Å for the  $S = 5/2$  state. This pair (positive  $S = 5/2$ ) is consistent with the NL24 EPR centre [63,150,151,168] regarding spin and the low stability. Low binding energy (0.06 eV) was also obtained, and the pair has a donor at 0.44 eV above the VB edge. However, whether or not the previous calculations [147] resolved the experimental monoclinic-I symmetry [154] is not stated (3NN intrinsically has this symmetry). For 1NN, having monoclinic-I symmetry would require a geometric distortion from the trigonal symmetry that on-site  $\text{Fe}_i$  centres generate. Firstly, the results of this study are presented where, as far as is possible, the same parameters are used as described in the previous study [147]. These parameters include details of the host crystal, where 64 host-atoms periodic supercells were used, with MP2 mesh used to sample the BZ, and the geometries of the defects were optimized with GGA. The gap levels were obtained [147] with the marker method, and the ionizations energies and the resulting electron affinities that resulted in that study [147] were scaled to a marker which has been taken to be the perfect crystal. Furthermore, the same scaling was used to calculate the donor and acceptor levels of the defect. Similar results have been obtained in this work with the same parameters [147] regarding the stability of structures for the neutral and positive charge states, as well as regarding the reaction energy relative to  $\text{Fe}_i^+(S = 3/2)$  and  $\text{Fe}_i^0 (S = 1)$  which was 0.34 eV. The distance between the Fe-sites is 2.36 Å. Using the same parameters as previously [147], binding energies calculated for the

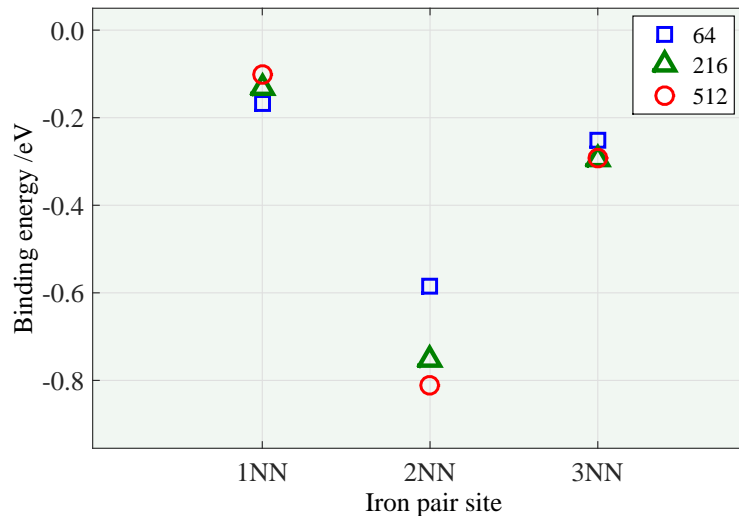


Figure 6.3: Binding energy of iron pair with the spin-average as a function of inter-nuclear separation, including first, second and third nearest neighbours (Figure 6.2) with different cell size. These calculation are achieved to compare with another study [147] in terms of the binding energy value for the pair at 1NN in a 64 host-atoms periodic supercell.

latter combinations are 0.21 and 0.03 eV for  $S_0$  and  $S_2$ , respectively (see figure 6.8).

In contrast, if the spin density is initialised such that at the beginning of the self-consistency process there is an effective spin of 1 on one Fe atom and  $-1$  on the second, a lower final energy is found. Indeed, this is the lowest energy arrangement of the nearest-neighbour pair, lying 0.37 eV lower in energy than the non-magnetic spin-singlet configuration, and 0.17 eV lower than the ferromagnetically coupled pair ( $S = 2$ ). Now, in this study, to converge the results regarding MP and the exchange-correlation, it is found that there is almost no significant difference when the  $k$ -point sampling is increased from 2 to 3. The calculated reaction energy, in this study, relative to  $\text{Fe}_i^+(S = 3/2)$  and  $\text{Fe}_i^0 (S = 1)$  using MP3 is 0.33 eV. The relative accurate energies of the spin states for the neutral and positive charge states are provided in table 6.2. The  $\text{Fe}_i$ -pair at 1NN is bound in both the neutral and positive charge states with  $S = 0$  and  $S = 5/2$  ground states respectively, but that the ground state of the neutral charge state is effectively that of an antiferromagnetically coupled pair of spin triplets.

Since  $\text{Fe}_i$  is understood to be a single donor (see section 5.3.1.3), as it creates a donor level at  $E_v + 0.15$  eV, it is possible that the pairs will act as double-donors, and with this in mind the properties of the  $+2$  charge state have been also determined and the double-donors of iron pair have been calculated from the formation energies as a function of electron chemical potential ( $\mu_e$ ), as plotted in figure 6.4-a. In support of this, based upon the electronic structure (Figure 6.4-b) of the 1NN neutral system, one might expect that the  $\text{Fe}_i$  pair can be ionised with different charge states. As seen from the plot, it is clear that the pair behaves as a donor defect with a  $+2$  charge state being stable at the valence band top. The donor levels located for 1NN lie at  $E_v + 0.07$  eV and  $E_v + 0.1$  eV. Although the precise location of the donor levels is uncertain, the estimates made here indicate that iron pairs tend to lead to n-type material.

### 6.3.1.2 $\text{Fe}_i$ - $\text{Fe}_i$ at second neighbour (2NN)

A second form of  $\text{Fe}_i$ - $\text{Fe}_i$  places them at second-neighbour T-sites, 2NN, which in the absence of any relaxation has  $C_{2v}$  symmetry. This structure (shown in figure 6.2(c)) can be viewed as a pair of Fe interstitials with a common Si atom neighbour. Again, this system has been optimised in a range of cell sizes, charges, and spin states, and the resulting relative energies are presented in table 6.2.

The first point of note is that 2NN has a similar energy to that of 1NN, but is slightly

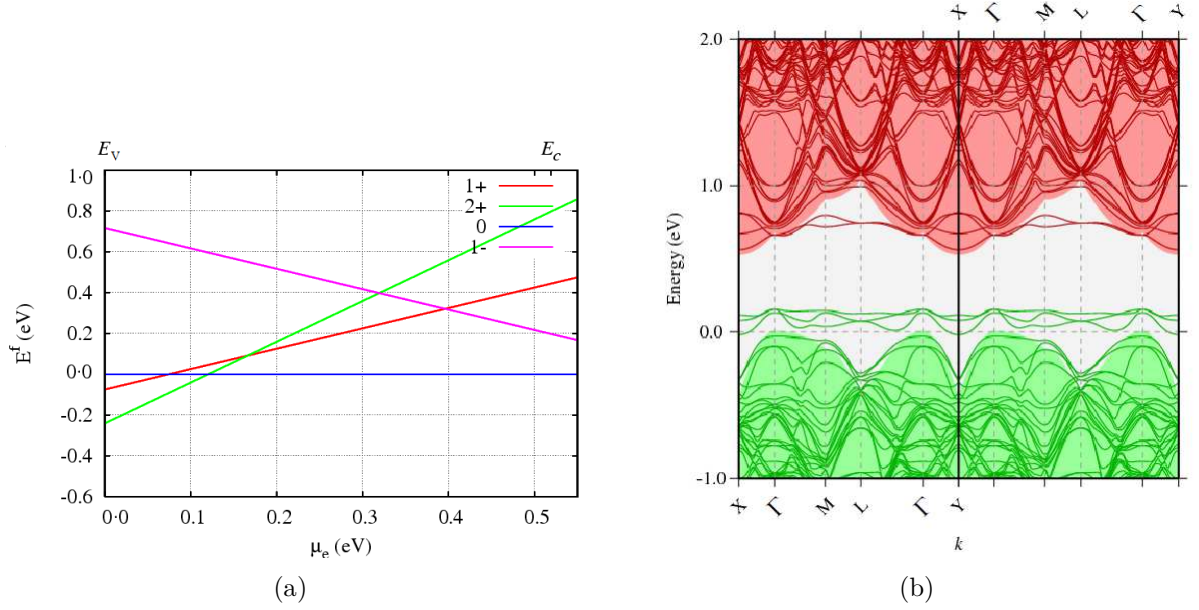


Figure 6.4: Plot showing: (a) the formation  $E^f(q)$  energy for three charge states of Fe pair at 1NN in 216 Si atoms as a function of electron chemical potential ( $\mu_e$ ).  $E^f$  is defined as zero for the neutral charge state. The sign of the slope indicates the sign of the charge state. The donor level is the value of  $\mu_e$  above which the neutral system (0 charge state) is preferred over the + charge state; (b) electronic band structures of  $Fe_i$  pair in neutral state (AFM,  $S=0$ ) for 1NN structure. Occupied and unoccupied states are depicted as solid green and dashed red lines, respectively. The underlying shaded regions show the electronic band structure for the corresponding bulk Si supercell. The energy scale for each system is defined such that the valence band maxima are at zero.

higher. A second point is that, when separated at a slightly larger distance, it is the ferromagnetically coupled pairing that is most favourable in energy, being around 0.1 eV lower in energy than the antiferromagnetically coupled spin singlet form. In the single positive charge state, the  $S = 5/2$  ferromagnetic system is favoured, and again it is more stable than the doublet and quartet by 0.23 and 0.29 eV respectively. For the double positive (+2) charge state, there is a small difference in energy between the spin structures with  $S = 3$  and  $S = 0$ , where the latter is lower. In the negative charge states, a small difference in energy exists between spin 1/2 and 5/2, and both are higher in energy than  $S = 3/2$  by 0.11 and 0.06 eV, respectively. The donor levels for the iron pair at 2NN have been located at about  $E_v+0.2$  eV, as shown in figure 6.5, even including the underestimate of the band-gap (as discussed in chapter 2), and also no acceptor levels can be observed for this structure. Besides this, the plot shows that the iron pair at 2NN can create a deeper donor level than the 1NN structure with several occupied-states associated with the iron pair orbitals. Consequently, Fe-pair at 2NN are bounded by about 0.15 eV for the neutral pair ( $S = 2$ ) and 0.48 eV for the positive state ( $S = 5/2$ ). Comparisons with

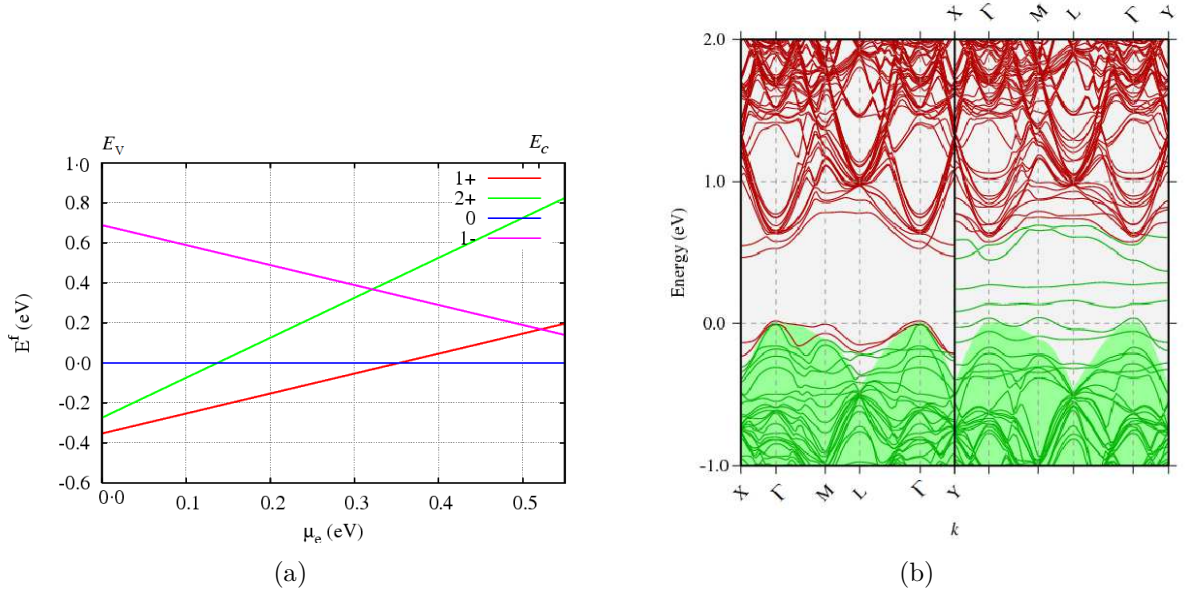


Figure 6.5: Plots showing: (a) the formation  $E^f(q)$  energy for different charge states of the Fe pair at 2NN in 216 Si atoms as a function of electron chemical potential ( $\mu_e$ ).  $E^f$  is defined as zero for the neutral charge state. The sign of the slope indicates the sign of the charge state. The donor level is the value of  $\mu_e$  above which the neutral system (0 charge state) is preferred over the + charge state; (b) electronic band structures of the  $Fe_i$  pair in neutral state (FM, S=2) for 2NN structure. Occupied and unoccupied states are depicted as solid green and dashed red lines respectively. The underlying shaded regions show the electronic band structure for the corresponding bulk Si supercell. The energy scale for each system is defined such that the valence band maxima are at zero.

other spin configurations and other Fe-pair sites are shown in figure 6.8.

### 6.3.1.3 $Fe_i$ – $Fe_i$ at third neighbour (3NN)

The most stable and significant structure is found for the third-neighbour T-site pair shown in figure 6.2(d). This is the model proposed for the NL24 EPR centre [137, 154], and it can be viewed as a pair of Fe interstitials neighbouring a shared Si–Si bond. It is found that in the neutral charge state the antiferromagnetically coupled pair with  $S = 0$  is lowest in energy, and more critically, lower in energy than either of the neutral ground states of 1NN and 2NN. The relative energy of 3NN to 1NN is small, at around 40–50 meV, but is consistent across the cell sizes. In the positive charge state, the 5/2 ferromagnetic system is favoured, and again is more stable than either 1NN or 2NN. In this structure, it is found further that the double positive charge state with  $S = 3$  is higher than  $S = 0$  by 0.1 eV. In contrast, the stable structure in the negative charge state is  $S = 5/2$  lower in energy by 0.12 and 0.20 eV than  $S = 1/2$  and  $S = 3/2$ , respectively. The double-donors of the iron pair have been calculated from the formation energies as a function

of electron chemical potential ( $\mu_e$ ) as plotted in figure 6.6(a). Along with the electronic structure (Figure 6.6(b)) of the neutral system, one might expect that the  $\text{Fe}_i$  pair can be ionised with different charge states. As seen from the plot, it is clear that the pair behaves as a donor defect with a +2 charge state being stable at the valence band top. The donor levels located for 3NN lie at  $E_v+0.4$  eV. The modification of the donor levels as

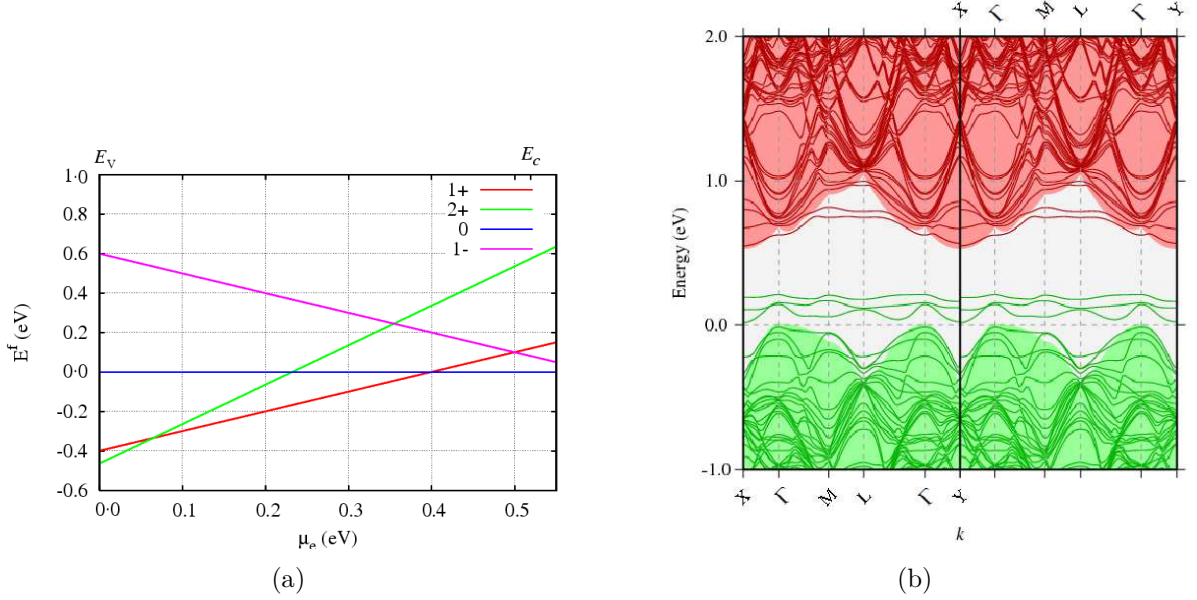


Figure 6.6: Plot showing: (a) the formation  $E^f(q)$  energy for three charge states of the Fe pair at 3NN in 216 Si atoms as a function of electron chemical potential ( $\mu_e$ ).  $E^f$  is defined as zero for the neutral charge state. The sign of the slope indicates the sign of the charge state. The donor level is the value of  $\mu_e$  above which the neutral system (0 charge state) is preferred over the + charge state; (b) electronic band structures of  $\text{Fe}_i$  pair in neutral state (AFM, S=0) for 3NN structure. Occupied and unoccupied states are depicted as solid green and dashed red lines respectively. The underlying shaded regions show the electronic band structure for the corresponding bulk Si supercell. The energy scale for each system is defined such that the valence band maxima are at zero.

a function of separation distance between the pair would have ramifications for electrical conduction in this regions, and these Fe states are generally referred to as carrier traps, recombination centres or generation centres depending on the relative probabilities of the capture and emission of either electrons or holes. In particular, an internal transition between the states can occur around the valence band top, and the empty band around mid-gap. Since this site is more stable than the other sites for both neutral and charged states, it represents the reference for binding and bond-strain calculations that will be presented later in this chapter.

## 6.3.1.4 More distance pairs

$\text{Fe}_i\text{-Fe}_i$  at 2NN and 3NN may be accessed from a starting configuration of 1NN in one and two nearest-neighbour T-site hops, respectively. 2NN and 3NN also represent structures which are most proximal, being at distances of  $\sqrt{2}a_0/2$  and  $\sqrt{11}a_0/4$ , respectively, but there is another structure that may be accessed in two hops. This is the where the displacement of the second Fe site from the first is  $[331]a_0/4$ , which by distance is the fifth nearest-neighbour pair (a distance of  $\sqrt{19}a_0/4$ ). The fourth nearest-neighbour pairing requires three hops to access, as shown in figure 6.1. The calculations shows that the fourth, fifth and sixth neighbour pairs interact more weakly than those in the first three sites. In particular, the differences between ferro- and antiferromagnetically coupled uncharged interstitials is around zero eV for all these three neighbours, and the overall binding energy for all of them is very small as shown in section 6.3.3. In addition to that, these sites are included in the diffusion process calculations (see section 6.3.4). It is concluded that the interaction between nearby  $\text{Fe}_i$  centres is most strongly mediated by the proximity of the Fe atoms, or where they have a common Si neighbour or neighbours. Table 6.3 lists the energy differences associated with 4-, 5- and 6NN models with respect to the 3NN (the most stable structure).

Table 6.2: Energy differences ( $\Delta E$ ) in eV associated with the three  $\text{Fe}_i\text{-Fe}_i$  structures as a function of cell size and spin. These values indicate by how much each of the other structures and spin states are higher than the reference (3NN) model with for the  $S = 0$  AFM-coupled system for the neutral ( $q = 0$ ) and  $S = 5/2$  for single positive ( $q = +1$ ) charge states, respectively.

$n_{sc}$	$\Delta E$ (1NN)				$\Delta E$ (2NN)				$\Delta E$ (3NN)	
	$S = 0$ $q = 0$	$S = 2$ $q = 0$	$S = 5/2$ $q = +1$	$S = 1/2$ $q = +1$	$S = 0$ $q = 0$	$S = 2$ $q = 0$	$S = 5/2$ $q = +1$	$S = 1/2$ $q = +1$	$S = 2$ $q = 0$	$S = 1/2$ $q = +1$
2	0.05	0.23	0.32	0.27	0.22	0.12	0.17	0.36	0.005	0.16
3	0.04	0.16	0.37	0.30	0.24	0.12	0.16	0.40	0.04	0.18
4	0.08	0.16	0.30	0.34	1.08	0.13	0.18	0.42	0.01	0.19

Table 6.3: Energy differences ( $\Delta E$ ) in eV associated with the fourth-sixth  $\text{Fe}_i\text{-Fe}_i$  structures as a function of cell size and spin. These values indicate by how much each of the other structures and spin states are higher than the reference (3NN) model with the  $S = 0$  AFM-coupled system for the neutral ( $q = 0$ ) and  $S = 5/2$  for single positive ( $q = +1$ ) charge states, respectively.

$n_{sc}$	$\Delta E$ (4NN)				$\Delta E$ (5NN)				$\Delta E$ (6NN)			
	$S = 0$ $q = 0$	$S = 2$ $q = 0$	$S = 5/2$ $q = +1$	$S = 1/2$ $q = +1$	$S = 0$ $q = 0$	$S = 2$ $q = 0$	$S = 5/2$ $q = +1$	$S = 1/2$ $q = +1$	$S = 0$ $q = 0$	$S = 2$ $q = 0$	$S = 5/2$ $q = +1$	$S = 1/2$ $q = +1$
2	0.33	0.50	0.64	1.08	0.24	0.25	0.36	0.44	0.19	0.21	0.41	0.45
3	0.29	0.34	0.57	0.53	0.26	0.28	0.40	0.50	0.27	0.26	0.42	0.51
4	0.28	0.39	0.58	0.52	0.26	0.28	0.47	0.49	0.28	0.27	0.43	0.52

### 6.3.2 Bond-Strain deviation

In chapter 5, calculated the bond-strain changes caused by the isolated iron case were listed in table 5.1. Here, the effect of iron pairs with different nuclear distances on the surrounding Si–Si atoms has been presented based on a flowchart (Figure 5.4). The results for bond-strain are compared with those in pure,  $\text{Fe}_i$  and  $\beta\text{-FeSi}_2$  structures to show the effect of the presence of an Fe pair atoms on the surrounding Si atoms. Small and large cell sizes are used to include iron pairs in 1NN, 2NN and 3NN (which are the most important) to ensure the accuracy of the calculations. The bars in figure 6.7 shows the bond shifts of

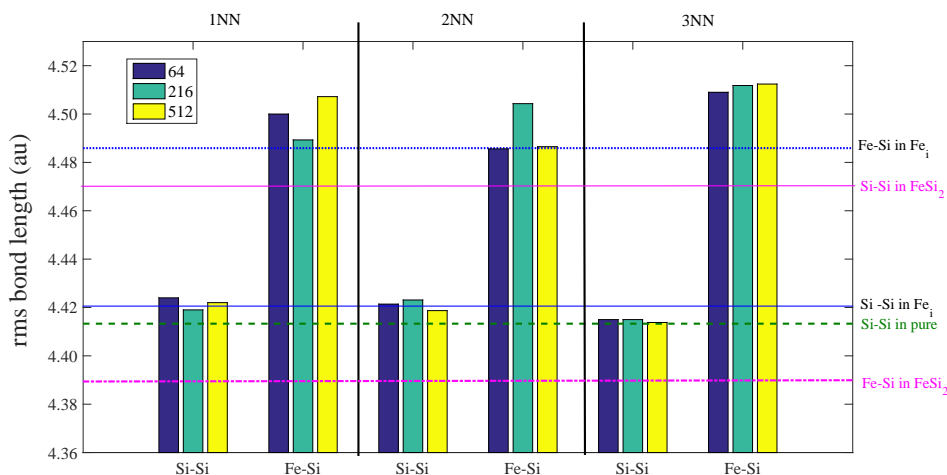


Figure 6.7: Evaluated root mean square bond lengths of Fe-pair, showing the amount of shift Si–Si and Fe–Si bonds than the bond lengths in pure and  $\text{Fe}_i$  structures. This bars are plotted as function of inter nuclear distance (first, second and third-neighbour pair) and cell sizes (64, 216 and 512-Si atom).

the Fe pair-Si, which are further strained compared to Si–Si for all investigated neighbour pair structures, resulting in as much as around 1.7 %, 1.5 % and 2 % for 1NN, 2NN and 3NN, respectively. For comparison, these calculations have been also compared with the structure before the inclusion of the iron atoms. Consequently, values of rms strain caused by the Fe pair-Si and Si–Si are listed in tables 6.4–6.6.

The results that indicate that Fe pair causes strain on the surrounding Si atoms which is more than the strain of Si–Si itself. In addition, it is found that the presence of the Fe-pair at 1NN yields Fe–Si and Si–Si strains higher than if the pair is present at 3NN, which is also more highly strained than the pair at 2NN.

Table 6.4: Si–Si and Si–Fe bond changes due to the formation of interstitial iron pairs at the first, second and third neighbours in bulk Si as a function of cell size. The reference used to calculate the rms strain is Si–Si in bulk Si.

Reference is pure Si (Si–Si=4.41 au)				
$n_{sc}$	Bond	rms strain (%) (1NN)	rms strain (%) (2NN)	rms strain (%) (3NN)
2	Si–Si	0.7	0.5	0.5
	Fe–Si	2.5	1.8	2.5
3	Si–Si	0.4	0.6	0.4
	Fe–Si	2.2	2.6	2.6
4	Si–Si	0.7	0.4	0.4
	Fe–Si	3.1	1.8	2.6

Table 6.5: Si–Si and Si–Fe bond deviations due to the formation of interstitial iron pairs at the first, second and third neighbours in bulk Si as a function of cell size. The reference used to calculate the rms strain is single interstitial iron.

Reference is $Fe_i$ in bulk Si (Si–Si=4.42, Fe–Si=4.49 au)				
$n_{sc}$	Bond	rms strain (%) (1NN)	rms strain (%) (2NN)	rms strain (%) (3NN)
2	Si–Si	0.6	0.4	0.4
	Fe–Si	1.5	1.6	1.3
3	Si–Si	0.4	0.6	0.4
	Fe–Si	1.4	1.6	1.3
4	Si–Si	0.7	0.4	0.5
	Fe–Si	2.3	0.5	1.3

Table 6.6: Si–Si and Si–Fe bond deviations due to the formation of interstitial iron pairs at the first, second and third neighbours in bulk Si as a function of cell size. The reference used to calculate the rms strain is  $\beta$ -FeSi<sub>2</sub>.

Reference is $\beta$ -FeSi <sub>2</sub> (Si–Si=4.76, Fe–Si=4.39 au)				
$n_{sc}$	Bond	rms strain (%) (1NN)	rms strain (%) (2NN)	rms strain (%) (3NN)
2	Si–Si	7.1	7.2	7.3
	Fe–Si	2.9	2.8	3.0
3	Si–Si	7.2	7.1	7.3
	Fe–Si	2.6	2.9	3.0
4	Si–Si	7.2	7.2	7.3
	Fe–Si	3.5	3.2	3.0

### 6.3.3 Binding energy

Previously, it was found [147] that  $Fe_i$ – $Fe_i$  was unbound in the neutral charge state (Figure 6.3). However, the AFM–coupled form of 1NN is found to be bound by around 0.22 eV.  $Fe_i$ – $Fe_i$  at 2NN and 3NN are also bound, the former in a FM form and the latter in an AFM form. The binding energies are modest at 0.14 eV and 0.55 eV, respectively. Binding energies are presented as a function of cell size, spin state and charge in figure 6.8.

For the systems indicated as  $S = 0$ , it is found that an AFM combination is universally favoured over a spin-averaged form (Figure 6.3), and the binding energies shown are based upon these lower energy electronic configurations. It should be noted that there is dependence of binding energy upon cell-size, which indicates clearly that there is more general agreement between the 216 and 512 atom cells than between the 64 and 216 atom cells. It is concluded that, for the case of  $\text{Fe}_i\text{-Fe}_i$ , the 64-atom cell is insufficient to describe the binding energetics.

The binding energies for  $\text{Fe}_i\text{-Fe}_i$  at 4NN, 5NN and 6NN as a function of spin and charge state have also been calculated, and are presented in figure 6.9 where the overall binding energies for these structures are less than 0.2 eV.

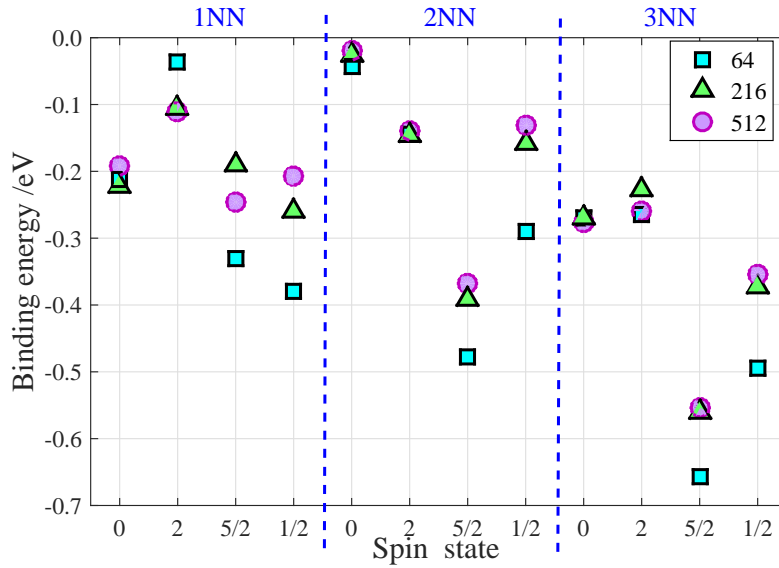


Figure 6.8: Binding energy of iron pairs at the first, second and third nearest neighbour sites as a function of site and charge state. The half-integer spin systems are for a single positive charge state.

### 6.3.4 Iron pair migration pathways

As illustrated in chapter 5 (Figure 5.8), the symmetrical process of  $\text{Fe}_i$  diffusion via the hexagonal site shows good agreement with previous studies [155]. For comparison, the way in which  $\text{Fe}_i\text{-Fe}_i$  might migrate has also been examined in this section. The migration of  $\text{Fe}_i\text{-Fe}_i$  can involve other forms as considered in the following sections.

#### 6.3.4.1 Single hop for $\text{Fe}_i$ at 3NN

There are, of course, two possible mechanisms for the loss of a bound  $\text{Fe}_i\text{-Fe}_i$  pair in an annealing process. The first is dissociation, which would proceed initially by the formation

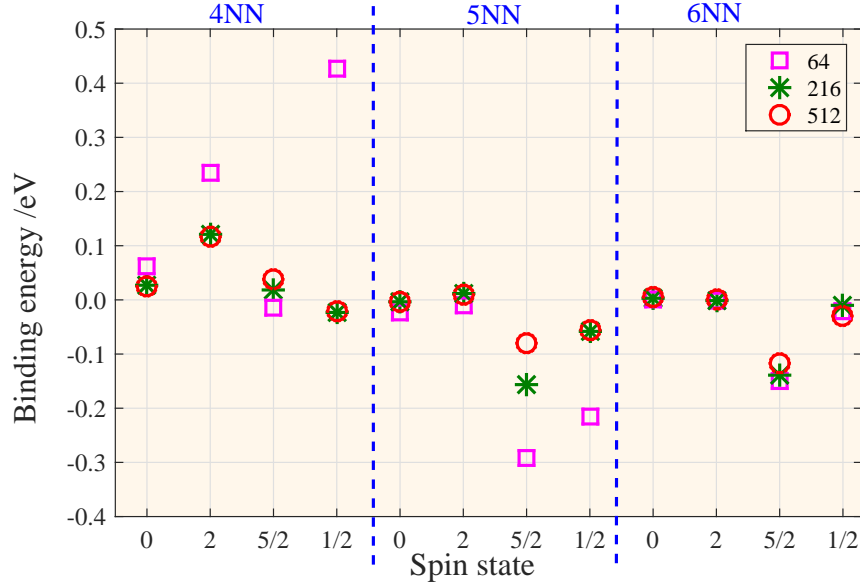


Figure 6.9: Binding energy of iron pairs at 4NN, 5NN and 6NN nearest neighbour sites as a function of site and charge state. The half-integer spin systems are for a single positive charge state.

of a more distant pairing, taking unrelaxed T-sites for simplicity and placing one Fe atom at the origin, in the equilibrium distance and the second Fe atom in 3NN at  $[\frac{3}{4}\frac{1}{4}\frac{1}{4}]_0$ . Without loss of generality, the initial step may be taken in the dissociation process to involve the motion of the second Fe atom to a neighboring T-site. The possible locations after one step are then  $[100]a_0$  (3NN  $\rightarrow$  4NN) and  $[21\bar{1}]a_0/2$  (3NN  $\rightarrow$  6NN), and the only possibility is a step closer to  $[110]a_0/2$  (3NN  $\rightarrow$  2NN). The calculations of the barrier energy for each of these paths are shown in figure 6.10. The results show that the barrier relative to the equilibrium form of the pair in moving from 3NN and 2NN for AFM spin configuration (Figures 6.10(a)) is less than 0.9 eV, which is lower than that of the motion from 3NN to 4NN or 6NN (Figures 6.10(b) and 6.10(c)), respectively. This means that the migration of the pair from 3NN  $\rightarrow$  2NN is more favoured than from 3NN to 4NN or 6NN. These values for AFM spin configurations are also compared with FM and recorded in table 6.7. Calculated values for the barrier energy for these migration pathways show that in most cases the energy for the pair with FM spin configuration is lower than AFM by about 0.2 eV. One might also note that these three diffusion profiles show the same intermediate minimum as that exhibited by a single  $Fe_i$  (Figure 5.8).

The most important outcome is that the diffusion barrier for the pair is lower (in FM) than that of  $Fe_i$  (Table 6.7).

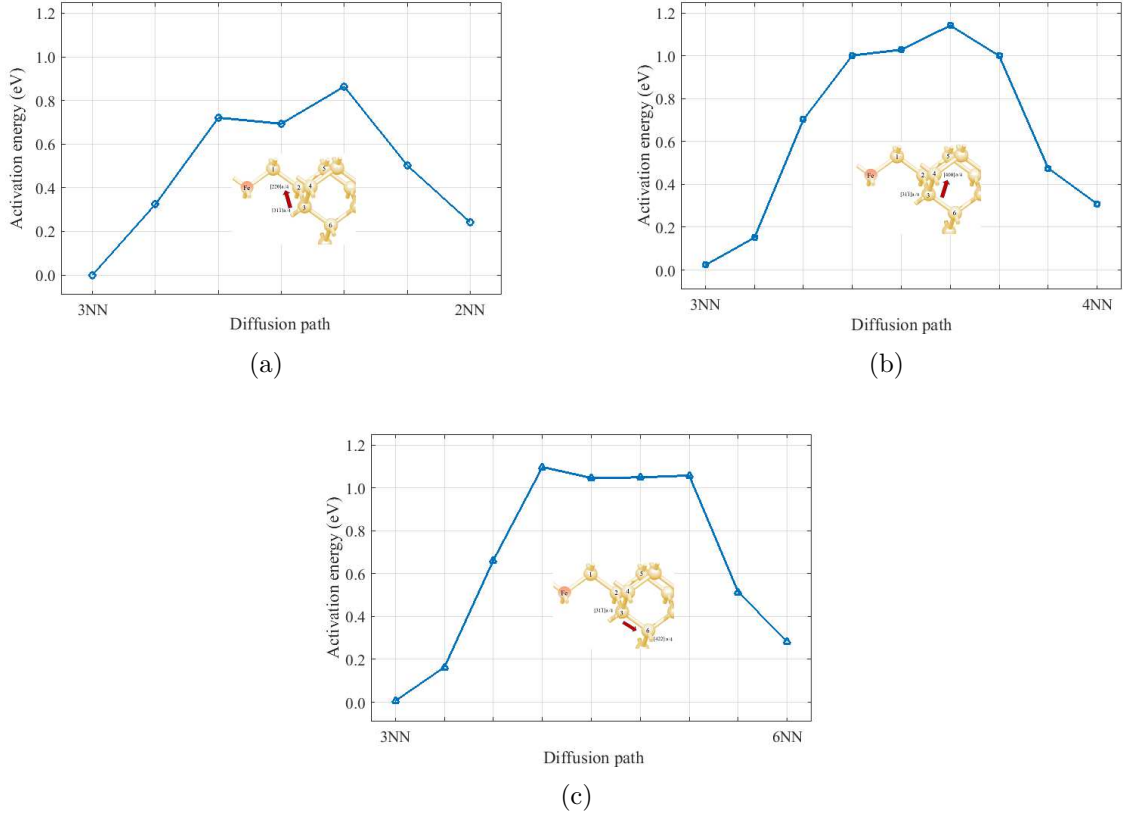


Figure 6.10: Minimum energy paths for anti-ferromagnetic iron pairs along a triangular axis starting from the third (3NN) to: (a) second nearest neighbour site (2NN); (b) fourth nearest neighbour site (4NN); and (c) sixth nearest neighbour site (6NN).

#### 6.3.4.2 Pair hop for $\text{Fe}_i$ at 3NN

The same process as in the previous section 6.3.4.1 can also involve the possible locations after two hops of the second  $\text{Fe}_i$  atom at 3NN. This can include the migration path  $3\text{NN} \rightarrow 2\text{NN} \rightarrow 5\text{NN}$  or  $3\text{NN} \rightarrow 2\text{NN} \rightarrow 1\text{NN}$ . In this process, when  $\text{Fe}_i$  at 3NN moves to 2NN and then towards 5NN, the barrier energy relative to the equilibrium form of the  $\text{Fe}_i\text{Fe}_j$  shows a higher barrier for moving from 2NN to 5NN (about 1 eV) than that needed to transport from site 3NN to 2NN, as shown in figure 6.11. This indicates that the migration of the pair along  $2\text{NN} \rightarrow 3\text{NN}$  is the most energetically favourable process compared to  $2\text{NN} \rightarrow 5\text{NN}$ . Based on the atomic coordination shown in figure 6.1, another possible prototypical site is embedded in the Si lattice where the second Fe can migrate in two hops along  $3\text{NN} \rightarrow 2\text{NN} \rightarrow 1\text{NN}$ . The processes among Fe-pair neighbours for both FM and AFM spin configurations has been shown in figure 6.12. As mentioned above, the energy barriers of the first hop from  $3\text{NN} \rightarrow 2\text{NN}$  are less than 0.9 eV and is 0.7 eV for AFM and FM respectively. In contrast, the diffusion barrier to migrate the iron atom from  $2\text{NN} \rightarrow 1\text{NN}$  exceeds 0.9 eV for the AFM, and is higher than in the case of FM by

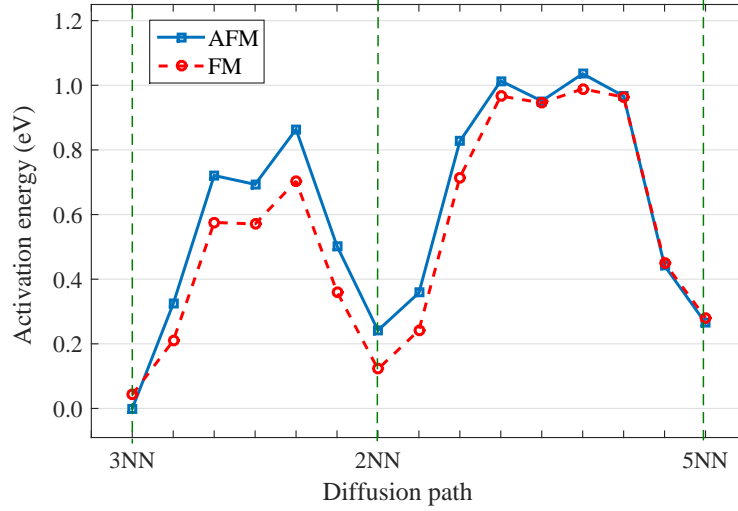


Figure 6.11: Minimum energy paths for anti-ferromagnetic iron pair (blue solid) and ferromagnetic iron pair (dashed red) along a triangular axis starting from the third nearest neighbour site to the second one and then to the fifth one.

about 0.2 eV. Again, the calculated data for the activation energy for each of these two possible migration hops are listed in table 6.7.

It is concluded that, regardless of whether the iron atom in the stable site is moved in a single hop or two hops, the diffusion profiles show the same intermediate minima as exhibited by a single  $\text{Fe}_i$  (Figure 5.8), and in all cases the diffusion barrier for the pair is lower than that of  $\text{Fe}_i$ , suggesting that the pairs may be a key contributor to Fe diffusion and precipitation.

The mechanisms of the possible migration pathways of Fe atom ( $1\text{NN} \rightarrow 2\text{NN} \rightarrow 3\text{NN}$  and  $3\text{NN} \rightarrow 2\text{NN} \rightarrow 5\text{NN}$ ) are illustrated in figures 6.13 and 6.14 respectively, starting from a higher- to lower- energy minimum atomic structure. These diffusion images also include Fe-Fe distances for each diffusion image, showing increasing  $\text{Fe}_i\text{-Fe}_i$  toward the final structure (minimum energy).

Table 6.7: Possible migration pathways for  $\text{Fe}_i$  pair.  $E^a$  is the activation energy in eV, calculated for both AFM and FM spin configurations. The displacement vectors between one Fe site and the second (in unit  $a_0/4$ ) are listed in table 6.1.

Diffusion process	Migration pathway	$E^a$ (AFM)	$E^a$ (FM)
Single hop	$3\text{NN} \rightarrow 2\text{NN}$	0.86	0.70
	$3\text{NN} \rightarrow 4\text{NN}$	1.14	1.11
	$3\text{NN} \rightarrow 6\text{NN}$	1.09	1.07
pair hops	$3\text{NN} \rightarrow 2\text{NN} \rightarrow 5\text{NN}$	1.03	0.98
	$3\text{NN} \rightarrow 2\text{NN} \rightarrow 1\text{NN}$	0.92	0.73

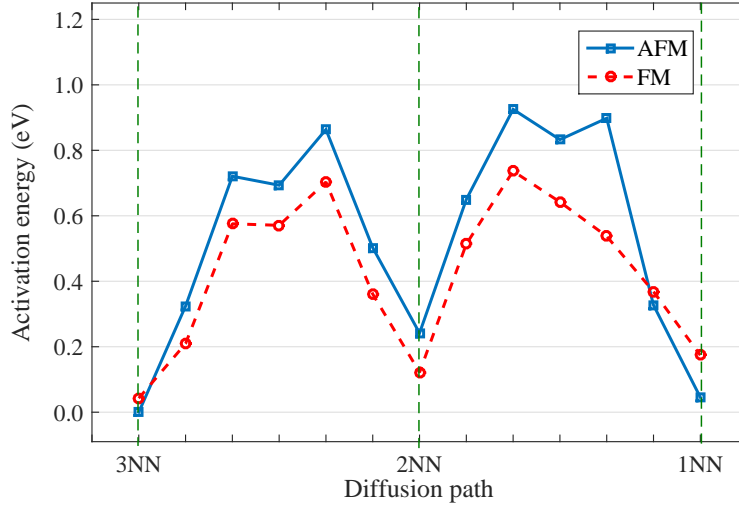


Figure 6.12: Minimum energy paths for anti-ferromagnetic iron pair (blue solid) and ferromagnetic iron pair (dashed red) along a triangular axis starting near a T-site, over the hexagonal site to the second and first T sites.

#### 6.3.4.3 Hopping $\text{Fe}_i$ pair as a unit

The alternative process for the above is one in which the  $\text{Fe}_i$  pair diffuses as a unit, where both Fe interstitials move together, so that at the beginning and end of a diffusion step the Fe-atoms are in an Fe-3-Fe configuration; for example, in the movement of the first  $\text{Fe}_i$  (at the origin) and the second  $\text{Fe}_i$  (at 3NN) together toward (1NN and 4NN), (2NN and 5NN), or (3NN and 6NN) respectively.

However, these calculations are not included in this study as it is found that the fourth, fifth and sixth neighbour pairs interact more weakly than those in the first three sites (see section 6.3.4).

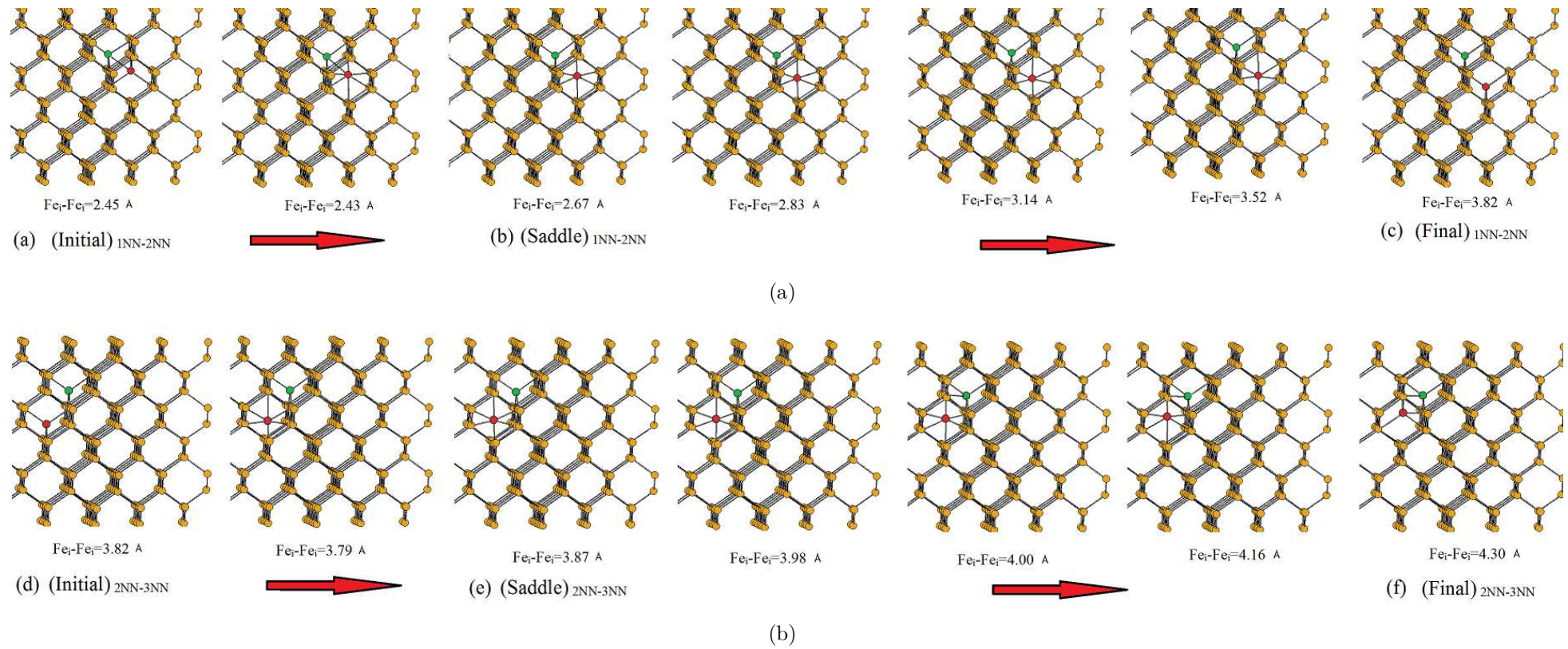


Figure 6.13: Initial, saddle-point, and final configurations for diffusing  $Fe_i$  atom: (a)  $1NN \rightarrow 2NN$ ; and (b)  $2NN \rightarrow 3NN$ . These images include Fe-Fe distances for each diffusion image.

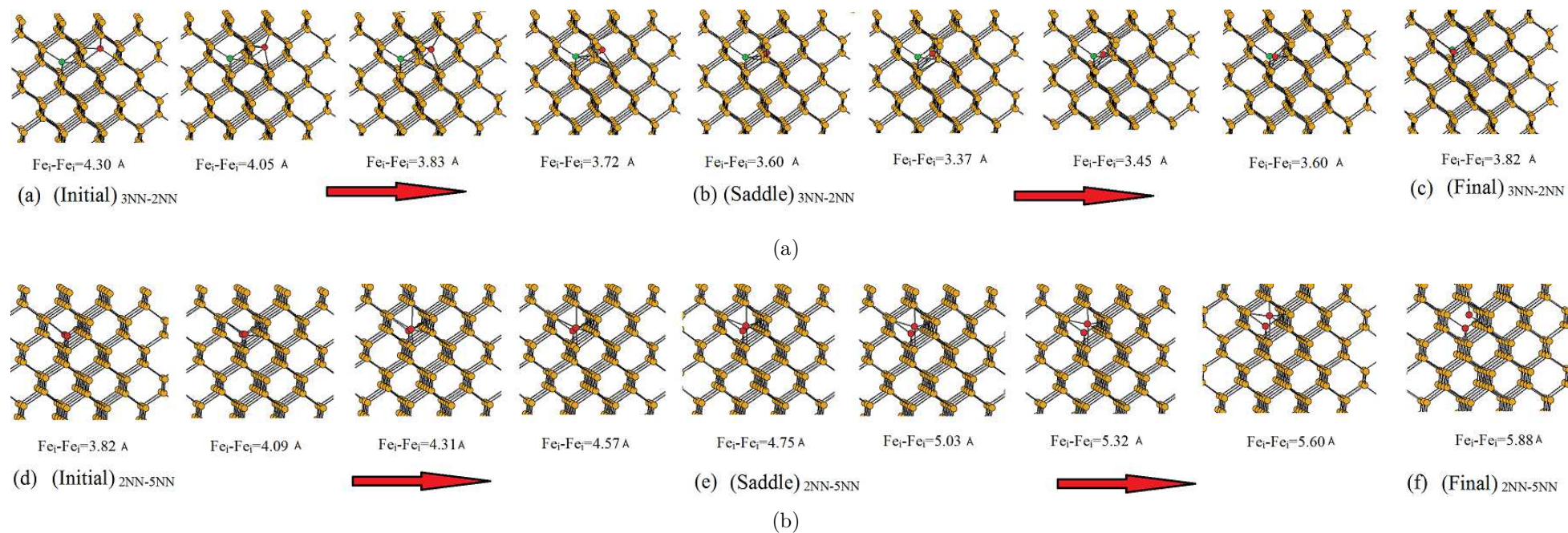


Figure 6.14: Initial, saddle-point, and final configurations for diffusing Fe<sub>i</sub> atom: (a) 3NN  $\rightarrow$  2NN; and (b) 2NN  $\rightarrow$  5NN. These images include Fe-Fe distances for each diffusion image.

## 6.4 Summary

As it is agreed that a significant fraction of Fe impurities do not precipitate during growth, but rather form a supersaturation in the highly mobile interstitial point-defect form, atomistic modelling of  $\text{Fe}_i\text{Fe}_i$  centres in bulk Si has been investigated in this chapter.

Obtained results using DFT show that, in contrast to previous simulations [147], the formation of interstitial iron pairs in bulk Si is energetically favourable. Critically, the parallel or anti-parallel nature of the spins on the two  $\text{Fe}_i$  centres is dependent upon inter-iron distance. The 3NN structure in an antiferromagnetic form is found to be the most stable, bound relative to two isolated Fe-interstitials by about 0.3 eV and 0.6 eV for the neutral and 1+ charge states, respectively.

The 3NN geometry is one of the models proposed for the NL24 EPR centre [154] but, based upon the current simulations, identification with this EPR-centre is problematic. It is predicted that the Fe-pair is bound by around 0.6 eV and is probably more mobile than isolated Fe interstitials, and it is unclear whether or not this is consistent with the loss of NL24 in a long room-temperature anneal [137].

Regardless of the correlation or otherwise of 3NN with NL24, given the lower migration energy of the interstitial Fe pair relative to the single  $\text{Fe}_i$  centre, the role  $\text{Fe}_i\text{Fe}_i$  plays in diffusion, iron-precipitation and segregation to, for example, extended defects, is likely to be of significance. This will be the subject of further investigations in the next chapters.

# Analysis of Iron Segregation at Stacking Faults in mc-Si

“The important thing in science is not so much to obtain new facts as to discover new ways of thinking about them.”

Sir William Bragg (1862—1942)

Removal of the deleterious effects of iron in silicon is critical for the performance of mc-Si solar cells, with internal gettering at extended defects including stacking faults and grain boundaries being one possibility. This chapter introduces the fundamentals of intrinsic stacking faults and reviews studies in the literature that support the hypothesis behind the gettering of iron by ISFs (section 7.1). The first principles DFT method used to study the behaviour of iron at this planar defect are outlined in section 7.2, and prior to the calculation of Fe gettering at the ISF, the structural, electronic and electrical properties of the ISFs themselves have to be validated in section 7.3. The energies and structures of  $\text{Fe}_i$  and  $\text{Fe}_i$  pairs in the vicinity of ISFs have been modelled and presented in section 7.3.4.

Finally, an analysis of iron segregation at ISFs in mc-Si has been published elsewhere [127]. In addition to that, an investigation into efficiency-limiting ISFs in mc-Si solar cells has also been published [128].

## 7.1 Introduction

Silicon does not grow as a perfect crystal under normal growth conditions. mc-Si-based photovoltaic cells have a relatively high concentration of point defects and EDs, and both defect types are understood to act as recombination centres, limiting the operating

efficiency of mc-Si solar cells [48]. Furthermore, EDs themselves are major defects affecting the stability, mechanical behaviour and transport properties of materials [49], and thus the performance of solar energy application devices [50]. Among the EDs (shown in figure 1.15), planar defects are common in mc-Si, especially stacking faults and grain boundaries. Intrinsic stacking faults are the main focus of this chapter, as they represent an example of fully four-fold bonded planar EDs in Si. In addition, studying ISFs decorated by Fe can contribute to the development of a fundamental understanding of the mechanism of any attractive interaction (gettering) between ISFs in mc-Si and diffusing Fe atoms.

Stacking faults are planar defects in the crystal structure [169], formed when the packing order of the atomic planes in the crystal is put out of atomic sequence. This can occur via the removal of a half plane, resulting in ISFs, or by the insertion of an extra half plane forming extrinsic stacking faults. These two kinds of stacking faults are shown in figure 7.1.

As a face-centered cubic crystal, Si has stacking faults lying on one of the  $\{111\}$  planes, which are the planes of the closest packing in the crystal [170]. The packing order of the atomic planes in the crystal is observed [171] using weak-beam electron microscopy. The separations of partial dislocations can be measured and the stacking-fault energies deduced from elasticity theory. The theory and geometry of ISFs have been described well in the literature [173]. It is agreed [173] that the stacking fault structure can be formed without breaking any Si–Si bonds, in spite of the irregular stacking of their crystal planes.

As shown in chapter 1, the Si solar cell is at risk of contamination by TM impurities like Fe, from the crucible or during cell processing. Therefore, it is important to understand the interaction of the impurities with ISFs.

Internal gettering by EDs, including stacking faults, is one possibility to getter Fe in order to improve solar cell efficiency [171], since the stacking faults act as nucleation sites for the main transition metal impurities [174].

## 7.2 Computational Method

A similar computational approach to that presented in both previous results chapters has been adopted in this chapter to model undecorated and Fe-decorated ISFs.

Fundamentally, the structure of the ISF can be determined by removing a pair of (111) atomic layers from the perfect stacking sequence, and moving the exposed faces together

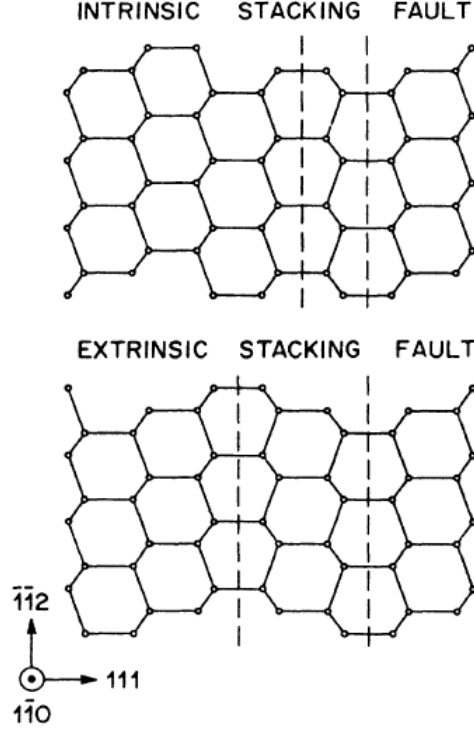


Figure 7.1: Projection of the stacking faults in Si along the  $[1\bar{1}0]$  direction. The long and short lines are represent bonds laying in- and that bonds connecting atoms in neighboring  $(1\bar{1}0)$  planes, respectively. The dashed lines represent twist boundaries that make up the stacking faults. Image taken from [172].

to form a continuous material, with very small bond deviation in the ISF compared to that of pure Si [172] as will be proven in the results section (Table 7.1).

For undecorated ISFs, the minimum cross-section defines the number of atoms per atomic plane. For the  $[111]$ -orientated ISF, the minimum cross-section is represented by  $[1\bar{1}0]a/2$  and  $[10\bar{1}]a/2$ , containing one atom per  $(111)$  plane. In this study, 22  $(111)$  layers, including those in the ISF, have been included in these simulations. When decorating the ISF with Fe, the primitive in-plane cross-section has been repeated, to be  $[3\bar{3}0]a/2$  and  $[30\bar{3}]a/2$  so that there are nine Si atoms per  $(111)$  layer resulting in a supercell containing 198 atoms.

The areal energy density ( $\gamma$ ) of EDs (excess free energy per unit area) has been obtained by calculating the ratio of the formation energy to the area of the periodic unit cell of the a planar defect in a specific plane [72]:

$$\gamma_{\text{ISF}} = \frac{E(\text{ISF}) - E(\text{bulk Si})}{A(\text{ISF})} \quad (7.1)$$

where  $E$  (ISF) is the total energy of the ISF supercell,  $E$  (bulk Si) is the total energy of bulk Si with an equivalent number of atoms (i.e.  $N_{\text{Si}} \mu_{\text{Si}}$ ) where  $N_{\text{Si}}$  is the number of Si

atoms,  $\mu_{\text{Si}}$  is the chemical potential of silicon (i.e. the total energy of a Si atom in the equilibrium diamond structure), and  $A$  (ISF) is the interface area of the ISF.

Beside this, the structure and  $\gamma_{\text{ISF}}$  have been obtained previously [173, 175] with relevant experiments [171, 176], showing a good agreement with the value calculated in this study (see section 7.3). The formation energy can be given as a function of the total energy of a super-cell containing a planar defect and the total energy of bulk Si with an equivalent number of Si atoms.

The lattice parameter normal to the boundary-plane has been varied to minimise the total energy, and the in-plane vectors fixed to the lengths determined for bulk silicon.

A similar strategy to that shown in figure 5.4 has been used for bond-strain calculations.

The lattice vector perpendicular to the boundary plane is longer than those in the plane, so the sampling meshes adopted are chosen such that each sampling point represents an approximately cubic section of reciprocal space. In the ISF containing Fe, the sampling chosen is a Monkhorst-Pack mesh of  $4 \times 4 \times 2$ , with the third value representing the sampling mesh in the long lattice vector directions. The calculations have also been checked for convergence, and the energies are converged to about 2 meV.

The binding energy of interstitial Fe to the ISF is obtained as an energy difference between sites within the defect and those in bulk regions of the supercells. For bulk regions, it is critical to establish the impact of the ISF on the  $\text{Fe}_i$  sites, and this has been achieved by comparing the geometric, electronic and electrical properties of iron in these sites to the properties determined in the large bulk supercell.

## 7.3 Results and Discussion

### 7.3.1 Undecorated intrinsic stacking faults

#### 7.3.1.1 Modelling ISF

The structure of the ISF is shown in figure 7.2. The labels (a–e) indicate non-equivalent sites relative to the boundary plane. The strain is very low, with all Si atoms being close to tetrahedrally co-ordinated, even in the stacking layers. This agrees with previous observations [177].

As mentioned in section 7.2, the accuracy of the ISF model can be evaluated further from the value of  $\gamma_{\text{ISF}}$  calculated using equation 7.1 as  $40 \text{ mJ/m}^2$ , comparing well with the

theoretical value (26–40 mJ/m<sup>2</sup> [173]) and the experimental result of 44 mJ/m<sup>2</sup> [178].

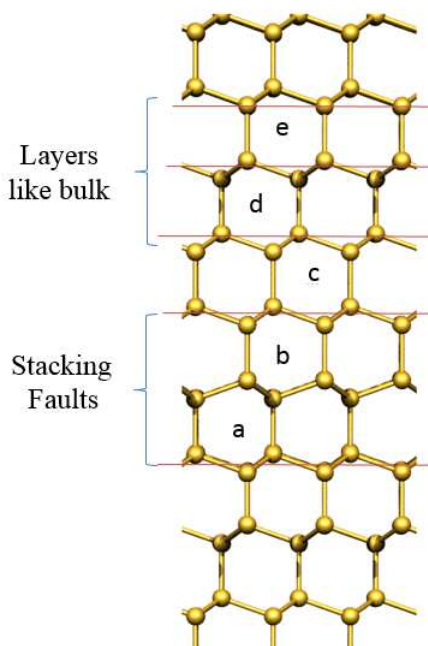


Figure 7.2: Projection of optimised structures of the ISF. Labels a|e indicate the non-equivalent interstitial sites investigated.

### 7.3.1.2 Electronic and electrical properties

The Kohn-Sham band-structure of the ISF (Figure 7.3) shows an absence of any bands deep in the gap, in good agreement with another previous study which included a 196- and 1936-atom cell relaxed with the same valence force field [179]. It is found that the bandgap for the ISF is very slightly smaller than that of bulk silicon. In addition, this difference has an impact on solar cell performance, as shown later in chapter 10.

## 7.3.2 Fe-ISF complexes

Based on the investigations of the interstitial iron and its pair in bulk Si (chapters 5 and 6), it is concluded that  $\text{Fe}_i\text{Fe}_i$  has a lower migration energy relative to  $\text{Fe}_i$ , which means that interstitial iron pair can diffuse faster than individual interstitial iron in Si. The positive outcomes obtained for  $\text{Fe}_i$  and  $\text{Fe}_i\text{Fe}_i$  in bulk Si provide the basis for the extension of the study to the more complex problem of Fe attached to EDs. In particular, the analysis for these calculations and the ISFs separately can improve the accuracy of the current methodology so as to be a sufficient basis upon which to present the results for the Fe-ISF interaction, where the interstitial Fe has been introduced at a range of non-equivalent

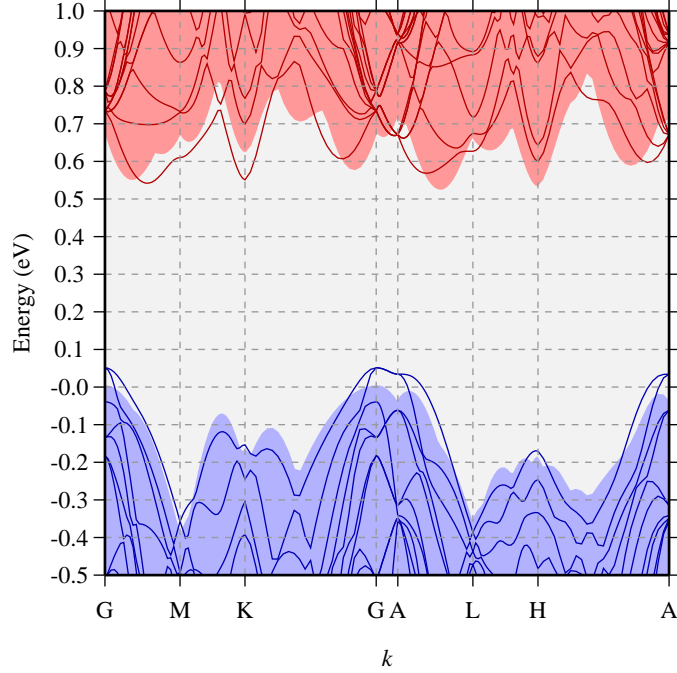


Figure 7.3: Electronic band structures of purely ISF, plotted along high-symmetry branches in the first BZ. Occupied and unoccupied states are depicted as solid blue and dashed red lines, respectively. The underlying shaded regions show the electronic band structure for the corresponding bulk Si supercell (198 atoms). The energy scale for the bulk structure is defined such that valence band top is at zero.

sites as indicated by the labelling in figure 7.2. At each site, the structures have been optimised for different charge and spin states.

### 7.3.2.1 Role of spin and charge states

A novel aspect of this study is the extent of the investigation of the role of spin ( $S$ ) and charge states ( $q = 0, +$  and  $-$ ) of  $\text{Fe}_i$  in ISFs. For the sites within the ISF (sites a and b in figure 7.2), it is found that the  $S = 0$  and  $S = 2$  configurations of  $\text{Fe}_i^0$  are 0.08 and 0.68 eV higher respectively than  $S = 1$ . Notably, this suggests that the  $S = 0$  is stabilised relative to the triplet ground-state in comparison to  $\text{Fe}_i$  in bulk silicon (section 5.3.1.2), where the ground state is a spin triplet, with the singlet and quintet energies determined to be 0.5 and 0.6 eV higher respectively, which is in good agreement with previous calculations [56]. At site d in the ISF cell,  $S = 0$  and  $S = 2$  are 0.45 and 0.56 eV above the ground state, which matches reasonably well the results obtained from the bulk silicon simulations, confirming additionally the environment of site d which can be considered as being relatively unperturbed by the ISF. Similarly, for  $\text{Fe}_i^+$ , within the

ISF, the energy difference between the doublet ground state and the quartet excited state is reduced to 0.02 eV compared to 0.15 eV in bulk silicon and 0.11 eV at site d. Moreover, the theoretical negative charge state has been examined and, as with the positive charge states, there are  $S = 1/2$  and  $S = 3/2$  configurations. The spin half is favoured by 0.24 eV, whereas in the bulk region (site d), the doublet and quartet are effectively degenerated with an energy difference of just 0.03 eV. The change in the relative energies of the different spin states is most likely a consequence of the increased volume associated with the cage site in the ISF, and the additional splitting of the  $d$ -orbitals of the iron due to the local reduction in symmetry (effectively an additional local crystal field splitting). The different energies associated with sites along the ISF structure as a function of spin and charge states are shown in figure 7.4. These values indicate how much each of the other spin states are higher than the references ( $S = 1$ ,  $S = 1/2$  and  $S = 3/2$ ) for neutral, single positive and negative charge states respectively.

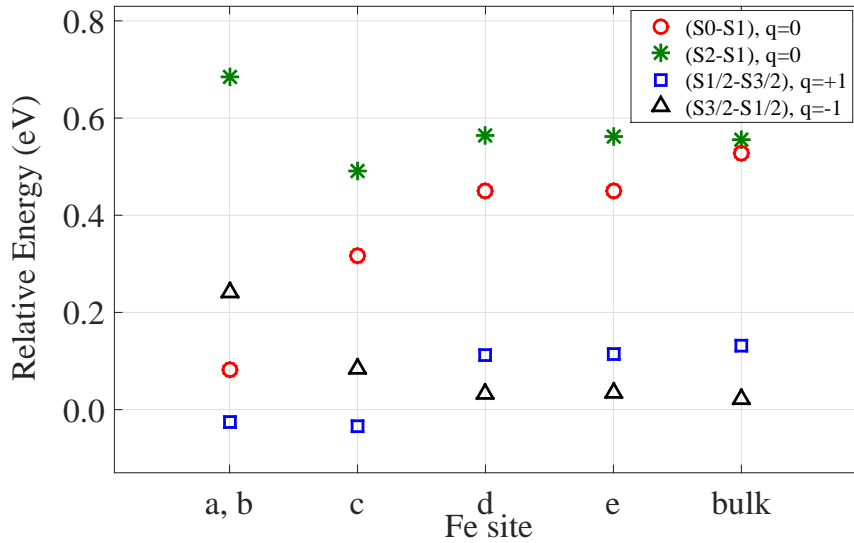


Figure 7.4: Relative energies for different spin configurations in neutral ( $q = 0$ ), positive ( $q = +$ ) and negative ( $q = -$ ) charge states examined for the sites in the ISF illustrated in figure 7.2. These values indicate how much each of the other spin states are higher than the references ( $S = 1$ ,  $S = 1/2$  and  $S = -3/2$ ) for neutral, single positive and negative charge states respectively.

### 7.3.2.2 Electronic and electrical properties

The electronic band structure for the equilibrium site (site a, b) of Fe at ISF is shown in figure 7.5, showing the occupied and unoccupied states introduced after segregating Fe as compared with the background shaded area (undecorated ISF). The occupied Fe-related states above the VB maximum are split and bend rapidly into the VB after leaving the

BZ centre. The degeneracy of states is noticed at  $\Gamma$  points of BZ as a result of cell size. The splitting of degeneracy states at about 0.2 eV results from the dispersion caused by the interaction of Fe along the small cell. Furthermore, there is a drop in energy due to the stability of singlet spin energy (i.e. the stability can reflect the raising 2 electrons spin-down level into the Si gap by exchange splitting). Therefore, removing 1 electron from the spin-up region (left) creates a positively doublet spin state, whereas removing one electron from the spin-up region (right) leads the formation of positively quartet spin.

By comparing the bandstructure of  $\text{Fe}_i$  in bulk (or at site d) and at that for the ISF, these states are shifted to higher energy as the Fe atom moves from the bulk to the stacking fault area.

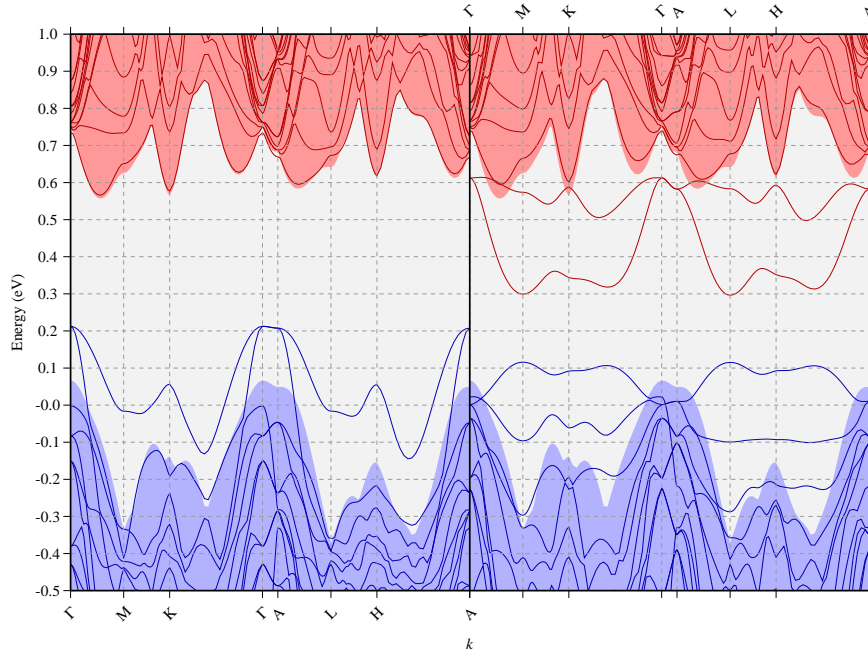


Figure 7.5: Electronic band structures corresponding to the most stable neutral state of Fe at site a and b of ISF structure ( $S = 1$ ), plotted along high-symmetry branches in the first BZ. Occupied and unoccupied states are depicted as solid blue and dashed red lines respectively. The underlying shaded regions show the electronic band structure for the corresponding undecorated ISF modelled in 198 Si-atom.

The ionisation energy of  $\text{Fe}_i$  has also been calculated as a function of position, calculated as the difference in the total energies of the neutral and positive charge states.

The electrical levels of  $\text{Fe}_i$  at the ISF (Figure 7.7 (a and b)) reflect the donor and acceptor levels that are created after segregating Fe at the ISF. The donor level of the ISF is very slightly closer ( $\sim 35$  meV) to the VB top than in bulk silicon, and being deeper within the energy gap outside the ISF, as schematically shown in figure 7.6)). This means

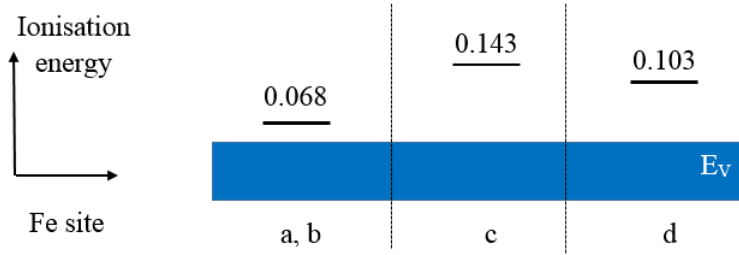


Figure 7.6: Diagram showing the ionisation energy in (eV) as a function of Fe-site in the ISF of figure 7.2.

that segregated Fe at a larger volume of ISF than the bulk can have an effect on the n-type region (i.e. removing one electron from the conduction band). In contrast, figure 7.7(c) shows an Fe-related donor level at site d, which matches reasonably the results obtained from the bulk Si simulations, confirming additionally the environment of site d that can be considered as being relatively unperturbed by the ISF. From this comparison, it is clear that the segregation of Fe at ISFs can alter the electrical properties of the ISF from being electrically inactive to an active region, and thus the ISF can play an important role in solar cell performance.

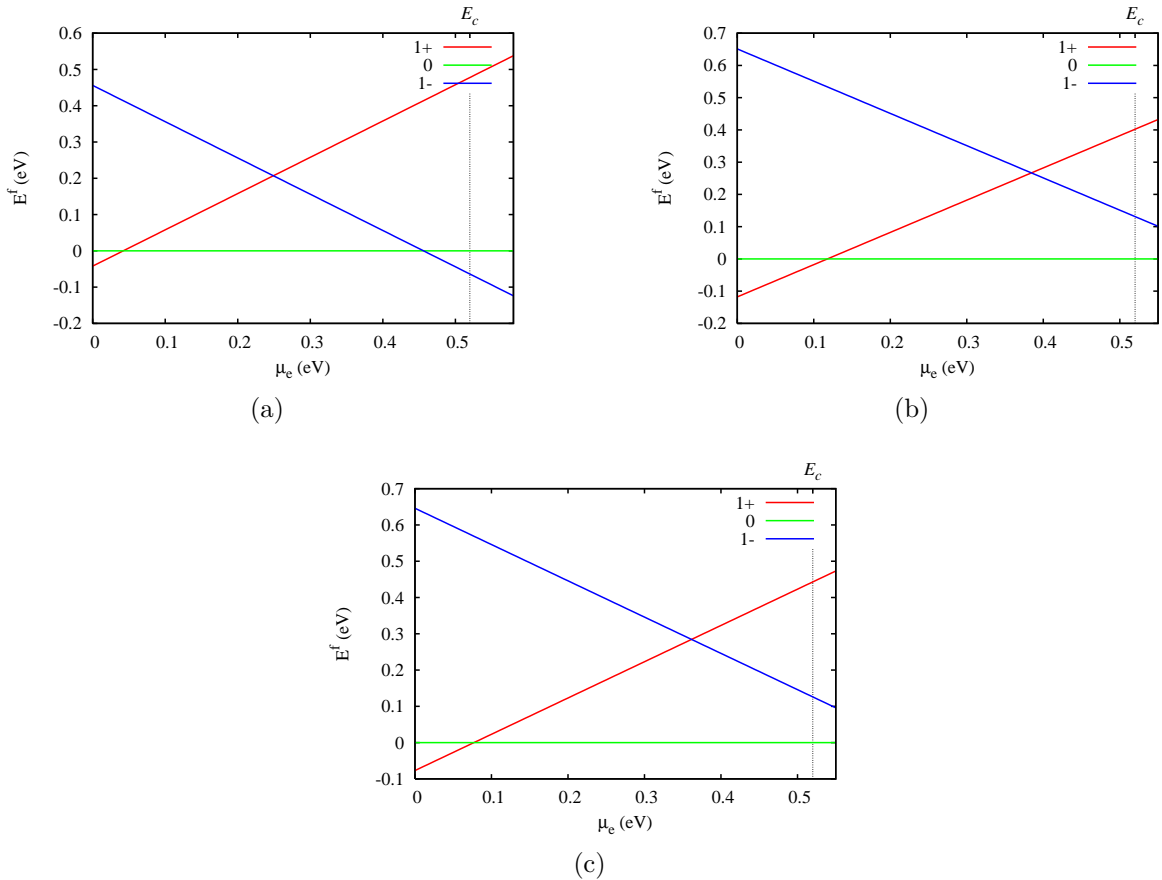


Figure 7.7: Schematic diagram showing the formation energy for  $\text{Fe}_i$  in: (a) the equilibrium site of ISF (site a and b); (b) site c, and (c) site d, which represent a bulk-like site. These labels indicate the sites in figure 7.2.

### 7.3.2.3 Optical properties

Figure 7.8 shows that the absorption coefficient for the supercell containing the ISF is similar to that of pure Si. The complex refractive index of the ISF is plotted in figures 7.9,

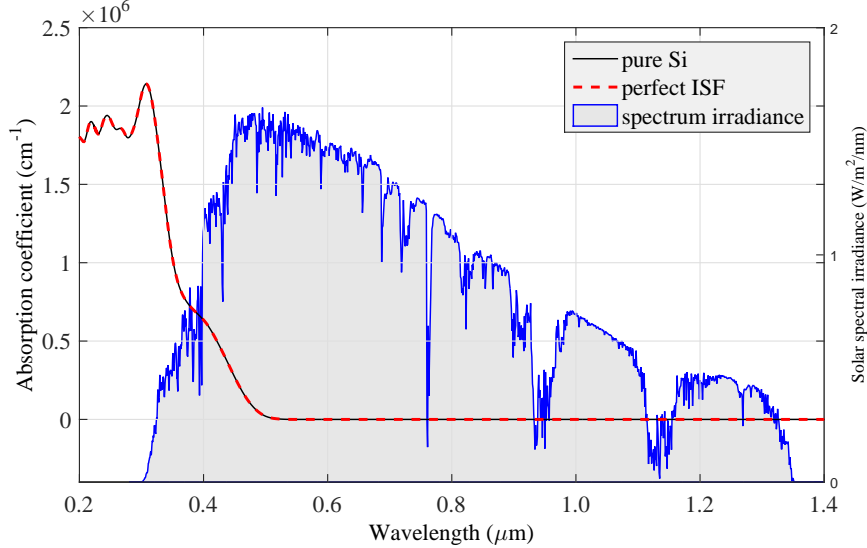


Figure 7.8: Calculated optical absorption coefficient versus wavelength for intrinsic stacking fault and ideal Si together with the AM1.5 [180] solar power spectrum for comparison.

where the real ( $n$ ) and imaginary ( $k$ ) parts are compared with bulk Si as a function of wavelength. As a reference, values of  $n$  and  $k$  for  $\text{Fe}_i$  in bulk silicon are shown in figure 7.9 (c) and (d) respectively. The minor impact of Fe in supercells containing ISFs (Figures 7.9 (e)–(f)) reflects the states introduced by the impurity.

### 7.3.2.4 Binding energy

To calculate binding energies, the reference sites taken to represent bulk silicon, labelled (d) in figure 7.2, with these sites are chosen as they yield Fe–Si inter-nuclear distances and spin splittings in the different charge states that are in reasonable agreement with those obtained from the bulk silicon supercell. Figure 7.10 shows a plot of  $E^b$  at different sites for the ISF. It is found that  $\text{Fe}_i$  is bound to the ISF by just 0.2 eV in the neutral case, and by slightly lower than this value in the positive spin state. It is important to mention here that the  $E^b$  for the negative case (Figure 7.10) merely shows the difference in energy between structures which lie at the ISF (which has donor and acceptor levels) and sites like bulk Si (which has a donor only). The relatively low binding at the ISF is most probably a consequence of the low strain relaxation even after introducing the Fe. However, this binding is significantly increased by  $\text{Fe}_i$  being trapped at vacancies at the ISF (forming  $\text{Fe}_s$ ) or, perhaps more critically, by iron already trapped there.

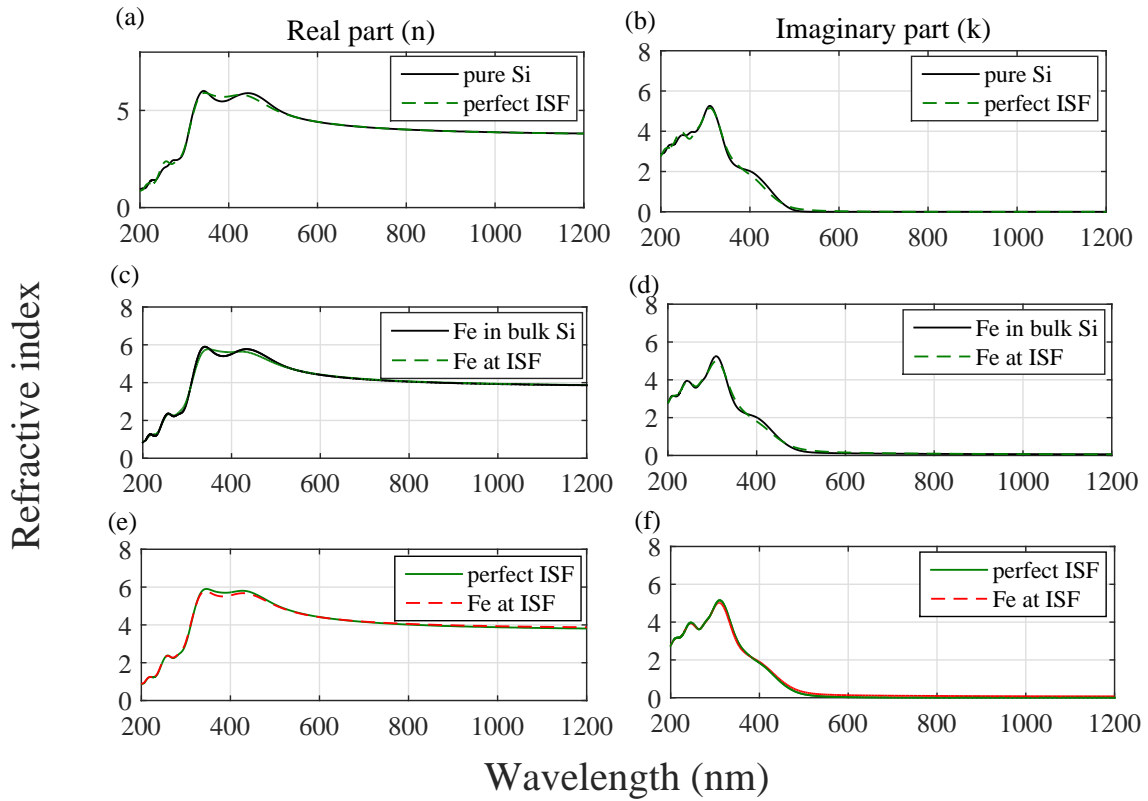


Figure 7.9: Computed real ( $n$ ) and imaginary ( $k$ ) parts of the refractive index showing: (a and b) the impact of ISF on pure Si, (c and d) the effect of Fe decorated ISF as compared with interstitial iron in bulk Si, and (e and f) the comparison between Fe-decorated ISF and Fe-free ISF regarding the refractive index.

More details of these related investigations are presented in sections 7.3.3 and 7.3.4 respectively.

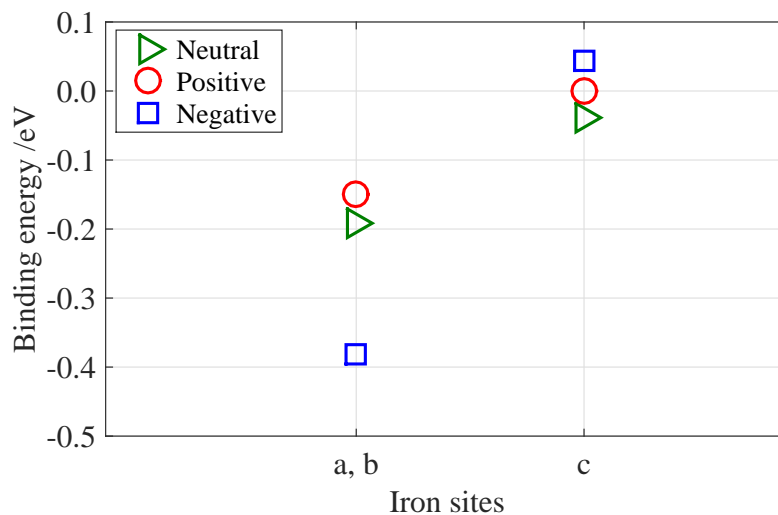


Figure 7.10: Binding energy of iron to the ISF as a function of site (figure 7.2) and charge state. In each case, the energies of the lowest energy spin configurations are used.

### 7.3.2.5 Bond-strain calculations

In an attempt to understand the trends observed in  $E^b$  (Figure 7.10), the outward relaxation of the nearest neighbours of  $Fe_i$  in each site have been examined. As a baseline, the average strain in the Fe-free ISF lies in the range  $-0.2\%$  to  $0.1\%$ .

According to the method illustrated in figure 5.4, where Si–Si bonds for the Fe nearest neighbours have been calculated and compared with those in other specific references; the root mean square for the calculated strain values are determined. Table 7.1 lists the rms strain caused by the combination of ISF and Fe in studying the behaviour of iron at the equilibrium sites of ISF and in the vicinity of the ISF. The data for Si–Si and Fe–Si bond-strain are compared with those in different structures, including pure Si,  $Fe_i$ , and  $\beta$ - $FeSi_2$ . By these comparisons, one can understand the impact of these Fe forms and ISFs on crystalline bulk Si. To overcome uncertainty behind these calculations, examination of the variation of the bond length values as a function of optimisation iteration is performed over the full range of calculations.

Table 7.1: Si–Si and Si–Fe bond-strain due to segregation of the diffusing iron at the sites provided by ISF. Different structures are compared to calculate rms strains 1 and 2 with respect to pure Si (Si–Si=4.41 au),  $Fe_i$  (Si–Si=4.42 au, Fe–Si=4.49 au) and  $\beta$ - $FeSi_2$  (Si–Si=4.76 au, Fe–Si=4.39 au) respectively.

Fe site	Bond	Bond length	Strain 1	Strain 2	Strain 3
<b>a, b</b>	Si–Si	4.44	4.65%	1.58%	6.75%
	Fe–Si	4.38	5.60%	5.98%	5.59%
<b>c</b>	Si–Si	4.42	0.43%	0.40%	7.20%
	Fe–Si	4.48	1.88%	0.84%	2.37%
<b>d</b>	Si–Si	4.41	0.43%	0.41%	7.22%
	Fe–Si	4.48	1.66%	0.12%	2.20%

The analysis shows that the segregation of Fe at the equilibrium sites (a and b) of the ISF yields the expansion of Si–Si distances by around  $0.6\%$  compared to in pure Si, and this value gradually decreases in the vicinity of the stacking fault area. This can reflect the bond-strain caused by the combination of Fe and ISF in the ISF system. On other hand, Fe at sites (c and d) behaves as interstitial iron since the bond lengths are very close to those in the  $Fe_i$  system. Moreover, the comparison of Si–Fe at the stacking fault area with those in the  $\beta$ - $FeSi_2$  structure indicates that the Fe behaves as a precipitate. Consequently, the calculated rms bond-strain for Si–Si and Fe–Si at the equilibrium sites (a and b) are higher than at sites in the vicinity of the stacking fault area. These investigations can show the relationship between the strain and magnitude

of the binding energy, where sites with larger strain are stronger sites to bind iron (i.e. with higher  $E^b$ ). Moreover, another investigation has been concluded for iron at the equilibrium site of the ISF to investigate its behaviour as interstitial or precipitate. In particular, there is some preliminary indication that sites in ISFs where Fe can adopt a higher co-ordination than in the tetrahedral form in bulk silicon tend to have lower energies. Figure 7.11 shows the coordination of Fe at the ISF, which is somewhat closer to  $\text{FeSi}_2$  co-ordination [181] than the interstitial system.

In addition to  $\text{Fe}_i$ , for the ISF, incorporation of  $\text{Fe}_i$  at a vacancy and the formation of  $\text{Fe}_i$ -pairs are examined in the following sections.

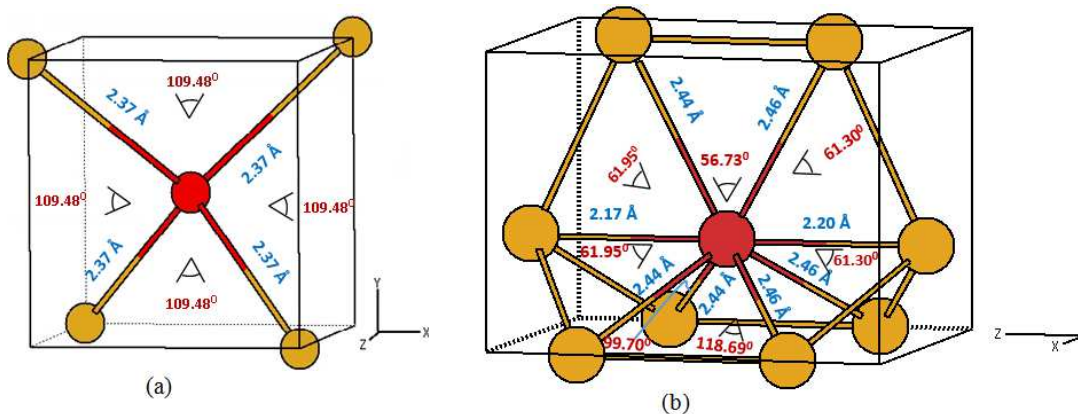


Figure 7.11: Schematics of equilibrium structures showing the differences in bond lengths and angles of iron in the bulk Si (a) compared with the higher coordination of Fe at the gettering site of the ISF (b). Yellow and orange atoms represent Si and Fe respectively.

### 7.3.3 Iron-vacancy pairing and substitutional iron at ISF

ISFs may contain vacancies that trap mobile  $\text{Fe}_i$ . If diffusing  $\text{Fe}_i$  encounters a neutral vacancy at the ISF, a near-neighbour  $\text{Fe}_i\text{V}$  pair may initially be formed. Indeed, the NL19 EPR centre has been suggested to consist of  $\text{Fe}_i$  and a vacancy in bulk Si [137], while this study extends to an investigation of the spin and binding energies for the  $\text{Fe}_i\text{V}$  pair as well as for  $\text{Fe}_s$  at the ISF.

Many sites inside the region of stacking faults have been investigated to include the  $\text{Fe}_i$  and a vacancy. The equilibrium structure for this pair inside the ISF can be obtained with a distance 1.5 Å with trigonal symmetry. Spin energy calculations show that  $S = 1$  and  $S = 2$  configurations of the  $\text{Fe}_i\text{V}$  pair are 0.3 and 0.8 eV higher than  $S = 0$ . Notably, this suggests that the spin singlet is stabilised for the same extent as the ground-state of the  $\text{Fe}_i\text{V}$  pair in bulk Si, where  $S = 1$  and  $S = 2$  are 0.2 eV and 0.6 eV above the ground state ( $S = 0$ ) of  $\text{Fe}_i\text{V}$  in bulk Si. For  $(\text{Fe}_i\text{V})^+$ , the energy differences between

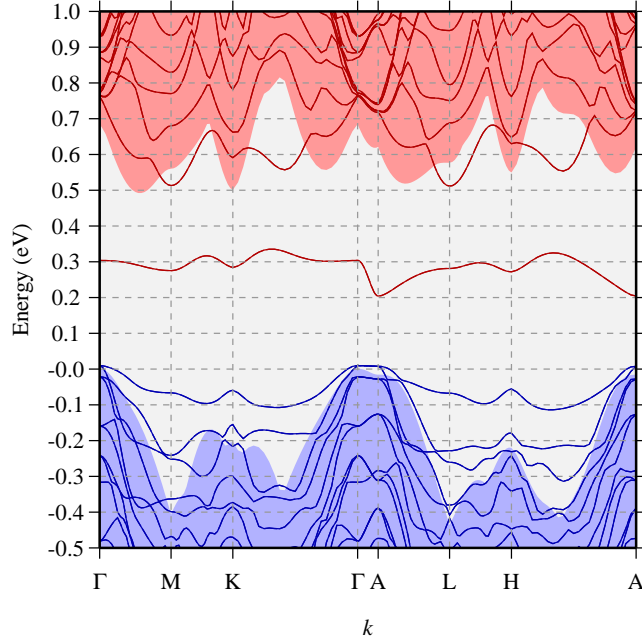


Figure 7.12: The electronic band structures corresponding to the most stable Fe-site at ISF structure in neutral spin polarise ( $S = 0$ ), plotted along high-symmetry branches in the first BZ. Occupied and unoccupied states are depicted as solid blue and dashed red lines, respectively. The underlying shaded regions show the electronic band structure for the corresponding undecorated ISF in 198 Si-atom. The energy scale for each system is defined such that the VB maximum are at zero.

$S = 1/2$  ground state and  $S = 3/2$  and  $S = 5/2$  are about 0.29 and 0.82 eV, compared to 0.25 and 0.80 eV in bulk silicon. The relative energies of these structures and other systems investigated in previous chapters are summarised in table 7.2. Generally, the change in the relative energies of the different spin states is most likely a consequence of the increased volume associated with the cage site in the ISF, and in particular with the presence of a vacancy.

The electronic band structure for the equilibrium site of  $\text{Fe}_i\text{V}$  pair at the ISF is shown in figure 7.12, in which the iron-related states introduced by trapping a segregated  $\text{Fe}_i$  by a vacancy at the ISF are compared with the background shaded area (undecorated ISF). It is noticed that a dispersion in the state due to cell size occurs in the state at  $\Gamma$ — $A$  points (i.e. at the transportation of an electron from the origin toward the Z-direction of the BZ points). Furthermore, in this study, there is a difference between this band structure and that of  $\text{Fe}_i\text{V}$  in bulk Si (Figure 5.9). It is clear that the presence of a vacancy at the ISF or in the bulk can reduce the distortion caused by Fe alone (see figure 5.6(a)), but with stronger binding as shown later.

The dramatic difference in bond lengths and angles relative to those of  $\text{Fe}_i\text{V}$  in bulk Si can be seen in figure 7.13, where the coordination of Fe with the presence a vacancy at the ISF is coordinated with more Si atoms than that in the bulk. This can support the idea behind the precipitation of Fe at ISFs with in the presence of vacancies, where the investigated coordination and Fe–Si bond-distance of  $\text{Fe}_i\text{V}$  at the ISF (Figure 7.13 (right)) agree reasonably well with that in the  $\text{FeSi}_2$  co-ordination [181]. In order to study the

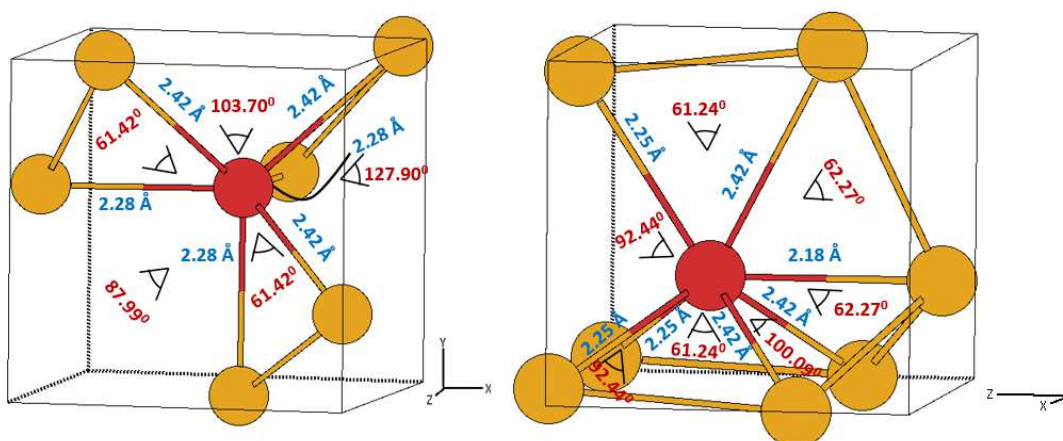


Figure 7.13: Schematics of equilibrium structures showing the differences in bond lengths and angles of  $\text{Fe}_i\text{-V}$  in the bulk Si (left) compared with the higher coordination of  $\text{Fe}_i\text{-V}$  at the ISF (right). Yellow and orange atoms represent Si and Fe, respectively.

reaction for  $\text{Fe}_i\text{-V}$  and then  $\text{Fe}_s$  at the ISF, two cases have been investigated. First, when both  $\text{Fe}_i$  and vacancy move together toward the ISF; and second when  $\text{Fe}_i$  move into the vacancy that trapped at the ISF. It is found that both these reactions are exothermic. Results show that the ground state of  $\text{Fe}_s$  at the ISF is  $S = 0$ , which is lower than  $S = 1$  by 0.34 eV. Moving  $\text{Fe}_i\text{-V}$  pair from bulk-like site toward the ISF to form  $\text{Fe}_i\text{-V}$  pair at the ISF and then  $\text{Fe}_s$  release energy at about 0.6 and 0.9 eV respectively (i.e more likely to form  $\text{Fe}_s$  at ISF than in bulk). The upper limit of the reaction energy compares favourably with the comparable bulk reaction which is estimated to release energy about 2 and 3 eV for  $\text{Fe}_i\text{V}$  and  $\text{Fe}_s$  in the bulk. In contrast, when the  $\text{Fe}_i$  moves into a vacancy that presence in the ISF, the nearest-neighbour  $\text{Fe}_i\text{-V}$  pair is formed with the release of energy around 2.4 eV. The forming of  $\text{Fe}_s$  by this reaction can release 2.7 eV, depending upon the site of Fe in the ISF with respect to the vacancy.

This mean the trapping of Fe by the vacancy at the ISF can bond Fe more strongly than that segregated by site provided by a clean ISF (without vacancies).

This provides an additional support for the idea behind the precipitation of iron at ISFs that contain vacancies.

### 7.3.4 Iron pairs at ISFs

It has been reported in chapter 6 that  $\text{Fe}_i$ -pairs are both bound in bulk Si (in contrast to an earlier report [147]) and mobile. This being the case, it is plausible that Fe atoms would arrive at the ISF in pairs or, should they arrive individually, that a pair would be formed in the ISF. Many possible sites have been tested to investigate the equilibrium sites of the Fe pair at the ISF. When  $\text{Fe}_i\text{-Fe}_i$  is inserted into the stacking fault area with a separating distance of  $3.85\text{\AA}$ , it is found that the AFM singlet ( $S = 0$ ) and  $S = 2$  configuration of  $\text{Fe}_i\text{Fe}_i$  lie 0.06 and 0.24 eV above the spin triplet, respectively. The positive charge states of  $\text{Fe}_i\text{Fe}_i$  have also been examined at the ISF, it is found that the  $S = 1/2$  is favoured over  $S = 3/2$  and  $S = 5/2$  by 0.09 and 0.49 eV respectively. It can be expected that the change in the relative energies of the different spin states is most likely a consequence of the additional splitting of the  $d$ -orbitals of the iron pair due to a local reduction in symmetry at the core of ISF. The resulting relative energies and values of heat reaction ( $\Delta H$ ) are summarised in table 7.2. Structures in this table refer to the presence of individual impurities (Fe and mono vacancy) in bulk or at the ground state of the ISF. For example,  $(\text{Fe}_i\text{V})_{\text{bulk}}$  means that the combination of an individual  $\text{Fe}_i$  and vacancy in bulk results in an  $\text{Fe}_i\text{V}$  pair (which can also denoted as  $(\text{Fe}_i)_{\text{bulk}} + \text{V} \rightarrow (\text{Fe}_i\text{V})_{\text{bulk}}$ ); whereas  $(\text{Fe}_i\text{Fe}_i)_{\text{ISF}}$  means diffusing interstitial iron from a bulk-like site like toward the ISF that contains another Fe to form an  $\text{Fe}_i\text{Fe}_i$  pair at the ISF, and so on for other structures). Other sites have been investigated for  $\text{Fe}_i$ -pairs with longer separation distances. For example, when Fe atoms are lying at sites a and c (distance  $4.11\text{\AA}$ ) of the ISF, the AFM ( $S = 0$ ) ground state is more stable than the triple and FM with very small differences in energy (0.05 and 0.08 eV respectively). This is similar to the case if the pair is located at sites a and d (distance= $7.66\text{\AA}$ ) in figure 7.2.

The binding of a second  $\text{Fe}_i$  atom to the ISF is found to be greater than in the presence of an individual Fe at the ISF, being 0.82 eV. In contrast, the interaction of the  $\text{Fe}_i\text{Fe}_i$  pair in bulk Si releases energy of about 0.22 eV. The stronger binding of the iron-pair at the ISF compared to the individual Fe indicates that the precipitation of Fe at the ISF is energetically more favourable, even in the absence of the direct chemical reaction bonding afforded by the substitution of Si by Fe.

Table 7.2: Spin energy differences ( $\Delta E$ ) in eV associated with the different structures. These values indicate how much each of the the other spin states are lower (negative) than the reference ( $S = 1$  and  $S = 1/2$ ) for neutral and single positive charge states respectively for the same structure. Furthermore, the value of enthalpy of chemical reaction ( $\Delta H$ ) for defect-complexes are also listed.

Structure	$\Delta E(S0 - S1)$	$\Delta E(S2 - S1)$	$\Delta E(S3/2 - S1/2)$	$\Delta E(S5/2 - S1/2)$	$\Delta H$ (eV)
$(\text{Fe}_i)_{\text{bulk}}$	0.52	0.55	0.13	0.55	–
$(\text{Fe}_i\text{V})_{\text{bulk}}$	-0.24	0.40	0.25	0.80	2.10
$(\text{Fe}_i\text{Fe}_i)_{\text{bulk}}$	-0.30	-0.26	0.15	-0.18	0.26
$(\text{Fe}_i)_{\text{ISF}}$	0.08	0.68	0.02	0.85	0.17
$(\text{Fe}_i\text{V})_{\text{ISF}}$	-0.30	0.49	0.29	0.82	2.45
$(\text{Fe}_i\text{Fe}_i)_{\text{ISF}}$	0.06	0.24	0.09	0.49	0.82

## 7.4 Summary

The segregation of  $\text{Fe}_i$  at the ISF has been studied as an example with very low-strain compared to other EDs in crystalline Si such as  $\Sigma 3$ -(111) and other twist GBs like  $\Sigma 5$ -(001) and  $\Sigma 3$ -(110) twist GBs which are investigated in the next chapter. The results of DFT show that ISFs represent binding sites for  $\text{Fe}_i$ , although the binding energy of a single Fe impurity is relatively small. The relatively low binding at the ISF is most probably a consequence of the low strain relaxation even after introducing the iron. This binding, however, is significantly increased by  $\text{Fe}_i$  being trapped at vacancies at the ISF (forming substitutional iron) or, perhaps more critically, by Fe already trapped there. This can reflect the fact that the precipitation of Fe at the ISF is strongly energetically favourable, even in the absence of direct chemical bonding afforded by the substitution of Si by Fe. In addition to that, modifications of the spin energies of these and other defects have been investigated and are summarised in table 7.2. Investigation toward  $\text{Fe}_i$ -twist GBs complexes is the main subject of next chapter.

# Analysis of Iron Segregation at Twist Grain Boundaries in mc-Si

“The great tragedy of science: the slaying of a beautiful hypothesis by an ugly fact.”

Thomas Huxley

Results in chapter 6 introduced the analysis of iron segregation at intrinsic stacking faults as an example of very low strain structure as compared with other extended defects such as grain boundaries, which are the main subject of this chapter. Section 8.1 introduces theoretical and experimental studies that support the hypothesis behind Fe gettering by twist GBs. The computational method used to investigate Fe behaviour at two types of twist GBs is outlined in section 8.2. Section 8.3 is dedicated to the structural, electronic, electrical and optical properties of these GBs, as well as their interaction with segregated iron and its complexes. Finally, an analysis of the iron segregation at the twist GBs in mc-Si has been published elsewhere [127,182]. Moreover, an investigation into efficiency-limiting twist GBs in mc-Si solar cell has also been published [128].

## 8.1 Introduction

One of the disadvantages of mc-Si is the existence of numerous structural defects (Figure 1.15) such as grain boundaries. GBs are the interface between two crystals (grains) of the same material having identical crystal structure but with different orientations within the mc-Si material [183], as shown in figure 8.1 [184]. GBs may be characterised

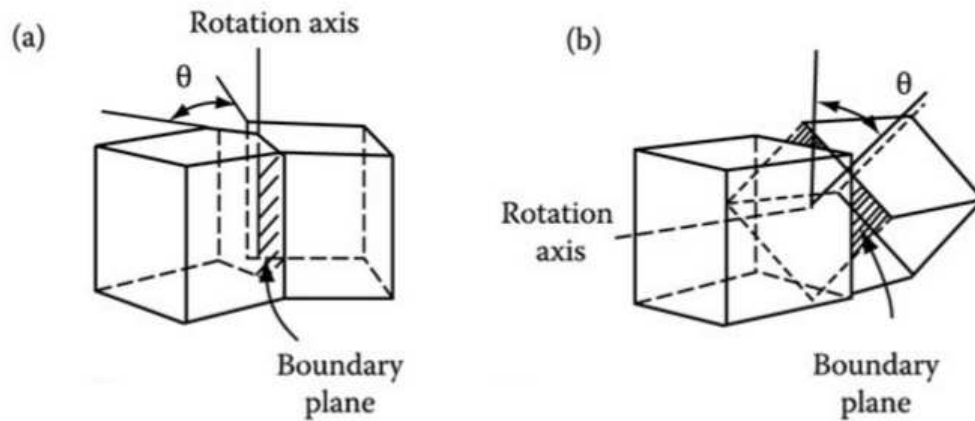


Figure 8.1: Schematic illustration for (a) tilt and (b) twist GB. This picture has been taken from [184].

by the misorientation of the two adjoining grains and the orientation of the boundary plane [183, 185].

Several parameters are required to describe a GB mathematically, including the rotation axis ( $\hat{u}$ ) and misorientation angle ( $\theta$ ) which are required to specify the misorientation of one grain relative to the other. Other parameters are required in describing the boundary plane normal ( $\nu$ ) and also to describe the relative displacement ( $\vec{R}$ ) of one crystal grain with respect to the other [186].

Accordingly, GBs in crystals can be geometrically classified and analysed as tilt and twist boundaries based on the concept of the coincidence site lattice (CSL). Both of these GBs are defined by the relationship between the rotation axis and the boundary plane, even though general boundaries may contain both tilt and twist components. The CSL is the intersection of the lattices of two grains, and the coincidence index ( $\Sigma$ ) is the reciprocal density of coincidence lattice sites with respect to the original lattice. The periodicity of the boundary structure can be analysed according to the periodicity in the plane in the CSL, where their boundaries with relatively small  $\Sigma$  values include short periods and can be formed for singular rotation angles [187]. For example, when a planar unit cell is five times larger than the primitive unit cell of the perfect crystal, a  $\Sigma 5$  twist GB is obtained [188], which displays the typical features of high-energy boundaries [189] compared to ISFs (see chapter 7), for example. It has been noted [190] that two distinct  $\Sigma 5$  boundary structures with the same CSL can be obtained by rotating one half-crystal with respect to another around the [001] direction by an angle of  $36.9^\circ$  or its complementary angle  $53.1^\circ$ .

In general, the presence of GBs in semiconductor material represents a major source

of degradation in their electrical, thermal and mechanical properties [191]. Furthermore, as mentioned in chapter 1, solar cell efficiency is governed by the concentration and type of impurity atoms, as well as the density and electrical activity of EDs such as GBs [192]. In particular, impurities in GBs can trap charge carriers, reducing the performance of the solar cell due to their acting as scattering centres for phonons, and hence causing a reduction in thermal conductivity [188].

The electron-beam-induced current technique (EBIC) was used to investigate the impact of Fe contamination on the recombination activities of GBs in mc-Si, and it is concluded that, in clean mc-Si, the recombination activities of large-angle GBs, including special  $\Sigma$  and random GBs, are rather weak at 300 K. However, these GBs become much more electrically active when contaminated with iron [176, 193]. It is indicated in these studies that there is a strong dependence of iron segregation in Si at GBs upon the misorientation of grains and the inclination of the GBs' ( $\Sigma$ ) value of the CSL [194] and Miller indices ( $hkl$ ) of the interface plane. X-ray microprobe fluorescence has been used to study Fe distribution, and the results show that Fe lies near or along GBs [195, 196]. However, most investigations only show indirect evidence of the existence of iron impurities. Therefore, the structural characterisation and imaging of iron at GBs may provide a better understanding of its exact gettering sites and existing form in mc-Si. Attempts have been made using the annular dark-field (ADF) to provide direct, compositionally sensitive structural images avoiding the phase problem [197]. ADF techniques are used for atom-by-atom identification at high spatial resolution [198]. Despite the high resolution of TEM, ADF has been utilised for imaging individual atomic columns in crystals and also single dopant atoms on the surface [199] or in the bulk [200].

$\Sigma 3$  GBs are generally most frequently observed in mc-Si (<50%) [193], providing useful suggestions for improvement in solar cells in particular if the behaviour of iron gettering is well understood.  $\Sigma 3$  GBs have relatively simple structures as compared with other GBs such as  $\Sigma 5$ . The EBIC method [201] has been used to investigate  $\Sigma 3$  GBs in clean and Fe-contaminated mc-Si. Furthermore, the structures of  $\Sigma 3$  GBs were investigated using TEM to find correlations with their recombination activities [202]. The ADF technique has also been used to detect gettering sites and existing forms of iron impurity at  $\Sigma 3$  GBs.

Based on a hypothesis associated with internal gettering by EDs as one possibility to getter Fe in order to improve solar cell efficiency [174], gettering Fe by ISF has been investigated in detail in chapter 7, whereas the analysis of Fe gettering by  $\Sigma 5$ -(001) and  $\Sigma 3$ -(110) twist GBs is the main focus of this chapter. In particular, various studies [171,

203–206] indicate the attractive interaction between GBs in mc-Si and diffusing Fe atoms, and internal gettering exploits this interaction. Furthermore, there is some evidence that the gettering of Fe at GBs is a viable route to the reduction of the deleterious effects of Fe in mc-Si solar cells [171].

The segregation of Fe atoms and the precipitation of Fe silicide particles at GBs have been investigated in several experimental studies using different methods such as PL spectroscopy [207], and EBIC measurements [208] in combination with TEM [209], SEM [201], and EBSD [201].

In this work, quantum-chemical simulations have been employed, with systems modelled using periodic boundary conditions and large supercells, in order to evaluate the binding of  $\text{Fe}_i$  and its complexes at  $\Sigma 5$ -(001) and  $\Sigma 3$ -(110) twist GBs. These GBs exhibit considerable bond-strain, although all atoms are fully co-ordinated. The crystals are separated by GB type defects created by rows of 5–7 member rings defects. While an individual 5–7 member rings in a perfect crystal creates a dislocation-type defect, rows of these defects with relatively large spacing form low-angle GBs. With decreasing spacing between 5–7 coordination defects, high-angle GBs are formed for which the misorientation between adjacent crystals is more than 10 degrees [210].

There is relatively little understanding of the mechanism of segregation of iron at these GBs types at an atomistic level, possibly because the modelling of GBs is challenging in terms of the system size required, and because the detailed structure of GBs in mc-Si remains a matter of debate [49]. However, it is important to develop a fundamental understanding of the mechanism of any gettering (attractive interaction) between GBs structures in mc-Si and diffusing Fe atoms.

Prior to introducing data for the twist GBs, a description of the methodology used is presented.

## 8.2 Computational Method

DFT, as implemented in AIMPRO (chapter 2), has been employed, with systems modelled using periodic boundary conditions for  $\Sigma 5$ -(001) and  $\Sigma 3$ -(110) twist GBs.

Fundamentally, to model the present twist GBs, individual Si atoms in the GB core are shifted and twisted from their regular crystal positions as compared to the crystal interior. For example, the  $\Sigma 5$ -(001) twist GB structure can be obtained by a purely geometric twisting operation on the (001) plane of silicon lattice, and this can be considered to be

representative of virtually all high-energy GBs in this crystallographic structure.

Indeed, by twisting two adjacent crystals, some bonds across the boundary plane can be reconstructed, resulting in higher excess energies compared to the GBs obtained by twisting one at two densest planes of the diamond structure such as (111), for example, where few bonds per atom are effected.

For the  $\Sigma 5$ -(001) and  $\Sigma 3$ -(110) CSL twist GBs, the periodic boundary conditions along the [001]- and [110]-directions respectively produce two, equivalent GBs. In this work, the model used is the  $\Sigma 5$ -(001) GB system with 24 atomic layers, which may be viewed as six atomic layers either side of each boundary. For the decorated form of the  $\Sigma 5$ -(001) GB, the in-plane footprint is repeated in each in-plane direction, yielding 20 atoms per layer and 480 silicon atoms overall. This separates Fe atoms from their periodic images whilst maintaining a feasible overall simulation size. For the  $\Sigma 3$ -(110) GB, the in-plane footprint is repeated in each in-plane direction to yield 24 atoms per layer, 16 layers and 384 silicon atoms overall. For both forms of GB, the lattice parameter normal to the boundary-plane has been varied to minimise the total energy, and the in-plane vectors fixed to the lengths determined for bulk silicon. These GBs exhibit considerable strain, but all silicon atoms are fully co-ordinated. A similar computational approach to that presented in the previous chapter has been adopted to calculate the binding energies of Fe to the GBs.

## 8.3 Results and Discussion

### 8.3.1 Undecorated twist grain boundaries

The atomic structure of the  $\Sigma 5$ -(001) and  $\Sigma 3$ -(110) twist GBs in Si, obtained after the thermodynamic equilibration procedure described in chapter 3, is schematically shown in figure 8.2 where the labels indicate sites examined.

The accuracy of the GB models can be evaluated further from the calculated areal energy densities using the same equation (7.1) used in the ISF case ( $\gamma = (E_{\text{GB}} - E_{\text{bulk}}) / 2A_{\text{GB}}$ ). Here,  $E_{\text{GB}}$  is the total energy of the supercell,  $E_{\text{bulk}}$  is the total energy of the same number of bulk Si atoms, and  $A_{\text{GB}}$  is the interface area. The factor of 2 in the denominator takes into account that there are always two GBs in supercells due to periodic boundary conditions [211].

It is found that  $\gamma(\Sigma 5)$  and  $\gamma(\Sigma 3)$  are 1.289 and 0.779 J/m<sup>2</sup> respectively, which compare

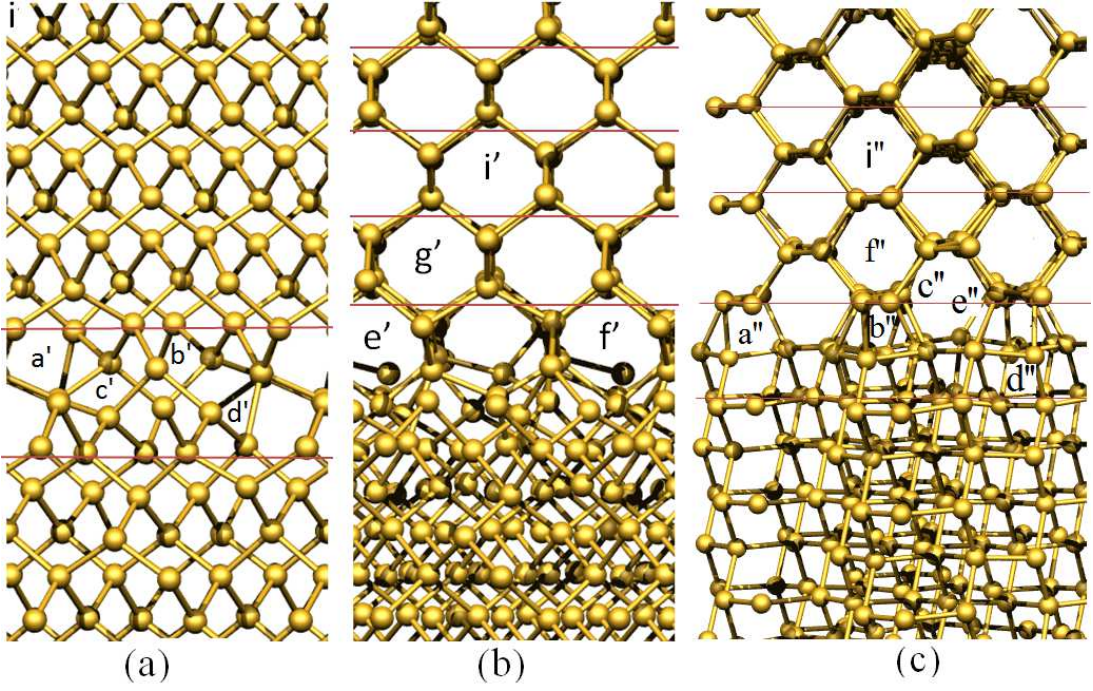


Figure 8.2: Optimised structures of (a)-(b)  $\Sigma 5$ -(001) and (c)  $\Sigma 3$ -(110) twist GBs. (a) and (b) illustrate the GB from different directions to facilitate identification of the GB layer. The terms  $a'-i'$  and  $a''-i''$  show the interstitial sites investigated.  $i'$  and  $i''$  are references for  $Fe_i$  in a bulk-like environment.

well with the literature values (1.288 J/m<sup>2</sup> for  $\Sigma 5$  [212] and 0.76 J/m<sup>2</sup> for  $\Sigma 3$  [211]).

In addition, to ensure convergence of the total energy, several test calculations were carried out to choose the most promising basis set and exchange-correlation potential for each GB. For example, basis functions that have been tested to give an accurate description of the  $\Sigma 3$ -(110) twist GBs system include 28 function per atom in case (*ddpp*) have been used with LDA and 18 function per atom in case (*C44G\*\**) with GGA (both the basis set and approximations are described in detail in chapter 2, sections 2.8 and 2.5 respectively). Calculations show that the difference in areal energy-densities between these two cases is just 7.6 mJ/m<sup>2</sup>. The same investigations are applied after introducing Fe to the GB systems to ensure that higher accuracy in the calculations is obtained in a short time.

Figures 8.3(a) and 8.3(b) show the Kohn-Sham band-structure for the  $\Sigma 5$  and  $\Sigma 3$  twist GBs respectively, showing an absence of any bands deep in the Si gap. The band gaps for both twist GBs deviate from the value of pure Si which is illustrated previously in figure 3.1. In the case of  $\Sigma 3$ GB, the bandgap is very slightly smaller than that of bulk silicon, whereas in the  $\Sigma 5$ GB, it is increased. This difference in the electronic band structure has a significant impact on solar cell performance, as will be shown later in chapter 10.

It is noted that the increase in the bandgap in  $\Sigma 5$ GB matches that formed in a recently reported study of the impact of extended defects on solar-cell efficiency [58]. The increase in the bandgap in the case of the  $\Sigma 5$ GB is 28% (see section 10.3).

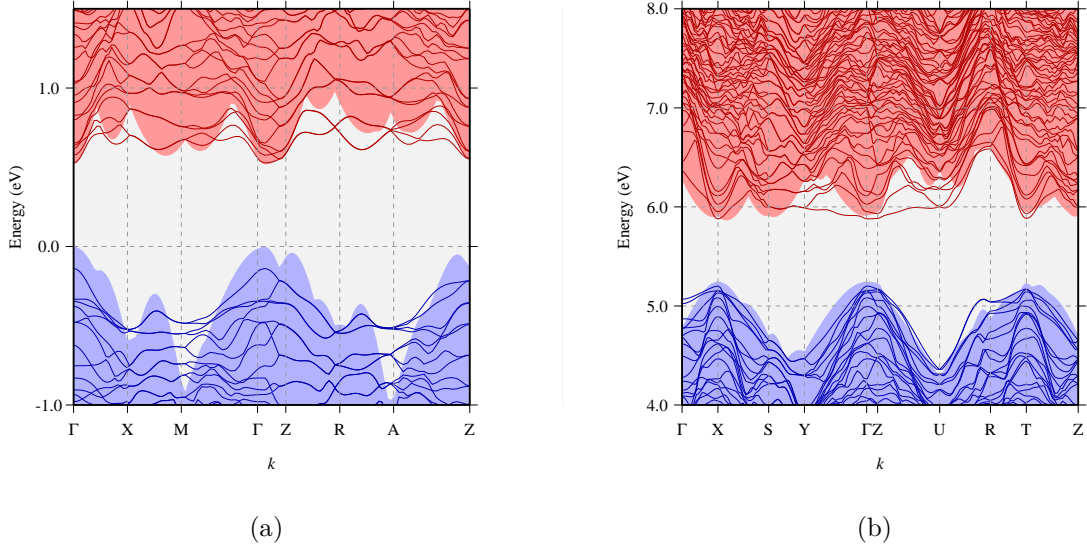


Figure 8.3: Electronic band structures of undecorated  $\Sigma 5$ -(001) and  $\Sigma 3$ -(110) twist GBs in 480 and 384 Si atoms, respectively, plotted along high-symmetry branches in the first BZ. Occupied and unoccupied states are depicted as solid blue and red lines, respectively. The energy scale for the system is defined such that the valence band maxima are at zero.

### 8.3.2 $\text{Fe}_i$ -GBs complexes

The positive outcomes obtained for  $\text{Fe}_i$  and its pair in bulk Si (chapters 5 and 6), as well as ISF (chapter 7) provide the basis for the extension of the study to the more complex problem of Fe attached to twist GBs. In particular, the results obtained in these analyses and for the GBs separately support the conclusion that the current methodology is accurate and therefore a sufficient basis upon which to present the results for Fe-GBs interaction, where  $\text{Fe}_i$  has been introduced at a range of non-equivalent sites as indicated by the labelling in figure 8.2. At each site, the structures have been optimised for different charge and spin states.

#### 8.3.2.1 Role of spin and charge states

In addition to the novel aspect presented in section 7.3.2.1 to investigate the spin energies of  $\text{Fe}_i$  in ISFs, this section describes the extent of the investigation of the role of spin and charge states of  $\text{Fe}_i$  in twist GBs. For the majority of sites examined within the  $\Sigma 5$ -(001)

GB (sites a'-d') in figure 8.2-a, the neutral charge state favours the spin-triplet state, in line with behaviour in bulk silicon [56, 155]. However, at the a' site, which is lower in energy than the other sites, and the spin triplet state is marginal. Notably, this suggests that  $S = 0$  is the ground state in comparison to  $\text{Fe}_i$  in bulk silicon (section 5.3.1.2). All the sites within the  $\Sigma 3$ -(110) GB favour the  $S = 1$  configuration for  $\text{Fe}_i^0$ , with site e'' being the most stable site, where the  $S = 0$  and  $S = 2$  configurations lie at 0.17 eV and 0.76 eV above the spin triplet. At sites i' and i'', the spin state energies resemble the energetics from bulk silicon simulations, confirming that these sites can be considered as a reference for  $\text{Fe}_i$  in a bulk-like environment as being relatively unperturbed by the GB.

The  $S = 1/2$  and  $S = 3/2$  configurations for the positive charge states have also been examined, showing that the doublet state is favoured for both GBs in stable sites. Furthermore, for all sites examined, a deep level arising from the Fe 3d-orbitals is found, and thus the electrical activity of  $\text{Fe}_i$  is predicted to remain irrespective of segregation to either of these GBs.

The different energies associated with sites along the  $\Sigma 5$ -(001) and  $\Sigma 3$ -(110) structures as a function of spin and charge states are shown in figures 8.4 and 8.5 respectively. These values indicate how much each of the other spin states are higher than the references ( $S = 1$  and  $S = 1/2$ ) for neutral and single positive charge states respectively for each structure. The change in the relative energies of the different spin states is most likely a consequence of the increased volume associated with the cage site in GBs, and the additional splitting of the d-orbitals of the iron due to the local reduction in symmetry (effectively an additional local crystal field splitting) [141, 213].

### 8.3.2.2 Electronic and electrical properties

The electronic band structure of the equilibrium sites (site a', e'') for the neutral charge state of Fe at  $\Sigma 5$  (480 Si-atom) and  $\Sigma 3$  (384 Si-atom) twist GBs are shown in figure 8.6, showing both occupied and empty bands within the Si gap which are related to the Fe orbitals split by the crystal field. Removing 1 electron from the spin up creates positively charged doublet spin state, whereas removing one electron from the spin down region leads to the formation of a positively charged quartet spin state. Comparing the band structure of  $\text{Fe}_i$  in bulk (or at sites i' and i'') and that within the GBs, these states are shifted to higher energy as the Fe atom moves from bulk to the GB area.

Based upon the band structures, it is natural to expect electrical levels to be present for

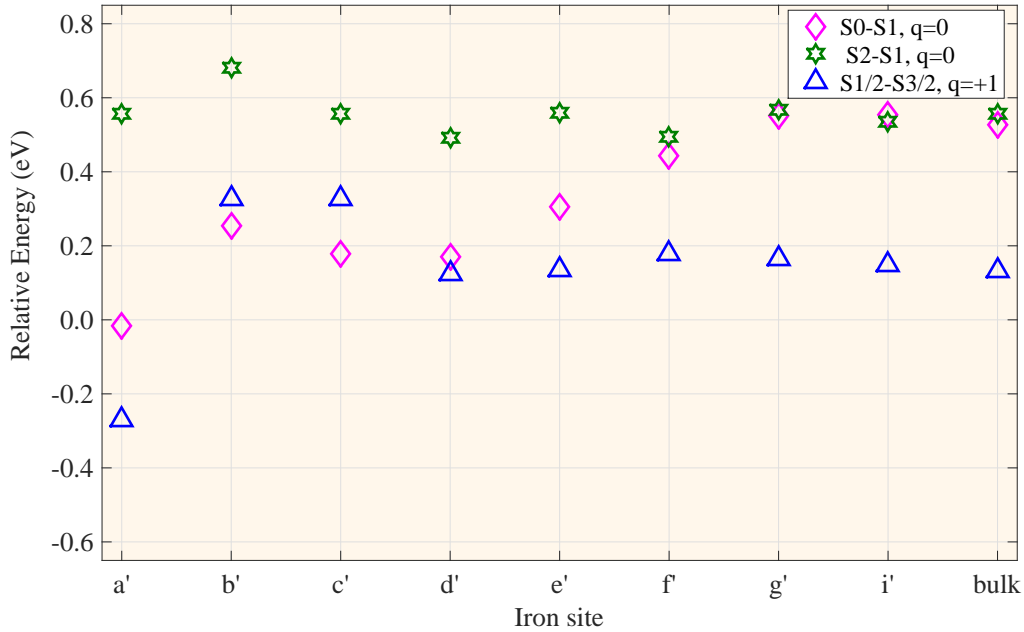


Figure 8.4: Relative energies for different spin configurations in neutral ( $q = 0$ ) and positive charge states examined for the sites in the  $\Sigma 5-(001)$  twist GBs illustrated in figure 8.2. These values indicate how much each of the other spin states are higher than the references ( $S = 1$  and  $S = 1/2$ ) for each site ( $a'-i'$ ) in neutral and single positive spin states respectively.

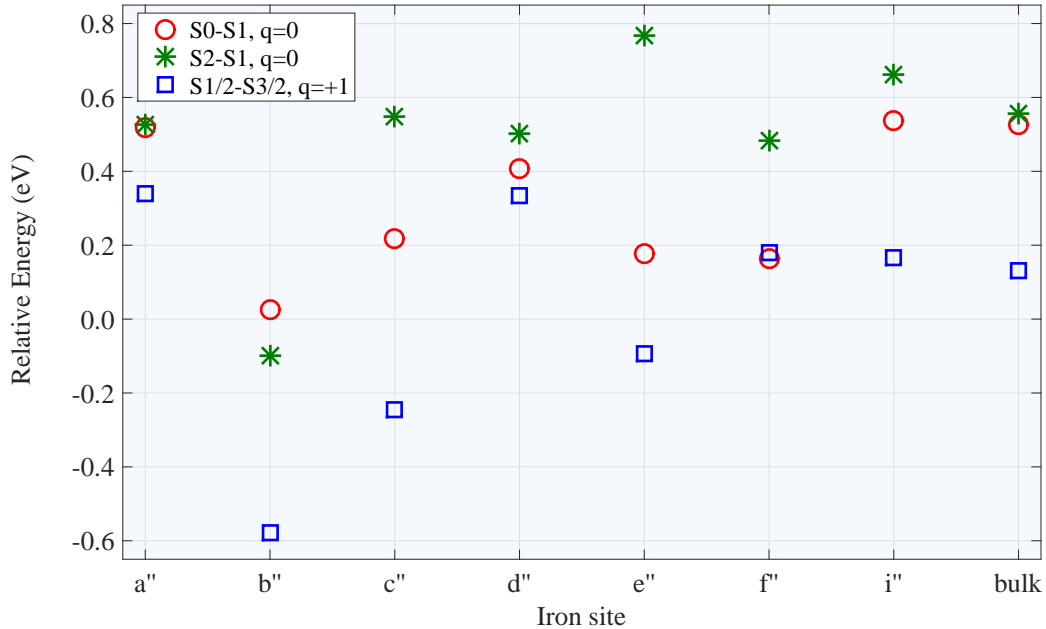


Figure 8.5: Relative energies for different spin configurations in neutral ( $q = 0$ ) and positive ( $q = +$ ) charge states examined for the sites in the  $\Sigma 3-(110)$  twist GBs illustrated in figure 8.2. These values indicates how much each of the other spin states are higher than the references ( $S = 1$  and  $S = 1/2$ ) for each site ( $a''-i''$ ) in neutral and single positive spin states respectively.

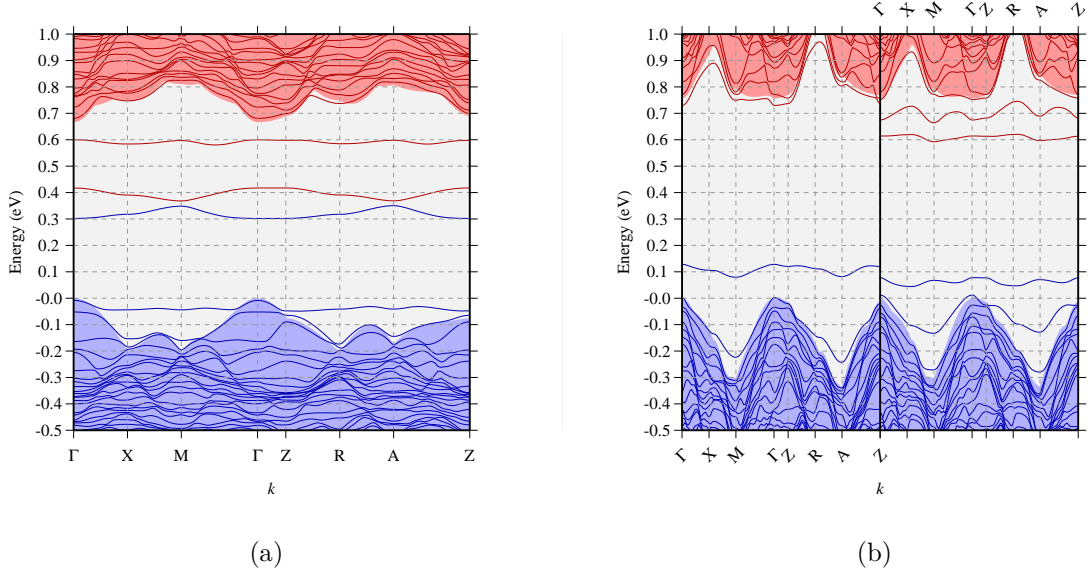


Figure 8.6: Electronic band structures of Fe at the more stable site (a' and e'') of  $\Sigma 5$  (480 Si-atom) and  $\Sigma 3$  (384 Si-atom) twist GBs in neutral charge state ( $S = 0$  and  $S = 1$  respectively), plotted along high-symmetry branches in the first BZ. Occupied and unoccupied states are depicted as solid blue and red lines, respectively. The underlying shaded regions show the electronic band structure for the corresponding undecorated GB supercells. The energy scale for each system is defined such that the VB maximum are at zero.

interstitial iron in the Si gap of both GBs. The calculations of both electrical levels have been performed using the formation energy method (described in chapter 3 section 3.4.1), where the formation energy of Fe at the equilibrium sites a' and e'' are plotted in figure 8.7 as a function of  $\mu_e$ . As seen in the plot, it is clear that Fe at  $\Sigma 5$ -(001) behaves as a very deep donor and deep acceptor defect with a +1 and -1 charge state being stable at the Si valence band top and conduction band bottom, respectively. This means the Fe can affect the n-type region of material containing  $\Sigma 5$ -(001), which is quite similar to the case of the behaviour of Fe in ISF (see figure 7.7(a)). The estimates made here indicate that Fe at  $\Sigma 5$ -(001) twist GB has a significant impact on the n-region of Si.

In contrast, figure 8.7(b) indicates that no states are introduced due to the segregation of Fe at  $\Sigma 3$ -(110)

The ionisation energy of  $\text{Fe}_i$  as a function of position has been further calculated as the difference in the total energies of the neutral and positive charge states.

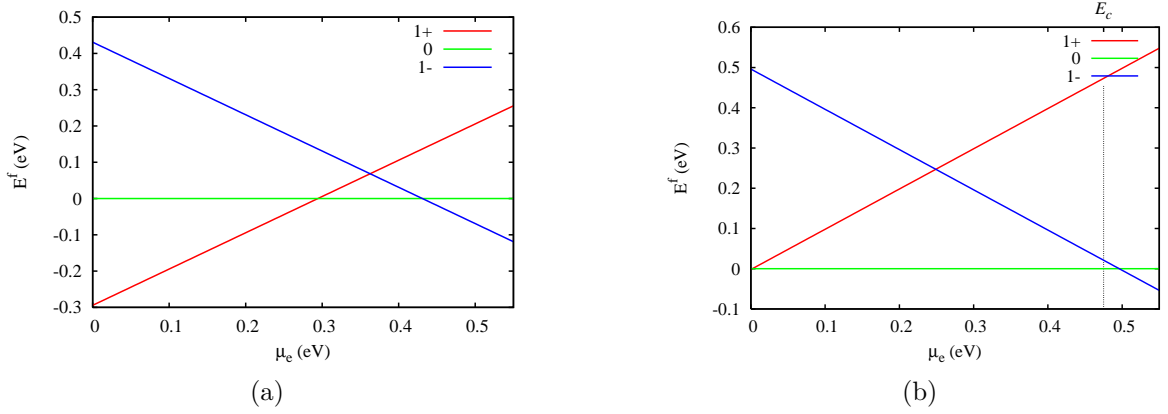


Figure 8.7: Plot of formation energy as function of electron chemical potential for Fe in the equilibrium sites of  $\Sigma 5$ -(001) (a') and  $\Sigma 3$ -(110) (e'') structures (Figure 8.2), calculated using 480 and 396 Si atoms in neutral case  $S = 0$  and  $S = 1$ , respectively.

### 8.3.2.3 Optical properties

In chapter 7, the absorption coefficient for the supercell containing the ISF has been studied, which gave results similar to those for pure Si. Here, it is found that absorption at the longer wavelength is more significant for the  $\Sigma 5$ GB, as shown in figure 8.8. This is likely to be due to the breaking of the symmetry at the core of the GBs which leads to non-zero transition dipoles between the valence band and interface states above the valence band edge. A further comparison between the ISF and  $\Sigma 5$ GB has been conducted regarding the complex refractive index, and the results are plotted in figure 8.9 (a) and (b) comparing the real and imaginary parts with bulk Si as a function of wavelength. Again, only the  $\Sigma 5$ GB shows significant deviation from bulk behaviour.

Turning to cases where an interstitial iron impurity has been added, as a reference  $n$  and  $k$  for  $\text{Fe}_i$  in bulk silicon are shown in figures 8.9(c) and (d) respectively. The minor impact of Fe in supercells containing EDs (Figures 8.9 (c–f)) reflects the states introduced by the impurity.

### 8.3.2.4 Binding energy

Figure 8.10 shows a plot of  $E^b$  for the two GBs. Negative values correspond to an attraction between the grain boundary and iron, while positive ones indicate that segregation is not favourable. It is found that Fe is bound to the  $\Sigma 5$ -(001) GB by around 0.4 eV, and to the  $\Sigma 3$ -(110) GB by about 0.3 eV. The positive values for sites a''–d'' in the case of the  $\Sigma 3$ -(110) GB can be understood in terms of the volume provided by cage available for the Fe impurity at these sites. For example, the average Fe–Si separation at site b'', for

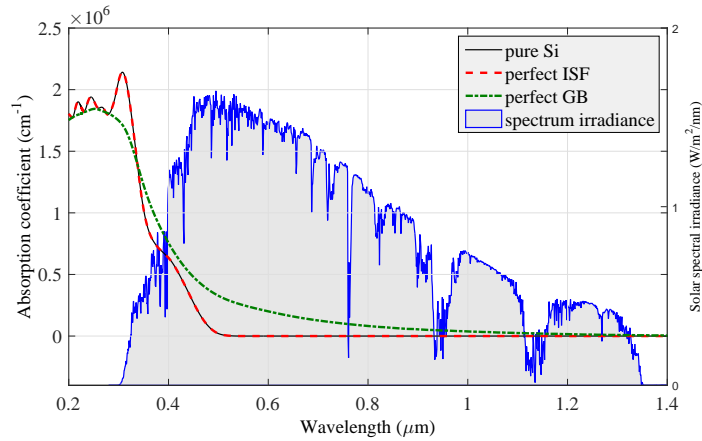


Figure 8.8: Calculated optical absorption coefficient versus wavelength for extended defects and ideal Si together with the AM1.5 [180] solar power spectrum for comparison.

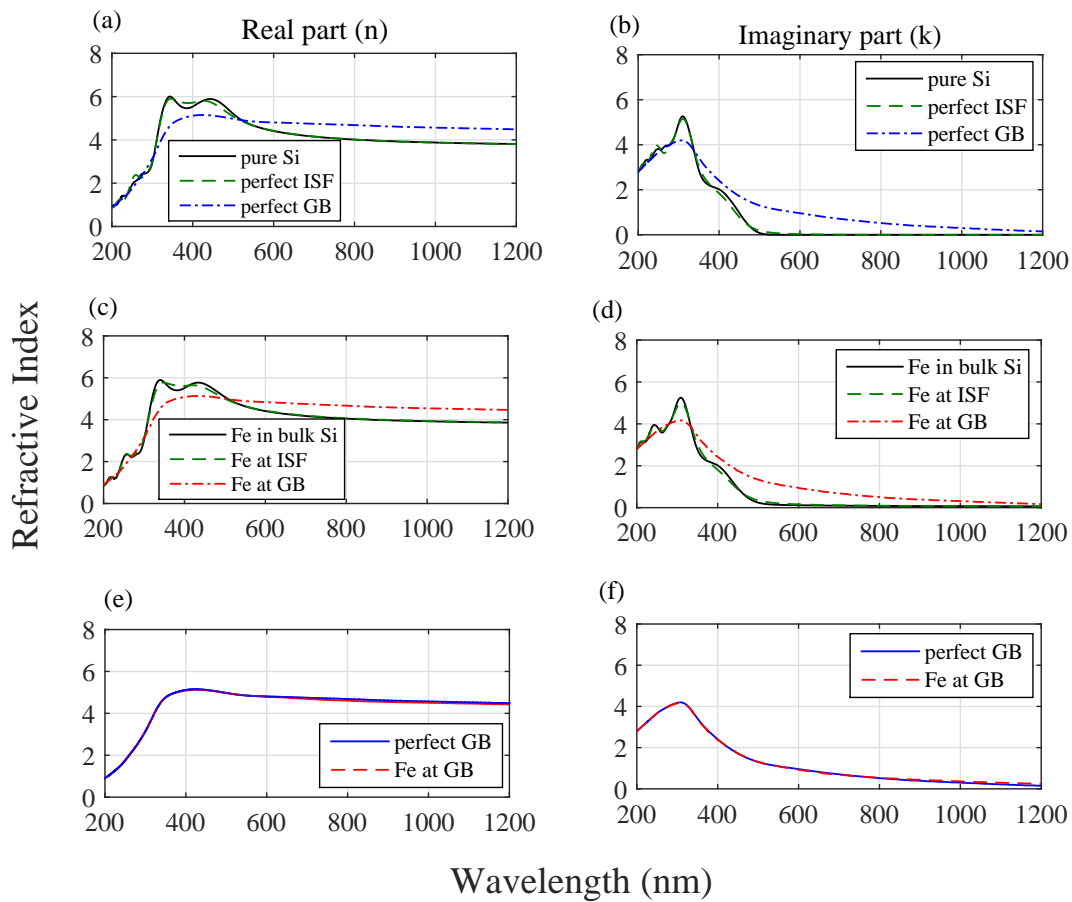


Figure 8.9: Computed real ( $n$ ) and imaginary ( $k$ ) parts of the refractive index for different structures as a function of wavelength showing the impact of ED and Fe contamination.

example, is around 3% shorter than at reference site ( $i''$ ), whereas the average distance is around 2% greater than the reference site for  $f''$ . This gives a hint that an important part of the stabilisation of interstitial Fe at GBs is the existence of open volume sites at the extended defects.

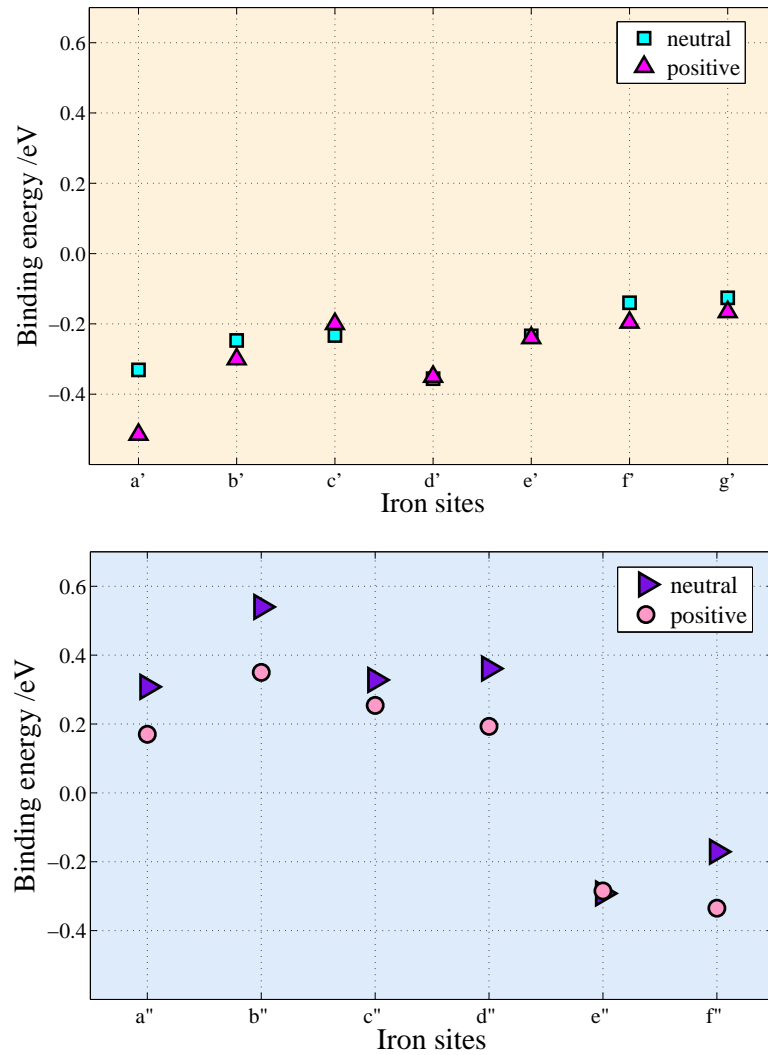


Figure 8.10: Binding energies (eV) of iron to the (top)  $\Sigma 5$ -(001) and (bottom)  $\Sigma 3$ -(110) twist grain-boundaries as a function of site (Figure 8.2) and charge state. Negative values correspond to an attraction between the GB and Fe, while positive values indicate that segregation is not favourable.

### 8.3.2.5 Bond-strain calculations

Where  $\text{Fe}_i$  is located at its equilibrium sites in the GBs (a' and e''), the Fe atom has a higher co-ordination than in the tetrahedral form in bulk silicon. The inter-nuclear distances and angles are indicated in figure 8.11, which resemble  $\text{FeSi}_2$  co-ordination [181] with eight Fe–Si distances of  $2.35\text{\AA}$ .

In an attempt to understand the observed trends in  $E^b$  (Figure 8.10), the outward relaxation of the nearest neighbours of  $\text{Fe}_i$  in each case have been examined.

According to the algorithm illustrated in section 5.2 (Figure 5.4), where Si–Si bonds for the Fe nearest neighbours have been calculated and compared with those in other specific references, and the root mean square for the vector that contains calculated strain

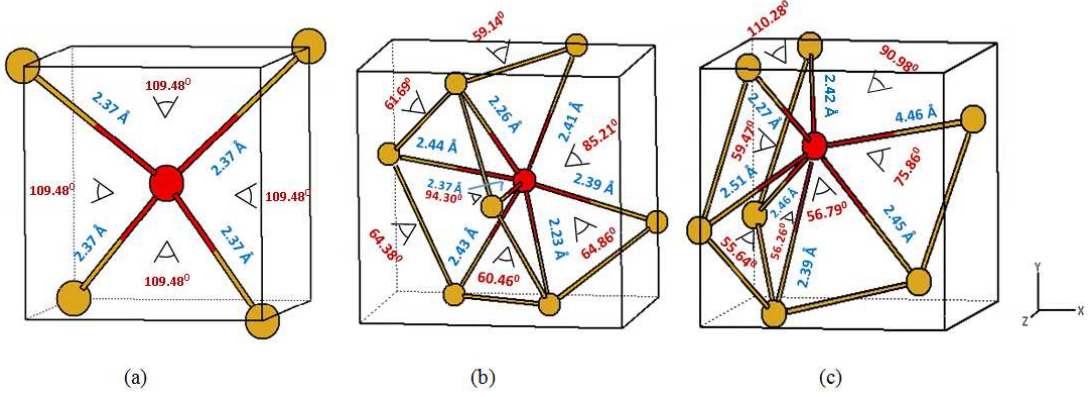


Figure 8.11: Schematic diagram showing the high coordination of iron at the ground state site of (b)  $\Sigma 5$ -(001) and (c)  $\Sigma 3$ -(110) twist GBs. (a) shows the calculated geometry of  $\text{Fe}_i$  in the bulk Si.

values are determined. Table 8.1 lists the rms strain caused by the present twist GBs and the impact of Fe-GB interaction with respect to Si-Si and Fe-Si bonds in other structures, including ideal Si, individual interstitial iron and  $\beta$ - $\text{FeSi}_2$  systems. From these comparisons, one can understand the impact of these defects and impurities on crystalline bulk Si. To overcome any uncertainty concerning these calculations, examinations of variations in value of bond length as a function of the optimisation iteration are performed over the full range of calculations. The analysis shows that the segregation of Fe at the equilibrium site (a') of the  $\Sigma 5$ -(001) twist GBs yields a change in bond-strain, and it is noticed that the strain is reduced significantly toward sites of bulk-like. This can reflect the relationship between strain and the magnitude of the binding energy, where sites with larger strain can more strongly bind to iron (with higher  $E^b$ ).

### 8.3.3 Fe-twist GBs complexes

In addition to  $\text{Fe}_i$ , the  $\Sigma 5$ -(001) GB incorporation of  $\text{Fe}_i$  at a vacancy, and the formation of  $\text{Fe}_i$ -pairs have been examined as described in the following sections.

#### 8.3.3.1 Iron-vacancy pairing and substitutional iron

GBs may contain vacancies that trap mobile  $\text{Fe}_i$ . If diffusing  $\text{Fe}_i$  encounters a neutral vacancy at the  $\Sigma 5$ -(001) GB, initially a near-neighbour  $\text{Fe}_i$ -V pair may be formed. Indeed, the NL19 EPR centre has been suggested to arise from such a structure [137].

Many sites inside the boundary have been investigated at the GB to find the equilibrium location of a vacancy with respect to Fe, and for the neutral charge state. Calculations show that the difference in energy between a structure which contains an individual

Table 8.1: Si–Si and Si–Fe bond-strain variation due to segregation of the diffusing iron at the sites provided by  $\Sigma 5$ -(001) twist GBs. Different structures are compared to calculate rms strains 1, 2 and 3 with respect to pure Si (Si–Si=4.41 au),  $\text{Fe}_i$  (Si–Si=4.42 au, Fe–Si=4.49 au) and  $\beta\text{-FeSi}_2$  (Si–Si=4.76 au, Fe–Si=4.39 au) respectively.

Fe site	Bond	Bond length	Strain 1	Strain 2	Strain 3
<b>a'</b>	Si–Si	4.41	1.65%	1.65%	7.46%
	Fe–Si	4.27	5.79%	5.79%	4.18%
<b>b'</b>	Si–Si	4.42	1.47%	1.44%	7.14%
	Fe–Si	4.34	3.68%	3.68%	1.93%
<b>c'</b>	Si–Si	4.42	1.58%	1.57%	7.29%
	Fe–Si	4.33	3.92%	3.92%	2.19%
<b>d'</b>	Si–Si	4.42	1.35%	1.34%	7.30%
	Fe–Si	4.48	1.76%	1.76%	2.86%
<b>e'</b>	Si–Si	4.44	1.64%	1.58%	6.84%
	Fe–Si	4.46	2.38%	2.38%	2.97%
<b>f'</b>	Si–Si	4.42	1.27%	1.25%	7.25%
	Fe–Si	4.52	2.91%	2.91%	4.15%
<b>i'</b>	Si–Si	4.43	0.69%	0.61%	6.98%
	Fe–Si	4.49	0.89%	0.89%	2.56%

vacancy and Fe (at site a') with a separation distance of 2.4Å is lower than when they are separated by 2.2Å by around 1 eV. With an increase in separation distance between the vacancy and  $\text{Fe}_i$  to 2.5Å, where Fe lies at site d', the structure obtained is found to be more stable than the structure with a distance of 2.3Å by about 0.4 eV.

The spin energies of a system containing a vacancy at different sites within the  $\Sigma 5$ -(001) twist GB are also investigated in this study. The results for ground state structure show that  $S = 1$  and  $S = 2$  are higher than  $S = 0$  by about 0.6 and 2 eV respectively. The ground state structure is lower in energy than other sites by around 0.3–0.7 eV, depending upon the vacancy site in the grain boundary.

The spin energies of the ground state of  $\text{Fe}_i\text{-}V$  at the  $\Sigma 5$ -(001) GB has been studied. It is found that structures with  $S = 0$  and  $S = 2$  are higher than  $S = 1$  by 0.05 eV and 0.60 eV respectively, as compared with  $\text{Fe}_i\text{-}V$  in the ISF (chapter 7) and bulk Si (chapter 5), where the  $S = 1$  and  $S = 2$  configurations of the  $\text{Fe}_i\text{-}V$  pair are higher than  $S = 0$ , suggesting the difference of the spin singlet to the ground-state of  $\text{Fe}_i\text{-}V$  for ISF and bulk as compared with the  $\Sigma 5$ -(001) GB. These comparisons are summarised in table 8.2.

Consequently, in the reaction to form the  $\text{Fe}_i\text{-}V$  pair from  $\text{Fe}_i$  in the grain and a vacancy in the  $\Sigma 5$ -(001) twist GB the energy is reduced by 1.6 eV, which is close to previous estimates for a similar reaction in bulk Si, which was 2 eV (section 5.3.2), and

also compares favourably with the findings of a previous study [147]. In contrast, the reaction to form an  $\text{Fe}_i\text{-}V$  pair from  $\text{Fe}_i$  in the bulk-like site and a vacancy in the ISF reduces the energy by 2.4 eV as described previously in section 7.3.3. This means that forming  $\text{Fe}_i\text{-}V$  pairs at planar defects is an exothermic interaction similar to that in bulk Si with varying energies.

When the  $\text{Fe}_i$  moves into the vacancy that may be present at the  $\Sigma 5\text{-}(001)$  GB, substitutional Fe ( $\text{Fe}_s$ ) is formed which is found to have a  $S = 0$  ground state lower than  $S = 1$  by 0.4 eV, and it is lower than other investigated sites by 0.9—2 eV depending upon the site in the grain boundary area. Consequently, the nearest-neighbour  $\text{Fe}_iV$  pair is 0.8—2.7 eV higher in energy than  $\text{Fe}_s$ , depending upon the site in the GB. Again the upper limit of the reaction energy compares favourably with the comparable bulk reaction which is estimated to release 2 eV [147]. It is concluded that forming the pair at the GB is more highly exothermic than the formation of the  $\text{Fe}_iV$  pair in ISFs (section 7.3.3) and bulk Si (section 5.3.2).

Table 8.2 summarises the spin energies for different structures, including  $\text{Fe}_i$ ,  $\text{Fe}_i\text{Fe}_i$  and  $\text{Fe}_iV$ ,  $\text{Fe}_s$ , in bulk and at the twist GBs. Structures in this table refer to the presence of individual impurities (Fe and mono vacancy) in bulk or at the ground state of the twist GBs. For example, the structure  $\text{Fe}_iV$  at the  $\Sigma 5\text{-}(001)$  GB means the formation an  $\text{Fe}_iV$  pair when  $\text{Fe}_i$  moves into the vacancy that may be present at the  $\Sigma 5$  GB. This interaction leads to modification in spin and charge states, as shown in the table. A positive value of  $\Delta H$  means that the interaction is exothermic, and so on for other structures in the table.

### 8.3.3.2 Iron pairs

It has been reported in chapter 6 that  $\text{Fe}_i$ -pairs are both bound (in contrast to an earlier report [147]) and mobile. This being the case, it is plausible that Fe atoms would arrive at the GBs in pairs or, should they arrive individually, that pairs would be formed in the  $\Sigma 5\text{-}(001)$  GB, and it has been concluded previously in chapter 7 that pairs have formed in the ISF. Many possible sites have been tested to investigate the equilibrium sites of the Fe pair at the  $\Sigma 5\text{-}(001)$  and  $\Sigma 3\text{-}(110)$  twist GBs. For example, the structure that includes  $\text{Fe}_i\text{Fe}_i$  at sites d' and c' of  $\Sigma 5$  (Figure 8.2) is release 0.9 eV higher in energy than the structure when the pair lie in sites a' and d'. Calculations of the ground state form of  $\text{Fe}_i\text{Fe}_i$  at  $\Sigma 5\text{-}(001)$  show that AFM ( $S = 0$ ) is more stable and lower in energy than the FM ( $S = 4$ ) and  $S = 1$  configurations by about 0.3 and 0.06 eV respectively, which are

similar to the case that obtained from the  $\text{Fe}_i\text{Fe}_i$  in bulk Si, whereas it differs from the case at the ISF (section 7.3.4). For  $\text{Fe}_i\text{Fe}_i^+$ , the energy difference between the doublet ground state and the  $S = 3/2$  and  $S = 5/2$  excited states is reduced to about 0.2 and 0.5 eV respectively. In contrast, the 5/2 ferromagnetic system is favoured in bulk Si, but similar to ISF.

Now, turning to the Fe-pair at  $\Sigma 3$ -(110) twist GBs,  $\text{Fe}_i\text{Fe}_i$  at sites d'' and e'' in figure 8.2 (c) are 1.4 eV higher in energy than if  $\text{Fe}_i$ -pairs lie at sites d'' and b''. The calculation of the spin energy of the ground state structure of the pair at  $\Sigma 3$  shows that AFM  $S = 0$  is favoured by 0.13 and 0.17 eV as compared with  $S = 1$  and  $S = 2$  respectively. For the positive charge state, a doublet spin is the most stable configuration.

The binding energy of a second  $\text{Fe}_i$  atom to the  $\Sigma 5$ -(001) GB is found to be greater than the first, at 1.5 eV. The energy gained by taking an iron-pair from the grain and locating it at the  $\Sigma 5$  is estimated to be 1.6 eV. In contrast, the energy lost by taking an iron-pair from the grain and locating it at the  $\Sigma 3$  is around 1 eV as this interaction is endothermic.

Table 8.2: Enthalpy of chemical reaction ( $\Delta H$ ) and the energy differences ( $\Delta E$ ) in eV associated with the different structures. These values indicate how much each of the other spin states are lower (negative) than the reference ( $S = 1$  and  $S = 1/2$ ) for neutral and single positive charge state respectively for each structure. Negative  $\Delta H$  means that the interaction is endothermic.

Structure	$\Delta E(S0 - S1)$	$\Delta E(S2 - S1)$	$\Delta E(S3/2 - S1/2)$	$\Delta H$ (eV)
$\text{Fe}_i$ at $\Sigma 5$	-0.01	0.55	0.26	0.40
$\text{Fe}_i\text{V}$ at $\Sigma 5$	0.05	0.60	0.07	1.60–1.99
$\text{Fe}_s$ at $\Sigma 5$	0.43	0.46	0.44	0.89–2.70
$\text{Fe}_i\text{Fe}_i$ at $\Sigma 5$	-0.06	0.21	0.16	1.64
$\text{Fe}_i$ at $\Sigma 3$	0.17	0.76	0.09	0.30
$\text{Fe}_i\text{V}$ pair at $\Sigma 3$	0.21	1.26	-0.07	-1.01
$\text{Fe}_i\text{Fe}_i$ at $\Sigma 3$	1.36	0.34	0.27	-1.13

## 8.4 Summary

There is some evidence of Fe gettering at grain boundaries is a viable route to reduction of the deleterious effects of Fe in mc-Si solar cells. In this chapter, the segregation of interstitial Fe at twist GBs has been studied as examples of structures with high strain as compared with the ISF studied in chapter 7. Based upon these atomistic calculations, it is found that Fe is bonded to the fully bonded  $\Sigma 5$ -(001) more strongly than to the  $\Sigma 3$ -(110), but with only modest energy ( $< 0.5$  eV).

However, this binding is greatly increased by  $\text{Fe}_i$  being trapped at vacancies at the GB or, perhaps more critically, by Fe already trapped there. The latter result indicates that the precipitation of Fe at GBs is strongly energetically favourable, even in the absence of the direct chemical bonding afforded by the substitution of Si by iron. Finally, table 8.2 summarises spin energy differences, and the values of enthalpy of the chemical reaction for the formation of defect-complexes, of the structures investigated in this chapter.

# Voids in Silicon as a Sink for Interstitial Iron

“The beautiful thing about learning is that no one can take it away from you.”

B.B. King

In the previous chapters 7 and 8, the analysis of iron gettering at ISF and GBs has been investigated as examples of planar defects (extended defects) that may be present in mc-Si, which can also contain volume (3D) defects. The main focus of this chapter is upon the gettering of Fe by voids as an example of volume EDs. A summary of published work on different void-related entities and their formation, structure, growth and evolution in silicon is introduced in section 9.1. Prior to the presentation of results obtained from simulations based upon the void model in section 9.3, the relevant computational methods are reported in section 9.2. Section 9.4 then summarises the main conclusions of this chapter. Perhaps surprisingly, it is found that the most stable site lies just outside the void, which may explain the experimental observation that only a single layer of iron forms at voids. The analysis of voids in Si as a sink for  $\text{Fe}_i$  has been published elsewhere [214].

## 9.1 Introduction

Many studies [215, 216] have been carried out on the irradiation of materials with light ions, particularly helium which is known to agglomerate into bubbles when implanted in semiconductors such as Si and involved in voids.

The growth and evolution of voids in Si have been investigated using both modelling and experimental techniques [217–220], including the role of strain [221]. Furthermore,

many have been attempted to describe the fundamentals and applications of these voids in Si device technology, particularly for gettering TMs [222–225]. The gettering of these impurities to less important (inactive) regions of devices is therefore a key mechanism in the optimisation of materials for applications such as photovoltaics. It has also been demonstrated [226,227] that atoms on the internal surfaces of voids are reactive to impurities and point defects like interstitials and vacancies, and so impact on dopant diffusivity and the suppression of secondary defects, where the suppression of EDs has been carried out using the presence of buried void layers.

### 9.1.1 Void formation

Typically, voids are formed in Si by the high-dose or plasma immersion [228] ion implantation of light ions (helium, hydrogen) followed by thermal annealing. Since helium is an inert gas, it does not interact with the Si atoms or other species, and thus no impurities can be left in the wafer and chemical interactions are avoided. Indeed, the formation of He bubbles is a quite complex phenomenon, involving a sequence of several independent procedures, and several technologies have been employed to explore all the peculiarities of this phenomenon. Although the role of the main components in bubble formation has been clarified in terms of radiation damage and the diffusion of implanted He atoms, a full understanding of the formation of bubbles and their evolution into voids can only be achieved via a comprehensive study of the experiments performed so far. During implantation, diffusion is enhanced because helium is repelled by vacancies. Conversely, He atoms are trapped by divacancies, stabilising them and favouring their evolution into more complex He-V clusters at temperatures higher than 400 °C. During implantation, interstitial Si atoms recombine at the surface in the same range of temperatures, resulting in a supersaturation of vacancies in the bulk Si. The density, morphology, and distribution of voids have been investigated with respect to an He beam energy of 20–300 KeV with a dosage range of  $1 \times 10^{16}/\text{cm}^2$ – $5 \times 10^{17}/\text{cm}^2$ , and an annealing temperature 800–1250 °C. It is important to mention that increasing dimensions of these clusters with increasing the dose (greater than  $1 \times 10^{16} \text{ cm}^{-2}$ ) enables the clusters to be observed by TEM analysis [229–231]. Narrow layers of voids can be formed at a depth controlled by the implant energy. The annealing temperature determines the size and density of these layers. It is also noticed that voids exhibit high levels of stability for long thermal processes (as long as 5 hours) with high temperatures up to 1250 °C [229–231]. A specific study [231]

of the formation of He–V clusters concluded that interaction occurred between He atoms and divacancies during the thermal process. Firstly, He–V clusters are formed when He ions are implanted in crystalline Si at temperatures around 100 °C and vacancies are still trapped in the cluster around 700 °C, whereas He atoms diffuse out from the Si samples. During that time, many silicon self-interstitials recombine directly at the surface, resulting in the supersaturation of vacancies in the bulk of Si. After He desorption, the remaining vacancy clusters evolve into voids in cases where their dimensions overcome the critical radius.

### 9.1.2 Role of voids in Si

Voids introduce mid-gap energy levels in Si, acting as recombination centres, and thus they control locally over the lifetime of minority carriers in Si power devices, since regions with poor lifetime can result in submicron tolerance [231]. Uniform layers of voids in Si can be obtained in an industrial environment by using standard processes in microelectronics [231].

Results obtained from real device operation can demonstrate the role of the dangling bonds present on the void surface as trap levels [231].

The formation of voids may be the only lifetime method so far devised that is stable for high thermal budgets and applicable in any step of device fabrication, allowing more versatile lifetime engineering in device design. The outcomes obtained are particularly advantageous for power devices, particularly where the presence of a well-localized carrier recombination region improves device performance [231]. It is noticed also that the fabrication of devices with voids can result in a lower on-state voltage drop than in devices with unlocalized lifetime control having the same turn-off time [231].

Gettering metal impurities due to the unsaturated silicon bonds present on the surfaces of voids has been studied in different devices such as diodes and transistors [231]. When processing temperature becomes higher than 900 °C, the trapped impurity atoms can be released without affecting the gettering efficiency of voids (as compared with other gettering centres). Thus, a subsequent segregation annealing allows the metal impurities to be relocalized in the void layer [231]. Recent studies [231, 232] agree that the internal surfaces of voids can getter metals such as Pt, Cu, Ni, and Fe. The binding energy of these species has been calculated at around 2 eV, in good agreement with the findings of another experimental study [233] which concluded that the binding energies of Fe and Cu

to voids are very similar (2.2 eV for Cu and 2.0 eV for Fe), and so the mechanisms driving the binding are likely to be similar for a variety of transition metal species. Although the values of  $E^b$  for all investigated metals are not so high, good getter capability is ensured by large numbers of traps introduced by the void layer (from  $10^{17}$  to  $10^{19}$  cm<sup>-3</sup>) [231].

DLTS has been used to determine the energy of the levels associated with the voids, where the near mid-gap levels for both electrons and holes are independent of void density, morphology, and distribution. These specifications can be utilised to locally control the lifetime of minority carriers in Si devices [231]. It has also been found [232] that the internal surfaces of voids getter TM impurities, with this mode of gettering having the advantage of not depending upon supersaturation or upon the nucleation and growth of a metal silicate precipitate.

All these uses for voids require a basic understanding of their structure, Si–Fe bond-formation, and the change in strain relative to Fe dissolved in the silicon lattice, as well as knowledge of their electrical impacts in Si. A description of the computational method used in this chapter is presented in the next section.

## 9.2 Computational Method

As described in chapter 2, DFT calculations are performed in all analyses in this and the previous chapters. The precise structure of microvoids is not well understood [234]. Therefore, in line with similar previous studies [235], a void was formed by removing all atoms up to one lattice constant from a central Si atoms in clockwise bulk silicon. For this study, 35-atoms have been removed from a 686 Si-atom, fcc supercell. By considering that the modelled void with radius ( $r$ ) has a spherical shape, the area ( $4\pi r^2$ ) and volume ( $V = \frac{4\pi r^3}{3}$ ) have been calculated. Atoms at the void surface which are initially under-coordinated are found to relax outwardly, with some also forming reconstructions. The optimised void structure is the reference state used for the evaluation of changes in Si–Si bond strain upon the introduction of Fe placed at different sites in the void cell. The energy required to bind Fe at the internal surface of a void is calculated using equation 9.1:

$$E^b = E^f(\text{complex}) - E^f(\text{void}) - E^f(\text{Fe}_i) \quad (9.1)$$

where  $E^f(X)$  is the formation energy. This method has been suggested in another theoretical study [235] to calculate  $E^b$  for different metal atoms in Si lying at a gettering site

of a void structure. Furthermore, using the same method that has been used to obtain values of  $E^b$  for ISFs and GBs in chapters 7 and 8,  $E^b$  of Fe at the sites provided by structures containing voids is calculated as the difference in energy between sites within the void and those in the bulk regions of the supercells which give the same results.

In an attempt to understand the calculated trends in  $E^b$ , the root mean square strain local to each iron site have been examined according to the method shown previously in section 5.2 (Figure 5.4). The Si–Si bonds for the Fe nearest neighbours have been determined and compared with those in other structures, including the theoretical bulk-silicon bond-length, as well as other specific references. In each case, Si–Si distances are included for Si-atoms within  $2.4\text{\AA}$  of the Fe atom, and their Si neighbours. Si-pairs are assumed to be bonded up to a maximum strain of 10% for the data presented. This threshold has been varied up to 20%, and this has no quantitative impact on most systems, and in particular the choice of this threshold has no impact upon the conclusions drawn.

## 9.3 Results and Discussions

### 9.3.1 Undecorated voids

As mentioned earlier in this chapter, a void is formed by removing 35-Si atoms from a 686 Si-atom fcc supercell, where non-equivalent sites relative to the void centre are investigated. In order to examine the direction of tension of the internal surface of the void, the diameters of atoms removed have been calculated before and after forwarding relaxation for the same Si atoms as  $1.25\text{\AA}$  and  $1.27\text{\AA}$  respectively.

By taking the structure as a rectangular prism (i.e.  $V = l \times w \times h$ ), where  $l=2.24\text{\AA}$ ,  $w=2.24\text{\AA}$  and  $h=1.92\text{\AA}$  are the cell length, width and height respectively, the void volume ratio with respect to the volume of the whole structure (i.e.  $V_{\text{void}}/V_{\text{structure}}$ ) is 10.65%.

The calculated absorption coefficient for the supercell containing a void is similar to pure Si at short wavelengths (200–450 nm), but it is found that the absorption at longer wavelengths is higher than in the pure Si case, as shown in figure 9.1. This is due to the increasing transition between occupied and empty states created by the dangling bonds of the internal surfaces of voids (Figure 9.3(a)).

Figure 9.2(a) and (b), comparing the real and imaginary parts with bulk Si as a function of wavelength, show a deviation of the refractive index for the structure containing a void from bulk behaviour.

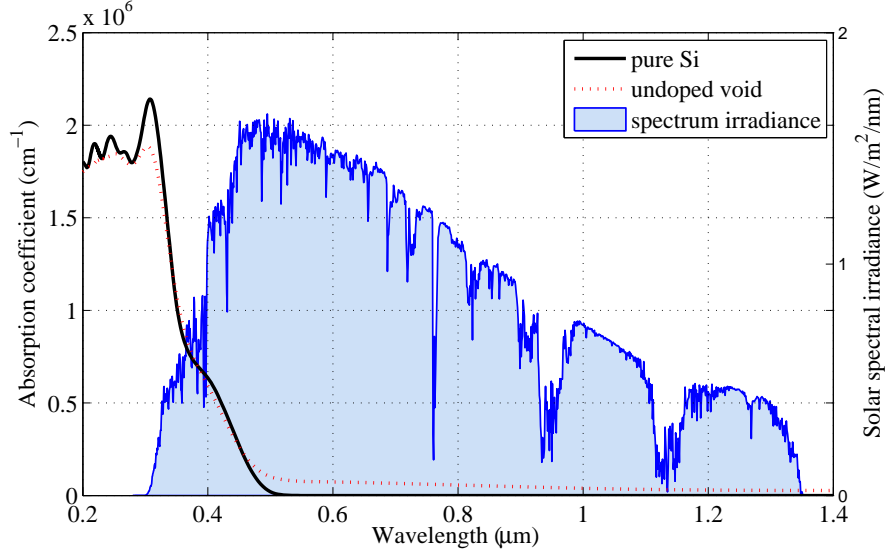


Figure 9.1: Calculated optical absorption coefficient versus wavelength for void and ideal silicon together with the AM1.5 solar power spectrum for comparison.

Fig. 9.3(a) shows the Kohn-Sham band structure of the undecorated voids, where unoccupied electronic states (deep acceptor levels) are introduced into the Si band gap, which are associated with dangling bonds of the internal surfaces of voids. These dangling bonds result from the removing Si atoms centre of the ideal Si structure. It has been predicted [231] that the chemical environment of bulk Si containing voids has a strong influence on its electrical behaviour due to these introduced surface states. This is because the empty states can increase the opportunity of the material containing voids to absorb long wavelengths of incident light (i.e. the difference in energy between occupied and empty states is about 0.1 eV). Although, the voids can modify the path of incident light where paths with longer wavelength have a higher possibility to trap light, the absorbed long wavelengths (IR) can raise the temperature of the PV device. In particular, it is agreed that both the electrical efficiency and the power output of a photovoltaic module depend linearly on operating temperature [236].

## 9.3.2 Interactions of Fe with a model void

### 9.3.2.1 Geometrical structure

The pseudo-spherical structure of the void used in this study generates a number of non-equivalent sites at its surface, as well as sites within the silicon at various distances from the core. Along these sites, the role of the spin and charge states of  $\text{Fe}_i$  has been investigated as a novel aspect of this study. With the void centre at (0,0,0), the distances

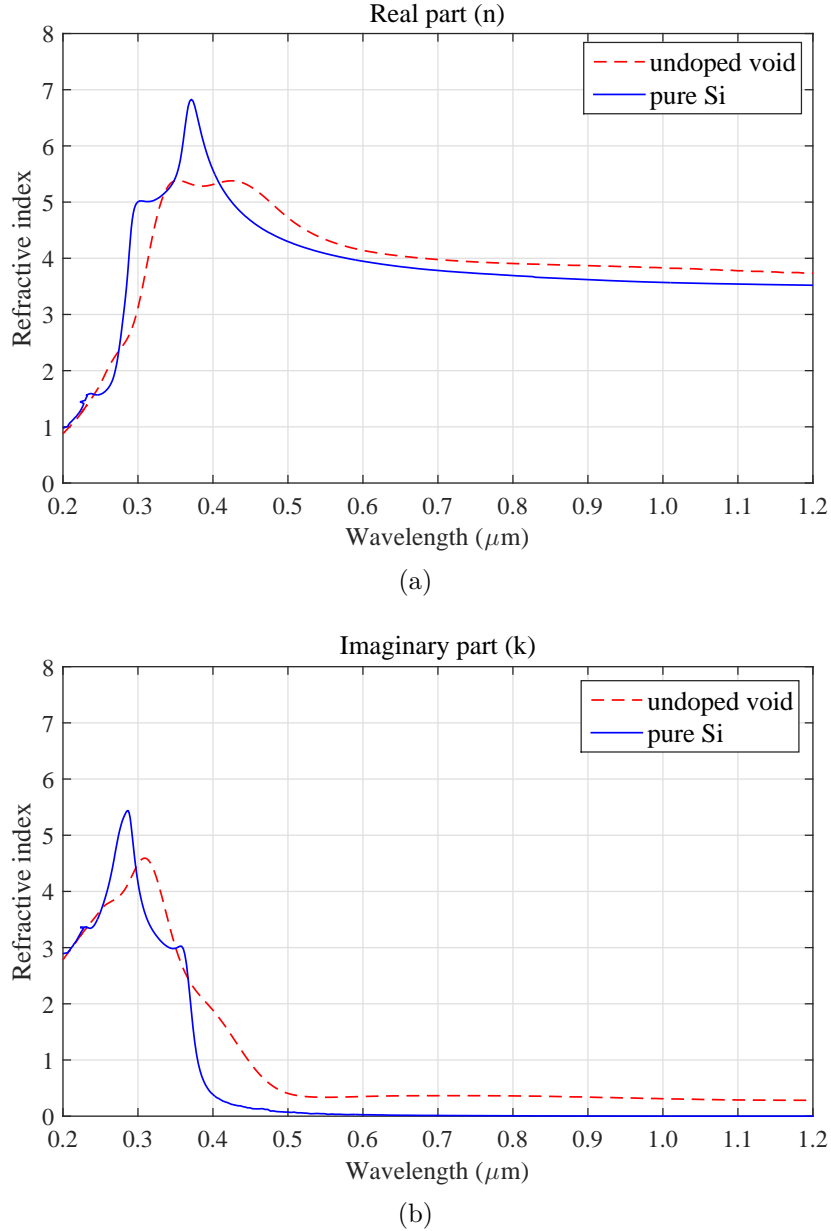


Figure 9.2: Computed real and imaginary parts of the refractive index for undecorated void showing its impact on bulk Si.

from the void centre to the Fe-site have been calculated and are listed in table 9.1.

### 9.3.2.2 Electronic properties

For sites within the internal surface, it is found that the  $S = 1$  and  $S = 2$  configurations of  $\text{Fe}_i^0$  are higher in energy than  $S = 0$ . Among these sites, and by labelling the distances from the void centre (0,0,0) to Fe-sites along the whole void structure ( $d_{(o,v)}$ ), it is found that an Fe-site at a distance  $d_{(o,v)} = 7.49 \text{ \AA}$  from the void centre (0,0,0) is the most stable site, where the  $S = 1$  and  $S = 2$  configurations of  $\text{Fe}_i^0$  are higher than  $S = 0$  by 0.03 and 0.05 eV, respectively. Notably, this suggests that the spin singlet is stabilised

relative to the triplet ground-state in comparison to  $\text{Fe}_i$  in bulk silicon. At an Fe-site with  $d_{(o,v)}=18.06\text{\AA}$ , it is found that  $S = 0$  and  $S = 2$  are 0.11 and 0.40 eV above the ground state, confirming that the environment after this distance can be considered as being relatively unperturbed by the cavity. In this work, sites which have the bulk environment are called bulk-like sites for clarification.

Similarly, for  $\text{Fe}_i^+$ , within the internal surface the energy difference between the doublet ground state and the quartet excited state is reduced to 0.06 eV, compared to 0.15 eV in bulk silicon and 0.12 eV at bulk-like sites. Changes in the relative energies of the different spin states is most likely a consequence of the increased volume associated with the hole due to the void, and the additional splitting of the  $d$ -orbitals of the iron due to local reductions in symmetry (effectively an additional local crystal field splitting).

Figure 9.3(b) shows the band structure for the iron located in a low-energy site ( $d_{(o,v)}=7.49\text{\AA}$ ) in the modelled void. By comparing this figure with the band structure of a Fe-free void (Figure 9.3(a)), it is obvious that Fe has no significant impact on the energy states created by the dangling bonds of the internal surfaces of the voids. However, the voids can segregate Fe more strongly than ISFs (chapter 7) and GBs (chapter 8), as shown in the following section.

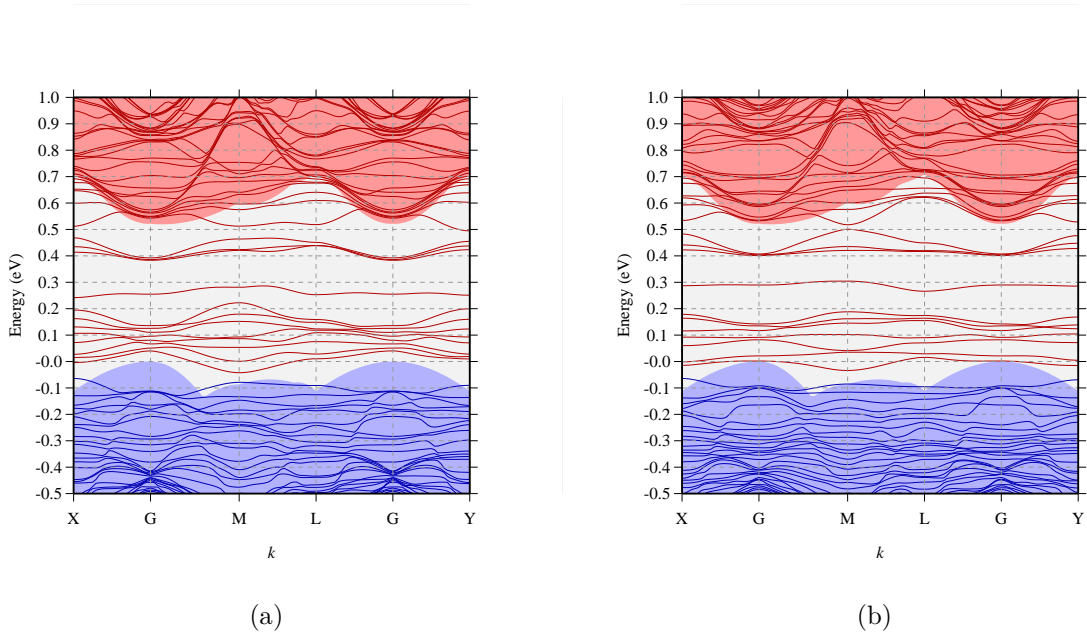


Figure 9.3: The Kohn-Sham band structures in the vicinity of the band-gap for a) clean voids (651 Si atoms); b) the most stable neutral state ( $S = 0$ ) of Fe site at distance  $d_{(o,v)}=7.49\text{\AA}$  from the void centre of void structure, plotted along high-symmetry branches in the first BZ. Occupied and unoccupied states are depicted as solid blue and dashed red lines respectively. The underlying shaded regions show the electronic band structure for the corresponding bulk Si. Red and blue lines show filled and empty bands respectively. The energy scale is defined by the valence band-top of Si at zero energy.

### 9.3.2.3 Binding energy and bond-strain

In general, creating a surface in crystalline material costs energy, and the atoms located at the boundaries of the surface behave differently from those in the rest of the bulk. The Si atoms in the vicinity of the internal surface may form reconstructions with each other, and are more free than atoms in bulk silicon to form re-arrangements to accommodate the chemistry associated with iron.

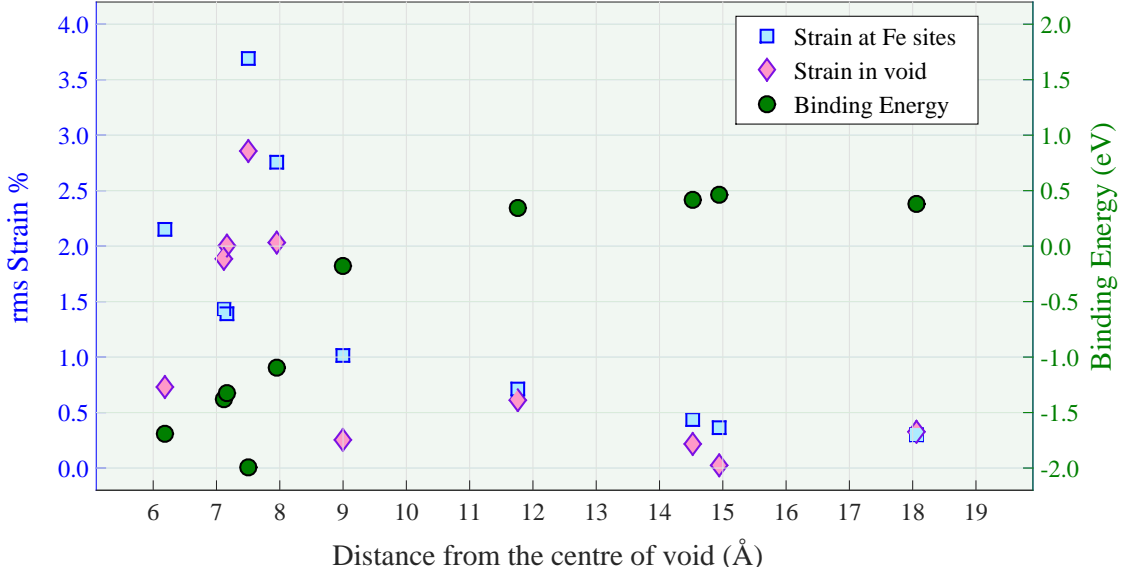


Figure 9.4: Binding energy (eV) of iron to the void as a function of distance from the void centre (circles), and rms strain in the Fe-neighbouring Si–Si bonds as described in the text (squares). For comparison, the strains for the same Si atoms in the Fe-free cases have also been plotted (triangles).

Figure 9.4 shows a plot of the binding energy and rms strain in the silicon neighbouring the Fe atom as a function of distance from the void centre. Similar bond length calculations for the same Si–Si bonds before adding Fe have also been carried out and presented for comparison purposes.

Both methods that have been used to calculate  $E^b$  (section 9.2) gave the same result. It is found that  $E^b$  has an upper bound of  $\sim 2$  eV, in agreement with the average binding energy obtained from another previous calculation [235]. Furthermore, in this study, calculated values for  $E^b$  compare well with experimentally obtained estimates [131, 231] which place the binding energy in the range of 1.4–1.5 eV and 2.0 eV [217]. The relatively high values of  $E^b$  indicate that Fe will be gettered effectively by void structures.

The sites which are bound by more than 1 eV are only in the immediate vicinity of the surface, but lying within the silicon: the Fe atom lies outside the void, and it does not sit

on top of the internal surface. This might be viewed as surprising, as one might imagine that Fe could chemically react with the under-co-ordinated surface Si atoms, but instead it is found that iron adopts a location within the first cages neighbouring the void where it has a high co-ordination number.

For iron located in low-energy sites in our model void (at distances of 7–8 Å from the void centre) in figure 9.4, a spin singlet ground state is found in contrast to the triplet ground-state of  $\text{Fe}_i$  in bulk silicon. This highlights the electronic and magnetic differences between iron dissolved in the bulk lattice and iron at gettering sites, which has also been noted for iron located at a grain boundary [182]. The low spin-state may also point to a different chemical state for Fe in low-energy sites in the vicinity of the void.

Figure 9.4 also shows that, where the binding energy is greatest (most negative), there is an higher strain in the surrounding silicon after the introduction of the Fe atom relative to the strain in the same region of the simulation cell when only the void is present. The introduction of the Fe atom therefore increases the Si–Si strain, which would obviously represent a cost in energy. Since the total energy is evidently lower in these “high-strain regions”, which, is in agreement with other simulations, Fe-segregation into Si  $\Sigma 5(310)$  GBs occurs despite increasing strain [72].

In addition, the Si–Si and Fe–Si bond-strains for Fe sites along the structure containing voids are listed in table 9.1, showing the changes in the bonds as compared with those in  $\text{Fe}_i$  in bulk Si and iron silicate. To overcome any uncertainty concerning these calculations, an examination of the variation in bond length values as a function of optimisation iterations is also performed over the full range of calculations.

#### 9.3.2.4 Coordination of Fe at the internal surface

The critical factor is that, although the bond-strain is large for Fe adjacent to the void, the presence of the iron changes the local co-ordination of the Si atoms. This is reflected in the geometry of the site that has been determined to be most stable in the modelled void system (7–8 Å, figure 9.4). The dramatic difference in bond lengths and angles relative to those of Fe at the tetrahedral interstitial location in bulk Si can be seen in figure 9.5, where the coordination of Fe at the void before and after relaxation, on the middle and right respectively, are clearly different from that in the bulk (left). The Fe–Si distance is perhaps only slightly different from those determined for  $\text{Fe}_i$  in the bulk, but there is clearly a much higher co-ordination number in the location adjacent to the void, and the

Table 9.1: Distances from the void centre with respect to the whole void structure, where  $d_{(o,v)}$ , is calculated as the distance of Fe after relaxation  $\times a_0$ , where  $a_0=10.19\text{\AA}$ . Furthermore, Si—Si and Si—Fe bond changes due to segregation of the diffusing iron at the sites provided by internal surface of void are also listed. Different structures are compared to calculate rms strains 1 and 2 with respect to  $\text{Fe}_i$  (Si—Si=4.42 au, Fe—Si=4.49 au) and  $\beta\text{-FeSi}_2$  (Si—Si=4.76 au, Fe—Si=4.39 au), respectively.

$d_{(o,v)}$	Bond	Strain 1 (%)	Strain 2 (%)
6.18	Si—Si	6.673	1.556
	Fe—Si	3.591	5.241
7.11	Si—Si	7.316	0.126
	Fe—Si	0.572	1.711
7.15	Si—Si	7.314	0.124
	Fe—Si	0.575	1.708
7.49	Si—Si	7.331	0.146
	Fe—Si	0.567	1.716
7.95	Si—Si	7.325	0.136
	Fe—Si	0.558	1.727
7.50	Si—Si	7.321	0.132
	Fe—Si	0.570	1.711
11.75	Si—Si	7.313	0.132
	Fe—Si	0.570	1.713
14.51	Si—Si	7.314	0.125
	Fe—Si	0.573	1.710
14.94	Si—Si	7.347	0.199
	Fe—Si	0.508	1.886
18.06	Si—Si	7.316	0.127
	Fe—Si	0.575	1.712

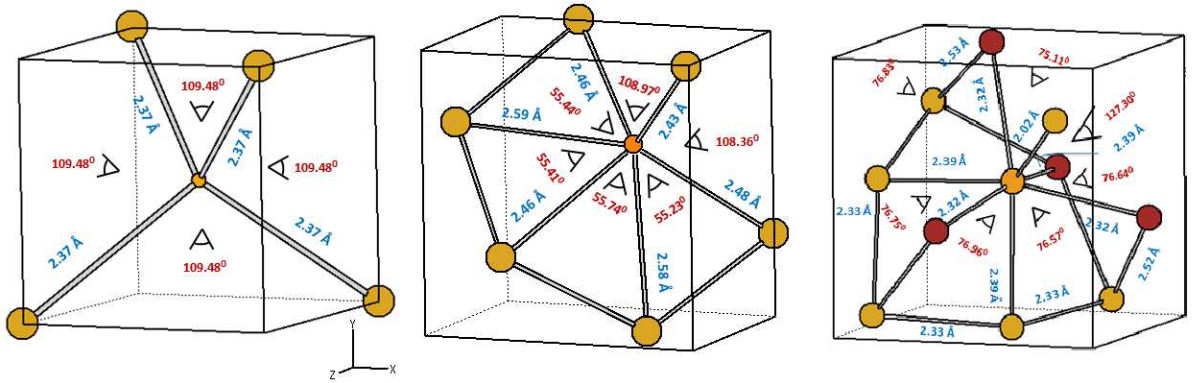


Figure 9.5: Schematics of equilibrium structures showing differences in bond lengths and angles of iron in the bulk Si (left) compared with the higher coordination of Fe at the gettering site of the void after relaxation (right). The centre panel shows the right structure prior to optimisation, so that the significant re-arrangement induced by the presence of Fe may be seen. Yellow and orange atoms represent Si and Fe respectively. Red atoms represent additional Si atoms only co-ordinated to Fe after relaxation.

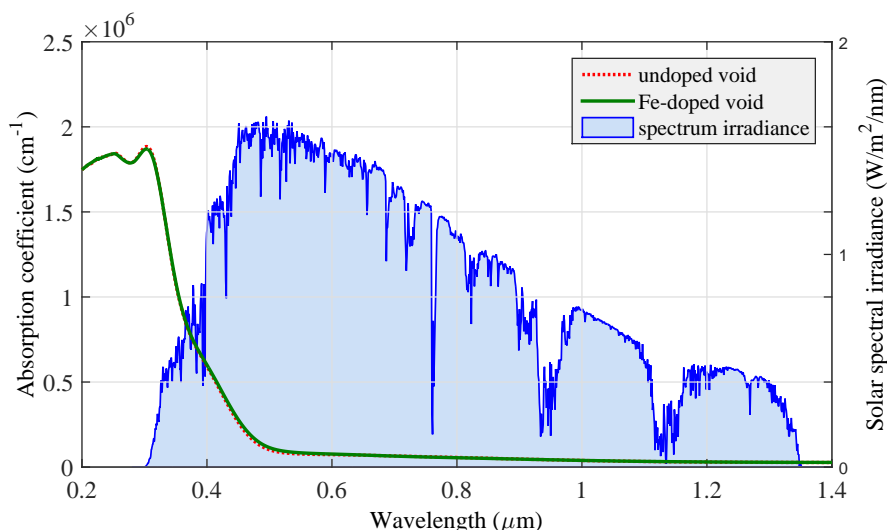


Figure 9.6: Calculated optical absorption coefficient versus wavelength for undoped and Fe-doped voids together with the AM1.5g solar power spectrum for comparison.

bond-angles are longer than those of a tetrahedron. The higher co-ordination may be viewed as resembling the equilibrium atomic coordination of iron silicide ( $\text{FeSi}_2$ ), which has Fe–Si distances of  $2.35\text{\AA}$  [181], and a co-ordination of eight with neighbouring silicon atoms.

The obtained low-energy structure may explain the experimental observation that only a single layer of iron forms at voids [237]. Due to the low migration enthalpies of Fe atoms in Si, rapid motion of Fe is investigated to be absorbed as a monolayer on the internal surface of the voids. The low-energy sites outside the void may act as a barrier to Fe moving to fill the voids [237].

Once the low energy sites just outside the void are exhausted, subsequent additions are likely to more closely resemble the bulk interstitial site, for which no significant binding energy is determined. However, given the importance of the relationship between the location of transition metals and the void volume in single-crystal silicon [238], resolving under what conditions voids might incorporate Fe directly is of some interest.

### 9.3.2.5 Optical properties

As mentioned before (Figure 9.1), the calculated computed absorption coefficient for the supercell containing the void is similar to pure Si for short wavelengths. For the case where iron has been placed either at the void structure, it is found that there is no significant impact of the iron on the optical properties of pure Si, as shown in figure 9.6.

Figure 9.7 shows the complex refractive index of the void, showing significant deviation from bulk behaviour. This could reflect the localised states introduced by the Fe.

The minor impact of Fe in supercells containing voids (Figure 9.7) reflects the small number of states introduced by the Fe relative to the density of states from the underlying Si structures, with the main impact of Fe being discernible in the long wavelength ranges where transition from the gap states plays a role.

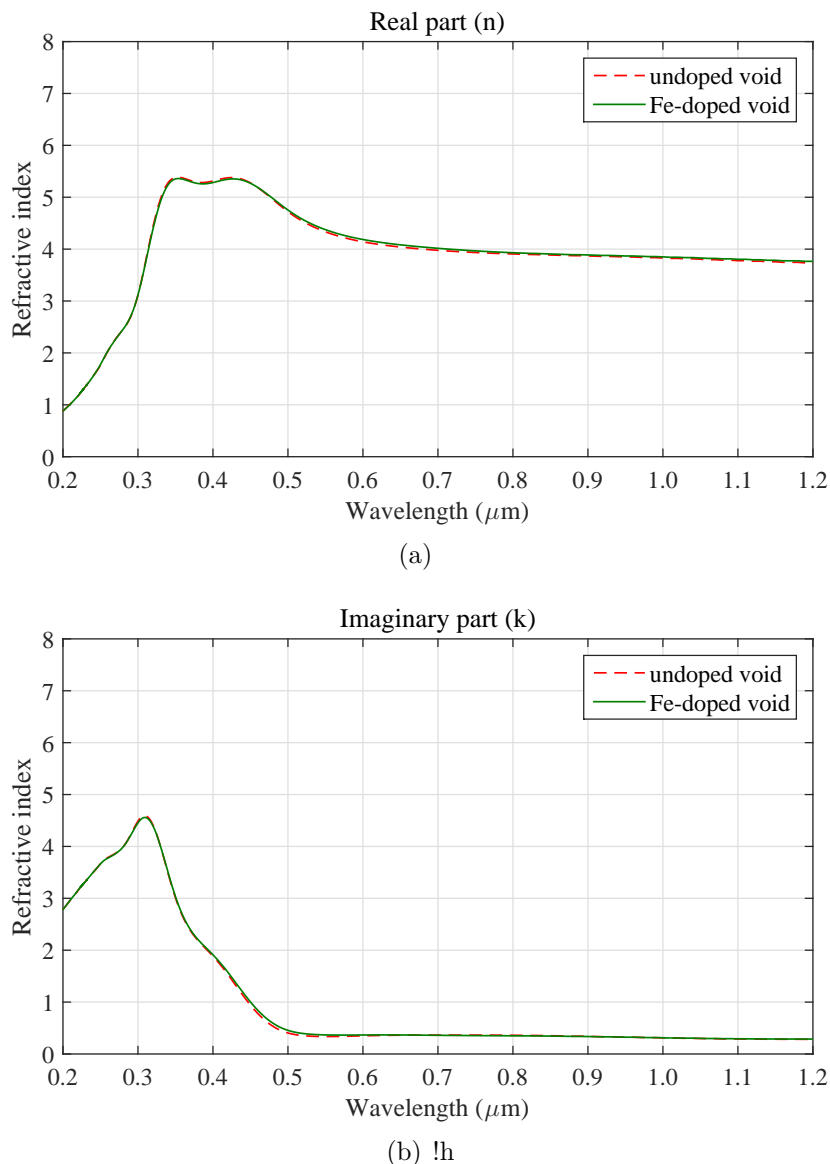


Figure 9.7: Computed real and imaginary parts of the refractive index for Fe-doped voids showing the impact of Fe contamination.

## 9.4 Summary

It is agreed that voids are one potential gettering site for iron. The mechanism of void formation is described in this chapter, and the growth and evolution studies of voids in Si using both modelling and experimental techniques have been reviewed. Using density functional theory, the segregation energy of an interstitial Fe impurity in a modelled void

in crystalline silicon has been investigated. At the void surface, non-tetrahedrally coordinated atoms represent sites with considerable levels of outward bond-strain. Binding the diffusing iron at the internal surface gives rise to a binding energy in the range of 1–2 eV. This reflects an effective role for such voids in the segregation of iron, with the binding being a change in the surface strain but which predominantly results from the formation of a chemical co-ordination similar to  $\text{FeSi}_2$ . The chemical reaction is also consistent with the much higher binding energy of Fe to the void in comparison to other extended defects such as the intrinsic stacking fault,  $\Sigma 3$ -(110) and  $\Sigma 5$ -(001) twist GB, which provides binding by just 0.2–0.5 eV which strain differences are largely responsible. It is not yet clear whether or not Fe–Fe interactions at the void would further stabilise the segregation of these impurities. This will be the subject of further investigation.

# Engineering of Extended Defects with Iron Contamination for Improved mc-Si Solar Cells

“Almost every way we make electricity today, except for the emerging renewable and nuclear, puts out CO<sub>2</sub>. And so, what we are going to have to do at a global scale, is create a new system. And so, we need energy miracles.”

William Henry Gates III

In the previous five chapters (5–9), first-principles quantum-chemical simulations have been used to investigate the electronic and optical properties as well as other properties of Fe<sub>i</sub> in c-Si as well as at selected extended defects representative of mc-Si. The data obtained at the quantum-mechanical level provide a basis for whole-device level simulation using TCAD tools (see chapter 4), and the results are presented in this chapter. A combination of these methods is employed to understand the effect of ISFs and GBs on the relevant properties of Fe-doped Si, and then on solar cell performance. This study provides some physical insights into how these planar defects and Fe<sub>i</sub> impurities affect solar cell performance. In particular, the strain associated with such defects was expected to have the potential to both beneficially alter the bandgap and optical absorption coefficient, and play a role in the segregation of iron.

This chapter is organised as follows. Section 10.1 reviews other relevant studies. In section 10.2, a brief review of the atomic parameters employed in device simulation, including the parameters of the solar cell model, are pointed out. The analysis of results

for different cases (pure Si, undecorated planar defects, Fe-doped Si and Fe-decorated planar defects) on the performance of solar cells is presented in section 10.3. Finally, section 10.4 summarises the main conclusions of this chapter.

The investigation into efficiency-limiting defects in mc-Si solar cell has already been published [128], whereas the analysis of the engineering of extended defects with iron contamination for improved mc-Si solar cells has been submitted for publish in the IEEE journal of photovoltaics.

## 10.1 Introduction

As explained in chapter 1, mc-Si can offer a cost-effective option to gain reasonable cell efficiency compared to mono-crystalline Si [239], but it generally contains EDs and contamination by transition elements that are present during the ingot growth and fabrication process [131]. In addition, it has been mentioned in previous chapters that  $Fe_i$  acts as an effective recombination centre, reducing solar cell performance even at less than 1 ppb [57], and it is generally agreed that iron and its complexes and precipitates are detrimental for Si devices due to its deep levels and reduction in minority carrier lifetime [57].  $Fe_i$  in bulk Si has been studied in chapters 5 and 6, whereas its interaction with ISFs, GBs and voids has been considered in chapters 7–9, respectively, which also mention the numerous theoretical [189, 240] and experimental [171, 176, 241] studies of the properties of EDs in Si. Structures and areal energy-densities of the EDs have been obtained previously [171, 173, 175, 176]. There is some evidence that the presence of strained EDs, such as in twist GBs, reduces overall carrier mobility, and that they act as recombination centres significantly reducing carrier lifetimes [242]. However, EDs may also reduce the undesirable impact of iron by internal gettering, reducing iron concentrations in the rest of the material and improving solar-cell efficiency. Indeed, and as mentioned before, there is strong evidence that EDs interact with mobile iron defects [171, 203], and recent experimental studies demonstrate that the minority carrier lifetime can be increased in as-grown mc-Si by low temperature internal gettering [243]. Additionally, there is evidence that GBs may enhance PV performance [58], where the internal strain and local effects on band-structure in nano- and micro-crystalline Si improve optical absorption, increase the open-circuit voltage, and decrease intrinsic carrier concentration.

For relatively high concentrations of Fe, there is evidence of the formation of iron silicide secondary phases, and the presence of these precipitates has been studied exten-

sively [195]. Precipitation has been identified in the GB [244, 245] and stacking faults, where precipitation occurs mainly through gettering into structural defects at high temperature [54]. Two distinct groups of iron silicide precipitates have been observed in mc-Si solar cells: nano- and micro-precipitates [195]. Nano-precipitates (small size and high density) are more significant for carrier lifetime and diffusion-length than micro-precipitates (large size and low density). The formation of nano-precipitates occurs at Fe concentrations exceeding  $10^{15}\text{cm}^{-3}$  [195, 245], which is much greater than the regime that forms the basis of this study at  $10^{12}\text{cm}^{-3}$ .

Based upon the lower concentrations of Fe, a similar methodology to that in previous work [58] has been applied in this work to examine the role of prototypical fully bonded planar EDs in mc-Si. Combination has been achieved in this chapter between. First principles DFT to model the energies and structures of interstitial Fe in bulk silicon and in the vicinity of an ISF and on the other hand TCAD device modelling to predict the effect on solar energy conversion. It has been noted [246], as reviewed in chapter 4, that TCAD tools have been widely utilized to model solar cells with different material systems to calculate electrical and optical properties.

## 10.2 Methodology

### 10.2.1 Atomic simulations

Details of the modelling of bulk silicon using the primitive fcc cell, and with defects in 216- and 512-atom simple cubic supercells, are presented in section 5.3, along with a description of the properties of  $\text{Fe}_i$  in bulk Si. Furthermore, the modelling of different structures with planar defects doped and un-doped by iron using LDA have been discussed in detail in chapters 7 and 8. The structures of both the ISF and  $\Sigma 5$ -(001) twist GB are shown in figure 10.1. Based on the calculations reported in chapters 5–7 for both  $\text{Fe}_i$  and the EDs separately, the accuracy of the methodology used has been found to be a sufficient basis upon which to present the results for Fe-ED interactions.

Optical absorption coefficients are obtained from the dielectric functions (described in section 3.8) shown separately for Fe-decorated and undecorated EDs structures referencing pure Si and Fe-doped bulk Si. However, all the graphs related to these structures in this chapter are combined in one figure to study the effects of optical properties on solar cell performance. Further details are presented later in section 10.3.

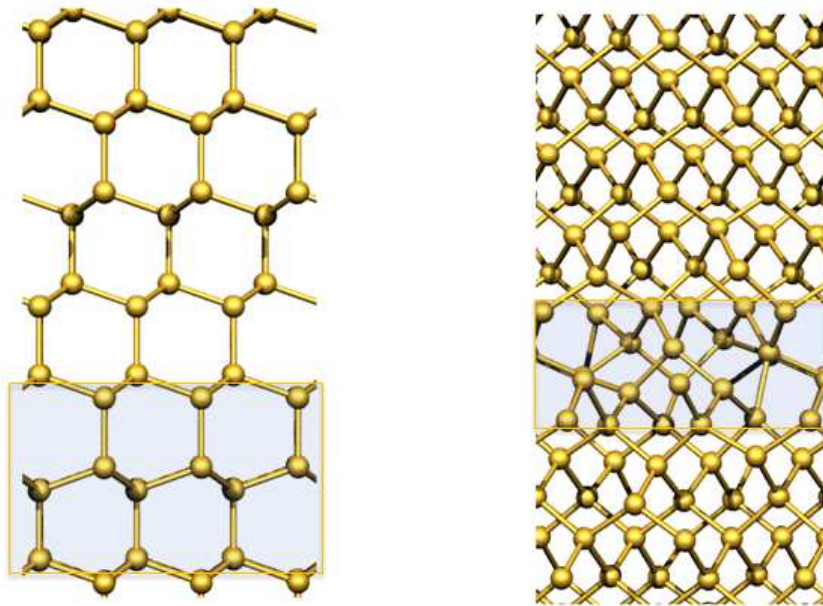


Figure 10.1: Projection of optimised structures of the ISF (left) and  $\Sigma 5$ GB (right). Shaded area highlight the interface region.

### 10.2.2 Device simulations

TCAD calculations are performed using the Sentaurus package [247], and the background behind this package had been reviewed in detail in chapter 4.

### 10.2.3 Photovoltaic device modelling

By using Sentarus Structure Editor (SDE), in which device geometry and doping profiles are specified, the Si solar cell structure was built. For simplicity, a basic 2D solar cell structure has been adopted for this study. The parameters of the solar cell, including the impact of dissolved Fe, correspond to a standard silicon device [247] where illumination is under the AM1.5 Global model at normal incidence [180]. The solar-cell model is comprised from a  $600 \times 250 \mu\text{m}$  p-type substrate ( $p = 2 \times 10^{16} \text{cm}^{-3}$ ), a 150 nm n-type emitter layer ( $n = 6 \times 10^{19} \text{cm}^{-3}$ ) and a top 75 nm silicon-nitride layer as an anti-reflection-coating, with a refractive index between 2.0 to 2.1 within the visible light region. The back contact is a  $3 \mu\text{m}$  p+ boron layer of  $600 \mu\text{m}$  width and the doping concentration is  $10^{19} \text{cm}^{-3}$ .

### 10.2.4 Grain specification

Typically grain sizes in mc-Si are larger than one millimetre. Since the thickness of grain-boundary layers is much smaller than this scale, the majority of the volume of the solar cell

corresponds to silicon grain interiors. Based on experimental studies [248, 249], the GBs comprise 5–30% of the relevant wafer area in mc-Si depending on height and location inside the ingot, and to simulate this the device is divided into 80% crystalline silicon and 20% associated with material modified by the existence of the grain boundary. It is assumed that all GBs are characterized by the properties determined for the  $\Sigma 5$ GBs. The grains are oriented between contacts in the PV device, so that transport is either effectively through the grain (single-crystal-like silicon), or through the GB. The assumption is that grain size is significantly greater than the diffusion length of the carriers. Viewed in cross-section, the GBs present a proportion of the device, albeit in a connected network. The effective width essentially allows for a reasonable density, including a reasonable distance within which generated carriers would be captured.

### 10.2.5 Meshing distribution

Throughout the SDE script, refinements of the generated solar cell structure are used during meshing, where the simulation domain consists of a cut perpendicular to the front metallisation grid. The symmetry element of  $600 \mu\text{m}$  in width expands from the middle of the contact to the mid-point between two contacts. It has been taken into account that the anti-reflection coating is modelled as a single SiN layer to reduce reflection losses. In addition, the formation of the pn-junction is modelled as a  $0.50 \mu\text{m}$  thin p-doped region (modelled by a Gaussian profile) on top of a thick n-doped substrate. The back-side contact stretches over the whole width of the solar cell structure [250].

In the iron diffusion process described in section 4.6.1, the horizontal line spacing (depicted in figure 10.2) of the grid has been varied to study the grid impact on device efficiency at three iron concentrations of  $10^8$ ,  $10^{12}$  and  $10^{15}$ . The different grid line spacing values used in this study were 0.1, 0.5, 2, 5 and  $10 \mu\text{m}$ . The results show that grid size has no significant impact on device efficiency at low iron concentrations, while it exhibits noticeable variation at high concentrations especially at the line spacing of  $10 \mu\text{m}$  as illustrated in figure 10.3. Since the line spacing of  $0.1 \mu\text{m}$  (dense mesh) gives similar results to the line spacing of  $5 \mu\text{m}$ , the latter has been adopted throughout the work in this thesis as it needs less computational time.

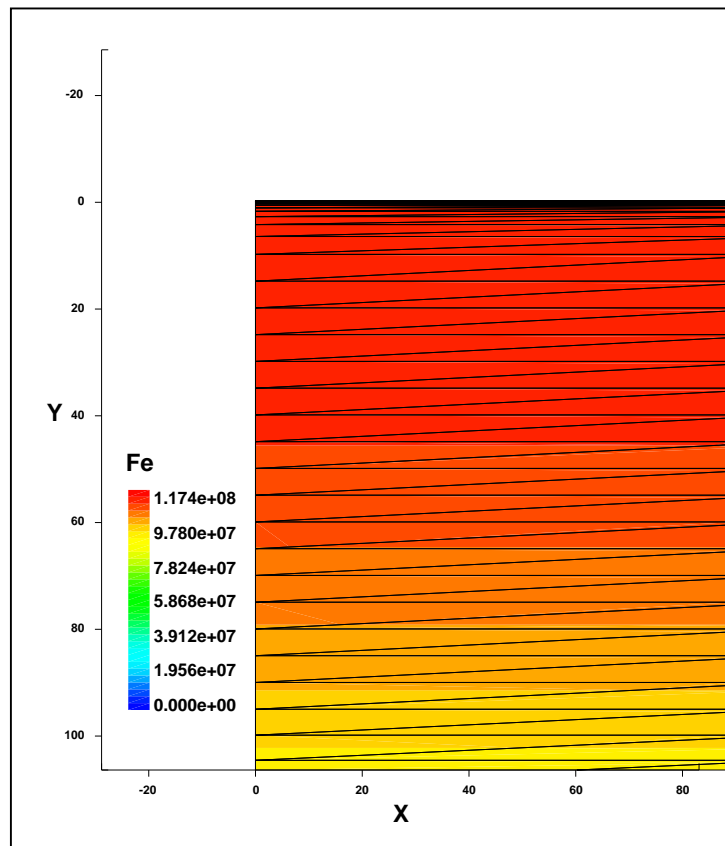


Figure 10.2: Part of solar cell structure generated by Sentaurus Structure Editor shows the horizontal line spacing of the grid through the Fe diffusion process in the Si substrate.

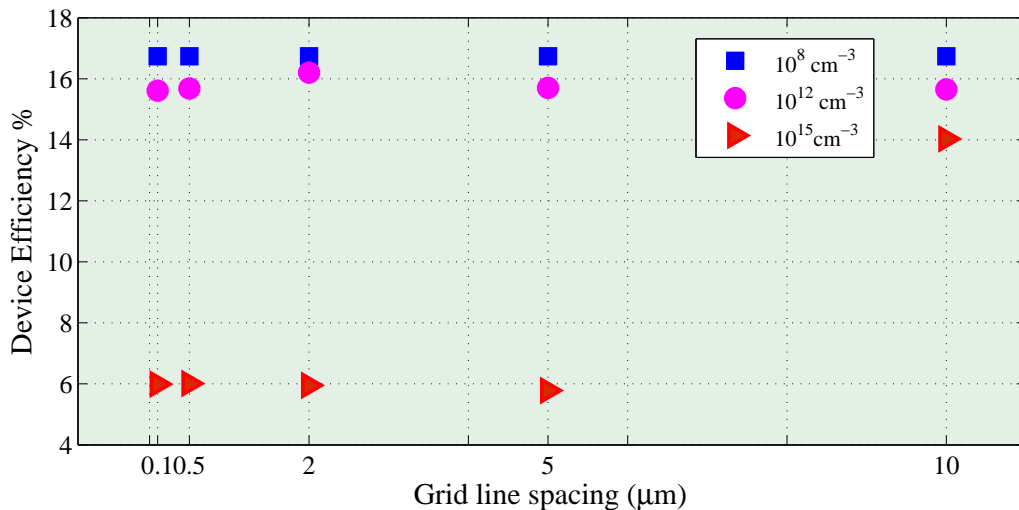


Figure 10.3: Impact of the horizontal line spacing of the grid on the solar cell efficiency at different iron concentrations.

### 10.2.6 Incident light

Simulations using Sentaurus Device were performed where a solar spectrum is utilised to simulate light incident on the solar cell. The reflection and transmission of light at material interfaces and light absorption in silicon are determined using the wavelength-dependent complex refractive index of materials via the transfer matrix method (see Sec. 4.5.1) to

calculate the propagation of plane waves through layered media [115]. This method gives a fast and accurate model for planar layered structures. In the solar cell model used in this thesis, it is assumed that the light incident on the solar cell is completely absorbed or reflected by the metallisation of the top contact. In addition to that, the depths of the material's layers and the complex refractive coefficients are taken into account in the calculations of reflectance and transmittance coefficients.

### 10.2.7 Fe-contamination in PV

For Fe-contamination, the trap distribution, capture cross-section (See section 4.6.2) and energy levels are translated into a spatially dependent SRH recombination process, with an electron capture cross-section of  $1.3 \times 10^{-14} \text{cm}^2$  [125].

It is considered that iron produces a donor level into mc-Si at approximately 0.4 eV above the  $E_v$  [251, 252], and, in order to study the tolerance of this level position with reference to  $E_v$ , different values of the possible position of the donor level have been examined at a range of 0.2 eV to the mid-band line as illustrated in figure 10.4. The impact of donor location on the conversion efficiency is presented later in section 10.3.2. The simulations include generation and recombination processes via the transfer matrix,

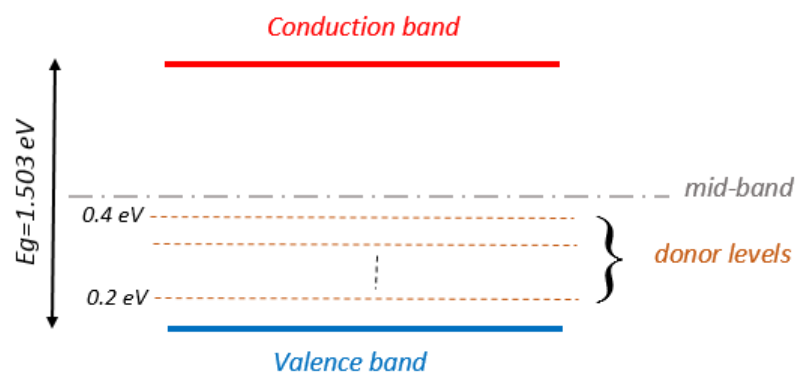


Figure 10.4: Schematic illustration of donor levels produced due to iron impurities for the case of the GB structure.

Auger and SRH recombination rates (section 1.3.2) respectively, and a doping-dependent mobility (Section 4.7) has been adopted [126]. The optical and electronic parameters of EDs were calculated at atomic level and employed in TCAD, with bulk recombination parameters used.

A value of the intrinsic electron density of  $9.65 \times 10^9 \text{cm}^{-3}$  has also been adopted [253], and bandgap narrowing due to heavily doped substrates has been employed [254].

Based on the aforementioned modelling parameters, extensive simulations have been

carried out to compare solar cells with different defects to the ideal Si-based solar cell, with particular reference to the short-circuit current-density ( $J_{sc}$ ), open-circuit voltage ( $V_{oc}$ ) and device efficiency. The principal aim of this chapter is to evaluate the performance of mc-Si solar cells with ED-related effects and the interaction with Fe impurities by combining atomic and device-level simulations.

## 10.3 Results and Discussion

### 10.3.1 Extended defects

The ISF and  $\Sigma 5$ GB structures are illustrated in figure 10.1 with the structural determination described previously in chapters 7 and 8, where it has been concluded that bond-strain is very low for the ISF in agreement with previous observations [177]. In contrast, although all Si atoms in the  $\Sigma 5$ GB are four-fold co-ordinated, the structure contains 5- and 7-member rings and significant deviations from tetrahedral bonding, also in line with previous reports [187, 211]. The areal energy densities of the ISF and  $\Sigma 5$ GB structures are calculated in sections 7.3.1 and 8.3.1 respectively. From the band-structure data (Figures 7.3 and 8.3(a)), it is found that the bandgaps for the ISF and  $\Sigma 5$ GB deviate from the value for pure Si. In the case of the ISF, the bandgap is very slightly smaller than bulk silicon, whereas in the  $\Sigma 5$ GB the bandgap is increased. It is noted in this study that the increase in the bandgap in the  $\Sigma 5$ GB matches the findings of a recent study of the impact of extended defects on solar-cell efficiency [58]. The increase in the bandgap in the case of the  $\Sigma 5$ GB is 28%. The calculations of absorption coefficient for different structures were analysed separately in previous chapters. However, in this chapter, the figures are combined together in studying the optical properties of the structure on solar cell performance. For that, and as mentioned before in chapters 7 and 8, the absorption coefficient calculated for the supercell containing the ISF is similar to that of pure Si, but it is found that absorption at longer wavelengths is more significant for the  $\Sigma 5$ GB, as shown in figure 10.5. This is due to the breaking of symmetry at the core of EDs that leads to non-zero transition dipoles between the states around the bandgap. The complex refractive indices of the ISF and  $\Sigma 5$ GB are plotted in figures 10.6(a) and (b), comparing the real ( $n$ ) and imaginary ( $k$ ) parts with bulk Si as a function of wavelength. Again, it is only the  $\Sigma 5$ GB that shows significant deviation from bulk behaviour.

Turning to cases where an interstitial iron impurity has been added, as a reference,

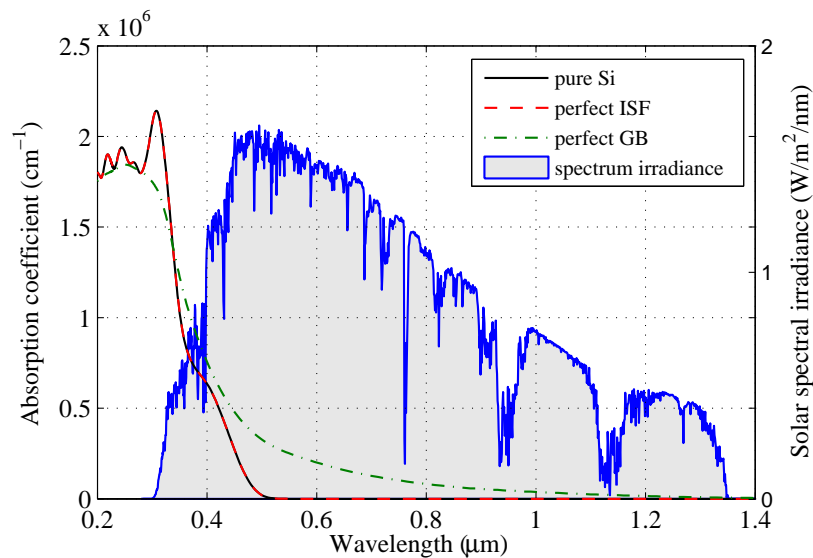


Figure 10.5: Calculated optical absorption coefficient versus wavelength for extended defects and ideal Si together with the AM1.5 solar power spectrum for comparison.

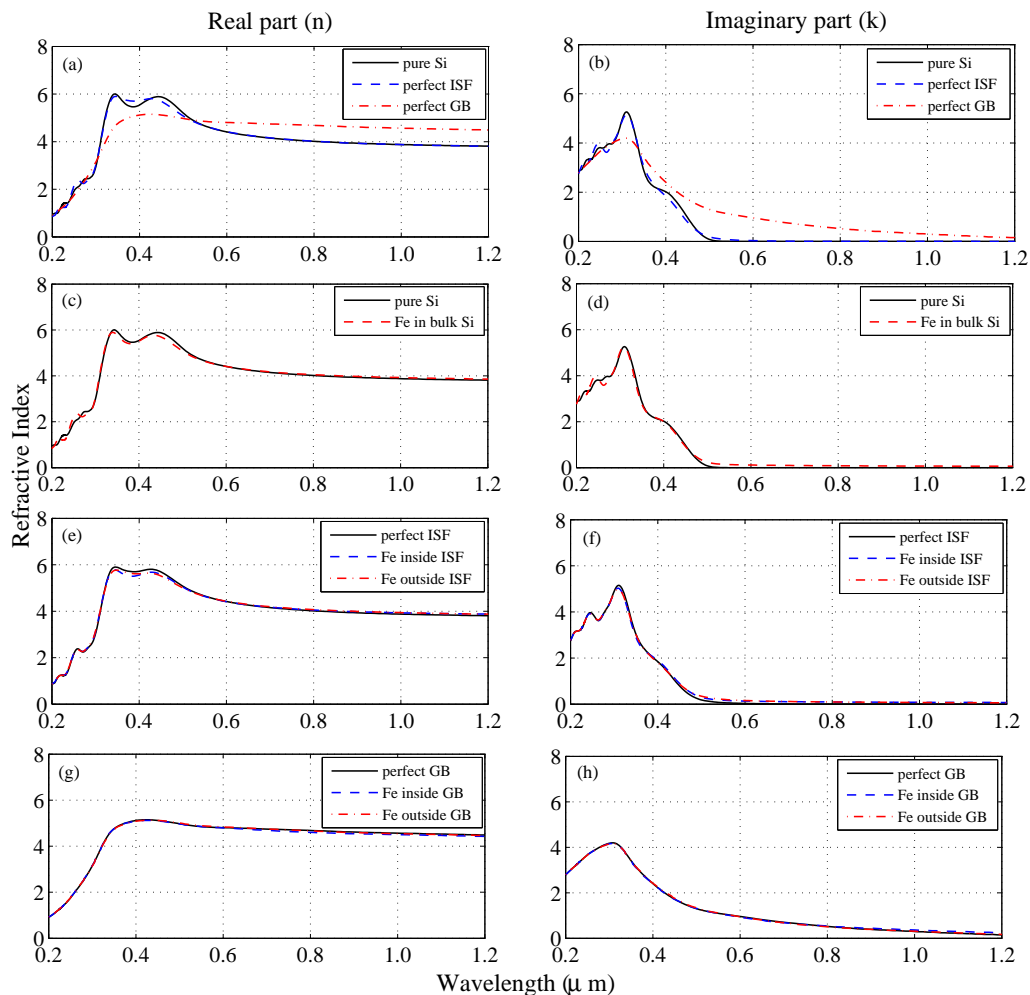


Figure 10.6: Computed real ( $n$ ) and imaginary ( $k$ ) parts of the refractive index for different structures, showing the impact of ED and Fe contamination.

values of  $n$  and  $k$  for  $\text{Fe}_i$  in bulk silicon are shown in figures 10.6(c) and (d) respectively.

The minor impact of Fe in supercells containing EDs. Figures 10.6 (e)–(h) reflects the

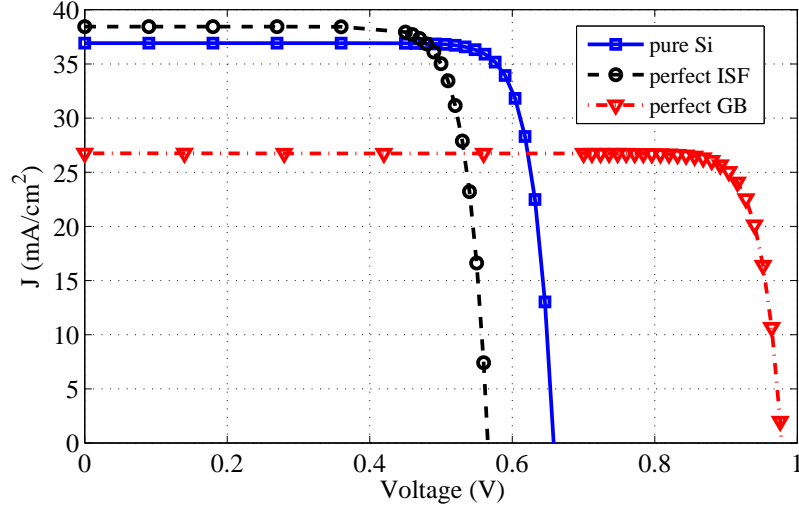


Figure 10.7:  $J$ - $V$  characteristics of a silicon solar cell in comparison to simulations involving silicon containing ISF and  $\Sigma 5$ GB defects. The device is divided into 80% crystalline silicon and 20% associated with material modified by the existence of the extended defect and this curve is plotted for only the 20% of the ISF or GB region and not the entire device to so as study performance at these specific regions.

localised states introduced by the impurity.

The direct influence of the ISF and  $\Sigma 5$ GB on conversion efficiency has been investigated using the results of the DFT calculations within a 2D TCAD model of a silicon solar-cell. It is found that the EDs have a clear impact on the  $J$ - $V$  characteristics of the device, as shown in figure 10.7. The ISF has a value of  $J_{sc}$  close to that of a pure silicon solar-cell, but the  $V_{oc}$  is lower, rendering the overall conversion efficiency lower. In contrast, the simulations involving the  $\Sigma 5$ GB exhibit a lower  $J_{sc}$  but higher conversion efficiency as the value of  $V_{oc}$  is higher due to the locally increased value of  $E_g$ .

Results for  $V_{oc}$ ,  $J_{sc}$ , the fill factor, FF, and conversion efficiency,  $\eta$ , are summarized in table 10.1.

Table 10.1: Summary of solar-cell electrical parameters and efficiency with and without the EDs shown in figure 10.7 under AM1.5 illumination.

Structure	$J_{sc}$ (mA/cm <sup>2</sup> )	$V_{oc}$ (V)	FF	$\eta$ (%)
Pure	36.92	0.65	83.36	20.25
ISF	38.44	0.56	81.29	19.73
GB	26.73	0.97	87.65	20.78

### 10.3.2 $\text{Fe}_i$ in pure silicon

As mentioned in chapter 4,  $\text{Fe}_i$  diffuses with a low activation energy, and so it is expected that iron contamination will lead to a rapid spatial distribution within a silicon structure. In this study, the Fe concentration has been varied from  $10^8$  to  $10^{16} \text{ cm}^{-3}$ , aiming to provide some insight into its impact upon solar-cell performance. Figure 10.8 shows the variation of carrier density versus Fe concentration. The average carrier densities were calculated along the cross-sectional area of the solar cell rather than the illuminated surface; and the cell performance was computed at each iron concentration value (fixed carrier density). In this work, it is found that hole density has been reduced slightly with increasing Fe concentration, as one would expect given that  $\text{Fe}_i$  is a single donor. The electron density also shows a dependence upon iron concentration, particularly when it exceeds  $10^{12} \text{ cm}^{-3}$ .

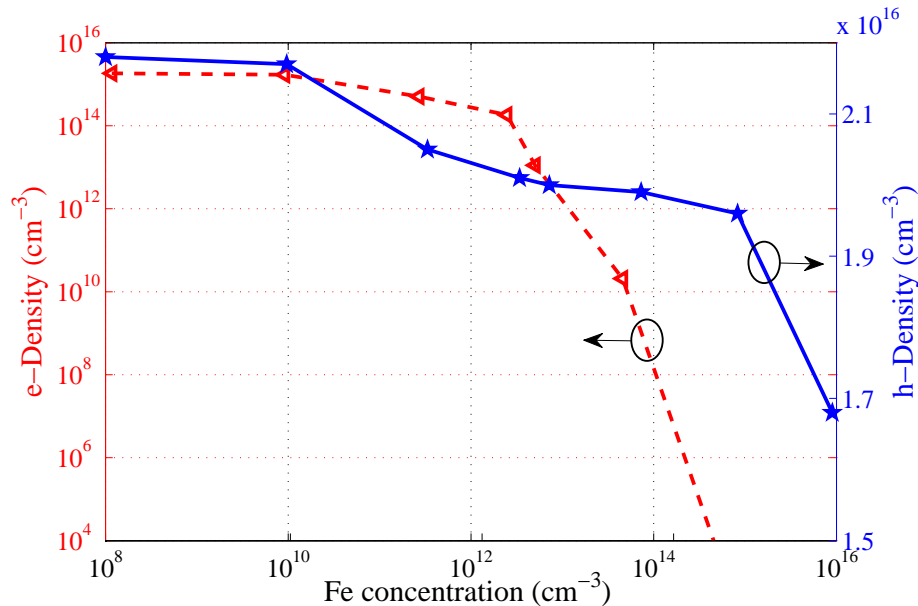


Figure 10.8: Variation of carrier densities under illumination (Figure 10.5) as a function of Fe concentration (independent of voltage).

In order to investigate the influence of Fe impurities upon  $J$ - $V$  characteristics, a range of device simulations have been carried out, with the results depicted in figures 10.9 and 10.10. The data highlight the impact of Fe contamination, showing the variation of  $J_{\text{sc}}$ ,  $V_{\text{oc}}$  and  $\eta$  with increasing concentration from  $10^8 \text{ cm}^{-3}$  to  $10^{16} \text{ cm}^{-3}$ , where  $J_{\text{sc}}$  and  $V_{\text{oc}}$  are reduced by around 18% and 34% respectively, and these reductions degrade  $\eta$  from 18% to 8%. It is also noted from figure 10.9 that, for Fe concentrations below  $10^{14} \text{ cm}^{-3}$ , the value of  $J_{\text{sc}}$  is higher than that of pure Si (Table 10.2). This increment in  $J_{\text{sc}}$  might be due to an enhancement in the collection probability that depends heavily on minority

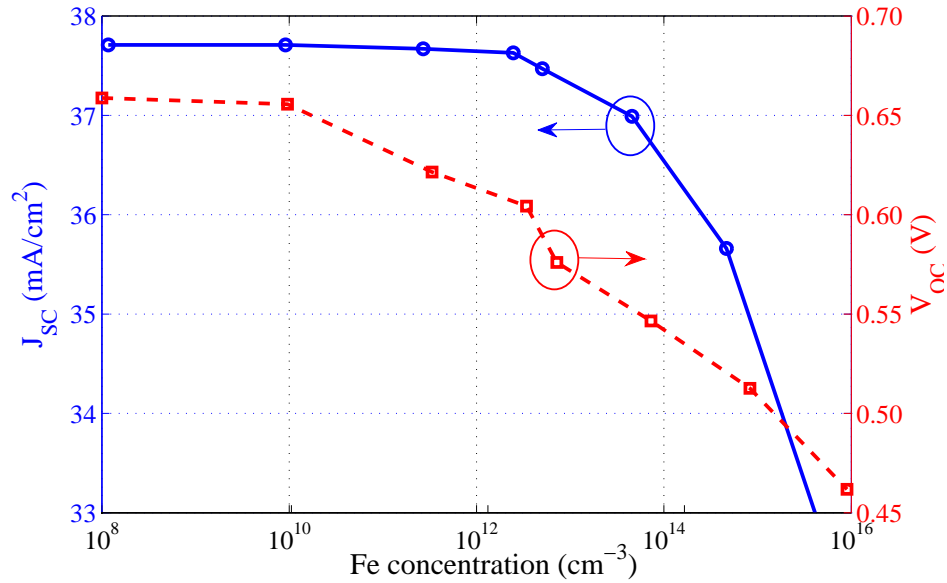


Figure 10.9: Current density (left) and open circuit voltage (right) versus impurity concentration for Fe in pure Si. Data recorded under AM1.5 illumination.

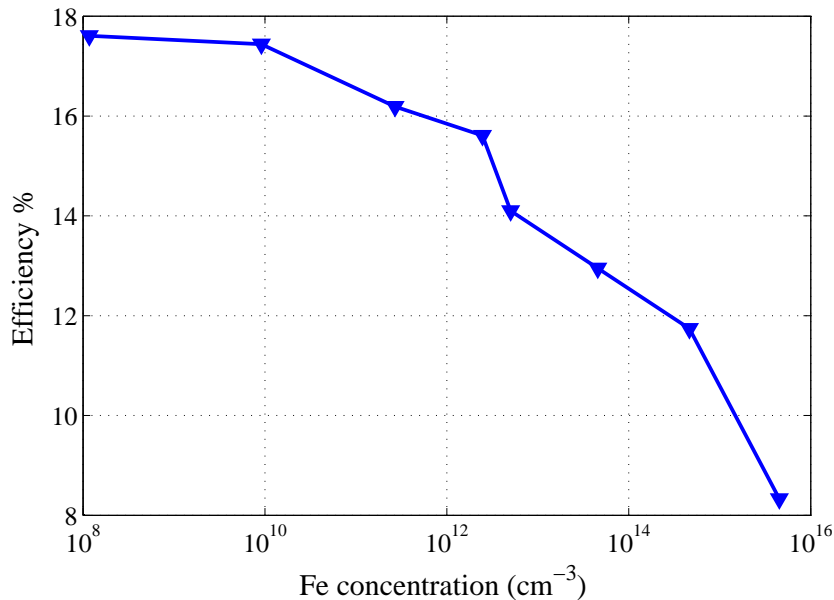


Figure 10.10: Conversion efficiency versus impurity concentration for Fe in pure Si. Data recorded under AM1.5 illumination.

carrier lifetime. However, for iron concentrations higher than  $10^{14} \text{ cm}^{-3}$ ,  $J_{sc}$  declines.

In the trap model described in section 4.6.2, and as shown in figure 10.4, the impact of placing the iron to introduce a donor level has been compared at 0.38 eV [71] and 0.4 eV above the valence band [252,255], with these small variations yielding no significant difference in device performance. However, to establish the sensitivity of the device parameters to these suggested donor level values, a range of values (between 0.2 eV above the Si valence band and the mid-gap) has been examined in this study. Surprisingly, even with such substantial variations, only a very slight difference in conversion efficiency is found,

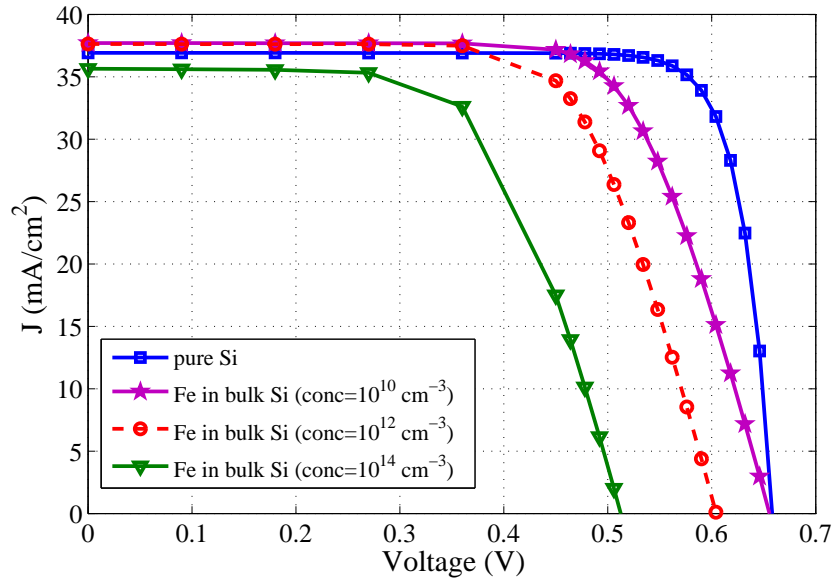


Figure 10.11:  $J$ - $V$  characteristics for the model solar-cell constituted from pure silicon and three different Fe-doping concentrations.

and it is concluded that the details of the location of the donor level is not important for the modelling employed in this study.

Figure 10.11 shows a comparison between Fe-free and Fe-doped single crystal silicon solar cells. The value of  $J_{sc}$ , for an iron concentration of  $10^{12} \text{ cm}^{-3}$  is slightly higher than of the current density determined for pure Si, but the levels of  $V_{oc}$ , and fill factor are significantly reduced, leading to reduced overall efficiency. The  $J$ - $V$  characteristics for three concentrations of Fe are shown in figure 10.11, and the efficiency is reduced from about 20% to 16% with increasing  $Fe_i$  concentration from  $10^{10}$  to  $10^{14} \text{ cm}^{-3}$  (Figure 10.10). Based on an experimental study [256], five samples taken from different heights of one mc-Si ingot were employed to study the internal gettering of Fe in mc-Si. The average measured  $Fe_i$  concentration for all samples was  $8.6 \times 10^{11} \text{ cm}^{-3}$ . Thus, for the remainder of this chapter, the  $Fe_i$  concentration is fixed at  $10^{12} \text{ cm}^{-3}$ , which represents a density typically reported in the literature [256], and the donor level is fixed at 0.38 eV.

The impact of the value of the  $Fe_i$  electron cross section ( $\sigma_n$ ) has been determined by varying its value according to the different values in the literature. The device performance statistics are shown in table 10.2, indicating that there is an impact upon predicted efficiency; with all other quantities fixed, efficiency varies from around 15% to 17%, depending upon the value of  $\sigma_n$ .

Table 10.2: Impact of electron cross-section ( $\sigma_n$ ) of interstitial iron on device performance.

$\sigma_n$ (cm <sup>2</sup> )	$J_{sc}$ (mA/cm <sup>2</sup> )	$V_{oc}$ (V)	FF	$\eta$ (%)
$2 \times 10^{-15}$ [257]	37.69	0.63	69.89	16.72
$1.3 \times 10^{-14}$ [125]	37.63	0.60	69.65	15.61
$4 \times 10^{-14}$ [71, 255, 258]	37.55	0.58	67.00	14.79

### 10.3.3 Fe–extended-defect complexes

The atomistic simulations for Fe at or close to an ED have established that the donor level of interstitial Fe is not significantly affected when  $Fe_i$  is associated with an ISF, but it lies closer to the valence band (around 0.2 eV) when located in the lowest energy site in the  $\Sigma 5GB$  [127, 211]. The binding energies,  $E^b$ , of  $Fe_i$  to the ISF and  $\Sigma 5GB$  are estimated to be 0.2 and 0.4 eV respectively.

The optical and electrical properties of EDs and Fe impurities obtained from DFT simulations were combined with the TCAD trap model. Figure 10.12 shows a comparison of the performance of solar cells containing ISFs with and without Fe contamination.

Although the values of  $J_{sc}$  and  $V_{oc}$  are reduced slightly, there is a significant reduction in  $V$  and  $J$  at the maximum power point. The fill factor is reduced by 22%, leading to predicted efficiency reduction from about 20% to 19%.

In a similar fashion,  $J_{sc}$  and  $V_{oc}$  are slightly lowered upon addition of  $Fe_i$  to  $\Sigma 5GB$ , but in this case the FF is reduced by only 7%, reducing the efficiency from about 21% to 20%. The results of total conversion efficiency after combination of the ED and bulk contributions are listed in table 10.3.

Table 10.3: Summary of solar-cell electrical parameters and efficiency for Fe-containing systems illustrated in figures 10.11, 10.12 and 10.13 under AM1.5 illumination.

Structure	$J_{sc}$ (mA/cm <sup>2</sup> )	$V_{oc}$ (V)	FF	$\eta$ (%)
Fe in bulk Si	37.63	0.60	68.65	15.61
Fe in ISF	39.42	0.51	63.7	18.77
Fe in $\Sigma 5GB$	26.89	0.92	80.39	20.20

Based on the influence of  $Fe_i$  on the  $J$ - $V$  characteristics shown in figures 10.11–10.13, it is concluded that the addition of  $Fe_i$  can be thought of as adding a series resistance to the solar-cell, since it is mainly voltages that are affected. The series resistance,  $R_s$ , illustrated in the equivalent circuit shown in figure 10.14 can be calculated as follows [259]:

$$FF_s = FF_0(1 - 1.1R_s) + \frac{R_s^2}{5.4} \quad (10.1)$$

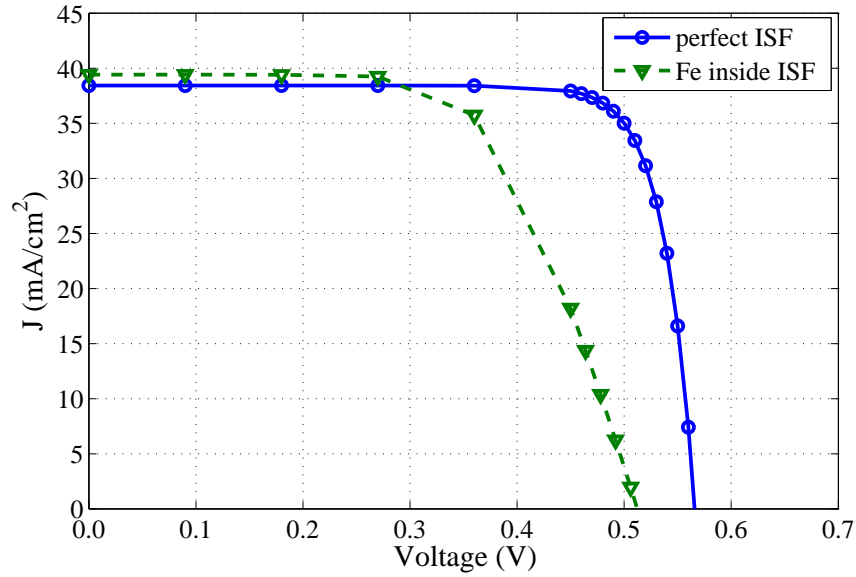


Figure 10.12:  $J$ - $V$  characteristics for solar-cells containing both ISFs and  $\text{Fe}_i$ . The device is divided into 80% crystalline silicon and 20% associated with material modified by the existence of the ISF, and this curve is plotted at only the 20% ISF region and not the entire device to study the performance at this specific region.

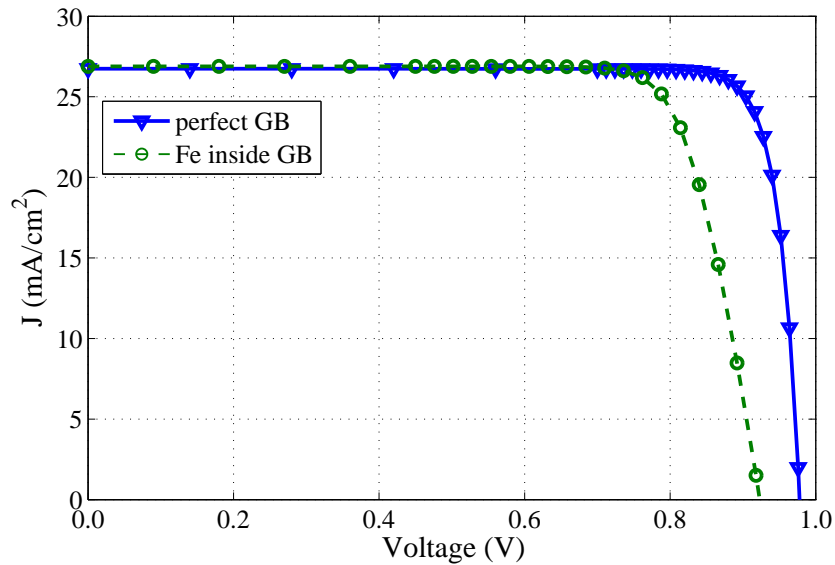


Figure 10.13:  $J$ - $V$  characteristics for solar-cells containing both  $\Sigma 5\text{GB}$  and  $\text{Fe}_i$ . The device is divided into 80% crystalline silicon and 20% associated with material modified by the existence of the GB, and this curve is plotted at only the 20% GB region and not the entire device to study the performance at this specific region

where  $\text{FF}_0$  is the fill factor for pure crystalline Si and  $\text{FF}_s$  is the fill factor after adding the series resistance,  $R_s$ , arising from the addition of  $\text{Fe}_i$ . Taking the values of the fill-factors from tables 10.1 and 10.3, the calculated values of  $R_s$  for  $\text{Fe}_i$  in bulk Si, inside the ISF and  $\Sigma 5\text{GB}$  are 0.147, 0.194 and 0.071  $\Omega$  respectively.

The value of  $E_g$  in the TCAD calculations is guided by the DFT calculations ( $E_g =$

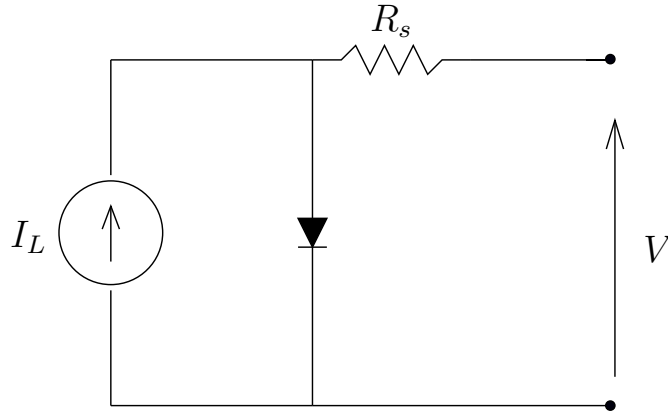


Figure 10.14: Parasitic series resistance in a solar cell circuit.

1.08 eV and 1.50 eV for Fe-free ISF and GB, respectively). The impact of  $E_g$  upon the simulated solar-cell performance is illustrated in figures 10.15 and 10.16. In this work, it is found that  $E_g$  has a significant impact upon  $V_{oc}$ , with  $V_{oc}$  increasing with increasing  $E_g$  as the open-circuit voltage depends upon carrier concentration. Such a direct relationship is derived from the Shockley-Queisser model [58]:

$$V_{oc} = \frac{E_g}{q} - CT, \quad (10.2)$$

where  $q$  is the electron charge,  $C$  is the temperature coefficient and  $T$  is the temperature.

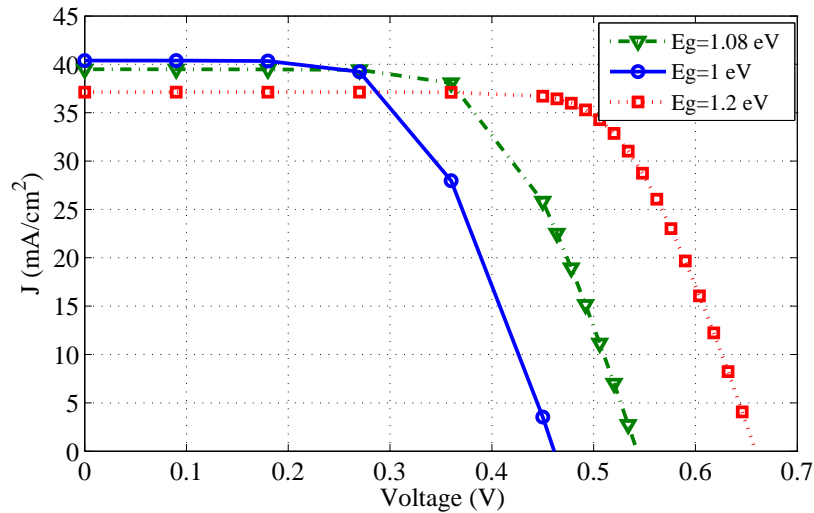


Figure 10.15: Effect of energy gap of silicon on the  $J$ - $V$  characteristics with the presence of ISF. The device is divided into 80% crystalline silicon and 20% associated with material modified by the existence of the ISF, and this curve is plotted at only the 20% ISF region and not the entire device so as to study the performance at this specific region.

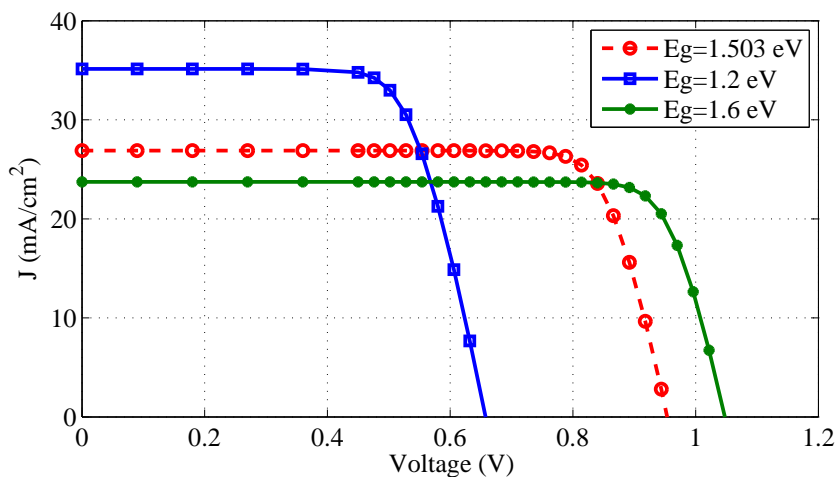


Figure 10.16: Effect of energy gap of silicon on the  $J$ - $V$  characteristics with the presence of GB. The device is divided into 80% crystalline silicon, and 20% associated with material modified by the existence of the GB and this curve is plotted for only the 20% GB region not the entire device to study the performance at this specific region.

## 10.4 Summary

Quantum-chemical simulations were combined with TCAD device simulations to investigate the role that extended defects considered in chapters 7 and 8 with and without decoration by mobile iron play in the performance of mc-Si solar cells. The results show that the perfect ISF, which closely resembles the  $\Sigma 3$ -(111) twist GB, as well as the higher-strained  $\Sigma 5$ -(001) twist GBs, behave similarly to ideal Si in terms of electrical, electronic and optical characteristics when the intervening bulk silicon regions are sufficiently large. In contrast, reasonable efficiency gains are obtained due to the increase in  $V_{oc}$  where the bandgap changes local to the GB are assumed to apply proportionately across the entire device.

Recombination at Fe bound to these EDs reduces solar-cell efficiency;  $J$ - $V$  characteristics are affected so that the fill-factor is reduced. The reduction in the fill-factor can be thought of as arising from a series resistance in the solar-cell equivalence circuit.

It is concluded that the impact of EDs in terms of device efficiency is therefore not via a direct increase in carrier generation due to changes in the optical and electronic properties of the GBs, but rather from their gettering of Fe (and other impurities) from the volume of the grains. This outcome can add a significant role in real solar cell fabrication world.

## **Part III**

# **Conclusions**

# Summary, Conclusions and Future Work

“A conclusion is the place where you got tired of thinking.”

Arthur Block

Although detailed summaries have been presented in the appropriate places in each individual chapter, it is worth presenting a few more general comments about the results obtained using atomic and device simulations to examine the various defects in mc-Si. By drawing conclusions from the outcomes presented in this thesis, suggestions are made for how areas considered in this work might be extended.

## 11.1 Summary and Conclusion

The objective of this work has been to explore the behaviour and interaction of the most common point defects at the atomic scale in mc-Si, and notably their interaction with EDs including stacking faults, grain boundaries, and voids. Defect segregation is explored in detail along with coupling, with a notable focus on interstitial iron impurities as the most common and unavoidable TM contaminants in Si [53, 54, 57, 71]. In particular, the iron coupling as an example of fast-diffusing defect pairs toward sites provided by these EDs. Then, the work derives modelling of a larger scale via whole device-level simulation using TCAD tools, which can be used for process simulation and device modelling in microelectronics [73] and increasingly for research into the design of solar cells.

Extensive introduction to commercially available PV technologies with their respective market shares is presented in the first chapter of this thesis, focusing on mc-Si which offers

a more cost-effective option to gain reasonable cell efficiency compared with crystalline Si. This chapter also provides details about high concentrations of transition metal impurities in general, and iron in particular as unavoidable impurities in mc-Si [53, 130] which are incorporated during growth and processing [131].

Then, an overview of the computational methods employed of the atomic and device levels has then been presented via DFT and TCAD simulations in chapters 2-4. The combination of these computational methods provides the basis for the main outcomes and conclusions as highlighted in the following sections.

### 11.1.1 Atomic level

The first part of this thesis reports the results of density functional theory implemented with AIMPRO [81], as described in chapters 5-9, where atoms are simulated using ab initio pseudopotentials and total energies and forces are obtained with a local density approximation for the exchange-correlation. For more details of AIMPRO, see chapters 2 and 3.

Under this approach, DFT has been employed to investigate the behaviour of Fe in bulk Si and at EDs, including ISFs,  $\Sigma 5$ -(001),  $\Sigma 3$ -(110) twist GBs and voids as case studies. For all structures, the calculated areal energy densities of these EDs compare favourably with values in the literature. Trends in the binding, magnetic, geometric, electronic and electrical properties of Fe in different forms were studied as substitutional, Fe-vacancy, interstitial and interstitial pairs.

Calculations have provided evidence that  $\text{Fe}_i$  resides at the tetrahedral interstitial site, and the experimental observation [137] is confirmed that  $\text{Fe}_i$  has a high diffusivity in pure Si, with theory suggesting that the diffusion pathway is a hop between neighbouring tetrahedral interstitial sites, via the hexagonal (H)-site transition state [159]. It is also found that the H-site is metastable, with the transition state lying slightly away from the  $D_{3d}$  symmetry H-site structure.

The activation energies for both the 216 and 512 Si atom structures are 0.80 and 0.74 eV for the neutral and positive charge states respectively, which is in good agreement with previous calculations [155], confirming the convergence of the diffusion energy in the 216 atom cell. The ground state of  $\text{Fe}_i^0$  is a spin triplet, with the singlet and quintet energies determined to be 0.5 and 0.6 eV respectively; also in good agreement with previous calculations [56].

Modifications of the spin energies of  $\text{Fe}_i\text{V}$  and  $\text{Fe}_s$  in bulk Si have also been noticed, with significantly iron-related gap levels. Furthermore, the interstitial position of Fe is favoured over the substitutional one in Si as the energy cost to form  $\text{Fe}_s$  in Si from the interaction of  $\text{Fe}_i$  and a monovacancy is 1 eV, yielding binding energies of  $\text{Fe}_i\text{V}$  and  $\text{Fe}_s$  relative to isolated  $\text{Fe}_i$  plus an isolated vacancy of 2 and 3 eV respectively, which is in good agreement with theoretical values and EPR observations.

The agreement with values in the literature regarding  $\text{Fe}_i$  provides the basis for using this approach to determine the properties of interstitial iron pairs. The properties of  $\text{Fe}_i\text{-Fe}_i$  are examined as a function of the distance between the initial T-sites at which the Fe atoms are located. Relative to one T-site, the first three non-equivalent T-sites at increasing distances lie at  $[111]a/4$ ,  $[110]a/2$  and  $[3\bar{1}\bar{1}]a/4$ , where  $a$  is the host lattice constant. It is concluded that the formation of pairs is energetically favourable. The uncharged pairs may be considered to be formed by ferromagnetic or antiferromagnetic coupling of two  $S = 1$   $\text{Fe}_i$  centres (FM and AFM). Of particular note are the magnetic orders predicted for pairs as a function of internuclear distance, and that the third-neighbour pair is the most favourable form. However, it is predicted to exist in AFM form, bound relative to isolated interstitials. In addition to that, the AFM coupled form of Fe-1-Fe is found to be bound by 0.22 eV. Fe-2-Fe and Fe-3-Fe are also bound; the former in an FM form and the latter in an AFM form. The binding energies are modest at 0.14 eV and 0.26 eV respectively. It is noticed that there is a dependence of cell-size upon binding energy, which indicates clearly that there is more general agreement between the 216 and 512 atom cells than between the 64 and 216 cells. In this work, the way in which the  $\text{Fe}_i\text{-Fe}_i$  might migrate has been also examined. The data obtained show that the barrier relative to the equilibrium form of the pair in moving from Fe-1-Fe to Fe-2-Fe is around 0.9 eV for AFM, which is higher than that of the FM case at around 0.7 eV. Similarly, the barrier to move from Fe-2-Fe to Fe-3-Fe is a little below 0.9 eV for the AFM, which again is higher than that of the FM case which is just 0.7 eV. One might also note that three of the diffusion profiles show the same intermediate minima as exhibited by a single  $\text{Fe}_i$  (Fig. 5.8). The most important outcome is that the migration barrier for the Fe-pair is lower than that for individual interstitials, suggesting that pairs are a key contributor to Fe diffusion, precipitation and segregation to, for example, extended defects, and are likely to be of significance.

Relying on this outcome, unstrained and strained examples of EDs have been investigated, including ISFs and twist GBs. The structure of the ISF, where the strain is very

low, is that all Si atoms are close to being tetrahedrally co-ordinated, even in the stacking layers. This agrees with previous observations [177]. As mentioned above, the accuracy of the ISF model has been evaluated further and found to be  $40 \text{ mJ/m}^2$ , comparing well with the theoretical value ( $26\text{--}40 \text{ mJ/m}^2$  [173]) and the experimental result of  $44 \text{ mJ/m}^2$  [178].

The Kohn-Sham band-structure of the ISF shows an absence of any bands deep in the gap, which is in good agreement with another previous study [179]. It is found that the bandgap for the ISF is very slightly smaller than that of bulk Si. A novel aspect of this study is the extent of the investigation of the role of the spin and charge states of  $\text{Fe}_i$  in ISFs. It is found that the  $S = 0$  and  $S = 2$  configurations of  $\text{Fe}_i^0$  are  $0.08$  and  $0.68 \text{ eV}$  higher respectively than  $S = 1$ . Notably, this suggests that the  $S = 0$  is stabilised relative to the triplet ground-state in comparison to  $\text{Fe}_i$  in bulk silicon, where the ground state is a spin triplet, with the singlet and quintet energies determined to be  $0.5$  and  $0.6 \text{ eV}$  higher respectively, which is in good agreement with previous calculations [56]. The change in the relative energies of the different spin states is most likely to be a consequence of the increased volume associated with the cage site in the ISF, and the additional splitting of the  $d$ -orbitals of the iron due to the local reduction in symmetry (effectively an additional local crystal field splitting). The electrical levels of  $\text{Fe}_i$  at the ISF reflect the donor and acceptor levels that are created after segregating Fe at the ISF. The donor level of the ISF is very slightly closer ( $\sim 35 \text{ meV}$ ) to the VB top than in bulk Si, and is deeper within the energy gap outside the ISF. It is concluded that the segregation of Fe at ISFs can alter the electrical properties of the ISF from being electrically inactive to becoming an active region, and thus the ISF can play an important role in solar cell performance.

For more complicated structures than ISFs, DFT implemented in AIMPRO has been employed, with systems modelled using periodic boundary conditions for  $\Sigma 5$ -(001) and  $\Sigma 3$ -(110) twist GBs. It is found that  $\sigma(\Sigma 5)$  and  $\sigma(\Sigma 3)$  are  $1.289$  and  $0.786 \text{ J/m}^2$ , respectively, which compare well with values in the literature [211, 212]. Then,  $\text{Fe}_i$  has been introduced at a range of non-equivalent sites. At each site, the structure has been optimised for different charge and spin states. For the majority of sites examined within the  $\Sigma 5$ -(001) GB, the neutral charge state favours the spin-triplet state, which is in line with behaviour in bulk silicon [56, 155]. However, the ground state site is lower in energy than the other sites, and the spin singlet is degenerate with the triplet to the accuracy of the calculation. All the sites within the  $\Sigma 3$ -(110) GB favour the  $S = 1$  configuration for  $\text{Fe}_i^0$ , where the  $S = 0$  and  $S = 2$  configurations lie at  $0.17 \text{ eV}$  and  $0.76 \text{ eV}$  above the spin triplet. It is noticed also that the doublet state is favoured for both GBs in the stable sites. For all sites

examined, a deep level is found arising from the Fe  $3d$ -orbitals, and thus the electrical activity of  $\text{Fe}_i$  is predicted to remain irrespective of whether or not it is segregated to either of these GBs.

It is found that all of these forms of planar defects (ISFs and GBs) represent binding sites for interstitial Fe, with a much higher coordination number in locations adjacent to the EDs, and the bond angles are far from those of a tetrahedral. The high coordination may be viewed as resembling the equilibrium atomic coordination of iron silicide, which is proposed to represent evidence for Fe-precipitation at the EDs.

Although  $\text{Fe}_i$  binds relatively weakly at fully bonded ISFs and GBs (at less than 0.5 eV), it is more strongly trapped by vacancies at these EDs and also, and more critically, by Fe already trapped there. This leads to the conclusion that the precipitation of Fe at EDs is energetically favourable, even in the absence of the direct chemical bonding afforded by the substitution of Si by iron. It is concluded that the variation in binding energies is most probably a consequence of the strain relaxation afforded by the introduction of the iron at different sites within these regions.

For example, if diffusing  $\text{Fe}_i$  encounters a neutral vacancy at the  $\Sigma 5$ -(001) GB, a near-neighbour  $\text{Fe}_i$ - $V$  pair may initially be formed. Indeed, the NL19 EPR centre has been suggested to arise from such a structure [137]. Many sites inside the boundary have been investigated in this work, and it is found for the neutral charge state that the  $S = 1$  configuration is marginally favoured over  $S = 0$ . The reaction to form  $(\text{Fe}_i-V)$  from  $\text{Fe}_i$  in the grain and a vacancy in the GB reduces the energy by 1.6 eV, which is close to previous estimates for a similar reaction in bulk Si [147]. When the  $\text{Fe}_i$  moves into the vacancy, substitutional Fe is formed which is found to have an  $S = 0$  ground state. The nearest-neighbour  $\text{Fe}_i$ - $V$  pair is 0.8–2.4 eV higher in energy than  $\text{Fe}_s$ , depending upon the site in the GB. Again the upper limit of the reaction energy compares favourably with the comparable bulk reaction, estimated to release 2.6 eV [147]. In addition, it is reported here that the binding of a second  $\text{Fe}_i$  atom to the GB is found to be greater in energy than the first, at 1.5 eV. The energy gained by taking an iron-pair from the grain and locating it at the GB is estimated to be 1.6 eV.

In this thesis, a void structure was formed by removing all atoms up to one lattice constant from a central Si atom in otherwise bulk silicon. Atoms at the void surface which are initially under-coordinated are then found to relax outward, with some also forming reconstructions. The pseudo-spherical structure of the void used in this study generates a number of non-equivalent sites at its surface, as well as sites within the silicon at various

distances from the core.

In general, creating a surface in crystalline material costs energy, and the atoms located at the boundaries of the surface behave differently from those in the rest of the bulk. The Si atoms in the vicinity of the internal surface may form reconstructions with each other, and are more free than atoms in bulk silicon to form re-arrangements so as accommodate the chemistry associated with iron.

It is reported in this thesis that binding energy has an upper bound of  $\sim 2$  eV, which is in an agreement with the average binding energy obtained from another previous calculations [235]. Furthermore, the values obtained for  $E^b$  compare well with experimentally obtained estimates [131, 231], which place the value of  $E^b$  in the range of 1.4–1.5 eV. The relatively high values of  $E^b$  indicate that Fe will be gettered effectively by void structures. The sites which are bound by more than 1 eV are only in the immediate vicinity of the surface, but lying within the silicon; the Fe atom lies outside the void and does not sit on top of the internal surface. This might be viewed as surprising, as one might imagine that Fe could chemically react with the under-co-ordinated surface Si atoms, but instead we find that it adopts a location within the first cages neighbouring the void, where it has a high co-ordination number.

In the void structure, a spin singlet ground state is found in contrast to the triplet ground-state of  $\text{Fe}_i$  in bulk Si. This highlights the electronic and magnetic differences between iron dissolved in the bulk lattice and iron at gettering sites. The low spin-state may also point to a different chemical state for Fe in the low-energy sites in the vicinity of the void.

Data obtained also shows that, where the binding energy is greatest (most negative), there is a higher strain in the surrounding silicon after the introduction of the Fe atom relative to the strain in the same region of the simulation cell when only the void is present.

The introduction of the Fe atom therefore increases the Si–Si strain, which would obviously represent a cost in energy. Since the total energy is evidently lower in these high-strain regions, which is noted as being in agreement with other simulations, where Fe-segregation into Si  $\Sigma 5(310)$  GBs occurs despite increasing strain [72].

The Fe–Si distance is perhaps only slightly different from those determined for  $\text{Fe}_i$  in the bulk, but there is clearly a much higher co-ordination number in the location adjacent to the void, and the bond-angles are far from those of a tetrahedron. The high co-ordination may be viewed as resembling the equilibrium atomic coordination of iron

silicide ( $\text{FeSi}_2$ ), which has Fe–Si distances of 2.35Å [181], and a co-ordination of eight with neighbouring silicon atoms.

The low-energy structure we have obtained may explain the experimental observation that only a single layer of iron forms at voids [237]. Due to the low migration enthalpies of Fe atoms in Si, the rapid motion of Fe has been envisaged to be absorbed as a monolayer on the internal surface of the voids. The low-energy sites outside the void may act as a barrier to Fe moving to fill the voids [237].

Once the low energy sites just outside the void are exhausted, subsequent additions are likely to more closely resemble the bulk interstitial site, for which no significant binding energy has been determined. However, given the importance of the relationship between the location of transition metals and the void volume in single-crystal silicon [238], resolving under what conditions voids might incorporate Fe directly is of some interest. The data obtained at the quantum-mechanical level provide the basis for device-level simulation using TCAD Sentaurus to simulate an Si solar cell, as shown in the following section.

### 11.1.2 Device level

Another aim of this study was to observe the direct impact of Fe–EDs complexes on PV device performance. To this end, first-principles quantum-chemical simulations were combined with TCAD device modelling to examine the impact of these defects on Si solar cell performance. The results of this combination showed that the perfect ISF, which closely resembles  $\Sigma 3$ -(111) twist GBs, behave similarly to ideal Si in terms of optical characteristics when the intervening bulk Si regions are sufficiently large. However, it is found that the absorption at longer wavelengths is more significant for the  $\Sigma 5$ GB. This is due to the symmetry breakage at the core of EDs which leads to non-zero transition dipoles between the states around band-gap. Moreover, reasonable efficiency gains are obtained due to the increase in  $V_{oc}$  where the band-gap changes local to the GB are assumed to apply proportionately across the entire device.

Recombination at Fe bound to these EDs reduces solar-cell efficiency;  $J$ - $V$  characteristics are affected so that the fill-factor is reduced. The reduction in the fill-factor can be thought of as arising from a series resistance in the solar-cell equivalent circuit.

It is concluded that the impact of EDs in terms of device efficiency is therefore not a direct increase in the carrier generation due to changes in the optical and electronic

properties of grain-boundaries, but rather from their gettering of Fe (and other impurities) from the volume of the grains.

## 11.2 Future Work

This study contributes to a better understanding of the mechanism of iron segregation at the EDs in Si, and it can be useful for both the interpretation of experimental observations and improvements in processing techniques to passivate iron contaminations in mc-Si wafers for PV applications.

From the results, it is recommended that the mechanism revealed for Fe gettering into the EDs can be generalised for other partially filled 3d (TMs) and their complexes, and other types and models for these EDs, including tilt GBs and dislocations. How they are affected by the presence of doping elements such as boron and phosphorus could therefore be investigated.

In addition, a development of the current approximation employed by AIMPRO can largely eliminate the underestimation in some results obtained using LDA, in particular in studying the electronic structure of materials and thus the properties of their defects. It is expected that using the screen exchange approach [260] would eliminate the errors obtained from some AIMPRO results. For example, the screen exchange approach allows a more accurate electronic structure of the examined system and its defect properties to be determined.

# Bibliography

- [1] D. Ginley, M. A. Green, and R. Collins, “Solar energy conversion toward 1 terawatt,” *Mrs Bulletin*, vol. 33, no. 4, pp. 355–364, 2008.
- [2] E. Alsema, “Energy pay-back and co2 emissions of pv systems, chapter v-2,” *Practical Handbook of Photovoltaics Fundamentals and Applications*, pp. 869–886, 2003.
- [3] M. Green, “Recent developments in photovoltaics,” *Solar energy*, vol. 76, no. 1, pp. 3–8, 2004.
- [4] European Patent Office, “Development and deployment of climate change mitigation technologies: evidence to support policy making policy brief,” p. 4, 2015.
- [5] R. Exell, “The intensity of solar radiation,” *King Mongkut’s University of Technology Press, Thornburi*, vol. 549, p. 554, 2000.
- [6] P. Wyers, “Photovoltaics: an overview of technologies and market potentials,” *ECN Solar Energy, Glass Performance Days*, 2007.
- [7] Department of Energy and Climate Change, “Statutory security of supply report,” 2014.
- [8] S. J. HOUGHTON, “Overview of the climate change issue. presentation to “forum 2002” at st. anne’s college,” 2002.
- [9] M. A. Green, Y. Hishikawa, W. Warta, E. D. Dunlop, D. H. Levi, J. Hohl-Ebinger, and A. W. Ho-Baillie, “Solar cell efficiency tables (version 50),” *Progress in Photovoltaics: Research and Applications*, vol. 25, no. 7, pp. 668–676, 2017.
- [10] Fraunhofer ISE, “Photovoltaics report,” Updated Nov. 2016.

- 
- [11] V. Popovich, *Microstructure and mechanical aspects of multicrystalline silicon solar cells*. Boxpress, 2013.
- [12] J. Ramanujam, A. Verma, B. González-Díaz, R. Guerrero-Lemus, C. del Cañizo, E. García-Tabarés, I. Rey-Stolle, F. Granek, L. Korte, M. Tucci *et al.*, “Inorganic photovoltaics—planar and nanostructured devices,” *Progress in Materials Science*, vol. 82, pp. 294–404, 2016.
- [13] Fraunhofer ISE, “Photovoltaics report,” Updated July 2017.
- [14] A. Luque and S. Hegedus, *Handbook of photovoltaic science and engineering*. John Wiley & Sons, 2011.
- [15] A. Goodrich, P. Hacke, Q. Wang, B. Sopori, R. Margolis, T. L. James, and M. Woodhouse, “A wafer-based monocrystalline silicon photovoltaics road map: Utilizing known technology improvement opportunities for further reductions in manufacturing costs,” *Solar Energy Mater. and Solar Cells*, vol. 114, pp. 110–135, 2013.
- [16] R. M. Swanson, “A vision for crystalline silicon photovoltaics,” *Progress in photovoltaics: Research and Applications*, vol. 14, no. 5, pp. 443–453, 2006.
- [17] T. Bruton, “General trends about photovoltaics based on crystalline silicon,” *Solar Energy Mater. and Solar Cells*, vol. 72, no. 1, pp. 3–10, 2002.
- [18] D. Sarti and R. Einhaus, “Silicon feedstock for the multi-crystalline photovoltaic industry,” *Solar Energy Mater. and Solar Cells*, vol. 72, no. 1, pp. 27–40, 2002.
- [19] J. F. Nijs, J. Szlufcik, J. Poortmans, S. Sivothythaman, and R. P. Mertens, “Advanced manufacturing concepts for crystalline silicon solar cells,” *IEEE Trans. Electron Devices*, vol. 46, no. 10, pp. 1948–1969, 1999.
- [20] F. C. Krebs, “Fabrication and processing of polymer solar cells: a review of printing and coating techniques,” *Solar Energy Mater. and Solar Cells*, vol. 93, no. 4, pp. 394–412, 2009.
- [21] H.-B. Fang, J.-Q. Liu, Z.-Y. Xu, L. Dong, L. Wang, D. Chen, B.-C. Cai, and Y. Liu, “Fabrication and performance of mems-based piezoelectric power generator for vibration energy harvesting,” *Microelectronic Journal*, vol. 37, no. 11, pp. 1280–1284, 2006.

- [22] A. Blakers, N. Zin, K. R. McIntosh, and K. Fong, “High efficiency silicon solar cells,” *Energy Procedia*, vol. 33, pp. 1–10, 2013.
- [23] O. Schultz, S. Glunz, and G. Willeke, “Accelerated publication: Multicrystalline silicon solar cells exceeding 20% efficiency,” *Progress in Photovoltaics: Research and Applications*, vol. 12, no. 7, pp. 553–558, 2004.
- [24] P. Auger, “Secondary beta rays produced in a gas by x-rays,” *CR Acad. Sci*, vol. 177, pp. 169–171, 1923.
- [25] W. Shockley and W. Read Jr, “Statistics of the recombinations of holes and electrons,” *Phys. Rev.*, vol. 87, no. 5, p. 835, 1952.
- [26] R. N. Hall, “Electron-hole recombination in germanium,” *Phys. Rev.*, vol. 87, no. 2, p. 387, 1952.
- [27] O. Schultz, “High-efficiency multicrystalline silicon solar cells,” Ph.D. dissertation, 2005.
- [28] R. A. Sinton and R. M. Swanson, “Recombination in highly injected silicon,” *IEEE Trans. Electron Devices*, vol. 34, no. 6, pp. 1380–1389, 1987.
- [29] P. P. Altermatt, R. A. Sinton, and G. Heiser, “Improvements in numerical modelling of highly injected crystalline silicon solar cells,” *Solar Energy Mater. and Solar Cells*, vol. 65, no. 1, pp. 149–155, 2001.
- [30] D. K. Schroder, “Carrier lifetimes in silicon,” *IEEE Trans. Electron Devices*, vol. 44, no. 1, pp. 160–170, 1997.
- [31] M. Bertolli, “Solar cell materials,” *Course: Solid State II. Department of Physics, University of Tennessee, Knoxville*, 2008.
- [32] V. Bharam and D. Day, “Advantages and challenges of silicon in the photovoltaic cells.”
- [33] S. Glunz, R. Preu, and D. Biro, “16: Crystalline silicon solar cells—state-of-the-art and future developments,” *Comprehensive renewable energy*, vol. 1, pp. 353–387, 2012.
- [34] R. Miles, “Photovoltaic solar cells: Choice of materials and production methods,” *Vacuum*, vol. 80, no. 10, pp. 1090–1097, 2006.

- 
- [35] F. Ferrazza, A. Endros, W. Koch *et al.*, “Cost effective solar silicon technology,” in *Proc. 2nd World Conf. on Photovoltaic Solar Energy Conversion*, 1998, pp. 6–10.
- [36] O. Mah, “Fundamentals of photovoltaic materials, national solar power research institute,” *Inc., California*, 1998.
- [37] Y. Nishi and R. Doering, *Handbook of semiconductor manufacturing technology*. CRC Press, 2000.
- [38] M. A. Green, “Silicon solar cells: evolution, high-efficiency design and efficiency enhancements,” *Semicond. Sci. Technol.*, vol. 8, no. 1, p. 1, 1993.
- [39] D. Margadonna and F. Ferrazza, “The status of crystalline si modules,” *Renewable energy*, vol. 15, no. 1-4, pp. 83–88, 1998.
- [40] D.-H. Neuhaus and A. Münzer, “Industrial silicon wafer solar cells,” *Advances in OptoElectronics*, vol. 2007, 2008.
- [41] C. Honsberg and S. Bowden. (2017) Photovoltaic education network. [Online]. Available: <http://pveducation.org/pvcdrom/solar-cell-structure>
- [42] H. C. Card and E. S. Yang, “Electronic processes at grain boundaries in polycrystalline semiconductors under optical illumination,” *IEEE Trans. Electron Devices*, vol. 24, no. 4, pp. 397–402, 1977.
- [43] K. Nakayashiki, “Understanding of defect passivation and its effect on multicrystalline silicon solar cell performance,” Ph.D. dissertation, Georgia Institute of Technology, 2007.
- [44] Fraunhofer ISE Photovoltaics Report, 2017, “How efficient will solar pv be in the future? 10-year predictions for the industry,” Updated August 2017.
- [45] J. Trube. (2018) International technology roadmap for photovoltaic results 2017. [Online]. Available: <http://www.itrpv.net/>
- [46] A. Schneider, “Charakterisierungsverfahren und industriekompatible herstellungsprozesse für dünne multikristalline siliziumsolarzellen,” Ph.D. dissertation, 2004.
- [47] W. Callister Jr and D. Rethwisch, “Materials science and engineering: An introduction,” vol. 7, 2007.

- [48] G. Coletti, “Sensitivity of state-of-the-art and high efficiency crystalline silicon solar cells to metal impurities,” vol. 21, no. 5, pp. 1163–1170, 2013.
- [49] C. V. Ciobanu, C.-Z. Wang, and K.-M. Ho, *Atomic Structure Prediction of Nanostructures, Clusters and Surfaces*. Wiley, 2013.
- [50] T. A. Arias and J. D. Joannopoulos, “Electron trapping and impurity segregation without defects: Ab initio study of perfectly rebonded grain boundaries,” *Phys. Rev. B*, vol. 49, no. 7, p. 4525, 1994.
- [51] H. Alexander, “Dislocations in solids,” *Ed. FRN Nabarro*, vol. 7, 1986.
- [52] S. R. M. R. D. Y. H.J. Möller, L. Long and M. Werner, “Proceedings of the 7th workshop on the role of impurities and defects in silicon device processing,” *National Renewable Energy Laboratory, Golden, USA*, no. 41, p. 41, 1997.
- [53] A. A. Istratov, T. Buonassisi, R. McDonald, A. Smith, R. Schindler, J. Rand, J. P. Kalejs, and E. R. Weber, “Metal content of multicrystalline silicon for solar cells and its impact on minority carrier diffusion length,” *J. Appl. Phys.*, vol. 94, no. 10, pp. 6552–6559, 2003.
- [54] D. MacDonald, A. Cuevas, A. Kinomura, Y. Nakano, and L. Geerligs, “Transition-metal profiles in a multicrystalline silicon ingot,” *J. Appl. Phys.*, vol. 97, no. 3, p. 033523, 2005.
- [55] G. Coletti, R. Kvande, V. D. Mihailetchi, L. J. Geerligs, L. Arnberg, and E. J. Øvrelid, “Effect of iron in silicon feedstock on p-and n-type multicrystalline silicon solar cells,” *J. Appl. Phys.*, vol. 104, no. 10, p. 104913, 2008.
- [56] M. Sanati, N. G. Szwacki, and S. K. Estreicher, “Interstitial Fe in Si and its interactions with hydrogen and shallow dopants,” *Phys. Rev. B*, vol. 76, no. 12, p. 125204, 2007.
- [57] A. Istratov, H. Hieslmair, and E. Weber, “Iron contamination in silicon technology,” *Appl. Phys. A*, vol. 70, no. 5, pp. 489–534, 2000.
- [58] R. Raghunathan, E. Johlin, and J. C. Grossman, “Grain boundary engineering for improved thin silicon photovoltaics,” *Nano Letters*, vol. 14, no. 9, pp. 4943–4950, 2014.

- [59] G. Ludwig and H. Woodbury, “Electronic structure of transition metal ions in a tetrahedral lattice,” *Phys. Rev. Lett.*, vol. 5, pp. 98–100, 1960.
- [60] G. W. Ludwig, H. H. Woodbury, and R. O. Carlson, “Spin of Fe 57,” *Phys. Rev. Lett.*, vol. 1, no. 8, p. 295, 1958.
- [61] G. W. Ludwig and H. H. Woodbury, “Magnetic moment of Fe 57,” *Phys. Rev.*, vol. 117, no. 5, p. 1286, 1960.
- [62] H. Katayama-Yoshida and A. Zunger, “Calculation of the spin-polarized electronic structure of an interstitial iron impurity in silicon,” *Phys. Rev. B*, vol. 31, no. 12, p. 7877, 1985.
- [63] F. Beeler, O. K. Andersen, and M. Scheffler, “Electronic and magnetic structure of 3d-transition-metal point defects in silicon calculated from first principles,” *Phys. Rev. B*, vol. 41, no. 3, p. 1603, 1990.
- [64] H. Wehrich and H. Overhof, “Ground-state properties of isolated interstitial iron in silicon: Electronic structure and hyperfine interactions,” *Phys. Rev. B*, vol. 54, no. 7, p. 4680, 1996.
- [65] D. Macdonald, H. Mäckel, and A. Cuevas, “Effect of gettered iron on recombination in diffused regions of crystalline silicon wafers,” *Appl. Phys. Lett.*, vol. 88, no. 9, p. 092105, 2006.
- [66] S. Dubois, O. Palais, P. Ribeyron, N. Enjalbert, M. Pasquinelli, and S. Martinuzzi, “Effect of intentional bulk contamination with iron on multicrystalline silicon solar cell properties,” *J. Appl. Phys.*, vol. 102, no. 8, p. 083525, 2007.
- [67] H. Hieslmair, A. A. Istratov, S. A. McHugo, C. Flink, T. Heiser, and E. R. Weber, “Gettering of iron by oxygen precipitates,” *Appl. Phys. Lett.*, vol. 72, no. 12, pp. 1460–1462, 1998.
- [68] M. Horikawa and K. Terashima, “Comparison of iron gettering effectiveness in silicon between ion-implantation-induced damage and poly-crystalline silicon,” *Japan J. Appl. Phys.*, vol. 41, no. 12R, p. 7267, 2002.
- [69] J. L. Benton, P. A. Stolk, D. J. Eaglesham, D. C. Jacobson, J. Cheng, J. M. Poate, N. T. Ha, T. E. Haynes, and S. M. Myers, “Iron gettering mechanisms in silicon,” *J. Appl. Phys.*, vol. 80, no. 6, pp. 3275–3284, 1996.

- 
- [70] M. Syre, S. Karazhanov, B. R. Olaisen, A. Holt, and B. G. Svensson, "Evaluation of possible mechanisms behind p gettering of iron," *J. Appl. Phys.*, vol. 110, no. 2, p. 024912, 2011.
- [71] A. A. Istratov, H. Hieslmair, and E. R. Weber, "Iron and its complexes in silicon," *Appl. Phys. A*, vol. 69, no. 1, pp. 13–44, 1999.
- [72] T. Shi, Y. Li, Z. Ma, G. Qu, F. Hong, F. Xu, Y. Yan, and S.-H. Wei, "First-principles study of iron segregation into silicon's 5 grain boundary," *J. Appl. Phys.*, vol. 107, no. 9, pp. 093713–093713, 2010.
- [73] S. Li and Y. Fu, "Smart power technology and power semiconductor devices," in *3D TCAD Simulation for Semiconductor Processes, Devices and Optoelectronics*, 2012, pp. 187–236.
- [74] M. Born and R. Oppenheimer, "On the quantum theory of molecules," *Ann. Phys.*, vol. 84, no. 4, pp. 457–484, 1927.
- [75] F. Mittendorfer and J. Hafner, "Initial steps in the desulfurization of thiophene/ni (100)—a DFT study," *Chemosphere*, vol. 214, no. 2, pp. 234–241, 2003.
- [76] W. Kohn and L. Sham, "Quantum density oscillations in an inhomogeneous electron gas," *Phys. Rev.*, vol. 137, no. 6A, p. A1697, 1965.
- [77] P. Hohenberg and W. Kohn, "Inhomogeneous electron gas," *Phys. Rev.*, vol. 136, no. 3.
- [78] J. P. Goss, M. J. Shaw, and P. R. Briddon, "Marker-method calculations for electrical levels using Gaussian-orbital basis sets," *Topics in Appl. Phys.*, vol. 104, p. 69, 2007.
- [79] U. von Barth and L. Hedin, "A local exchange-correlation potential for the spin polarized case," *J. Phys. C*, vol. 5, no. 13, pp. 1629–1642, 1972.
- [80] A. D. Becke, "A new mixing of Hartree-Fock and local density-functional theories," *J. Chem. Phys.*, vol. 98, no. 2, pp. 1372–1377, 1993.
- [81] R. Jones and P. R. Briddon, *The ab initio cluster method and the dynamics of defects in semiconductors*, ser. Semiconductors and Semimetals. Boston: Academic Press, 1998, vol. 51A, ch. 6.

- [82] M. Rayson and P. Briddon, “Highly efficient method for Kohn-Sham density functional calculations of 500-10 000 atom systems,” *Phys. Rev. B*, vol. 80, no. 20, p. 205104, 2009.
- [83] M. J. Rayson and P. R. Briddon, “First principles method for the calculation of zero-field splitting tensors in periodic systems,” *Phys. Rev. B*, vol. 77, no. 3, p. 035119, 2008.
- [84] M. J. Rayson, “Low-complexity method for large-scale self-consistent ab initio electronic structure calculations without localization,” *Phys. Rev. B*, vol. 75, no. 15, p. 153203, APR 2007.
- [85] P. R. Briddon and R. Jones, “LDA calculations using a basis of Gaussian orbitals,” *Phys. Status Solidi B*, vol. 217, no. 1, pp. 131–171, 2000.
- [86] B. Henderson, *Defects in crystalline solids*. Crane Russak and Company, Incorporated, 1972, vol. 1.
- [87] D. A. Liberman, “Slater transition-state band-structure calculations,” *Phys. Rev. B*, vol. 62, no. 11, pp. 6851–6853, 2000.
- [88] K. Seino and F. Bechstedt, “First-principles calculations of energetics and electronic structure for reconstructed surfaces,” *Phys. Rev. B*, vol. 90, no. 16, p. 165407, 2014.
- [89] O. Schultz, S. W. Glunz, and G. P. Willeke, “Short communication: Accelerated publication: Multicrystalline silicon solar cells exceeding 20%,” *Progress in Photovoltaics: Research and Applications*, vol. 12, no. 7, pp. 553–558, 2004.
- [90] C. Kittel and P. McEuen, *Introduction to solid state physics*. Wiley New York, 1976, vol. 8.
- [91] E. Ziambaras and E. Schröder, “Theory for structure and bulk modulus determination,” *Phys. Rev. B*, vol. 68, no. 6, p. 064112, 2003.
- [92] A. G. Beattie and J. E. Schirber, “Experimental determination of the low-temperature Grüneisen parameter of silicon from pressure derivatives of elastic constants,” *Phys. Rev. B*, vol. 1, no. 4, pp. 1548–1551, 1970.
- [93] H. J. McSkimin and P. Andreatch Jr, “Elastic moduli of silicon vs hydrostatic pressure at 25.0 c and 195.8 c,” *J. Appl. Phys.*, vol. 35, no. 7, pp. 2161–2165, 1964.

- [94] F. Fuchs, J. Furthmüller, F. Bechstedt, M. Shishkin, and G. Kresse, “Quasiparticle band structure based on a generalized Kohn-Sham scheme,” *Phys. Rev. B*, vol. 76, no. 11, p. 115109, 2007.
- [95] R. Rurali, B. Aradi, T. Frauenheim, and A. Gali, “Accurate single-particle determination of the band gap in silicon nanowires,” *Phys. Rev. B*, vol. 76, no. 11, p. 113303, 2007.
- [96] H. J. Monkhorst and J. D. Pack, “Special points for Brillouin-zone integrations,” *Phys. Rev. B*, vol. 13, no. 12, pp. 5188–5192, 1976.
- [97] M. Yin and M. L. Cohen, “Theory of static structural properties, crystal stability, and phase transformations: Application to Si and Ge,” *Phys. Rev. B*, vol. 26, no. 10, p. 5668, 1982.
- [98] M. L. Cohen and T. Bergstresser, “Band structures and pseudopotential form factors for fourteen semiconductors of the diamond and zinc-blende structures,” *Phys. Rev.*, vol. 141, no. 2, p. 789, 1966.
- [99] C. Hartwigsen, S. Goedecker, and J. Hutter, “Relativistic separable dual-space gaussian pseudopotentials from H to Rn,” *Phys. Rev. B*, vol. 58, no. 7, p. 3641, 1998.
- [100] E. Polak, *Computational methods in optimization: a unified approach*. Academic press, 1971, vol. 77.
- [101] W. H. Press, *Numerical recipes in Fortran 77 and Fortran 90: the art of scientific and parallel computing- diskette v 2.06 h*. Cambridge University Press, 1996.
- [102] M. J. Rayson, “On advances in the kernel and functionality of ab initio electronic-structure calculations,” Ph.D. dissertation, University of Newcastle upon Tyne, 2005.
- [103] S. Zhang and J. E. Northrup, “Chemical potential dependence of defect formation energies in GaAs: Application to Ga self-diffusion,” *Phys. Rev. Lett.*, vol. 67, no. 17, p. 2339, 1991.
- [104] G. Makov and M. Payne, “Periodic boundary conditions in ab initio calculations,” *Phys. Rev. B*, vol. 51, no. 7, p. 4014, 1995.

- [105] M. Sanati and S. Estreicher, “Temperature and sample dependence of the binding free energies of complexes in crystals: The case of acceptor-oxygen complexes in si,” *Phys. Rev. B*, vol. 72, no. 16, p. 165206, 2005.
- [106] G. Henkelman, B. P. Uberuaga, and H. Jónsson, “A climbing image nudged elastic band method for finding saddle points and minimum energy paths,” *J. Chem. Phys.*, vol. 113, no. 22, pp. 9901–9904, 2000.
- [107] G. Henkelman and H. Jonsson, “Improved tangent estimate in the nudged elastic band method for finding minimum energy paths and saddle points,” *J. Chem. Phys.*, vol. 113, no. 22, pp. 9978–9985, 2000.
- [108] R. L. Sells, *Elementary modern physics*. Allyn and Bacon, 1980.
- [109] U. Bangert, R. Barnes, L. Hounsome, R. Jones, A. T. Blumenau, P. R. Briddon, M. J. Shaw, and S. Öberg, “Electron energy loss spectroscopic studies of brown diamonds,” *Phil. Mag.*, vol. 86, no. 29-31, pp. 4757–4779, 2006.
- [110] E. W. Weisstein, “Cauchy principal value,” 2002.
- [111] M. Carroll and R. Jones, “Theoretical low-loss eels analysis of transition metal silicide interfaces in “dirty” silicon,” 2009.
- [112] G. Moore, “Cramming more components onto integrated circuits. electronics april 19, 1965,” *The original paper where Moore’s Law was first published*, pp. 114–117, 1965.
- [113] S. M. Sze and K. K. Ng, *Physics of semiconductor devices*, 2006.
- [114] J. Pohl, “Structure and properties of defects in photovoltaics absorber material: Atomic scale computer simulations of si and cu (in, ga) se<sub>2</sub>,” Ph.D. dissertation, Technische Universität, 2013.
- [115] Synopsys, “Sentaurus Device User Guide,” Version K-2015.06, Mountain View, CA, 2015.
- [116] C. J. Chen, *Physics of solar energy*. John Wiley and Sons, 2011.
- [117] T. Rahman and K. Fobelets, “Efficient tool flow for 3d photovoltaic modelling,” *Computer Physics Communications*, vol. 193, pp. 124–130, 2015.

- 
- [118] D. Whittaker and I. Culshaw, “Scattering-matrix treatment of patterned multilayer photonic structures,” *Physical Review B*, vol. 60, no. 4, p. 2610, 1999.
- [119] V. Kumar and A. Nayfeh, “Tcad simulation and modeling of impact ionization (ii) enhanced thin film c-si solar cells,” *Journal of Computational Electronics*, vol. 15, no. 1, pp. 248–259, 2016.
- [120] K. Emery and D. Myers, “Reference solar spectral irradiance: air mass 1.5,” *Center, RERD, Ed*, 2009.
- [121] W. Fichtner, D. J. Rose, and R. E. Bank, “Semiconductor device simulation,” *SIAM Journal on Scientific and Statistical Computing*, vol. 4, no. 3, pp. 391–415, 1983.
- [122] J.-M. Jin, *The finite element method in electromagnetics*. John Wiley & Sons, 2015.
- [123] B. Sopori, “Procd. icds-19,” *Trans Tech Pub., Edited by Gordon Davies and Maria Helena Nazare*, vol. 527, 1997.
- [124] Sentaurus Tutorial, Inc., “Sentaurus process, 7. custom model with alagator,” *âĀĀ*, Tech. Rep., 2012.
- [125] D. Macdonald, J. Tan, and T. Trupke, “Imaging interstitial iron concentrations in boron-doped crystalline silicon using photoluminescence,” *J. Appl. Phys.*, vol. 103, no. 7, p. 073710, 2008.
- [126] G. Masetti, M. Severi, and S. Solmi, “Modeling of carrier mobility against carrier concentration in arsenic-, phosphorus-, and boron-doped silicon,” *IEEE Trans. Electron Devices*, vol. 30, no. 7, pp. 764–769, 1983.
- [127] O. A. Al-Ani, J. P. Goss, N. E. B. Cowern, P. R. Briddon, M. Al-Hadidi, R. Al-Hamadany, and M. J. Rayson, “A density functional study of iron segregation at ISFs and  $\Sigma 5$ -(001) GBs in mc-Si,” *Solid State Phenomena*, vol. 242, pp. 224–229, 2016.
- [128] O. A. Al-Ani, A. M. Sabaawi, J. P. Goss, N. E. B. Cowern, P. R. Briddon, R., and M. J. Rayson, “Investigation into efficiency-limiting defects in mc-Si solar cells,” *Solid State Phenomena*, vol. 242, pp. 96–101, 2016.

- [129] O. A. Al-Ani, J. Goss, P. Briddon, M. Rayson, and N. Cowern, “Interstitial Fe-pairs in silicon,” *J. Cryst. Growth*, vol. 468, pp. 54–56, 2017.
- [130] J. Reiss, R. King, and K. Mitchell, “Characterization of diffusion length degradation in czochralski silicon solar cells,” *Appl. Phys. Lett.*, vol. 68, no. 23, pp. 3302–3304, 1996.
- [131] S. Myers, M. Seibt, and W. Schröter, “Mechanisms of transition-metal gettering in silicon,” *J. Appl. Phys.*, vol. 88, no. 7, p. 3795, 2000.
- [132] S. W. Jones, “Diffusion in silicon,” *IC Knowledge LLC*, 2008.
- [133] H. H. Woodbury and G. Ludwig, “Spin resonance of transition metals in silicon,” *Phys. Rev.*, vol. 117, no. 1, p. 102, 1960.
- [134] S. Greulich-Weber, J. R. Niklas, E. R. Weber, and J. M. Spaeth, “Electron nuclear double resonance of interstitial iron in silicon,” *Phys. Rev. B*, vol. 30, no. 11, p. 6292, 1984.
- [135] P. Schwalbach, S. Laubach, M. Hartick, E. Kankeleit, B. Keck, M. Menningen, and R. Sielemann, “Diffusion and isomer shift of interstitial iron in silicon observed via in-beam mössbauer spectroscopy,” *Phys. Rev. Lett.*, vol. 64, no. 11, p. 1274, 1990.
- [136] G. Weyer, S. Degroote, M. Fanciulli, V. N. Fedoseyev, G. Langouche, V. I. Mishin, A. M. Van Bavel, A. Vantomme, and I. collaboration, “Mössbauer spectroscopy of fe in silicon with the novel laser-ionized 57 mn+ ion beam at isolde,” in *Materials Science Forum*, vol. 258. Trans Tech Publ, 1997, Conference Proceedings, pp. 437–442.
- [137] H. Muller, M. Tuynman, G. Sieverts, and C. Ammerlaan, “Electron paramagnetic resonance on iron-related centers in silicon,” *Phys. Rev. B*, vol. 25, no. 1, p. 25, 1982.
- [138] G. Ludwig and H. Woodbury, “Electron spin resonance in semiconductors,” in *Solid State Phenomena*. Elsevier, 1962, vol. 13, pp. 223–304.
- [139] Y. Yoshida and G. Langouche, *Defects and Impurities in Silicon Materials*. Springer, 2015.

- [140] J. Van Kooten, E. Sieverts, and C. Ammerlaan, “Electron-nuclear double resonance of interstitial positively charged iron in silicon,” *Phys. Rev. B*, vol. 37, no. 15, p. 8949, 1988.
- [141] E. R. Weber, “Transition metals in silicon,” *Applied Physics A: Materials Science & Processing*, vol. 30, no. 1, pp. 1–22, 1983.
- [142] T. Isobe, H. Nakashima, and K. Hashimoto, “Diffusion coefficient of interstitial iron in silicon,” *Japan J. Appl. Phys.*, vol. 28, no. 7R, p. 1282, 1989.
- [143] U. Wahl, J. Correia, E. Rita, J. P. Araújo, J. Soares, I. collaboration *et al.*, “Lattice sites of implanted fe in Si,” *Phys. Rev. B*, vol. 72, no. 1, p. 014115, 2005.
- [144] S. Estreicher, M. Sanati, and N. G. Szwacki, “Iron in silicon: Interactions with radiation defects, carbon, and oxygen,” *Phys. Rev. B*, vol. 77, no. 12, p. 125214, 2008.
- [145] U. Wahl, J. Correia, E. Rita, J. Araújo, J. Soares, I. Collaboration *et al.*, “Fe and Cu in Si: Lattice sites and trapping at implantation-related defects,” *Nucl. Instrum. Methods B*, vol. 253, no. 1, pp. 167–171, 2006.
- [146] T. Mchedlidze and M. Suezawa, “Properties of an iron–vacancy pair in silicon,” *Japan J. Appl. Phys.*, vol. 41, no. 12R, p. 7288, 2002.
- [147] M. Sanati and S. Estreicher, “First-principles study of iron and iron pairs in si,” vol. 401, pp. 105–108, 2007.
- [148] G. Weyer, S. Degroote, M. Fanciulli, V. Fedoseyev, G. Langouche, V. Mishin, A.-M. Van Bavel, A. Vantomme, I. collaboration *et al.*, “Mössbauer spectroscopy of fe in silicon with the novel laser-ionized 57mn+ ion beam at isolde,” in *Mater. Sci. Forum*, vol. 258, 1997, pp. 437–442.
- [149] Y. Yoshida, S. Ogawa, and K. Arikawa, “Direct observation of substitutional fe atoms in si and soi wafers at 1273k,” vol. 340, pp. 605–608, 2003.
- [150] F. Beeler, O. Andersen, and M. Scheffler, “Theoretical evidence for low-spin ground states of early interstitial and late substitutional 3 d transition-metal ions in silicon,” *Phys. Rev. Lett.*, vol. 55, no. 14, p. 1498, 1985.

- 
- [151] A. Zunger and U. Lindefelt, “Theory of substitutional and interstitial 3d impurities in silicon,” *Phys. Rev. B*, vol. 26, no. 10, p. 5989, 1982.
- [152] C. Fall, R. Jones, P. Briddon, A. Blumenau, T. Frauenheim, and M. Heggie, “Influence of dislocations on electron energy-loss spectra in gallium nitride,” *Phys. Rev. B*, vol. 65, no. 24, p. 245304, 2002.
- [153] C. Fall, A. Blumenau, R. Jones, P. Briddon, T. Frauenheim, A. Gutierrez-Sosa, U. Bangert, A. Mora, J. Steeds, and J. Butler, “Dislocations in diamond: Electron energy-loss spectroscopy,” *Phys. Rev. B*, vol. 65, no. 20, p. 205206, 2002.
- [154] J. Van Kooten, E. Sieverts, and C. Ammerlaan, “Electron paramagnetic resonance of an Fe-Fe pair in silicon,” *Solid State Commun.*, vol. 64, no. 12, pp. 1489–1494, 1987.
- [155] H. Takahashi, M. Suezawa, and K. Sumino, “Charge-state-dependent activation energy for diffusion of iron in silicon,” *Phys. Rev. B*, vol. 46, pp. 1882–1885, 1992.
- [156] C. Collins and R. Carlson, “Properties of silicon doped with iron or copper,” *Phys. Rev.*, vol. 108, no. 6, p. 1409, 1957.
- [157] K. Wünstel and P. Wagner, “Interstitial iron and iron-acceptor pairs in silicon.”
- [158] R. Soref and B. Bennett, “Electrooptical effects in silicon,” *IEEE J. Selected Topics in Quant. Electronics*, vol. 23, no. 1, pp. 123–129, 1987.
- [159] S. V. Kovesnikov and G. A. Rozgonyi, “Iron diffusivity in silicon: impact of charge state,” *Appl. Phys. Lett.*, vol. 66, no. 7, pp. 860–862, 1995.
- [160] J. Utzig, “An elastic energy approach to the interstitial diffusion of 3d elements in silicon,” *J. Appl. Phys.*, vol. 65, no. 10, pp. 3868–3871, 1989.
- [161] T. Heiser and A. Mesli, “Charge-state-dependent diffusion and carrier-emission-limited drift of iron in silicon,” *Phys. Rev. Lett.*, vol. 68, no. 7, p. 978, 1992.
- [162] S. K. Estreicher, D. J. Backlund, C. Carboogno, and M. Scheffler, “Activation energies for diffusion of defects in silicon: The role of the exchange–correlation functional,” *Ang. Chem. Int. Ed. Engl.*, vol. 50, no. 43, pp. 10 221–10 225, 2011.
- [163] J. P. Perdew, K. Burke, and M. Ernzerhof, “Generalized gradient approximation made simple,” *Phys. Rev. Lett.*, vol. 77, no. 18, p. 3865, 1996.

- 
- [164] Y. Zhang and W. Yang, “Comment on ‘Generalized gradient approximation made simple,’” *Phys. Rev. Lett.*, vol. 80, no. 4, p. 890, 1998.
- [165] B. Hammer, L. Hansen, and J. Norskov, “Improved adsorption energetics within density-functional theory using revised Perdew-Burke-Ernzerhof functionals,” *Phys. Rev. B*.
- [166] K. Graff and H. Pieper, “The properties of iron in silicon,” *J. Electrochemical Soc.*, vol. 128, no. 3, pp. 669–674, 1981.
- [167] D. Macdonald, T. Roth, P. N. Deenapanray, K. Bothe, P. Pohl, and J. Schmidt, “Formation rates of iron-acceptor pairs in crystalline silicon,” *J. Appl. Phys.*, vol. 98, no. 8, p. 083509, 2005.
- [168] G. Kresse and D. Joubert, “From ultrasoft pseudopotentials to the projector augmented-wave method,” *Phys. Rev. B*, vol. 59, pp. 1758–1775, 1999.
- [169] D. Hull and D. J. Bacon, *Introduction to dislocations*. Butterworth-Heinemann, 2001.
- [170] P. J. King, “Crystal defect imaging using transmission ion channelling.” Ph.D. dissertation, University of Oxford, 1993.
- [171] M. Rumler, M. Rommel, J. Erlekampf, M. Azizi, T. Geiger, A. J. Bauer, E. Meißner, and L. Frey, “Characterization of grain boundaries in multicrystalline silicon with high lateral resolution using conductive atomic force microscopy,” *J. Appl. Phys.*, vol. 112, no. 3, p. 034909, 2012.
- [172] M. Stiles and D. Hamann, “Electron transmission through silicon stacking faults,” *Phys. Rev. B*, vol. 41, no. 8, p. 5280, 1990.
- [173] M. Y. Chou, M. L. Cohen, and S. G. Louie, “Theoretical study of stacking faults in silicon,” *Phys. Rev. B*, vol. 32, no. 12, p. 7979, 1985.
- [174] K. Graff, “Transition metals in silicon and their gettering behaviour,” *Mater. Sci. Eng. B*, vol. 4, no. 1-4, pp. 63–69, 1989.
- [175] K. Uchida and S. Tsuneyuki, “Theoretical investigation on the electronic states localized at grain boundaries in semiconductors,” *Appl. Surf. Sci.*, vol. 190, no. 1, pp. 129–133, 2002.

- [176] J. Chen, T. Sekiguchi, D. Yang, F. Yin, K. Kido, and S. Tsunekawa, “Electron-beam-induced current study of grain boundaries in multicrystalline silicon,” *J. Appl. Phys.*, vol. 96, no. 10, pp. 5490–5495, 2004.
- [177] L. F. Mattheiss and J. R. Patel, “Electronic stacking-fault states in silicon,” *Phys. Rev. B*, vol. 23, no. 10, pp. 5384–5396, 1981.
- [178] S. L. Altmann, A. Lapicciarella, K. W. Lodge, and N. Tomassini, “A valence force field for the silicon crystal,” *J. Phys. C*, vol. 15, no. 27, p. 5581, 1982.
- [179] N. Lehto, “Shallow electron states of bounded intrinsic stacking faults in silicon,” *Phys. Rev. B*, vol. 55, no. 23, p. 15601, 1997.
- [180] R. Hulstrom, R. Bird, and C. Riordan, “Spectral solar irradiance data sets for selected terrestrial conditions,” *Structural Chem.*, vol. 15, no. 4, pp. 365–391, 1985.
- [181] B. Egert and G. Panzner, “Bonding state of silicon segregated to  $\alpha$ -iron surfaces and on iron silicide surfaces studied by electron spectroscopy,” *Phys. Rev. B*, vol. 29, no. 4, p. 2091, 1984.
- [182] O. A. Al-Ani, J. P. Goss, M. Al-Hadidi, P. R. Briddon, N. E. B. Cowern, and M. J. Rayson, “Impact of grain boundary structures on trapping iron,” *J. Cryst. Growth*, vol. 468, pp. 448–451, 2017.
- [183] A. T. Lim, “Migration and mobility of low-angle grain boundaries,” Ph.D. dissertation, Princeton University, 2012.
- [184] SlidPlayer. (2017) crystal interfaces and microstructure. [Online]. Available: <http://slideplayer.com/slide/10914537/>
- [185] R. E. Reed-Hill and R. Abbaschian, “Principles of physical metallurgy,” 1994.
- [186] G. Gottstein and L. S. Shvindlerman, *Grain boundary migration in metals: thermodynamics, kinetics, applications*. CRC press, 2009.
- [187] M. Kohyama and R. Yamamoto, “Tight-binding study of grain boundaries in si: Energies and atomic structures of twist grain boundaries,” *Physical Review B*, vol. 49, no. 24, p. 17102, 1994.
- [188] F. Cleri, “Atomic and electronic structure of high-energy grain boundaries in silicon and carbon,” *Comp. Mater. Sci.*, vol. 20, no. 3, pp. 351–362, 2001.

- 
- [189] J. Zhang, C.-Z. Wang, and K.-M. Ho, “Finding the low-energy structures of si [001] symmetric tilted grain boundaries with a genetic algorithm,” *Phys. Rev. B*, vol. 80, no. 17, p. 174102, 2009.
- [190] J. Bacmann, G. Silvestre, M. Petit, and W. Bollmann, “Partial secondary dislocations in germanium grain boundaries: I. periodic network in a  $\Sigma=5$  coincidence boundary,” *Phil. Mag. A*, vol. 43, no. 1, pp. 189–200, 1981.
- [191] S.-M. Lee, J.-H. Kim, and J.-H. Ahn, “Graphene as a flexible electronic material: mechanical limitations by defect formation and efforts to overcome,” *Materials Today*, vol. 18, no. 6, pp. 336–344, 2015.
- [192] C. Haessler, G. Stollwerck, W. Koch, W. Krumbe, A. Müller, D. Franke, and T. Rettelbach, “Multicrystalline silicon for solar cells: Process development by numerical simulation,” *Advanced Materials*, vol. 13, no. 23, pp. 1815–1819, 2001.
- [193] J. Chen and T. Sekiguchi, “Carrier recombination activity and structural properties of small-angle grain boundaries in multicrystalline silicon,” *Japan J. Appl. Phys.*, vol. 46, no. 10R, p. 6489, 2007.
- [194] A. P. Sutton, “Interfaces in crystalline materials,” *Monographs on the Physice and Chemistry of Materials*, pp. 414–423, 1995.
- [195] T. Buonassisi, A. A. Istratov, M. Heuer, M. A. Marcus, R. Jonczyk, J. Isenberg, B. Lai, Z. Cai, S. Heald, W. Warta *et al.*, “Synchrotron-based investigations of the nature and impact of iron contamination in multicrystalline silicon solar cells,” *J. Appl. Phys.*, vol. 97, no. 7, p. 074901, 2005.
- [196] T. Buonassisi, M. Heuer, A. Istratov, M. Pickett, M. Marcus, B. Lai, Z. Cai, S. Heald, and E. Weber, “Transition metal co-precipitation mechanisms in silicon,” *Acta Mater.*, vol. 55, no. 18, pp. 6119–6126, 2007.
- [197] S. Pennycook and D. Jesson, “High-resolution incoherent imaging of crystals,” *Phys. Rev. Lett.*, vol. 64, no. 8, p. 938, 1990.
- [198] A. V. Crewe, J. Wall, and J. Langmore, “Visibility of single atoms,” *Science*, vol. 168, no. 3937, pp. 1338–1340, 1970.
- [199] P. Nellist and S. Pennycook, “Direct imaging of the atomic configuration of ultra-dispersed catalysts,” *Science*, vol. 274, no. 5286, p. 413, 1996.

- [200] P. Voyles, D. Muller, J. Grazul, P. Citrin, and H.-J. Gossmann, “Atomic-scale imaging of individual dopant atoms and clusters in highly n-type bulk si,” *Nature*, vol. 416, no. 6883, pp. 826–829, 2002.
- [201] J. Chen, D. Yang, Z. Xi, and T. Sekiguchi, “Recombination activity of  $\Sigma$  3 boundaries in boron-doped multicrystalline silicon: Influence of iron contamination,” *J. Appl. Phys.*, vol. 97, no. 3, p. 033701, 2005.
- [202] B. Chen, J. Chen, T. Sekiguchi, M. Saito, and K. Kimoto, “Structural characterization and iron detection at  $\Sigma$  3 grain boundaries in multicrystalline silicon,” *J. Appl. Phys.*, vol. 105, no. 11, p. 113502, 2009.
- [203] A. Liu, D. Walter, S. P. Phang, and D. Macdonald, “Investigating internal gettering of iron at grain boundaries in multicrystalline silicon via photoluminescence imaging,” *IEEE J. Photovolt.*, vol. 2, no. 4, pp. 479–484, 2012.
- [204] D. Macdonald, A. Y. Liu, and S. P. Phang, “External and internal gettering of interstitial iron in silicon for solar cells,” *Solid State Phenomena*, vol. 205, pp. 26–33, 2014.
- [205] J. Hofstetter, D. P. Fenning, D. M. Powell, A. E. Morishige, and T. Buonassisi, “Iron management in multicrystalline silicon through predictive simulation: point defects, precipitates, and structural defect interactions,” *Solid State Phenomena*, vol. 205, pp. 15–25, 2014.
- [206] M. Seibt and V. Kveder, *Advanced Silicon Materials for Photovoltaic Applications*. Wiley, 2012, ch. 4, pp. 127–188.
- [207] A. Liu, Y.-C. Fan, and D. Macdonald, “Interstitial iron concentrations across multicrystalline silicon wafers via photoluminescence imaging,” *Prog.in Photovoltaics: Research and Applications*, vol. 19, no. 6, pp. 649–657, 2011.
- [208] J. Chen, T. Sekiguchi, R. Xie, P. Ahmet, T. Chikyo, D. Yang, S. Ito, and F. Yin, “Electron-beam-induced current study of small-angle grain boundaries in multicrystalline silicon,” *Scripta Materialia*, vol. 52, no. 12, pp. 1211–1215, 2005.
- [209] N. Sakaguchi, H. Ichinose, and S. Watanabe, “Atomic structure of faceted  $\Sigma$ 3 csl grain boundary in silicon: Hrtem and ab-initio calculation,” *Metall. Trans. A*, vol. 48, no. 10, pp. 2585–2589, 2007.

- [210] K. C. Lee and U. Erb, “Grain boundaries and coincidence site lattices in the corneal nanonipple structure of the mourning cloak butterfly,” *Beilstein journal of nanotechnology*, vol. 4, no. 1, pp. 292–299, 2013.
- [211] B. Ziebarth, M. Mrovec, C. Elsässer, and P. Gumbsch, “Interstitial iron impurities at grain boundaries in silicon: A first-principles study,” *Phys. Rev. B*, vol. 91, no. 7, p. 035309, 2015.
- [212] M. C. Payne, P. D. Bristowe, and J. D. Joannopoulos, “Ab initio determination of the structure of a grain boundary by simulated quenching,” *Phys. Rev. Lett.*, vol. 58, no. 13, p. 1348, 1987.
- [213] G. G. DeLeo, G. D. Watkins, and W. B. Fowler, “Theory of interstitial transition-metal impurities in silicon,” *Phys. Rev. B*, vol. 23, no. 4, p. 1851, 1981.
- [214] O. A. Al-Ani, J. P. Goss, M. Al-Hadidi, P. R. Briddon, N. E. B. Cowern, and M. J. Rayson, “Voids in silicon as a sink for interstitial iron: a density functional study,” *J. Cryst. Growth*, vol. 468, pp. 101–103, 2017.
- [215] S. Myers, H. Stein, and D. Follstaedt, “Hydrogen interactions with cavities in helium-implanted germanium,” *Phys. Rev. B*, vol. 51, no. 15, p. 9742, 1995.
- [216] G. K. Hubler, *Ion implantation and ion beam processing of materials: symposium held November 1983 in Boston, Massachusetts, USA*, 1984, vol. 27.
- [217] V. Raineri, “Voids in silicon substrates for novel applications,” *Materials Science and Engineering: B*, vol. 73, no. 1, pp. 47–53, 2000.
- [218] V. Raineri and S. Campisano, “Voids in silicon as sink for interstitials,” *Nuclear Instruments and Methods in Physics Research Section B: Beam Interactions with Materials and Atoms*, vol. 120, no. 1, pp. 56–59, 1996.
- [219] F. Corni, C. Nobili, G. Ottaviani, R. Tonini, G. Calzolari, G. Cerofolini, and G. Queirolo, “Helium in silicon: Thermal-desorption investigation of bubble precursors,” *Phys. Rev. B*, vol. 56, no. 12, p. 7331, 1997.
- [220] H. Nishikawa, T. Tanaka, Y. Yanase, M. Hourai, M. Sano, and H. Tsuya, “Formation of grown-in defects during czochralski silicon crystal growth,” *Japan J. Appl. Phys.*, vol. 36, no. 11R, p. 6595, 1997.

- [221] V. Raineri, S. Coffa, E. Szilagyi, J. Gyulai, and E. Rimini, “He-vacancy interactions in si and their influence on bubble formation and evolution,” *Phys. Rev. B*, vol. 61, no. 2, p. 937, 2000.
- [222] M. Overwijk, J. Politiek, R. De Kruif, and P. Zalm, “Proximity gettering of transition metals in silicon by ion implantation,” vol. 96, no. 1-2, pp. 257–260, 1995.
- [223] B. Mohadjeri, J. Williams, and J. Wong-Leung, “Gettering of nickel to cavities in silicon introduced by hydrogen implantation,” *Appl. Phys. Lett.*, vol. 66, no. 15, pp. 1889–1891, 1995.
- [224] S. Myers and G. Petersen, “Transport and reactions of gold in silicon containing cavities,” *Phys. Rev. B*, vol. 57, no. 12, p. 7015, 1998.
- [225] V. Raineri, “Gettering by voids in silicon: A comparison with other techniques,” in *Solid State Phenomena*, vol. 57, 1997, pp. 43–52.
- [226] V. Raineri and S. Campisano, “Secondary defect dissolution by voids in silicon,” *Appl. Phys. Lett.*, vol. 69, no. 12, pp. 1783–1785, 1996.
- [227] ———, “Voids in silicon as sink for interstitials,” vol. 120, no. 1-4, pp. 56–59, 1996.
- [228] P. K. Chu and N. W. Cheung, “Microcavity engineering by plasma immersion ion implantation,” *Mater. Chem. Phys.*, vol. 57, no. 1, pp. 1–16, 1998.
- [229] E. Bruno, S. Mirabella, F. Priolo, E. Napolitani, C. Bongiorno, and V. Raineri, “He induced nanovoids for point-defect engineering in b-implanted crystalline si,” *Journal of applied physics*, vol. 101, no. 2, p. 023515, 2007.
- [230] C. Griffioen, J. Evans, P. De Jong, and A. Van Veen, “Helium desorption/permeation from bubbles in silicon: A novel method of void production,” *Nucl. Instrum. Methods B*, vol. 27, no. 3, pp. 417–420, 1987.
- [231] V. Raineri, M. Saggio, and E. Rimini, “Voids in silicon by he implantation: From basic to applications,” *J. Mater. Res.*, vol. 15, no. 07, pp. 1449–1477, 2000.
- [232] S. Myers, G. Petersen, and C. Seager, “Binding of cobalt and iron to cavities in silicon,” *J. Appl. Phys.*, vol. 80, no. 7, pp. 3717–3726, 1996.
- [233] V. Raineri, “Voids in silicon substrates for novel applications,” *Mater. Sci. Eng. B*, vol. 73, no. 1, pp. 47–53, 2000.

- 
- [234] C. Seager, S. Myers, R. Anderson, W. Warren, and D. Follstaedt, “Electrical properties of he-implantation-produced nanocavities in silicon,” *Physical Review B*, vol. 50, no. 4, p. 2458, 1994.
- [235] H. S. Radhakrishnan, C. Ahn, J. Van Hoeymissen, F. Dross, N. Cowern, K. Van Nieuwenhuysen, I. Gordon, R. Mertens, and J. Poortmans, “Gettering of transition metals by porous silicon in epitaxial silicon solar cells,” *Phys. Status Solidi A*, vol. 209, no. 10, pp. 1866–1871, 2012.
- [236] S. Dubey, J. N. Sarvaiya, and B. Seshadri, “Temperature dependent photovoltaic (pv) efficiency and its effect on pv production in the world—a review,” *Energy Procedia*, vol. 33, pp. 311–321, 2013.
- [237] C.-Y. Wen and F. Spaepen, “Filling the voids in silicon single crystals by precipitation of  $\text{Cu}_3\text{Si}$ ,” *Philosophical Magazine*, vol. 87, no. 35, pp. 5565–5579, 2007.
- [238] F. Spaepen and A. Eliat, “New methods for determining the void content of silicon single crystals,” *IEEE Transactions on Instrumentation and Measurement*, vol. 48, no. 2, pp. 230–232, 1999.
- [239] J. F. Nijs, J. Szlufcik, J. Poortmans, S. Sivoththaman, and R. P. Mertens, “Advanced manufacturing concepts for crystalline silicon solar cells,” *IEEE Trans. Electron Devices*, vol. 46, no. 10, pp. 1948–1969, 1999.
- [240] F. Cleri, P. Keblinski, L. Colombo, S. R. Phillpot, and D. Wolf, “Correlation between atomic structure and localized gap states in silicon grain boundaries,” *Phys. Rev. B*, vol. 57, no. 11, p. 6247, 1998.
- [241] K. Kutsukake, N. Usami, K. Fujiwara, Y. Nose, and K. Nakajima, “Influence of structural imperfection of  $\Sigma 5$  grain boundaries in bulk multicrystalline si on their electrical activities,” *J. Appl. Phys.*, vol. 101, no. 6, pp. 063 509–063 509, 2007.
- [242] D. Joshi and K. Sharma, “Effects of grain boundaries on the performance of polycrystalline silicon solar cells,” *Indian Journal of Pure and Applied Physics*, vol. 50, no. 9, pp. 661–669, 2012.
- [243] M. Al-Amin and J. D. Murphy, “Increasing minority carrier lifetime in as-grown multicrystalline silicon by low temperature internal gettering,” *Journal of Applied Physics*, vol. 119, no. 23, p. 235704, 2016.

- 
- [244] J. Schön, H. Habenicht, M. Schubert, and W. Warta, “Understanding the distribution of iron in multicrystalline silicon after emitter formation: Theoretical model and experiments,” *J. Appl. Phys.*, vol. 109, no. 6, p. 063717, 2011.
- [245] J. Schön, A. Haarahiltunen, H. Savin, D. P. Fenning, T. Buonassisi, W. Warta, and M. C. Schubert, “Analyses of the evolution of iron-silicide precipitates in multicrystalline silicon during solar cell processing,” *IEEE J. Photovolt.*, vol. 3, no. 1, pp. 131–137, 2013.
- [246] J. Schmidt, B. Lim, D. Walter, K. Bothe, S. Gatz, T. Dullweber, and P. Altermatt, “Impurity-related limitations of next-generation industrial silicon solar cells,” *IEEE J. Photovolt.*, vol. 3, pp. 114–118, 2013.
- [247] Synopsys, Inc., “Simulation of planar solar cells with transfer matrix method,” Tech. Rep., 2007.
- [248] P. Krenckel, S. Riepe, F. Schindler, and T. Strauch, “Optimized grain size of seed plates for high performance multicrystalline silicon,” in *32nd European PV Solar Conference and Exhibition*, 2016.
- [249] Y. Yang, A. Yu, B. Hsu, W. Hsu, A. Yang, and C. Lan, “Development of high-performance multicrystalline silicon for photovoltaic industry,” *Progress in Photovoltaics: Research and Applications*, vol. 23, no. 3, pp. 340–351, 2015.
- [250] Synopsys, Inc., “2d silicon solar cell simulation,” Release G-2012.06, Tech. Rep., 2012.
- [251] B. Sopori, “Impurities and defects in photovoltaic si devices: a review,” in *PROCEEDINGS-SPIE THE INTERNATIONAL SOCIETY FOR OPTICAL ENGINEERING*, vol. 2, 2000, pp. 1214–1226.
- [252] C. Collins and R. Carlson, “Properties of silicon doped with iron or copper,” *Physical Review*, vol. 108, no. 6, p. 1409, 1957.
- [253] P. Altermatt, A. Schenk, G. Heiser, and M. Green, “The influence of a new band gap narrowing model on measurements of the intrinsic carrier density in crystalline silicon,” in *Int. Photovoltaic Sci. Eng. Conf., Sapporo*, vol. 11, 1999, p. 719.

- [254] J. del Alamo, S. Swirhun, and R. Swanson, “Simultaneous measurement of hole lifetime, hole mobility and bandgap narrowing in heavily doped n-type silicon,” in *Electron Devices Meeting, 1985 International*, vol. 31. IEEE, 1985, pp. 290–293.
- [255] B. Sopori, “Impurities and defects in photovoltaic si devices: A review,” in *Proceedings of the 10th International Workshop on the Physics of Semiconductor Devices, Delhi, India*, vol. 1418, 1999.
- [256] R. Krain, S. Herlufsen, and J. Schmidt, “Internal gettering of iron in multicrystalline silicon at low temperature,” *Appl. Phys. Lett.*, vol. 93, no. 15, p. 152108, 2008.
- [257] C. Del Canizo, I. Tobias, R. Lago-Aurrekoetxea, and A. Luque, “Influence of depth-inhomogeneity of lifetime in silicon solar cells,” *J. Electrochemical Soc.*, vol. 149, no. 9, pp. G522–G525, 2002.
- [258] S. Rein and S. Glunz, “Electronic properties of interstitial iron and iron-boron pairs determined by means of advanced lifetime spectroscopy,” *J. Appl. Phys.*, vol. 98, no. 11, p. 113711, 2005.
- [259] M. A. Green, *Solar Cells - Operating Principles, Technology and System Application*. Kensington, Australia: University of NSW, 1992.
- [260] R. Gillen and J. Robertson, “The screened-exchange approximation as alternative method for dft calculations on graphene structures,” *Phys. Status Solidi B*, vol. 247, no. 11-12, pp. 2945–2948, 2010.